A NEW PARADIGM FOR INTERPRETING STRESS INVERSIONS FROM FOCAL MECHANISMS: HOW 3D STRESS HETEROGENEITY BIASES THE INVERSIONS TOWARD THE STRESS RATE

Thesis by

Deborah Elaine Smith

In Partial Fulfillment of the Requirements

for the Degree of

Doctor of Philosophy

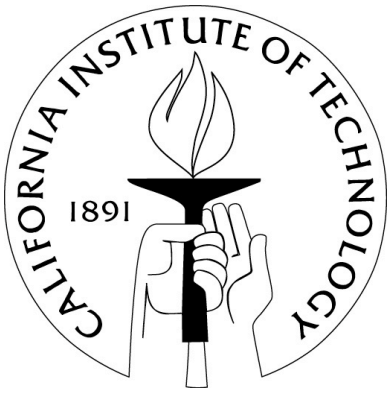

California Institute of Technology

Pasadena, California

2006

(Defended March 27, 2006)

Acknowledgements

I would like to thank my thesis committee, Tom Heaton, Joann Stock, Jeroen Tromp, Jean-Philippe Avouac, and Nadia Lapusta for their feedback and input. Tom Heaton, my thesis advisor and Joann Stock my academic advisor deserve a special thanks. I really appreciate Tom Heaton's support of me throughout my graduate career, his creativity, and our interesting, innovative research discussions. I'm also grateful that he inspired me to take risks research-wise. He was a great research advisor. I appreciate Joann Stock for her guidance in my graduate career and for her insightful, detailed feedback on my thesis. Jeanne Hardebeck from USGS Menlo Park was also helpful in providing me data and plots for comparison to my results. I also appreciate the help from the administrative staff at Caltech, especially Viola who brightened everyone's day and Tess at the Registrar's Office who was always helpful. Thank you to Caltech and the Southern California Earthquake Center for their support of this thesis work.

My officemates, apartmentmates, and friends have been great. I think some of my fondest memories are of Bill, Tad and I pulling off a couple of practical jokes on my advisor Tom Heaton (remember the exploding chalk and the crayfish!), learning to eat various new foods with my apartmentmates Min, Zhimei, and Yizhen, such as chicken's feet, cow stomach (I don't think I ever managed to eat squid legs though), going horseback riding with Maria from Sweden, and watching all five years worth of *Babylon 5* with Mike.

I miss my two cats, Solomon and Minuet, after having to give them up to a good home because of my asthma, but I have to especially thank my 18 lb Solomon for being a

faithful dog-cat. He would always great me at the door when I'd come home then snuggle up with me, purr, and drool all over.

Thanks to Tracy, Mike, Jean, Will, Shawna, Barbara and the women in my small group for the great times we've had hanging out together and praying. Pastor Sherri deserves a special thanks for all the time she's spent with me, encouraging me in the thesis process. My church as a whole, Vision Christian Fellowship, was extremely supportive of me, caring, and loving, which made all the difference. Last, I would like to thank my Lord, Jesus Christ, without whose grace this thesis would not have been possible.

I really don't quite know how to thank my mom and dad. They have consistently and faithfully supported me through all my times at Caltech both good and bad. They were always there when I needed them and they have been great encouragers.

Abstract

Current stress studies often utilize stress inversions of earthquake focal mechanisms to estimate four parameters of the spatially uniform stress tensor, three principal stress orientations, and a ratio of the principal stresses. An implicit assumption in these studies is that earthquakes are good random samplers of stress; hence, the set of earthquake focal mechanisms within some region can be used to estimate the spatial mean stress state within the region. Numerical simulations indicate some regions, such as Southern California, have sufficient stress heterogeneity to bias the stress inversions toward the stress rate orientation and that stress studies using stress inversions need to be reinterpreted by taking this bias into account. An outline of how to subtract out this bias to yield the actual spatial mean stress is presented.

Numerical simulations demonstrate that spatially heterogeneous stress in 3D can bias stress inversions of focal mechanisms toward the stress rate tensor instead of the stress. Stochastic models of 3D spatially heterogeneous stress are created, synthetic earthquake focal mechanisms are generated using the Hencky-Mises plastic yield criterion, and results are compared with Hardebeck's Southern California earthquake catalog [*Hardebeck,* 2006*]*. The presence of 3D spatial stress heterogeneity biases which orientations are most likely to fail, a bias toward the stress rate tensor. When synthetic focal mechanisms are compared to real data, estimates of two stress heterogeneity parameters for Southern California are obtained: 1) A spatial smoothing parameter, $\alpha \approx 0.8$, where α describes the spectral falloff of 1D cross sections through a 3D grid for the three principal stresses and three orientation angles. 2) A heterogeneity ratio, $HR \approx 1.25$, which describes the relative amplitude of the spatial stress heterogeneity to

the spatial mean stress. The estimate for α is tentative; however, varying α for $\alpha \leq 1.0$ has little to no effect on the observation that spatially heterogeneous stress biases failures toward the stress rate. The estimate for HR is more robust and produces a bias toward the stress rate of approximately 40%. If the spatial mean stress and the stress rate are not aligned, the average focal mechanism failure mechanism should yield a stress estimate from stress inversions, approximately halfway between the two.

Table of Contents

Chapter 1. Introduction

In geophysics there is increasing interest in modeling spatially nonuniform stress, i.e., spatially heterogeneous stress, on 2D planar faults as a means of explaining a variety of geophysical phenomena. This thesis goes beyond 2D and models the effect of 3D spatially heterogeneous stress on focal mechanism orientations, seismic clustering, stress rotations after mainshocks, and strength of the crust. We ask, what happens when one drops the assumption that stress is approximately spatially uniform in the crust. We find that there is ample reason to believe that stress is spatially heterogeneous in 3D for some regions (Figures 1.1–1.3), and including heterogeneity may profoundly change how one interprets seismic observables. It is our hope that by modeling stress heterogeneity statistically, we can encourage others to view stress in the crust from a substantially different perspective. The problems addressed in this thesis using heterogeneous stress are only the tip of the iceberg for what we hope will be a rich research field in the future.

Observations of Heterogeneous Stress

Observations of spatially varying slip along fault zones and in earthquakes suggest that both slip and stress are very spatially heterogeneous and possibly fractal in nature [*Andrews*, 1980; 1981; *Ben-Zion and Sammis*, 2003; *Herrero and Bernard*, 1994; *Lavallee and Archuleta*, 2003; *Mai and Beroza*, 2002; *Manighetti, et al.*, 2005; *Manighetti, et al.*, 2001]. For example, McGill and Rubin [1999] observed a 1 m change in slip over a distance of approximately 1 km in the Landers earthquake, which is a 10^{-3} strain change. This implies possibly a 100 MPa stress change over the distance of 1 km. The observed strain and stress change reported by McGill and Rubin is just one example

indicating the Earth may contain large stress fluctuations over small spatial wavelengths. Similar strain changes can be seen in the slip inversion from the Landers earthquake [*Wald and Heaton*, 1994] (Figure 1.1). Another example of highly variable, heterogeneous slip over short wavelengths comes from Manighetti et al. [2001] (Figure 1.2). Using altimetry data in the Afar depression, East African rift, they show heterogeneous cumulative slip as a function of distance, with short wavelength strains of the order $5x10^{-2}$. While it is true that non-elastic processes may come into play at such large shear strains, it does demonstrate a few features. Heterogeneous slip patterns exist not just for individual earthquake slip histories but persist for the entire cumulative slip history of fault zones, indicating that slip heterogeneity is a stable feature. In addition, the cumulative slip shows possibly self-similar, fractal patterns as seen in Figure 1.2b; i.e., subsections of cumulative slip have similar slip heterogeneity patterns as the sum of all the subsections.

Borehole studies, which measure the orientation of maximum horizontal compressive stress directly from borehole breakouts, also indicate that stress can be quite heterogeneous. Figure 1.3, a summary figure from Wilde and Stock [1997], shows the inferred directions of S_H, the maximum horizontal compressive stress, from borehole breakouts. Multiple boreholes with different orientations had been drilled at approximately the same locations, which Wilde and Stock analyzed to constrain the relative magnitudes of the principal stresses. What is most interesting to our study is that boreholes drilled within close proximity of each other can show greatly varying S_H orientations, indicative of heterogeneous stress (Figure 1.3). Figure 1.4, taken from a

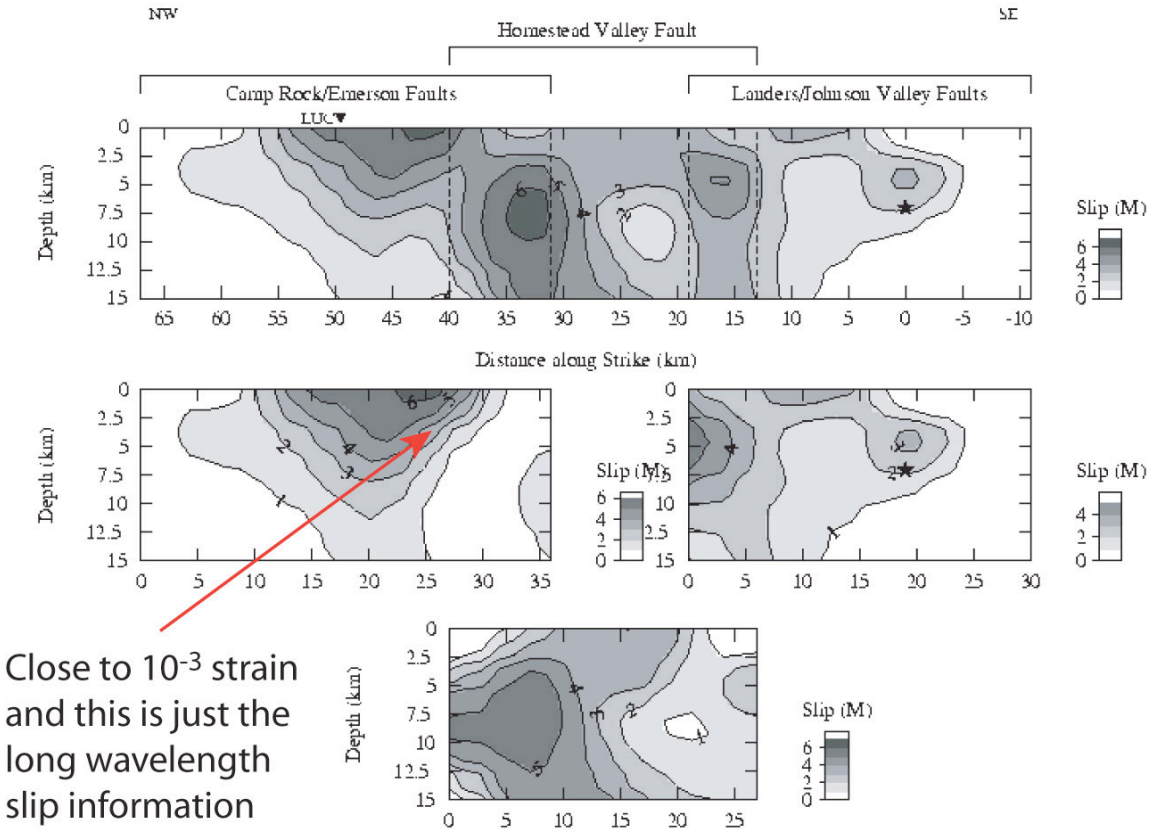

Figure 1.1. *Figure modified from Wald and Heaton [Wald and Heaton, 1994] showing the final slip distribution for the 1992 Landers earthquake. The contours are for 1m slip intervals with the higher slips shaded with darker greys. There are places within the slip distribution on this figure where the strain is approximately* 10^{-3}. *The strain varies over the surface of the rupture, which would produce stress changes over the surface of the rupture and lock in heterogeneous stress. This slip distribution is limited by the data to longer wavelength variations in slip; therefore, there may be even shorter wavelength spatial stress heterogeneity that was locked in by the dynamic rupture process.*

study of the Cajon pass borehole [*Barton and Zoback*, 1994], also shows significant heterogeneity in the orientations of borehole breakouts for an individual borehole near an active fault. The + signs or pulses represent the actual breakout data from the Cajon well, and the triangles represent the modeled breakouts from Barton and Zoback [1994]. There are variations in the breakout orientations over different lengthscales, and there is an anomaly at approximately 2850 m depth, but the feature we find most interesting is the short length-scale variations in the orientations of S_H. In places there is an approximately 90° rotation of S_H over a 1–10 m length. This would appear to support our hypothesis that stress can be quite heterogeneous over short length-scales in tectonically active regions.

Liu-Zeng et al. [2005] have also shown that the assumption of short wavelength heterogeneous fractal slip can reproduce distributions of earthquakes having slip vs. length ratios similar to real earthquakes and realistic Gutenberg-Richter frequency magnitude statistics. Using simple stochastic models, they showed that spatially connected slip can produce averaged stress drops (a constant times average slip divided by rupture length) similar to real data.

Perhaps the most interesting piece of data comes from Zoback and Beroza [1993] (Figure 1.5). They studied the orientations of aftershock planes from the Loma Prieta earthquake and plotted their distributions as a function of strike and dip. Interestingly, they found aftershocks that had both right-lateral and left-lateral orientations on similar fault planes as well as normal and reverse orientations. Given that this is considered a San Andreas fault earthquake and the San Andreas fault is a strongly right-lateral fault, the existence of left-lateral aftershocks on fault planes parallel to the San Andreas Fault

presents a curious problem. Zoback and Beroza proposed that the principal compressive stress direction was almost normal to the fault and that the aftershocks occurred on extremely weak faults of different orientations surrounding the mainshock zone. However, if one allows for the new paradigm of spatially heterogeneous stress in three dimensions, which is being advocated in this thesis, the left-lateral orientations naturally occur. Figure 1.6, taken from Chapter 5, shows our initial hypothesis for what a 1D cross section of shear stress in Northern or Southern California might look like. While most of the points have positive shear stress on the σ_{12} plane, a small percentage have negative shear stress on the σ_{12} plane. Heterogeneity similar to this could explain why Zoback and Beroza observed left-lateral aftershocks after the Loma Prieta earthquake; the large local stress change to the system from the mainshock, combined with stress heterogeneity in the left-lateral direction, would create the left-lateral aftershocks.

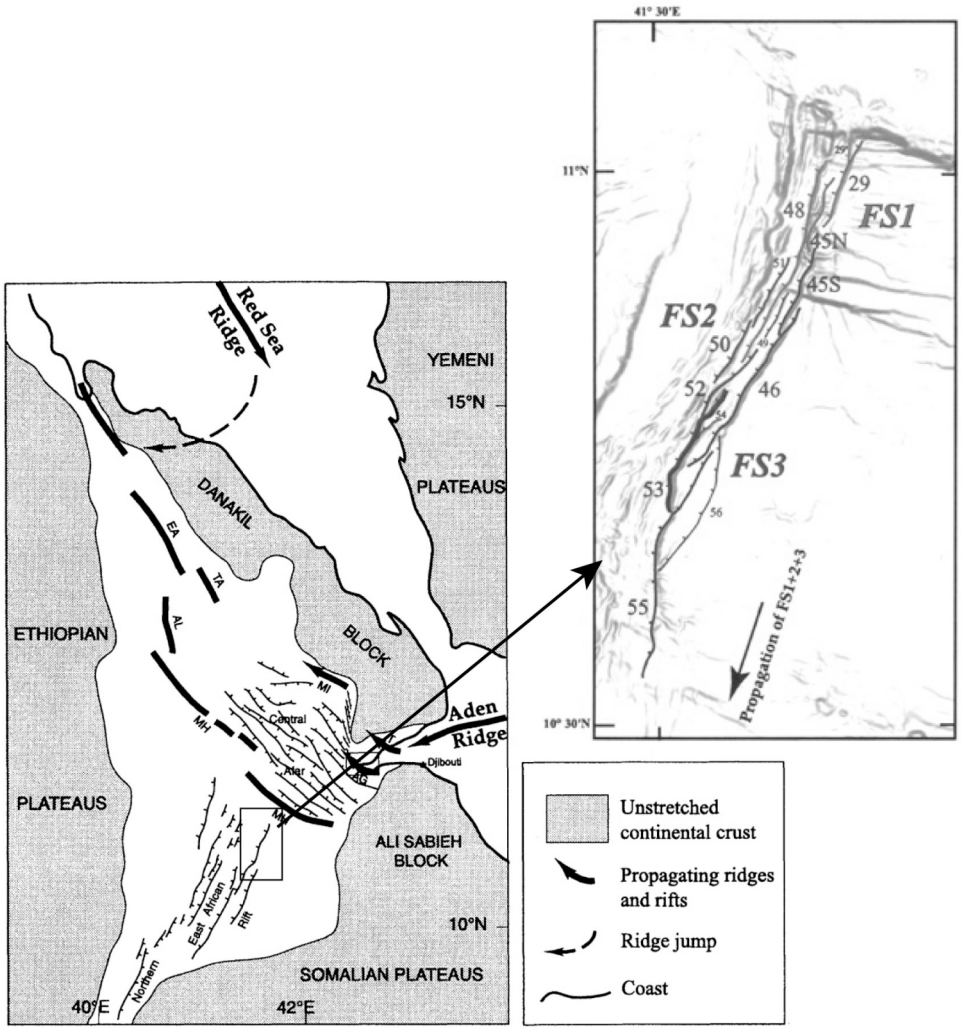

Figure 1.2 a)

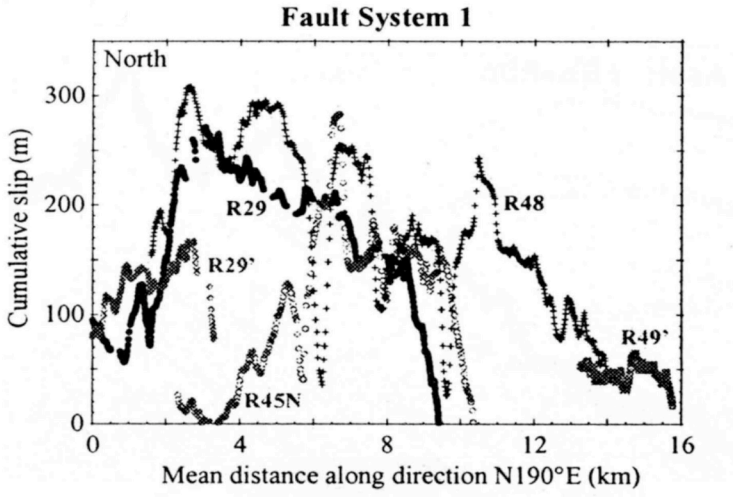

Figure 1.2 b)

Figure 1.2. *Sample evidence of large stress and strain spatial heterogeneity due to a series of earthquakes (from Manighetti et al., 2001).* ***a)*** *A map of the fault system 1, in the East African Rift.* ***b)*** *Typical slip vs. length plots within one of the fault systems. There is great spatial heterogeneity in slip, which implies short wavelength strains of the order* $5x10^{-2}$.

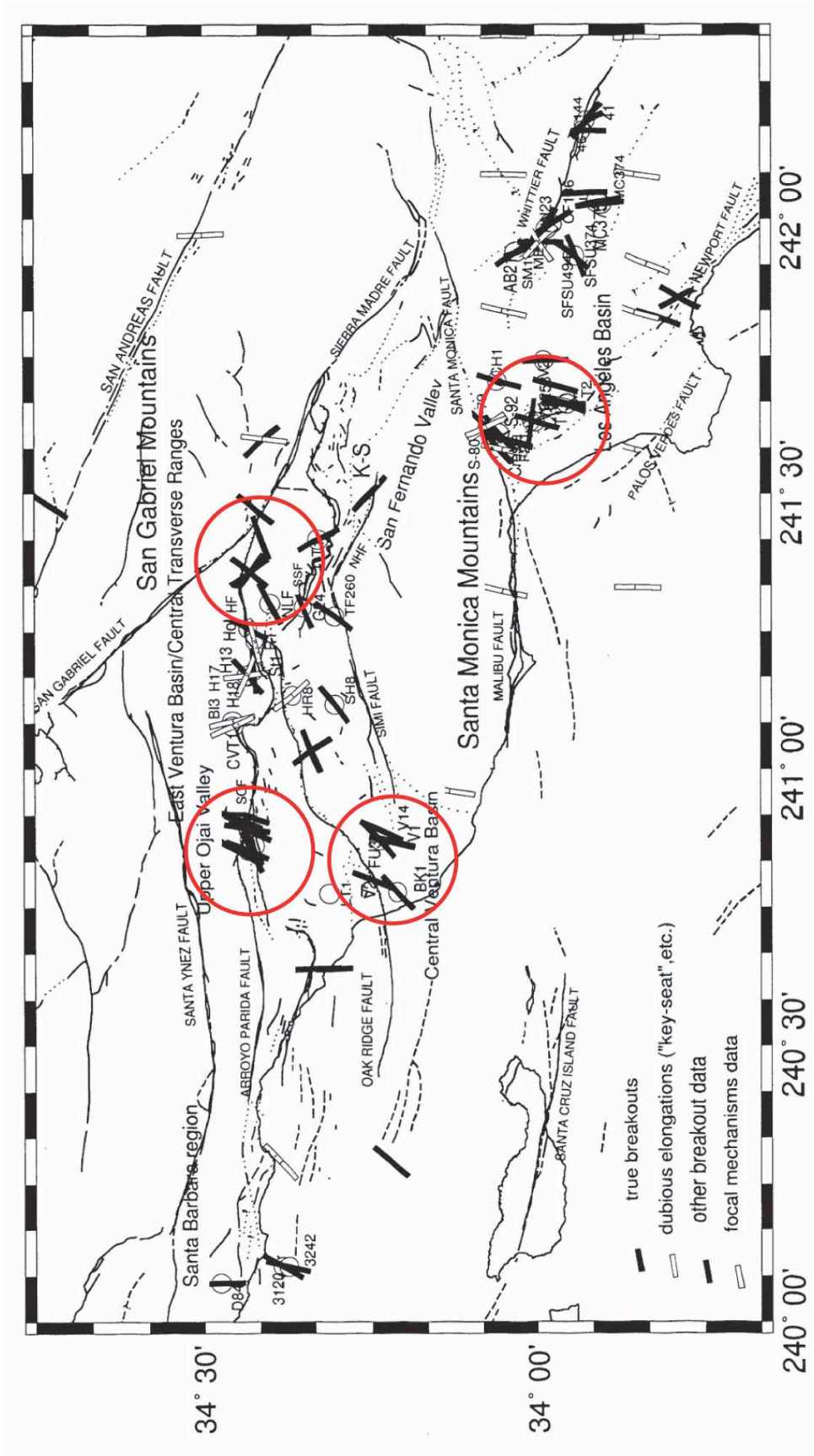
SAN ANDREAS FAULT
San Gabriel Mountains
East Ventura Basin/Central Transverse Ranges
SIERRA MADRE FAULT
SAN GABRIEL FAULT
Upper Ojai Valley
San Fernando Valley
SANTA MONICA FAULT
Santa Monica Mountains
Los Angeles Basin
WHITTIER FAULT
NEWPORT FAULT
PALOS VERDES FAULT
SANTA YNEZ FAULT
ABROYO PARIDA FAULT
OAK RIDGE FAULT
SIMI FAULT
MALIBU FAULT
Central Ventura Basin
SANTA CRUZ ISLAND FAULT
Santa Barbara region
true breakouts
dubious elongations ("key-seat",etc.)
other breakout data
focal mechanisms data
34° 30'
34° 00'
240° 00'
240° 30'
241° 00'
241° 30'
242° 00'

Figure 1.3. *Wilde and Stock [1997] plotted inferred maximum horizontal compressive stress, S_H, orientations from borehole breakouts in Southern California. There are a variety of orientations for borehole breakouts from the same borehole or from boreholes spatially close to one another. This suggests short-wavelength spatial stress heterogeneity. In this modified plot, we have used red circles to point out a few of the locations studied by Wilde and Stock that show evidence for S_H orientation heterogeneity.*

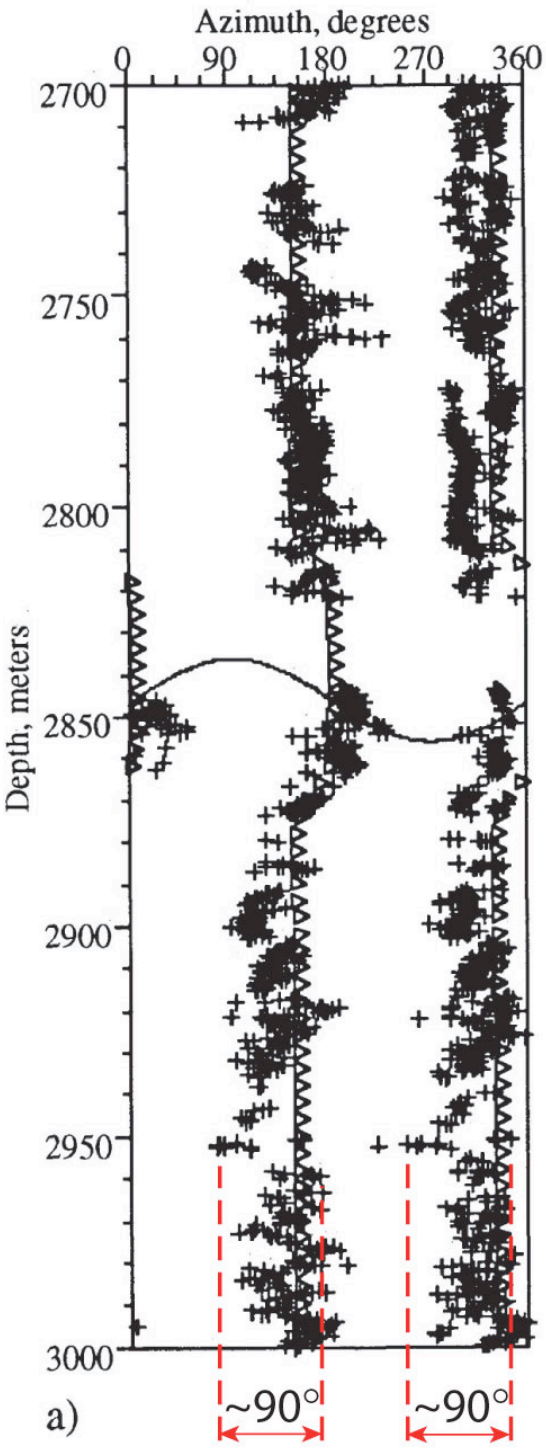

Example of an Approximately 90° Rotation of the Maximum Horizontal Compressive Stress over a Distance of 1–10 m

Figure 1.4. *Barton and Zoback [1994] plotted maximum horizontal compressive stress, S_H, azimuth as a function of depth for breakouts in the Cajon Pass borehole. The plus signs are the breakout data and the triangles represent Barton and Zoback's model. There is an anomaly at 2850 m depth, and there is significant short wavelength rotation of S_H as a function of depth. In this modified figure, we have shown a sample location with an approximately 90° rotation of S_H over a distance of 1–10 m. This provides support for our hypothesis that there can be significant short wavelength stress heterogeneity in tectonically active regions.*

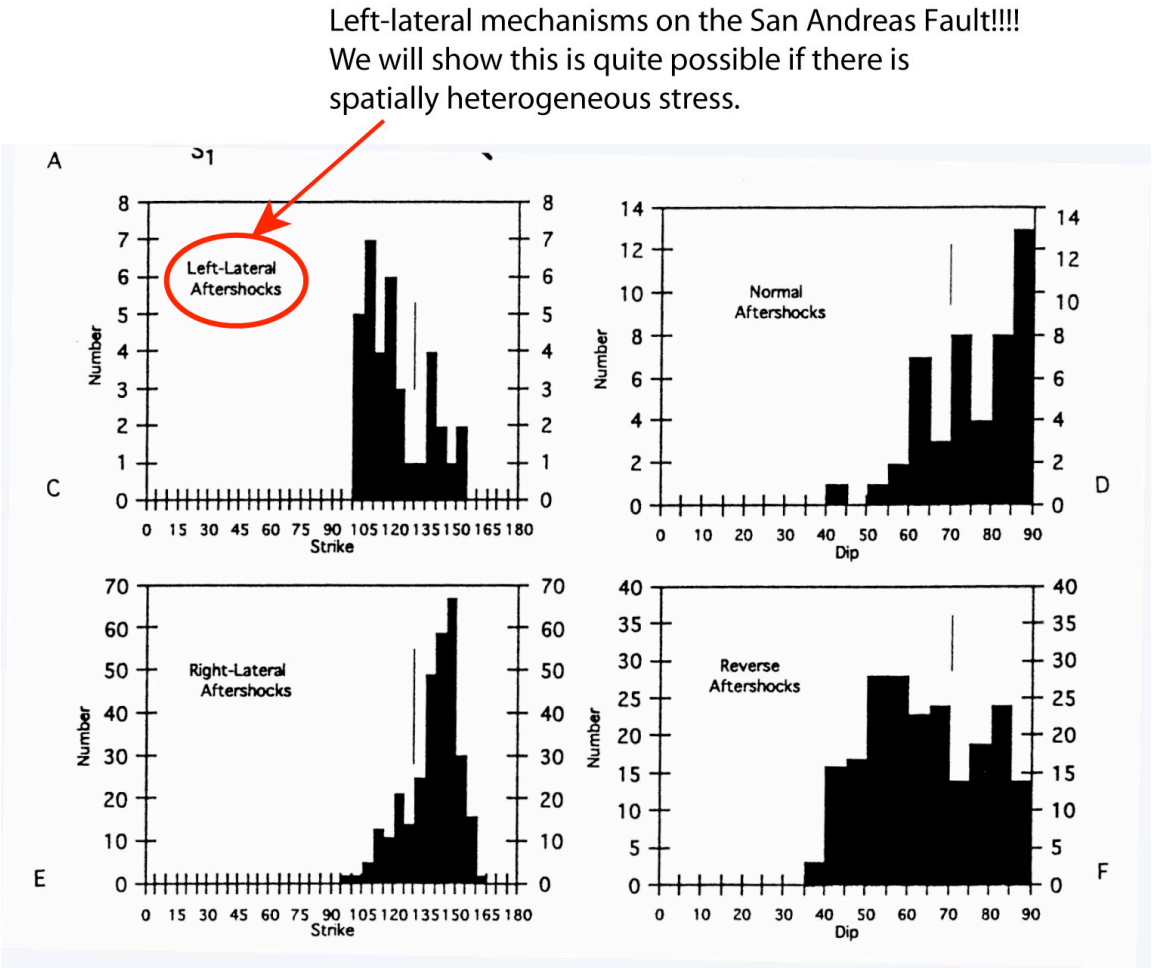

Figure 1.5. *Figure modified from Zoback and Beroza [1993] shows histograms of the different aftershock orientations. Most of the aftershocks had a right-lateral fault orientation. About 10% had left-lateral orientation. We propose that stress heterogeneity is the most natural explanation for left-lateral mechanisms on the right-lateral San Andreas Fault.*

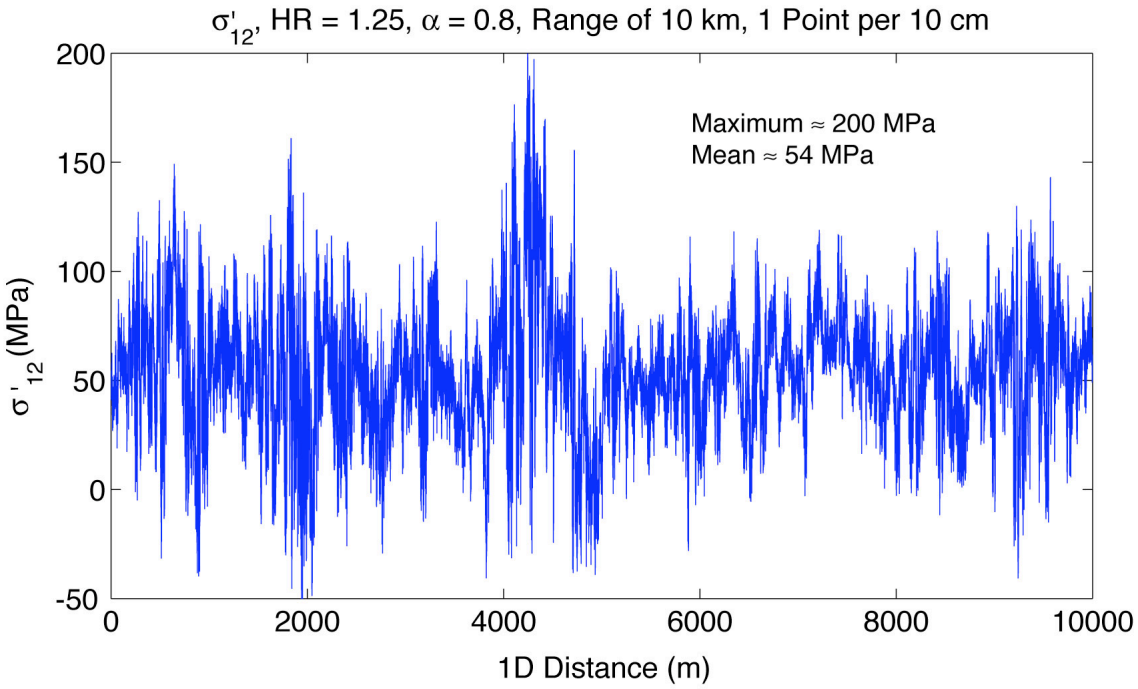

Figure 1.6. *Figure taken from Chapter 5 of this thesis. If the spatial stress heterogeneity has a moderate to large amplitude compared to the spatial mean stress, there will exist both points with positive shear stress and points with negative shear stress. Therefore, it is possible in a right-lateral shear stress regime to have a few left-lateral aftershocks as seen in Figure 1.5.*

Motivation for Heterogeneous Stress from Dynamics Ruptures

Now that we know fractal-like, spatially heterogeneous slip and heterogeneous stress is observed in the real Earth and that heterogeneous slip/stress is compatible with seismic observables, one may ask, how does the Earth possibly produce this spatial heterogeneity.

In the dynamic paradigm, we find that simulated dynamic earthquake ruptures produce increasingly heterogeneous slip as the dynamic friction becomes increasingly sensitive to the slip velocity. This is what Aagaard and Heaton [in preparation, 2006] discovered when they simulated long earthquake sequences on a planar fault subject to constant shear strain in time. If the value of dynamic friction in the real Earth is quite sensitive to changes in the slip velocity, it could explain observed slip heterogeneity; and indeed, there is evidence this may be true. The argument is as follows. Exhumed faults tend to yield thin primary deformation zones indicating there is little to no melting during the dynamic earthquake rupture [*Sibson*, 2003]. Given the typical sliding velocities of 1 m/s, it suggests that the dynamic friction value is quite small for the duration of the rupture; otherwise, one would see significant pseudotachylyte friction-melt. Heat flow studies of the San Andreas Fault also yield anomalously low heat flow values for a dynamic coefficient of friction of $\mu \approx 0.6$ [*Lachenbruch and Sass*, 1980], again indicating that the dynamic coefficient of friction may be small. A possible explanation is that there is a sudden transition from the high static friction, $\mu > 0.6$, to low dynamic friction, $\mu < 0.1$, in the vicinity of the rupture front, with a similar transition back to high friction as one moves away from the rupture front, i.e., extreme velocity weakening. Interestingly, this is similar to Rice's [1999] flash heating friction law and experimental

results reported by Tullis and Goldsby [2005] where they observed dramatic reductions in sliding friction for velocities $> 50\ cm/s$, possibly flash heating. Tullis, in a recent presentation [*Tullis*, 2005] available online at http://online.itp.ucsb.edu/online/earthq05/tullis, showed plots of friction coefficient as a function of sliding velocity for three different materials: quartz, granite, and gabbro. The low velocity friction coefficients range from a little over 0.6 to approximately 0.9 depending on the material. At sliding velocities of $> 50\ cm/s$, the sliding coefficient of friction approaches a value of 0.2. Interestingly, these experiments also observe instantaneous full healing. This combination of high static friction, low sliding friction, and instantaneous healing back to high static friction will freeze in short length-scale stress heterogeneity, i.e., abrupt spatial stress changes along the length of the fault.

In flash heating, as the two sides of the fault begin sliding past some threshold velocity under normal stress and with asperities, a thin layer melts and dramatically lowers the coefficient of friction for a short time. After flash heating, other mechanisms may be activated such as full or partial melting and pore pressure evolution. If the real Earth experiences flash heating or other strongly velocity dependent effects during earthquakes, then it is quite plausible that very heterogeneous stresses would be locked into the crust when high dynamic stresses are frozen in by the sudden transitions from static to dynamic friction, then back to static friction. This is a length-scale independent effect. Since the two types of stress states that are compatible with length-scale independent processes are homogeneous stress and fractal stress, we believe some type of fractal heterogeneous stress is a good initial hypothesis.

Of interest, Rice, Lapusta and Ranjith [2001] showed through theoretical studies that there are problems with only velocity-dependent friction that have no solution (i.e., are ill-posed). The problems do not converge; i.e. there is no solution as you reduce the grid size. We hypothesize that a fractal heterogeneous solution (with no inherent length-scale) might be the answer to this problem.

A static effect that can also produce heterogeneous stress was recently presented by Dieterich [2005]. Fault traces in nature are rarely if ever completely planar; there is usually some small-scale 3D geometry to the fault trace. Modeling fault traces with fractal geometry, solving for slip with boundary elements and using a $\mu = 0.6$, he found that even very small variations in fault trace can produce significant near-fault stress heterogeneity and create spatially heterogeneous aftershock rates. In this case, the coefficient of friction was not varied dynamically, so this is an entirely independent effect that also creates stress heterogeneity.

Stress Model to Be Used in the Thesis

In this thesis, we create 3D grids like Figure 1.7, where the full or deviatoric stress tensor is defined at each spatial grid point using equation (1.1). The principal stresses and orientations of the heterogeneous stress tensor, $\boldsymbol{\sigma}'_H(\mathbf{x})$, are randomly generated; then a discrete spatial filter is applied to produce power-law spatial stress heterogeneity. Chapters 2 and 3 explain how we do this in detail. A spatially and temporally homogeneous stress tensor, $\boldsymbol{\sigma}'_B$, what stress inversions approximately solve for, is added. Last, points are brought to failure by adding on a linearly increasing tectonic stress due to the stress rate, $\dot{\boldsymbol{\sigma}}'_T$, and applying a plastic yield failure criterion.

This generates point failures within our 3D grid, which we call earthquakes, and produces our set of synthetic focal mechanisms. Chapter 4 shows the steps of bringing points to failure as well as simulations that demonstrate how large amplitude spatially heterogeneous stress biases stress inversions toward the stress rate tensor, $\dot{\boldsymbol{\sigma}}'_T$.

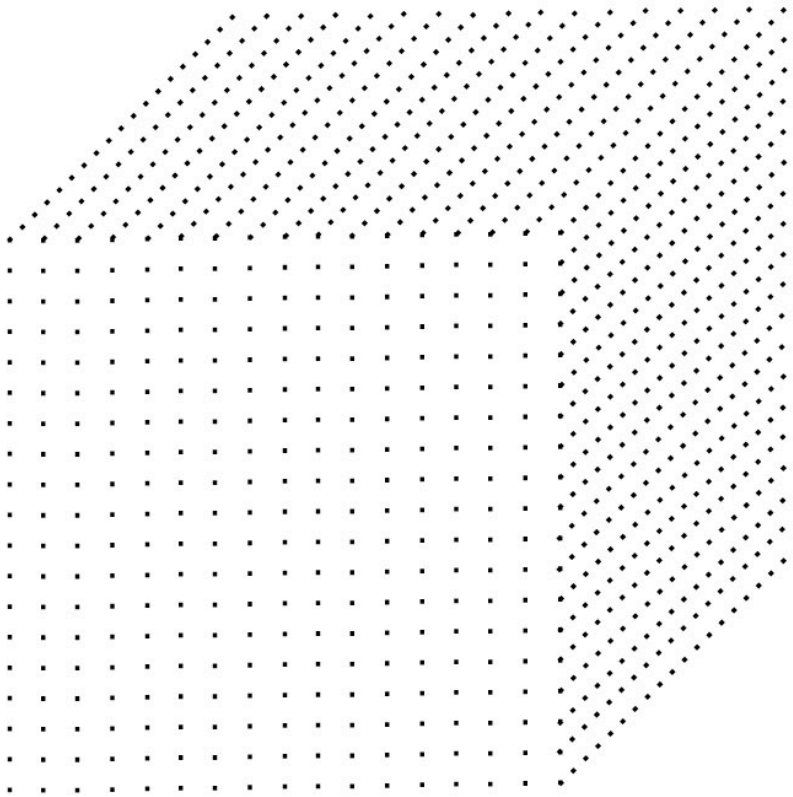

Figure 1.7. *A sample 3D grid of points. In our numerical simulations we would define the full or deviatoric stress tensor at each spatial grid point.*

In creating equation (1.1) we approximate stress in time and space as a decomposition that is a linear sum of parts that are 1) spatially and temporally uniform, 2) varying with time, but relatively homogeneous spatially, and 3) spatially very heterogeneous, but do not vary much over the time scale of decades. While there are many features of real mechanics that are not included in this description but are discussed more in the following section, this is the simplest decomposition that we could think of, which also contains the essential features of a temporally varying stochastic stress model.

$$\boldsymbol{\sigma}'(\mathbf{x},t) = \boldsymbol{\sigma}'_B + \dot{\boldsymbol{\sigma}}'_T t + \boldsymbol{\sigma}'_H(\mathbf{x}) \tag{1.1}$$

Where

$\boldsymbol{\sigma}'_B$ is the background stress, which is the spatially and temporally averaged stress tensor in the region of interest. This is the quantity that traditional stress inversions are designed to find.

$\dot{\boldsymbol{\sigma}}'_T(t)$ is the temporally varying stress due to plate tectonics. For example, if there is far-field loading but the fault in the brittle upper crust is locked, there can be a temporal increase of stress as a function of time (Figure 1.8). There may also be fault interactions that can produce regional stress rates similar to what is seen in Figure 1.9, modified from Becker et al. [2003] for Southern California. Or short-term stress rates could be created by post-seismic visco-elastic relaxation.

This term is assumed to grow linearly with time for our short simulation time windows of 10–20 years, but is assumed to be small compared to $\boldsymbol{\sigma}'_H(\mathbf{x})$ and $\boldsymbol{\sigma}'_B$. While, in reality, it varies with space, the spatial variations are small by St. Venant's principle since the forces are applied at a distance. In general, we

assume that $\boldsymbol{\sigma}'_B$ and $\dot{\boldsymbol{\sigma}}'_T$ have different orientations. For example, the principal compression of the average background stress might be oriented nearly perpendicular to the San Andreas Fault [*Townend and Zoback*, 2004]; whereas, the stress rate compression axis must be at a 45° angle, since shear on the San Andreas Fault accommodates most of the plate motion. Simulations in Chapter 4 explore this possibility.

$\boldsymbol{\sigma}'_H(\mathbf{x})$ is spatially varying stress. By definition, its spatial average is zero. The heterogeneous stress is assumed to be due to all of the stress changes caused by local inelastic deformations such as the slip distribution due to faulting, compaction, fluids, thermal stresses, topography, etc. The heterogeneity is described by two parameters,

1. α, where the amplitude spectrum of any 1D cross section through our 3D $\boldsymbol{\sigma}'_H(\mathbf{x})$ grid is proportional to $1/k^{\alpha}$ and [*Barnsely, et al.*, 1988]

2. ***Heterogeneity Ratio*** $= HR = \dfrac{\sqrt{Mean\left[Spatially\ Heterogeneous\ I'_2\right]}\ \left[\text{Units of Stress}\right]}{\sqrt{Spatially\ Uniform\ Background\ Stress\ I'_2}\ \left[\text{Units of Stress}\right]}$, which is a dimensionless number relating the size of the heterogeneity to the size of the background stress to create a dimensionless heterogeneity amplitude. I'_2, the second invariant of the deviatoric stress tensor, a nonnegative number, is a measure of maximum shear stress regardless of orientation, and is the quantity used in our primary failure criterion. That is why we use I'_2 for our measure of heterogeneity amplitude.

We also assume that the stochastic properties of $\boldsymbol{\sigma}'_H(\mathbf{x})$, described by *HR* and α, do not significantly evolve in time for the simulations we present in the thesis; therefore, we do not update $\boldsymbol{\sigma}'_H(\mathbf{x})$ after each event. Specifically, we are interested in stress inversions that are applied to background seismicity, in between major seismic events over a time window in the range of 1–20 years. A major event will significantly change the 3D stress pattern and would have to be taken into account, which is a future research direction we have begun delving into. However, we assume that the heterogeneous slip patterns, after some stress relaxation, regenerate heterogeneous stress that will have approximately the same stochastic properties as before the major earthquake.

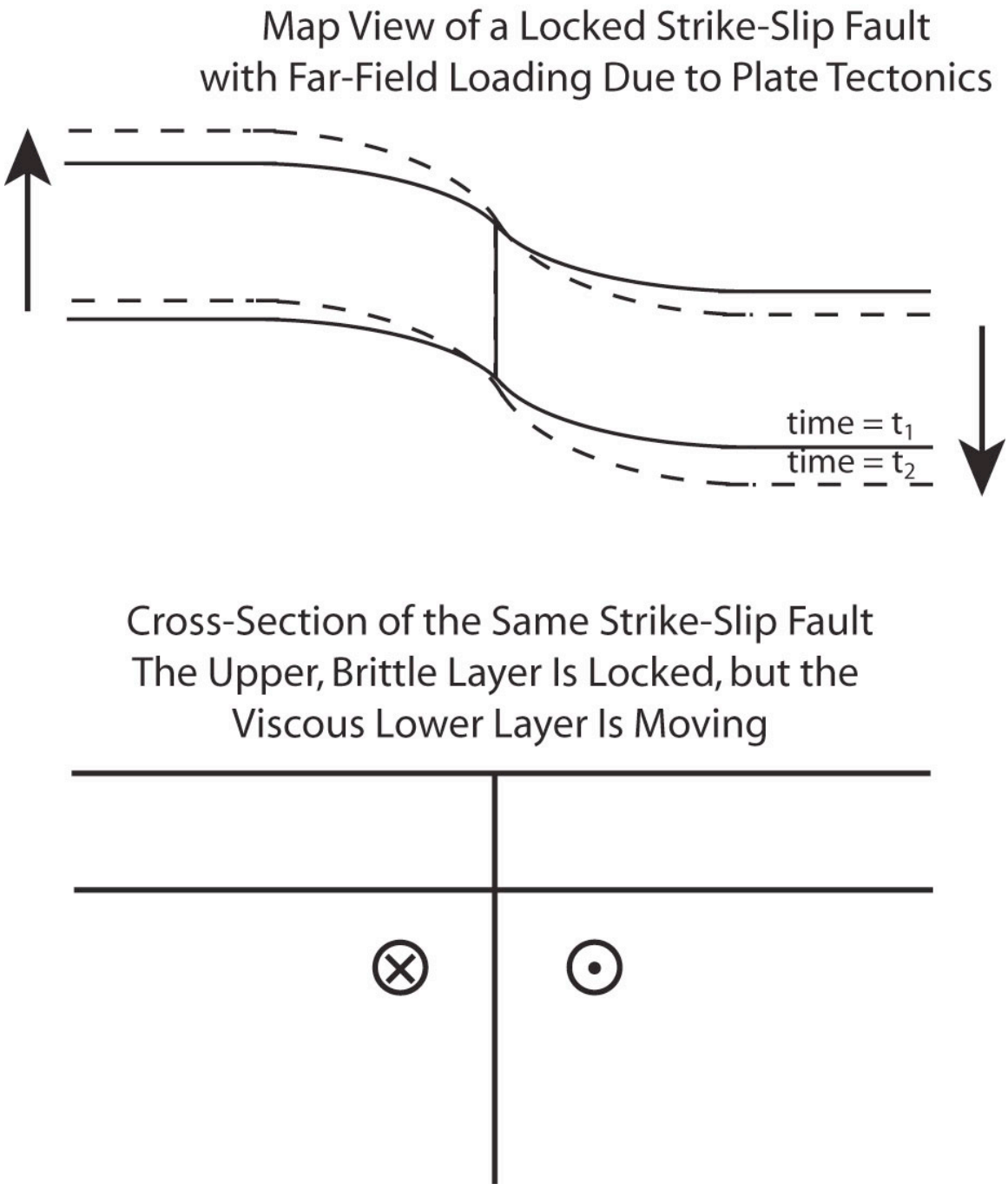

Figure 1.8. *Cartoon of one mechanism that could create our stress rate,* $\dot{\sigma}_T$. *There is far-field loading of a locked, strike-slip fault that will build up stress in time.*

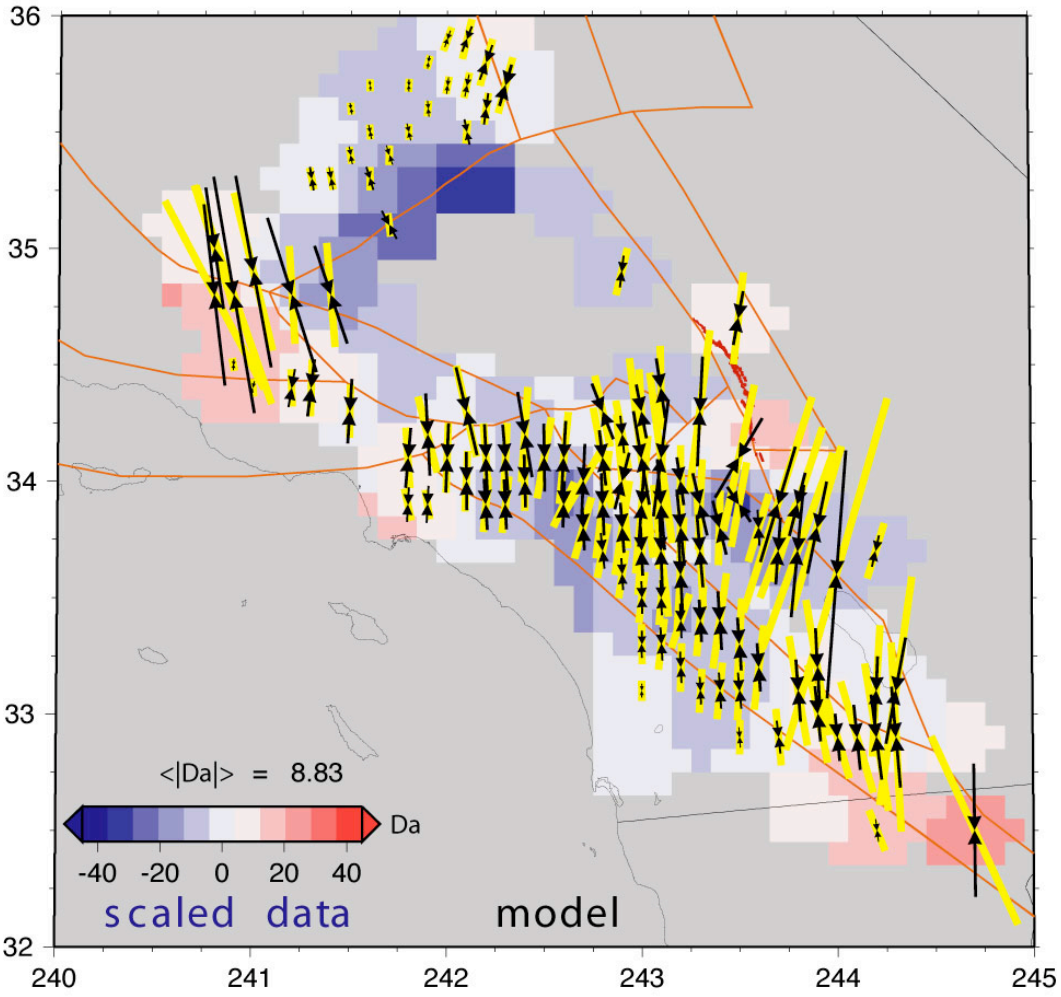

Figure 1.9. *Figure modified from Becker et al. [2003]. They compared the major horizontal compressive axes between: 1) Residual strain rates (in black) modeled from GPS data and block fault models and 2) regional stress inversions (in yellow) from earthquake focal mechanisms. While there is variation in the strain rate data from region to region, one can pick a region like the Los Angeles Basin where there is little to no variation in the orientation of the black strain rate vectors, indicating it is possible to use a spatially uniform stress rate tensor,* $\dot{\boldsymbol{\sigma}}_T$*, for some regional studies. At the very least, this shows that the strain rate orientations, and by implication the stress rate orientations, have much less spatial variability than the stress heterogeneity,* $\boldsymbol{\sigma}'_H(\mathbf{x})$.

Assumptions/Limitations of This Stress Formulation

From the outset it is important to clearly indicate the assumptions used in this thesis and the possible limitations. We do not attempt to create stress heterogeneity in 3D from first principals because of the inherent difficulties. Aagaard and Heaton have numerically created self-sustaining heterogeneous stress on a 2D plane that repeatedly ruptures in time through a dynamic calculation [*Aagaard and Heaton*, personal communication]. However, to faithfully create realistic 3D stress heterogeneity, one would have to numerically simulate all the faults in the region at all lengthscales, from a small 10 cm dislocation to a 100 km rupture, and simulate appropriate spatial distributions of slip for every rupture, throughout thousands of years, because the current stress heterogeneity pattern is a superposition of all the past faulting and fracture history in the crust. Not only does this require many assumptions, such as the distributions of fault orientations, fault lengths, slip on fault, etc., it is also currently numerically impossible using dynamic fracture simulations. Therefore, we have chosen to approach this problem statistically in a simple manner. On the plus side, this enables us to describe spatially heterogeneous stress with two statistical parameters, HR and α, generate synthetic focal mechanisms quickly, and compare our simulations with real data to constrain the statistical properties of the crust. On the other hand, this statistical approach makes many simplifying assumptions in an attempt to obtain a first-cut answer about the statistics of the Earth's crust and overlooks details that are necessary if one wishes to model stress heterogeneity from first principles.

First, while we satisfy rotational equilibrium when we create our stress tensors, we do not satisfy the other equilibrium equation, $\sum_{j=1}^{3} \frac{\partial \sigma_{ij}}{\partial x_j} = f_i$, which specifies no internal accelerations if there are no sources. In order to satisfy $\sum_{j=1}^{3} \frac{\partial \sigma_{ij}}{\partial x_j} = f_i$ and have spatially heterogeneous stress, we would have to include sources, which requires a whole set of additional assumptions; see the beginning of Chapter 3 for a more thorough explanation as to why we do not satisfy the equilibrium equation, $\sum_{j=1}^{3} \frac{\partial \sigma_{ij}}{\partial x_j} = f_i$.

This leads to some of our other assumptions: 1) We do not allow for slip on pre-existing faults. This means our seismicity tends to cluster in 3D clouds rather than lineations or planes as seen in the real Earth. 2) We only allow for point source dislocations. 3) We do not update the stress field after a failure; hence, there is no explicit interaction between events. Equation (1.1) is written for stress inversions of background seismicity where stress perturbations due to individual events are small and should have little to no effect on the other events included in the regional inversions. 4) There is no inclusion of creep, which could change the heterogeneous stress distribution. 5) We assume failure occurs on fresh-fracture, maximally oriented planes at $\pm 45°$ from the σ_1 and σ_3 principal stress axes. This is a consequence of using a plastic yield criterion. In Appendix C, we do use a Coulomb Failure criterion and find similar but more complicated results when we compare our results for Coulomb Failure criterion to our results for the plastic yield criterion in Chapter 4. 6) Last, the spatial stress heterogeneity in the Earth may not vary exactly as a fractal according to our formulation described in Chapters 2 and 3.

A major difference between the assumptions in this thesis vs. those in stress inversions is summarized in Table 1.1. We are assuming an end-member model, heterogeneous stress and homogeneous nucleation strength, whereas stress inversions [*Angelier*, 1975; 1984; *Carey and Brunier*, 1974; *Etchecopar, et al.*, 1981; *Gephart*, 1990; *Gephart and Forsyth*, 1984; *Mercier and Carey-Gailhardis*, 1989; *Michael*, 1984; 1987] represent the other end-member model, homogeneous stress but heterogeneous strength. To understand this difference it is helpful to review some of the basic steps of stress inversions. Figure 1.10, from Angelier [1990], diagrams part of this procedure. One begins by collecting a set of earthquake focal mechanisms in a study region for some time window. The focal mechanisms are converted into slip vectors on a plane that can be described by the parameters strike, dip, and rake, or by a slip vector, $\vec{s}_K$, and normal vector, $\hat{n}_K$, as shown in Figure 1.10 a). An estimated spatially uniform stress tensor, $\boldsymbol{\sigma}_K$, is resolved onto each plane to produce normal traction vectors, $\vec{\sigma}_{N_K}$, and shear traction vectors, $\vec{\tau}_K$, as shown in Figure 1.10 b). The relative angles between the actual slip vectors, $\vec{s}_K$, and the projected shear traction vectors, $\vec{\tau}_K$, are called the misfit angles as shown in Figure 1.10 c). The inversion routine attempts to find a best-fit spatially uniform stress tensor, $\boldsymbol{\sigma}_K$, that minimize the overall misfit statistics. A study by Rivera and Kanamori [2002] of data in Southern California showed that one needs either heterogeneous friction (strength), heterogeneous stress, or both to describe the inversion statistics of real data. Current interpretations of stress inversions assume the stress is spatially homogeneous, and the strength is heterogeneous. In contrast, for our modeling we explain the misfit statistics with heterogeneous stress and assume that the physical processes initiating rupture are homogeneous, i.e., homogeneous nucleation strength.

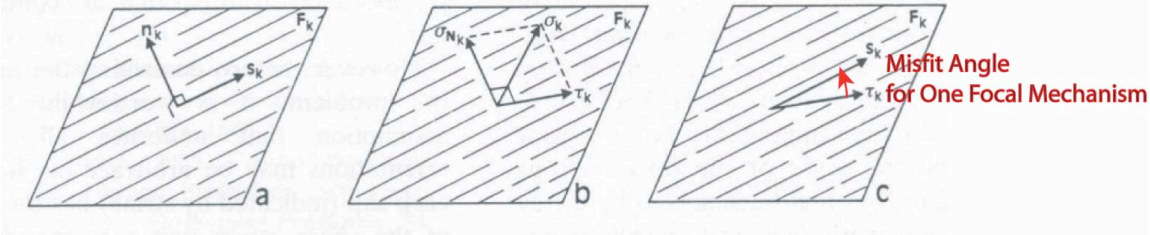

Figure 1.10. *Figure modified from Angelier [1990]. a) The slip plane, slip vector and normal vector to the slip plane for a single focal mechanism. b) Best guess spatially homogeneous stress tensor resolved into normal and shear tractions on the fault plane. c) The relative angle between the shear traction vector for the best guess spatially homogeneous stress tensor and the focal mechanism slip vector. This relative angle is called the misfit angle.*

Table 1.1. Two End Member Models for Explaining the Misfit Statistics of Focal Mechanism Inversions

Current Assumptions in Stress Inversion Modeling	**Assumptions Used in Our Modeling, the Other End-Member Case**
Heterogeneous Nucleation Strength	Homogeneous Nucleation Strength
Homogeneous Stress	Heterogeneous Stress

Overview of Thesis

The method used to generate the heterogeneous stress, $\boldsymbol{\sigma}'_H(\mathbf{x})$, is explained in detail in Chapters 2 and 3. Chapter 2 explains how to generate a scalar quantity with fractal characteristics in 3D. Chapter 3 explains how we generated a full tensorial quantity with fractal characteristics in 3D, i.e., where 5–6 independent quantities have been filtered spatially (5 if one is working with a deviatoric stress tensor, 6 if one is working with a full stress tensor).

In Chapter 4, we describe how we create our synthetic focal mechanism catalogs combining the Hencky-Mises plastic yield criterion with equation (1.1). That chapter explains why stress inversions will be biased towards the orientation of time-varying stress terms, be it the far-field plate tectonic stress rate, $\dot{\boldsymbol{\sigma}}'_T$, or the stress perturbations associated with a mainshock that occurs at time T_E. Appendix C demonstrates numerically that the same bias occurs when one uses the Coulomb Failure Criterion, but the results become more complicated for $\mu \neq 0.0$, because the two conjugate planes are no longer perpendicular. In Chapter 4, we also explore the consequences of the bias towards the stress rate, $\dot{\boldsymbol{\sigma}}'_T$, for the case of background seismicity, in between mainshocks. We find that if stress is highly heterogeneous, the standard stress inversions of focal mechanisms [*Angelier*, 1975; 1984; *Carey and Brunier*, 1974; *Etchecopar, et al.*, 1981; *Gephart*, 1990; *Gephart and Forsyth*, 1984; *Mercier and Carey-Gailhardis*, 1989; *Michael*, 1984; 1987] simply yield $\dot{\boldsymbol{\sigma}}'_T$, instead of $\boldsymbol{\sigma}'_B$, if $\dot{\boldsymbol{\sigma}}'_T$ and $\boldsymbol{\sigma}'_B$ have different orientations. Whereas, if there is little to no heterogeneity, the inversions do yield $\boldsymbol{\sigma}'_B$ as commonly thought.

In Chapter 5, we begin estimating stress heterogeneity parameters, α and HR, in the real Earth. Our estimates for the amplitude of the heterogeneity, HR, is more robust than our estimates for the spatial smoothing, α; however, we find that the increasing bias toward $\dot{\boldsymbol{\sigma}}'_T$ with increasing heterogeneity amplitude, HR, is independent of the α we use for $\alpha \leq 1.0$. Determining the value of α has important implications for calculating the strength of the crust as a function of length-scale, but it does not affect our observations that focal mechanism inversions are biased toward $\dot{\boldsymbol{\sigma}}'_T$ when there is spatially heterogeneous stress. Our best estimate for stress heterogeneity in Southern California, $HR \approx 1.25$, produces stress inversion orientations rotated approximately 30–40% from $\boldsymbol{\sigma}'_B$ toward the stress rate tensor, $\dot{\boldsymbol{\sigma}}'_T$, a non-trivial bias. This result suggests that stress studies using focal mechanism inversion routines [*Angelier*, 1975; 1984; *Carey and Brunier*, 1974; *Etchecopar, et al.*, 1981; *Gephart*, 1990; *Gephart and Forsyth*, 1984; *Mercier and Carey-Gailhardis*, 1989; *Michael*, 1984; 1987] need to be reinterpreted. In light of this, we suggest a new procedure for interpreting focal mechanism inversions where the bias toward $\dot{\boldsymbol{\sigma}}'_T$ would be subtracted out to yield the actual $\boldsymbol{\sigma}'_B$.

References

Aagaard, B., and T. H. Heaton (in preparation, 2006), The influence of prestress, fracture energy, and sliding friction on slip heterogeneity.

Andrews, D. J. (1980), A stochastic fault model: 1) Static case, *Journal of Geophysical Research*, *85*, 3867–3877.

Andrews, D. J. (1981), A stochastic fault model: 2) Time-dependent case, *Journal of Geophysical Research*, *86*, 821–834.

Angelier, J. (1975), Sur l'analyse de mesures recueilles dans des sites faillés: l'utilité d'une confrontation entre les méthodes dynamiques et cinématiques, *C.R. Acadamy of Science, Paris, D*, *283*, 466.

Angelier, J. (1984), Tectonic analysis of fault slip data sets, *Journal of Geophysical Research*, *89*, 5835–5848.

Angelier, J. (1990), Inversion of field data in fault tectonics to obtain the regional stress .3. A new rapid direct inversion method by analytical means, *Geophyiscal Journal International*, *103*, 363–376.

Barnsely, M., et al. (1988), *The Science of Fractal Images*, Springer-Verlag, New York.
Barton, C. A., and M. D. Zoback (1994), Stress perturbations associated with active faults penetrated by boreholes: Possible evidence for near-complete stress drop and a new technique for stress magnitude measurement, *Journal of Geophysical Research*, *99*, 9373–9390.

Becker, T. W., et al. (2003), Constraints on the mechanics of the Southern San Andreas fault system from velocity and stress observations, paper presented at 2003 SCEC Annual Meeting, Southern California Earthquake Center, Oxnard, California, September 7–11, 2003.

Ben-Zion, Y., and C. G. Sammis (2003), Characterization of fault zones, *Pure and Applied Geophysics*, *160*, 677–715.

Carey, E., and B. Brunier (1974), Analyse théorique et numérique d'un modèle méchanique élémentaire appliqué à l'étude d'une population de failles, *C.R. Acadamy of Science, Paris, D*, *279*, 891–894.

Dieterich, J. H. (2005), Role of stress relaxation in slip of geometrically complex faults, paper presented at American Geophysical Union, San Francisco, December 2005.

Etchecopar, A., et al. (1981), An inverse problem in microtectonics for the determination of stress tensors from fault striation analysis, *Journal of Structrual Geology*, *3*, 51–65.

Gephart, J. W. (1990), FMSI: A Fortran program for inverting fault/slickenside and earthquake focal mechanism data to obtain the regional stress tensor, *Computers and Geosciences*, *16*, 953–989.

Gephart, J. W., and D. W. Forsyth (1984), An improved method for deteremining the regional stress tensor using earthquake focal mechanism data: Application to the San Fernando earthquake sequence, *Journal of Geophysical Research*, *89*, 9305–9320.

Herrero, A., and P. Bernard (1994), A kinematic self-similar rupture process for earthquakes, *Bulletin of the Seismological Society of America*, *84*, 1216–1228.

Lachenbruch, A. H., and J. H. Sass (1980), Heat-flow and energetics of the San-Andreas fault zone, *Journal of Geophysical Research*, *85*, 6185–6222.

Lavallee, D., and R. J. Archuleta (2003), Stochastic modeling of slip spatial complexities of the 1979 Imperial Valley, California, earthquake, *Geophysical Research Letters*, *30*, Art. No. 1245.

Liu-Zeng, J., et al. (2005), The effect of slip variability on earthquake slip-length scaling, *Geophysical Journal International*, *162*, 841–849.

Mai, P. M., and G. C. Beroza (2002), A spatial random field model to characterize complexity in earthquake slip, *Journal of Geophysical Research-Solid Earth*, *107*, Art. No. 2308.

Manighetti, I., et al. (2005), Evidence for self-similar, triangular slip distributions on earthquakes: Implications for earthquake and fault mechanics, *Journal of Geophysical Research-Solid Earth*, *110*, Art. No. B05302.

Manighetti, I., et al. (2001), Slip accumulation and lateral propagation of active normal faults in Afar, *Journal of Geophysical Research*, *106*, 13667–13696.

McGill, S. F., and C. M. Rubin (1999), Surficial slip distribution on the central Emerson fault during the June 28, 1992 Landers earthquake, California, *Journal of Geophysical Research-Solid Earth*, *104*, 4811–4833.

Mercier, J.-L., and S. Carey-Gailhardis (1989), Regional state of stress and characteristic fault kinematics instabilities shown by aftershock sequence: the aftershock sequence of the 1978 Thessaloniki (Greece) and 1980 Campania-Lucania (Italy) earthquakes as examples, *Earth and Planetary Science Letters*, *92*, 247–264.

Michael, A. J. (1984), Determination of stress from slip data: Faults and folds, *Journal of Geophysical Research-Solid Earth*, *89*, 11517–11526.

Michael, A. J. (1987), Use of focal mechanisms to determine stress: A control study, *Journal of Geophysical Research-Solid Earth*, *92*, 357–368.

Rice, J. R. (1999), Flash heating at asperity contacts and rate-dependent friction, paper presented at American Geophysical Union, San Francisco.

Rice, J. R., et al. (2001), Rate and state dependent friction and the stability of sliding between elastically deformable solids, *Journal of the Mechanics and Physics of Solids*, *49*, 1865–1898.

Rivera, L., and H. Kanamori (2002), Spatial heterogeneity of tectonic stress and friction in the crust, *Geophysical Research Letters*, *29*, art. no. 1088.

Sibson, R. H. (2003), Thickness of the seismic slip zone, *Bulletin of the Seismological Society of America*, *93*, 1169–1178.

Townend, J., and M. D. Zoback (2004), Regional tectonic stress near the San Andreas fault in central and southern California, *Geophysical Research Letters*, *31*, 1–5.

Tullis, T. (2005), Dramatic reductions in fault friction at earthquake slip rates, edited. Tullis, T. E., and D. L. Goldsby (2005), paper presented at Chapman Conference on Radiated Energy and the Physics of Earthquake Faulting, Portland, Maine, June 13–17, 2005.

Wald, D. J., and T. H. Heaton (1994), Spatial and temporal distribution of slip for the 1992 Landers, California, earthquake, *Bulletin of the Seismological Society of America*, *84*, 668–691.

Wilde, M., and J. Stock (1997), Compression directions in southern California (from Santa Barbara to Los Angeles Basin) obtained from borehole breakouts, *Journal of Geophysical Research*, *102*, 4969–4983.

Zoback, M. D., and G. C. Beroza (1993), Evidence for near-frictionless faulting in the 1989 (M 6.9) Loma Prieta, California, earthquake and its aftershocks, *Geology*, *21*, 181–185.

Chapter 2. Creating a Spatially Heterogeneous Scalar Quantity

Our objective is to create spatially heterogeneous stress that has appropriate spectral properties for the real Earth. In this chapter, we will address how to produce one scalar component of heterogeneous stress, and in the next chapter, we will show how we construct the complete 3D deviatoric stress tensor with five independent components.

Liu-Zeng et al. [2005] estimated slip heterogeneity in the real Earth by comparing slip vs. length scaling in the real Earth to the scaling predicted by different mathematical models of slip heterogeneity. Their equation for generating heterogeneous slip is

$$D(x) = D_0 \left| R(x) * F(x) \right| = D_0 \left| FT^{-1}\left[\hat{R}(k) k^{-\gamma} \right] \right| \tag{2.1}$$

where $D(x)$ is slip as a function of position, $R(x)$ is a Gaussian random function of x with zero mean and variance of 1.0, $F(x)$ is a spatial filter, $\hat{R}(k)$ is the Fourier transform of $R(x)$, and $k^{-\gamma}$ is the Fourier transform of $F(x)$ where k is the spatial wavenumber, and γ is a constant [*Liu-Zeng, et al*., 2005]. We use γ as the filtering symbol for Liu-Zeng et al. instead of α, to distinguish between the slip filtering in their paper vs. the stress filtering in this thesis. They find that $1.25 < \gamma < 1.5$ best describes slip vs. length data in the real Earth.

In our studies, we are interested primarily in stress, which along faults should have the same spectrum as the spatial derivatives of slip. In particular, Hooke's law connects stress and strain

$$\sigma_{ij} = \lambda(\varepsilon_{kk})\delta_{ij} + 2\mu\varepsilon_{ij} \tag{2.2}$$

where $i = 1,2,3$ and $j = 1,2,3$, and λ and μ are constants known as Lamé parameters. Strain, $\varepsilon_{ij} = \frac{1}{2}\left(\frac{\partial u_i}{\partial x_j} + \frac{\partial u_j}{\partial x_i} \right)$, where $\frac{\partial u_i}{\partial x_j}$ is the derivative of the *i*th component of displacement in the *j*th direction. Therefore, stress along faults should have spatial roughness equivalent to the spatial derivative of slip.

If the displacement along a 1D cross section can be described as

$$D(x) = D_0 \left| FT^{-1}\left[\hat{R}(k_x) k_x^{-\gamma} \right] \right|, \tag{2.3}$$

then a single scalar component of the stress tensor along a 1D cross section can be filtered as follows:

$$\begin{aligned} \sigma_{xx}(x) \propto \frac{dD(x)}{dx} &= D_0 \left| FT^{-1}\left[\hat{R}(k_x) k_x k_x^{-\gamma} \right] \right| \\ &= D_0 \left| FT^{-1}\left[\hat{R}(k_x) k_x^{(1-\gamma)} \right] \right| = D_0 \left| FT^{-1}\left[\hat{R}(k_x) k_x^{-\alpha} \right] \right| \end{aligned} \tag{2.4}$$

where $\alpha = \gamma - 1$. Consequently, if we wish to have appropriate length vs. slip scaling in the real Earth, we should have heterogeneous stress with $0.25 < \alpha < 0.5$ along 1D cross sections.

For our purposes we produce a suite of different heterogeneous stresses ranging from $\alpha = 0.0$ to $\alpha = 1.5$ and compare these to real Earth data in Chapter 5 to find an optimal α. Note that $\alpha = 1.0$ produces spatially filtered stress that has smoothing equivalent to integrating Gaussian white noise once. An $\alpha = 0.5$ produces spatially filtered stress that has smoothing equivalent to fractionally integrating Gaussian white noise, 0.5 times, etc. Figures 2.1 and 2.2 demonstrate how this filter operates for filtered Gaussian white noise.

Figures 2.3 and 2.4 show spatially filtered Gaussian white noise for $\alpha = 0.0$ (our test case, which should have a flat spectral slope for no filtering) and $\alpha = 0.5$ (filtered white noise that yields smoothness equivalent to a fractional integration of 0.5).

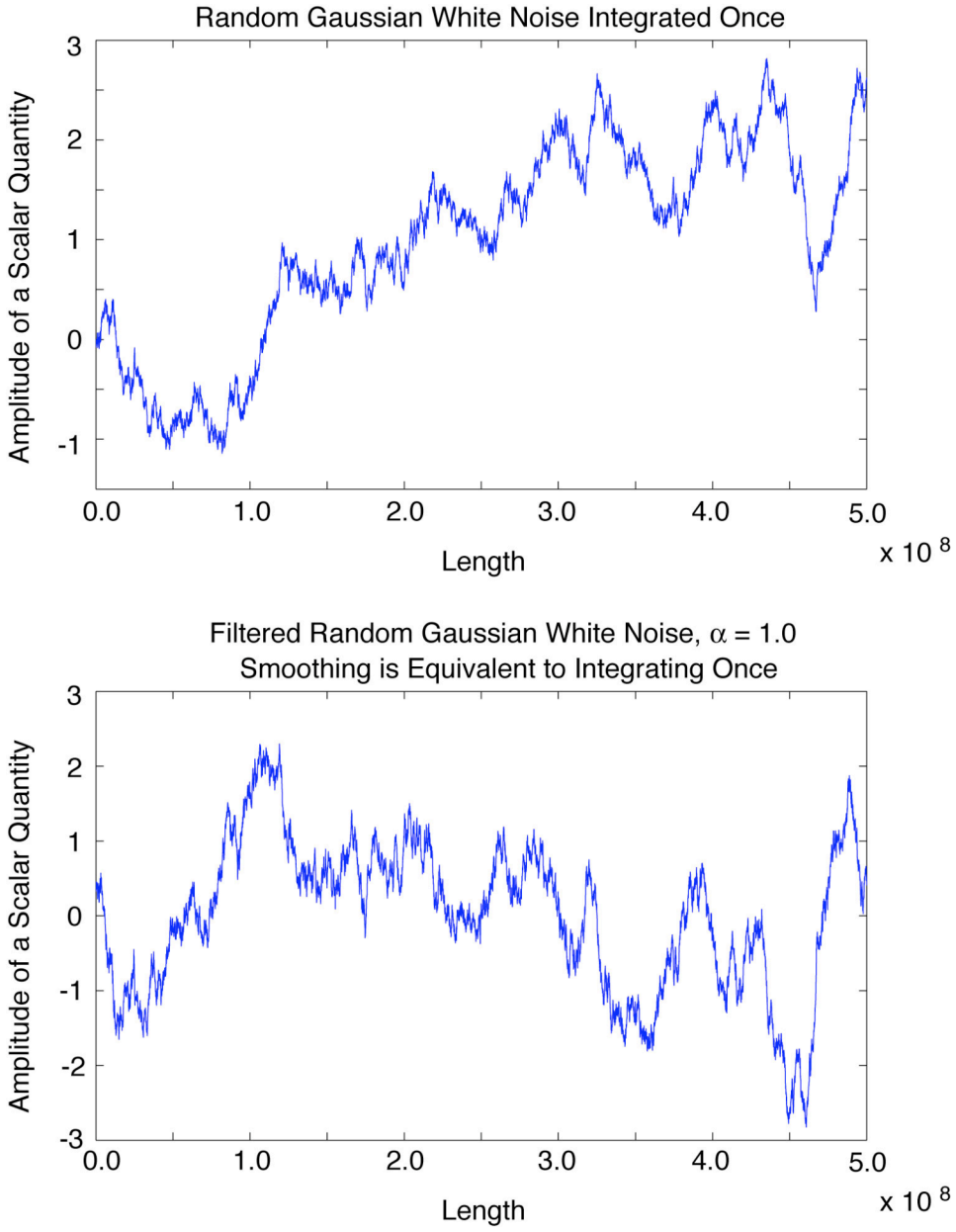

Figure 2.1. *Gaussian white noise is integrated once (top panel) and is filtered with* $\alpha = 1.0$ *(bottom panel). While the functions look different since one is an integral and the other is simply smoothing the Gaussian noise, they have approximately the same degree of spatial heterogeneity.*

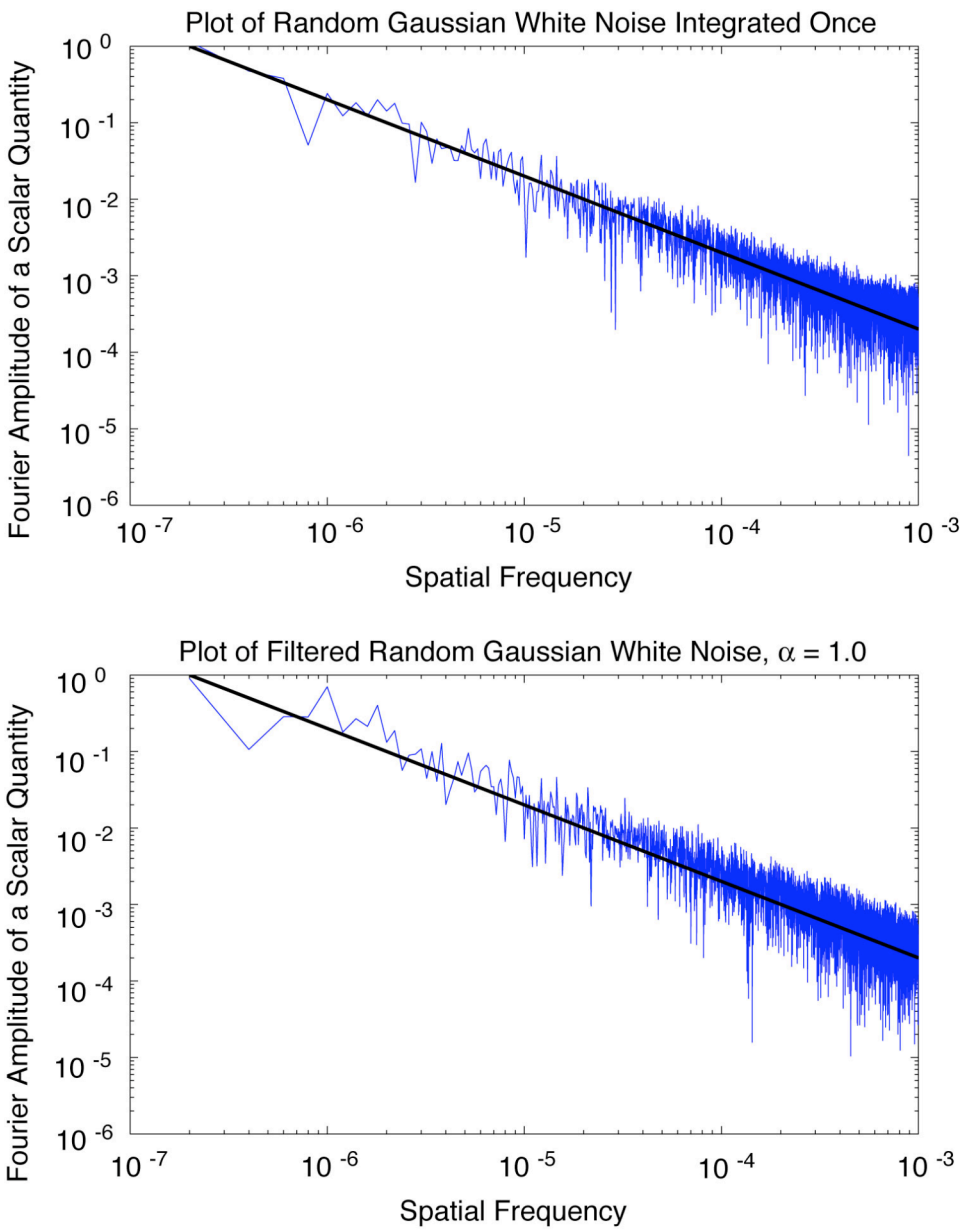

Figure 2.2. *The Fourier spectral amplitude is plotted for the integrated Gaussian white noise (top panel) and filtered Gaussian white noise with* $\alpha = 1.0$ *(bottom panel). A black line with slope = -1 is plotted on both the top and bottom panels.*

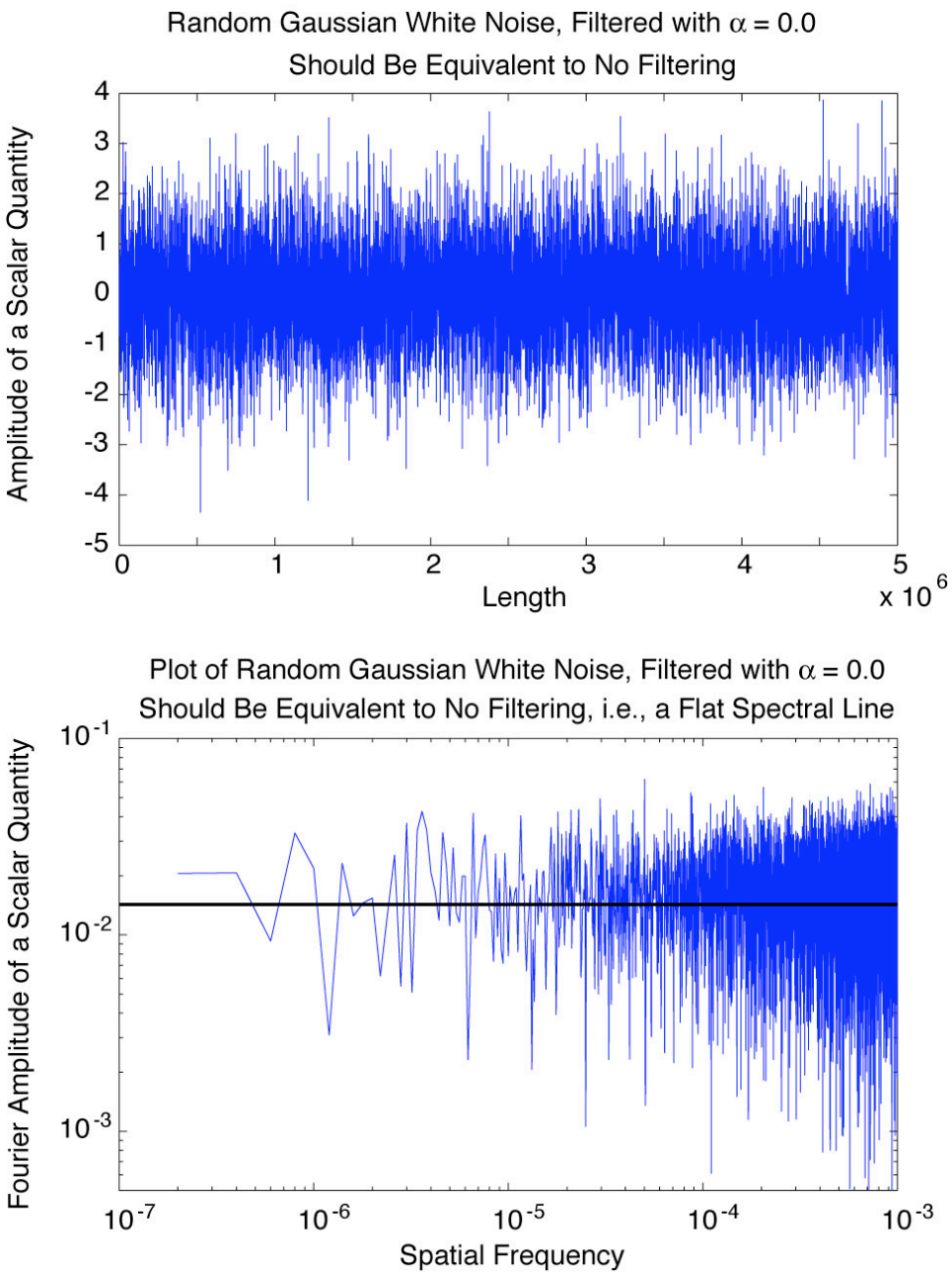

Figure 2.3. *Gaussian white noise in the top panel. Filtering with our smoothing parameter,* $\alpha = 0.0$, *which is equivalent to no smoothing. The bottom panel is a log-log plot of the Fourier amplitude spectra of the noise vs. spatial frequency. Since* $\alpha = 0.0$, *the slope of the Fourier amplitude spectra for the log-log plot = 0, as expected. This figure simply shows our baseline test case.*

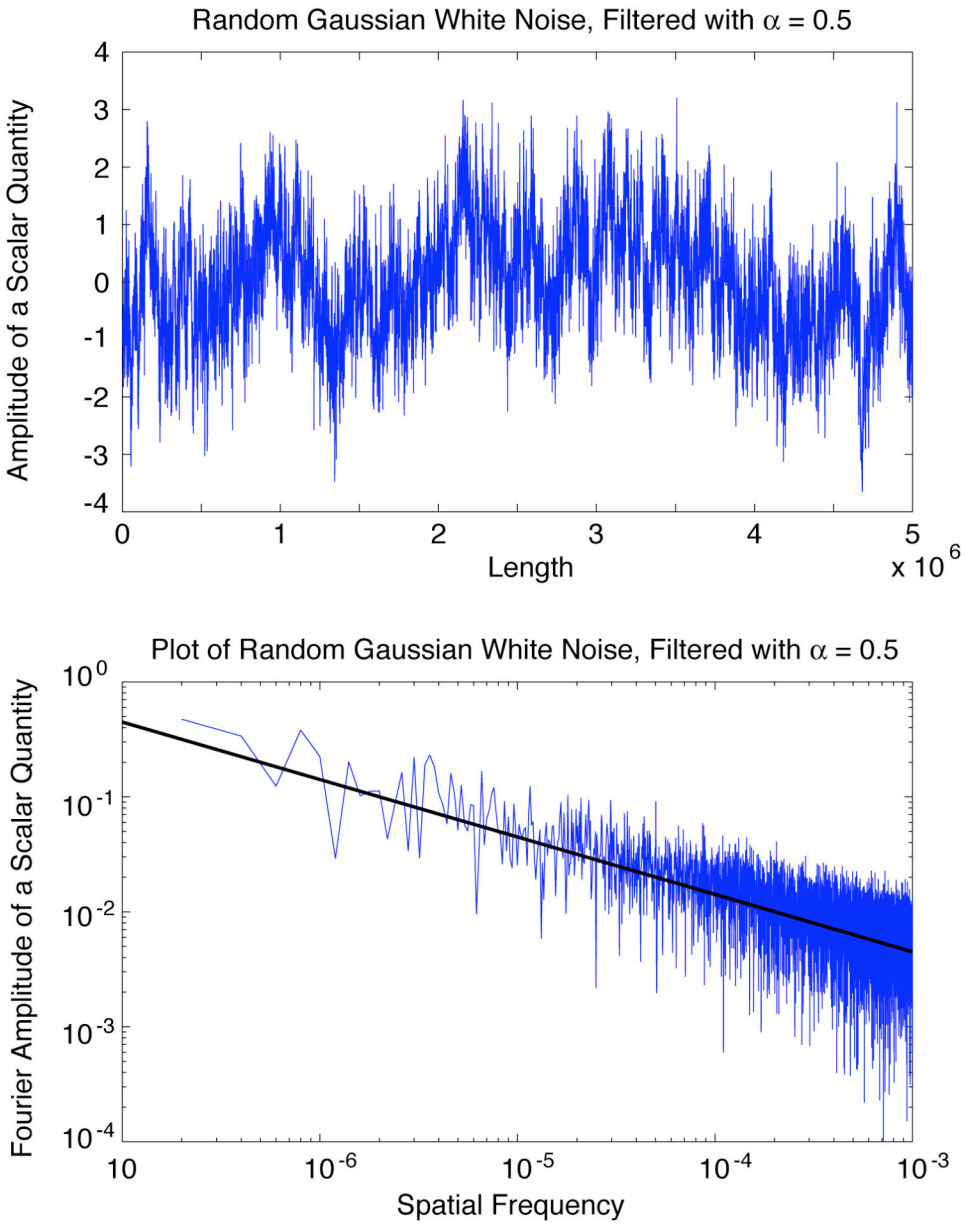

Figure 2.4. *In this case, our Gaussian white noise is filtered with an* $\alpha = 0.5$ *in the top panel. The bottom panel is the log-log plot of the Fourier amplitude spectrum of our filtered noise vs. spatial frequency. Note that the slope of the trend ≈ -0.5. This is the approximate desired slope for a filtering parameter of* $\alpha = 0.5$.

So far all the results presented have been for 1D Gaussian white noise. Now we need to extrapolate the results to 2D and 3D, since our simulations will require a 3D grid of spatially smoothed Gaussian white noise to represent the spatially heterogeneous stress. One constraint we place on this extrapolation is that any 1D cross section through a 2D or 3D grid should have the same spectral falloff as our simple 1D examples. A common equation that is used for filtering random Gaussian white noise in multiple dimensions is the Spectral Approximation [*Barnsely, et al.*, 1988],

$$F(k_1,k_2,...,k_n) \propto \frac{1}{\left(\sqrt{\sum_{i=1}^{n} k_i^2}\right)^{\frac{2H+n}{2}}} \tag{2.5}$$

where $F(k_1,k_2,...,k_n)$ is the n-dimensional filter we convolve with our noise, and H is the Hurst exponent. H relates to α as follows: $\alpha = \frac{2H+1}{2}$, where α describes the spectral falloff of any 1D straight line within our multidimensional grid. So we can rewrite this filter as

$$F(k_1,k_2,...,k_n) \propto \frac{1}{\left(\sqrt{\sum_{i=1}^{n} k_i^2}\right)^{A(\alpha,n)}} \tag{2.6}$$

where

$$A(\alpha,n) = \alpha + \frac{(n-1)}{2} \quad . \tag{2.7}$$

The filter exponent, $A(\alpha,n)$, in 1D simplifies to

$$A_{1D}(\alpha) = \alpha, \tag{2.8}$$

which means, $F(k_1) = \frac{1}{k_1^{\alpha}}$, the 1D falloff we want.

However for 2D and 3D, we find that the approximation is more limited. For 2D we have

$$A_{2D}(\alpha) = (\alpha + 0.5), \tag{2.9}$$

and in 3D

$$A_{3D}(\alpha) = (\alpha + 1). \tag{2.10}$$

These equations are typically used for the range, $0.5 < \alpha < 1.5$. As α approaches 0 (no filtering, just random Gaussian white noise), the Spectral Approximation breaks down, because we have

$$A_{2D}(0) = 0.5 \neq 0$$
$$A_{3D}(0) = 1.0 \neq 0$$

while we need $A(\alpha, n) \to 0$ as $\alpha \to 0$ to generate Gaussian white noise.

For example, in 2D we would have

$$F(k_1, k_2) \propto \frac{1}{\left(\sqrt{\sum_{i=1}^{2} k_i^2}\right)^{1/2}},$$

which produces filtered, fractal noise, instead of what we want,

$$F(k_1, k_2) \propto \frac{1}{\left(\sqrt{\sum_{i=1}^{2} k_i^2}\right)^{0}} = 1,$$

which maintains the Gaussian random noise. We will be testing a range of $0.0 < \alpha < 1.5$, which has values of α that fall out of the commonly accepted range of $0.5 < \alpha < 1.5$; therefore, we need to develop a better approximation.

To visually display this need for a better approximation, we filter 2D and 3D grids with many different exponents for the filtering transfer function, $F(k_1,k_2,...,k_n)$, plot their respective 1D spectral falloffs, and then plot $A(\alpha,n)$ vs. α. In essence, we are numerically computing the actual relationship between the exponent function, $f(\alpha,n)$, and α, where $F(k_1,k_2) \propto \frac{1}{\left(\sqrt{\sum_{i=1}^{2} k_i^2}\right)^{f(\alpha,n)}}$. Then we are comparing this numerically computed value to the spectral approximation, $A(\alpha,n)$, to demonstrate any discrepancies. Figure 2.5 shows the 2D and 3D results of this numerical test.

To address the problems with $A(\alpha,n)$ as $\alpha \to 0$, we develop a new approximation to $f(\alpha,n)$, the actual exponent function. Note that this new approximation is geared toward our particular size of grids, 201x201x201 points. When the number of points, N, along any one dimension is sufficiently large, the filtering exponent becomes stable, but for grids with N = 201, there is an added effect due to the finite size of the grid. Hence, our new approximation is only valid for this size of grid. For our new approximation we define:

$$F(k_1,k_2,...,k_n) \propto \frac{1}{\left(\sqrt{\sum_{i=1}^{n} k_i^2}\right)^{B(\alpha,n)}} \tag{2.11}$$

where $B(\alpha,n)$ is our new exponent function. For 2D

$$B_{2D}(\alpha) = 2\sqrt{\left[\left(\frac{\alpha+2.5}{2.25}\right)^2 - 1\right]} - 1, \tag{2.12}$$

and for 3D

$$B_{3D}(\alpha) = 4.5\sqrt{\left[\left(\frac{\alpha + 7.5}{7.45}\right)^2 - 1\right]} - 0.5. \qquad (2.13)$$

Figure 2.6 compares these new approximations to our numerically determined, $f(\alpha, n)$, exponent function. Note, by design they are so closely matched it is difficult to distinguish one from another. $B(\alpha, n)$ plots almost on top of $f(\alpha, n)$ for both 2D *(n = 2)* and 3D *(n = 3)*.

Now that we have a new approximation that produces the appropriate spectral properties for 2D and 3D data sets, we display some results in Figures 2.7 and 2.8, using $\alpha = 0.0,\ 0.5,$ and 1.0. We find that as α increases the scalar quantity becomes increasingly smooth spatially, i.e., the scalar values have increasing spatial correlation. Using the new approximation, the results for 2D and 3D have similar properties, with 1D spectral falloffs described by α.

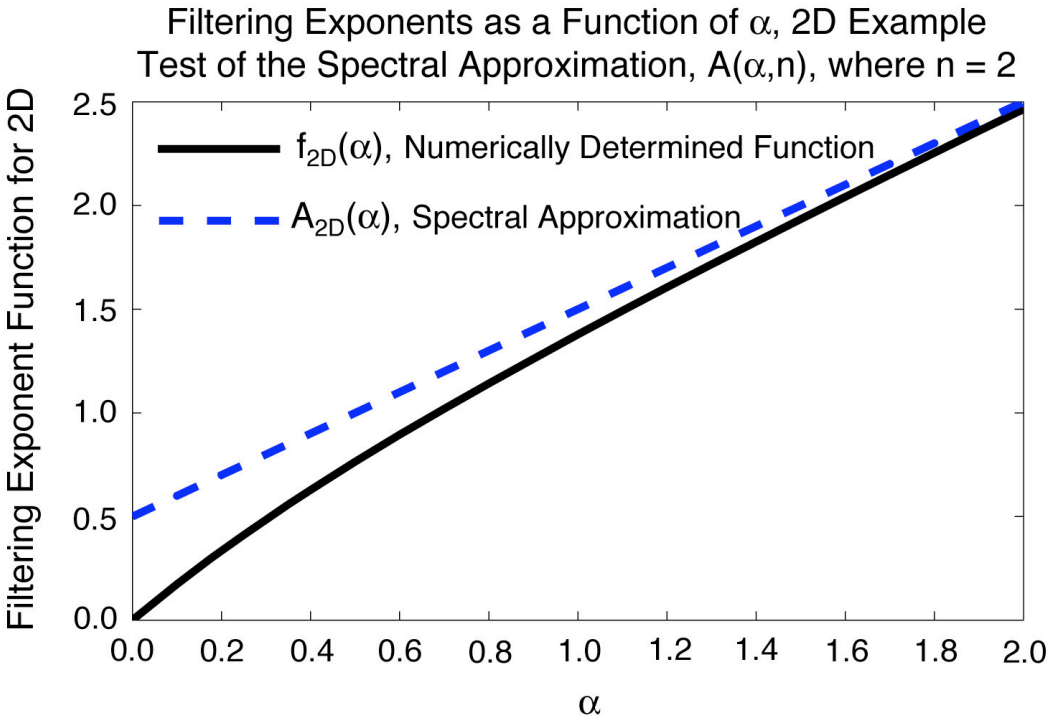
Filtering Exponents as a Function of α, 2D Example
Test of the Spectral Approximation, A(α,n), where n = 2
Filtering Exponent Function for 2D
f2D(α), Numerically Determined Function
A2D(α), Spectral Approximation
0.0
0.5
1.0
1.5
2.0
2.5
0.0
0.2
0.4
0.6
0.8
1.0
1.2
1.4
1.6
1.8
2.0
α

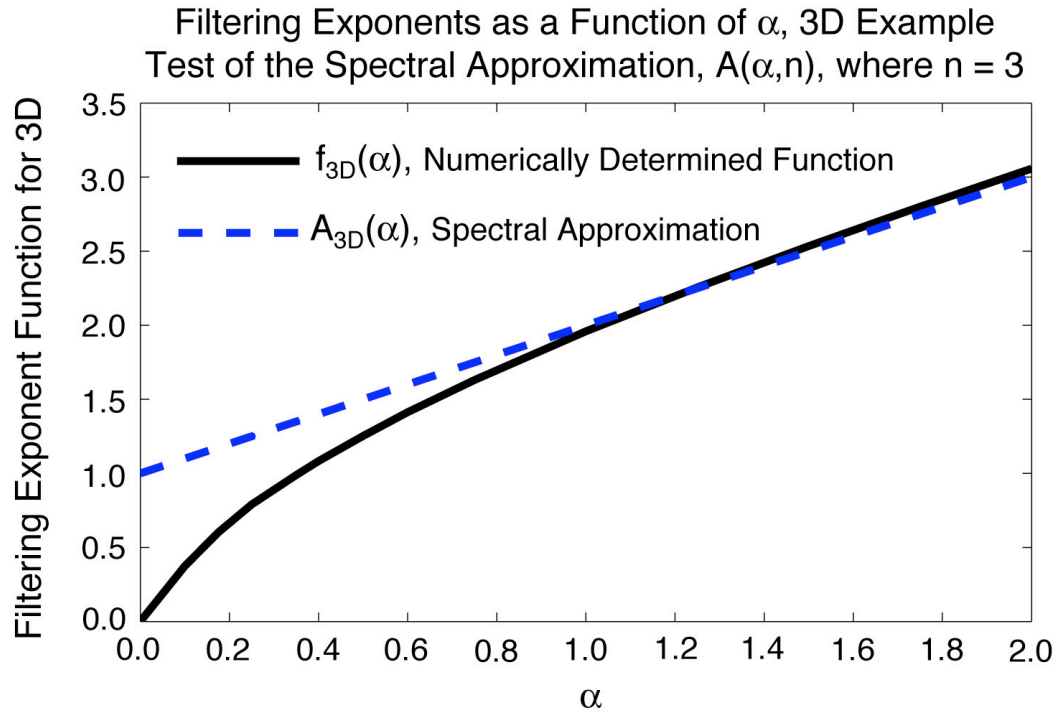
Filtering Exponents as a Function of α, 3D Example
Test of the Spectral Approximation, A(α,n), where n = 3
Filtering Exponent Function for 3D
f3D(α), Numerically Determined Function
A3D(α), Spectral Approximation
0.0
0.5
1.0
1.5
2.0
2.5
3.0
3.5
0.0
0.2
0.4
0.6
0.8
1.0
1.2
1.4
1.6
1.8
2.0
α

Figure 2.5. *When we filter scalar values in 2D and 3D, we still desire that any 1D cross section maintain the* $-\alpha$ *slope. For 1D grids, we could simply use the fractal filter,* $F(k_1) = \frac{1}{k_1^{\alpha}}$, *to produce a* $-\alpha$ *slope, but in 2D and 3D it becomes more complicated.*

For multiple spatial dimensions, the exponent on the filter can now be expressed as a function of α, *i.e., as a function of the desired 1D cross-sectional smoothness. This figure shows the following in 2D (top panel) and 3D (bottom panel). The solid black line is a plot of* $f(\alpha, n)$ *vs.* α, *determined from numerical simulations for a 201x201x201 grid, where* $F_f(k_1, k_2, ..., k_n) \propto \frac{1}{\left(\sqrt{\sum_{i=1}^{n} k_i^2}\right)^{f(\alpha,n)}}$, *and* α *describes the 1D spectral falloff of Gaussian white noise filtered with* $F_f(k_1, k_2, ..., k_n)$. *The dashed blue line is a plot of* $A(\alpha, n)$ *vs.* α *where* $A(\alpha, n)$ *is the Spectral Approximation function used in the filter,* $F_A(k_1, k_2, ..., k_n) \propto \frac{1}{\left(\sqrt{\sum_{i=1}^{n} k_i^2}\right)^{A(\alpha,n)}}$. $A(\alpha, n) = \alpha + \frac{(n-1)}{2}$ *[Barnsely, et al., 1988] where* n *is the number of spatial dimensions and* α *is the 1D spectral falloff of Gaussian white noise filtered with* $F_A(k_1, k_2, ..., k_n)$. *We wish to find a function that accurately describes the numerically determined curve,* $f(\alpha, n)$; *hence, if* $A(\alpha, n)$ *is a good approximation, it will plot directly on top of* $f(\alpha, n)$. *Unfortunately, this figure shows that the Spectral Approximation, designated by* $A(\alpha, n)$ *becomes a poor approximation for small values of* α. *Most of our simulations use a range of* $0.0 \le \alpha \le 1.0$, *where this approximation has trouble; hence, a better approximation for 2D (n = 2) and 3D (n = 3) is needed.*

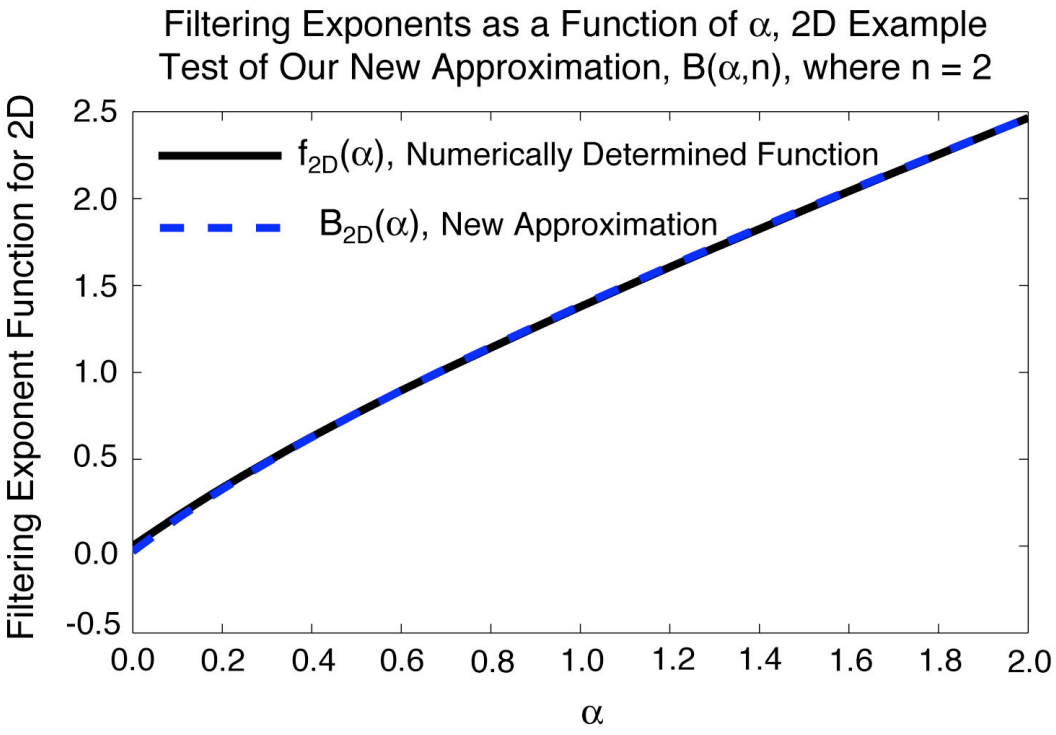
Filtering Exponents as a Function of α, 2D Example
Test of Our New Approximation, B(α,n), where n = 2
Filtering Exponent Function for 2D
f2D(α), Numerically Determined Function
B2D(α), New Approximation
2.5
2.0
1.5
1.0
0.5
0.0
-0.5
0.0
0.2
0.4
0.6
0.8
1.0
1.2
1.4
1.6
1.8
2.0
α

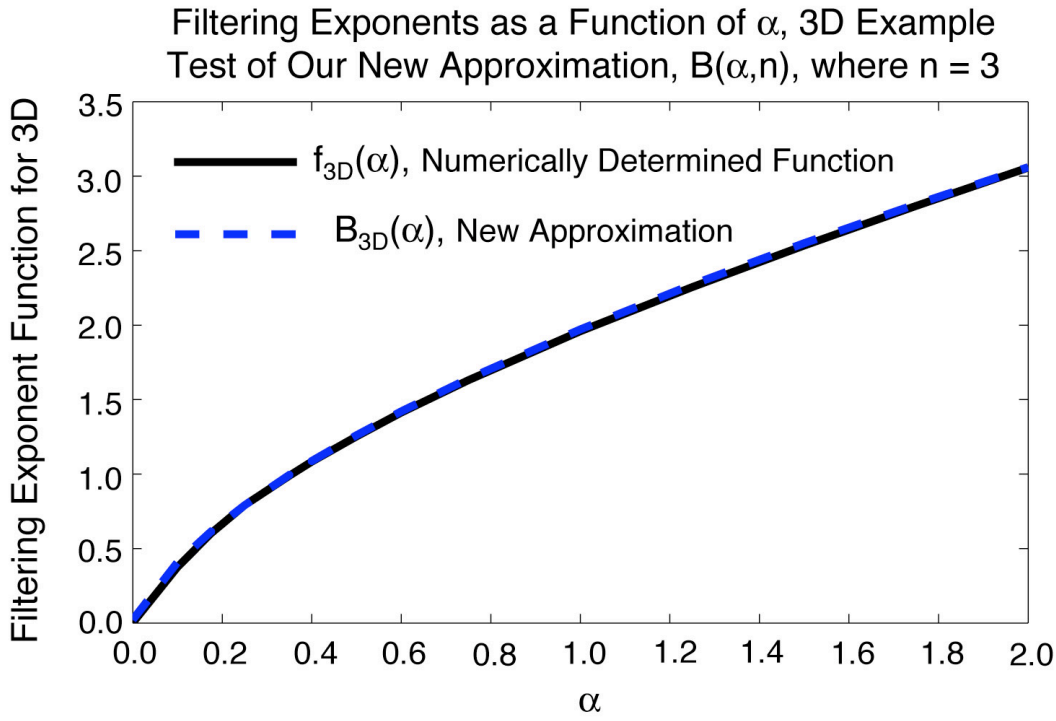
Filtering Exponents as a Function of α, 3D Example
Test of Our New Approximation, B(α,n), where n = 3
Filtering Exponent Function for 3D
f3D(α), Numerically Determined Function
B3D(α), New Approximation
3.5
3.0
2.5
2.0
1.5
1.0
0.5
0.0
0.0
0.2
0.4
0.6
0.8
1.0
1.2
1.4
1.6
1.8
2.0
α

Figure 2.6. *This is similar to Figure 2.5 except now our improved approximation,* $B(\alpha,n)$ *(dashed blue line), is plotted on top of the numerically determined curve,* $f(\alpha,n)$ *(solid black line). This time, our new approximation plots almost exactly on top of the numerically determined curve,* $f(\alpha,n)$*, indicating we have significantly improved our filtering exponent approximation. By visual inspection we choose hyperbolic functions to represent our new approximation. For 2D (n = 2) we have*

$$B(\alpha) = 2\sqrt{\left[\left(\frac{\alpha + 2.5}{2.25}\right)^2 - 1\right]} - 1$$

and for 3D (n = 3) it is

$$B(\alpha) = 4.5\sqrt{\left[\left(\frac{\alpha + 7.5}{7.45}\right)^2 - 1\right]} - 0.5\,.$$

These new approximations should be sufficient to produce our desired α *smoothing for 1D cross sections.*

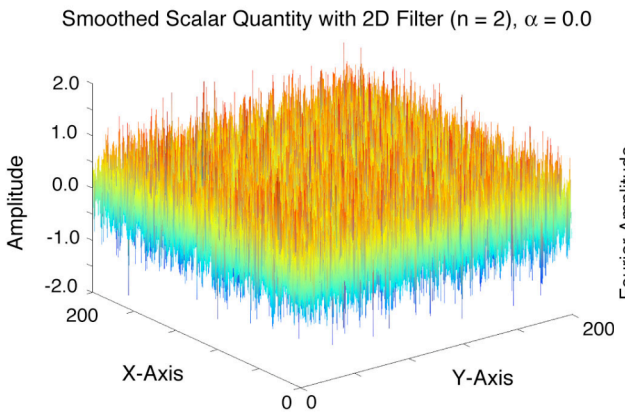
Smoothed Scalar Quantity with 2D Filter (n = 2), α = 0.0
Amplitude
2.0
1.0
0.0
-1.0
-2.0
200
X-Axis
0 0
Y-Axis
200

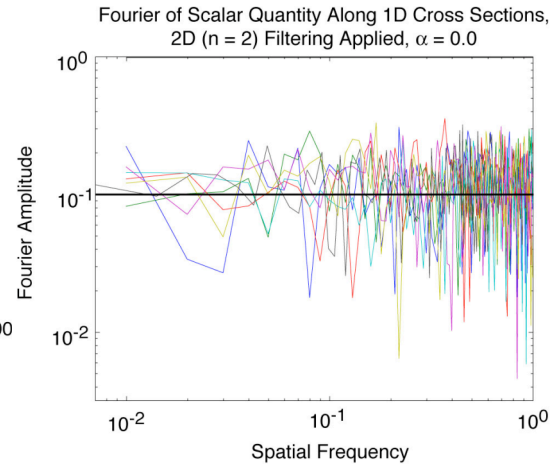
Fourier of Scalar Quantity Along 1D Cross Sections,
2D (n = 2) Filtering Applied, α = 0.0
Fourier Amplitude
10^0
10^-1
10^-2
10^-2
10^-1
10^0
Spatial Frequency

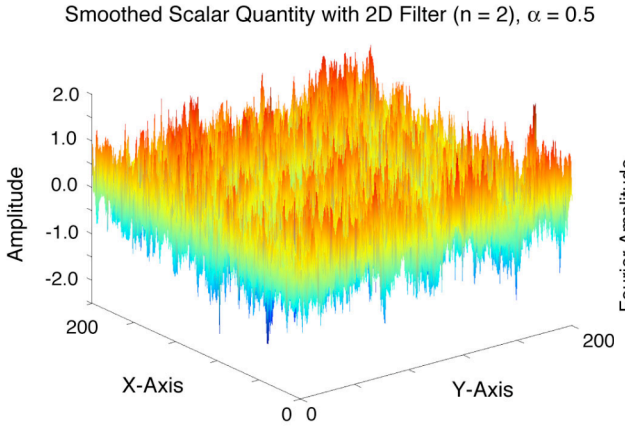
Smoothed Scalar Quantity with 2D Filter (n = 2), α = 0.5
Amplitude
2.0
1.0
0.0
-1.0
-2.0
200
X-Axis
0 0
Y-Axis
200

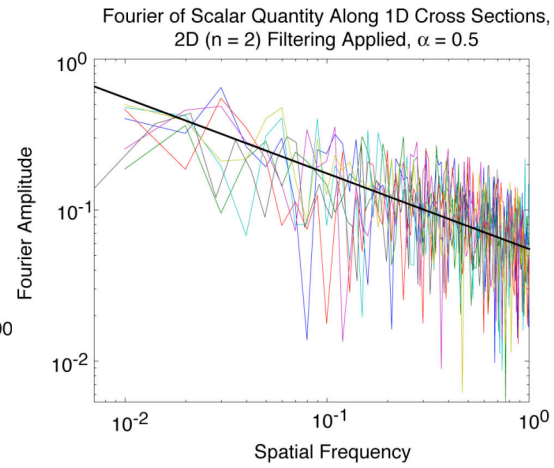
Fourier of Scalar Quantity Along 1D Cross Sections,
2D (n = 2) Filtering Applied, α = 0.5
Fourier Amplitude
10^0
10^-1
10^-2
10^-2
10^-1
10^0
Spatial Frequency

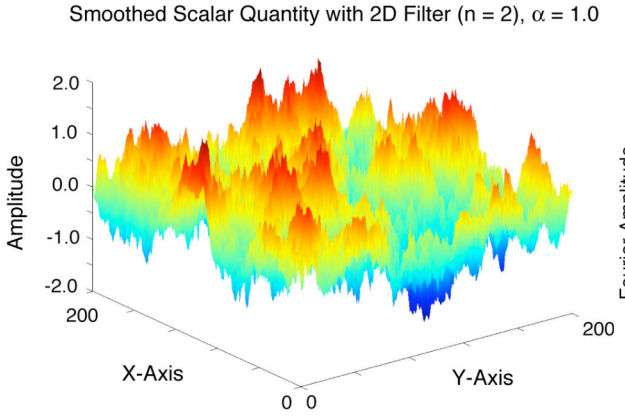
Smoothed Scalar Quantity with 2D Filter (n = 2), α = 1.0
Amplitude
2.0
1.0
0.0
-1.0
-2.0
200
X-Axis
0 0
Y-Axis
200

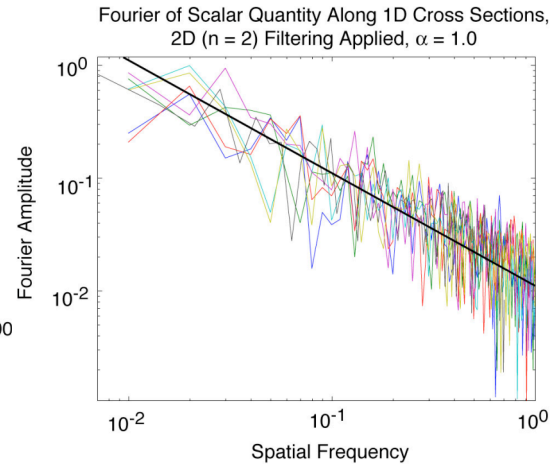
Fourier of Scalar Quantity Along 1D Cross Sections,
2D (n = 2) Filtering Applied, α = 1.0
Fourier Amplitude
10^0
10^-1
10^-2
10^-2
10^-1
10^0
Spatial Frequency

Figure 2.7. *Samples of our new smoothing approximation,* $B(\alpha,n)$*, for 2D (n = 2).* $\alpha = 0.0$ *for the top row,* $\alpha = 0.5$ *for the middle row, and* $\alpha = 1.0$ *for the bottom row. The left column is a 2D surface plot where the height and color indicate the amplitude of the scalar quantity. The right column shows a log-log Fourier amplitude spectra vs. spatial frequency for various 1D cross sections through the 2D grid where the solid black shows what the slope should be if our filter,* $B(\alpha,n)$*, is working properly. Note two features: 1) The slopes of the 1D cross sections are approximately correct. 2) As the filtering power,* α*, increases, the 2D spatial correlation of the values increases, i.e., it becomes spatially smoother as expected.*

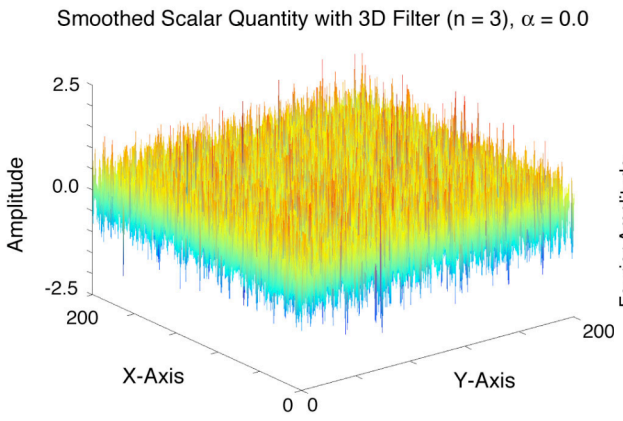
Smoothed Scalar Quantity with 3D Filter (n = 3), α = 0.0
Amplitude
2.5
0.0
-2.5
200
X-Axis
0 0
Y-Axis
200

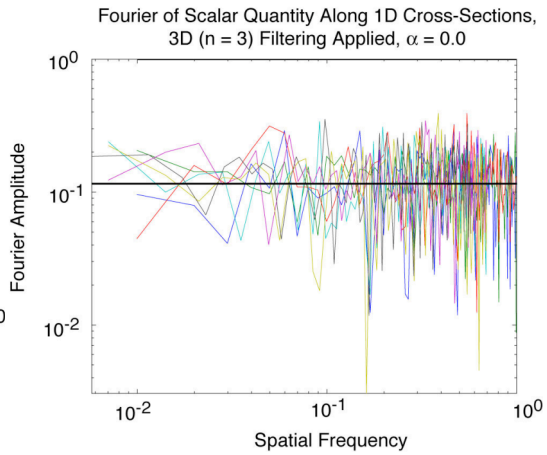
Fourier of Scalar Quantity Along 1D Cross-Sections,
3D (n = 3) Filtering Applied, α = 0.0
Fourier Amplitude
10^0
10^-1
10^-2
10^-2
10^-1
10^0
Spatial Frequency

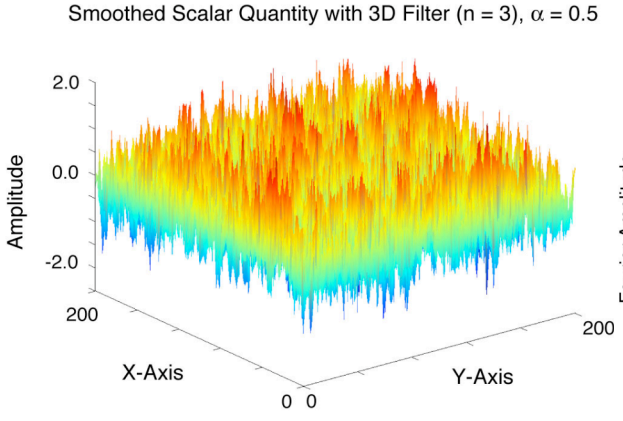
Smoothed Scalar Quantity with 3D Filter (n = 3), α = 0.5
Amplitude
2.0
0.0
-2.0
200
X-Axis
0 0
Y-Axis
200

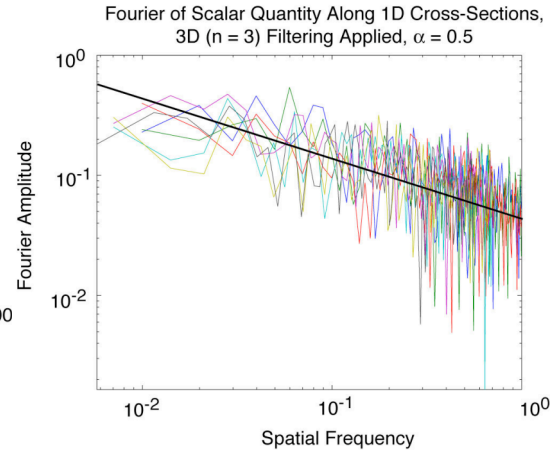
Fourier of Scalar Quantity Along 1D Cross-Sections,
3D (n = 3) Filtering Applied, α = 0.5
Fourier Amplitude
10^0
10^-1
10^-2
10^-2
10^-1
10^0
Spatial Frequency

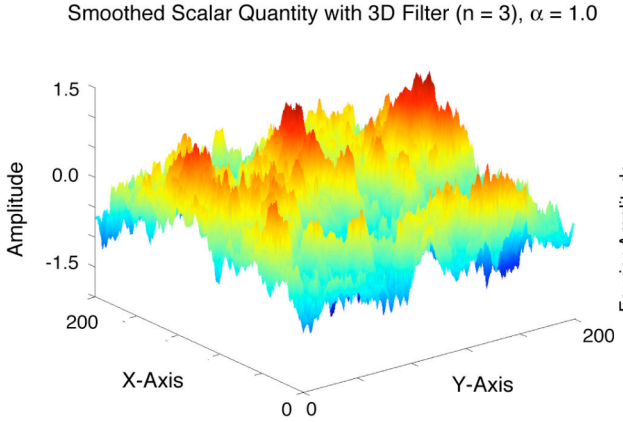
Smoothed Scalar Quantity with 3D Filter (n = 3), α = 1.0
Amplitude
1.5
0.0
-1.5
200
X-Axis
0 0
Y-Axis
200

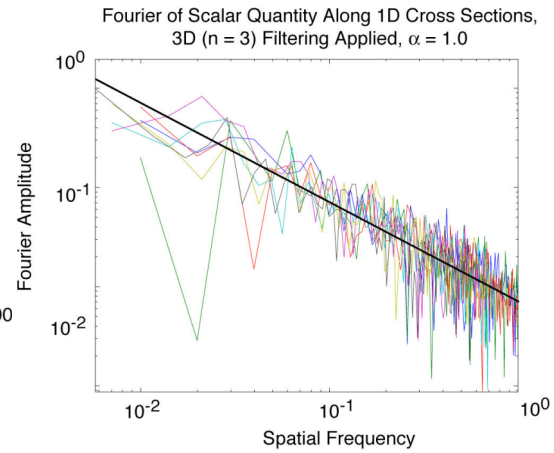
Fourier of Scalar Quantity Along 1D Cross Sections,
3D (n = 3) Filtering Applied, α = 1.0
Fourier Amplitude
10^0
10^-1
10^-2
10^-2
10^-1
10^0
Spatial Frequency

Figure 2.8. *This is very similar to Figure 2.7, except we have 2D cross sections through a 3D grid. It is meant to demonstrate our new 3D (n = 3) filtering approximation. In this case, the same seed data are used for the top ($\alpha = 0.0$), middle ($\alpha = 0.5$), and bottom ($\alpha = 1.0$) rows, to show what happens as α increases. Again 1D cross sections have approximately the proper spectral falloff, and as α increases, the observed spatial clumping in 2D and 3D increases.*

References

Barnsely, M., et al. (1988), *The Science of Fractal Images*, Springer-Verlag, New York.

Liu-Zeng, J., et al. (2005), The effect of slip variability on earthquake slip-length scaling, *Geophysical Journal International*, *162*, 841–849.

Chapter 3. Creating a Spatially Heterogeneous Full Stress Tensor

The previous chapter discussed how one would filter a scalar quantity in three dimensions. The ultimate goal is to filter both full and deviatoric stress tensors, which are comprised of six and five independent quantities respectively.

Rotational equilibrium requires that a 3D stress tensor is symmetric. This symmetry means that six degrees of freedom are required to specify stress. The other equilibrium condition, $\sum_{j=1}^{3} \frac{\partial \sigma_{ij}}{\partial x_j} = f_i$, which specifies no internal accelerations if there are no internal sources, provides an additional three constraints; however, the introduction of this equilibrium condition would force us to introduce random sources (dislocations) within the medium to produce our heterogeneous slip. Otherwise, by St. Venant's principle, the inside of a medium far away from the external boundaries and with no internal sources would have an approximately uniform stress distribution by definition if $\sum_{j=1}^{3} \frac{\partial \sigma_{ij}}{\partial x_j} = f_i$ is satisfied. Since the introduction of random sources requires additional assumptions about the statistics of fault distributions, fault sizes, slip on faults, etc., in this study we opt for not satisfying $\sum_{j=1}^{3} \frac{\partial \sigma_{ij}}{\partial x_j} = f_i$ so that we can produce stress heterogeneity without the introduction of internal sources. Again in this study we are primarily interested in producing a first-cut statistical description of the Earth's crust, parameterized by two numbers, *Heterogeneity Ratio* and α, without having to model the individual sources that create the heterogeneity.

For deviatoric stress tensors, the pressure is subtracted out such that the trace (summation of the diagonal elements) equals zero. This additional constraint reduces the degrees of freedom from six to five. The formula for pressure is

$$p = (1/3)(\sigma_{11} + \sigma_{22} + \sigma_{33}) \tag{3.1}$$

and when we subtract the pressure from our stress tensor, we have the following deviatoric stress tensor,

$$\begin{pmatrix} \sigma_{11} - p & \sigma_{12} & \sigma_{13} \\ \sigma_{12} & \sigma_{22} - p & \sigma_{23} \\ \sigma_{13} & \sigma_{23} & \sigma_{33} - p \end{pmatrix} = \begin{pmatrix} \sigma'_{11} & \sigma'_{12} & \sigma'_{13} \\ \sigma'_{12} & \sigma'_{22} & \sigma'_{23} \\ \sigma'_{13} & \sigma'_{23} & \sigma'_{33} \end{pmatrix}, \tag{3.2}$$

where

$$\sigma'_{11} + \sigma'_{22} + \sigma'_{33} = 0. \tag{3.3}$$

The constraint can also be written as

$$\sigma'_{22} = -(\sigma'_{11} + \sigma'_{33}), \tag{3.4}$$

and our deviatoric stress tensor can be rewritten as

$$\begin{pmatrix} \sigma'_{11} & \sigma'_{12} & \sigma'_{13} \\ \sigma'_{12} & -(\sigma'_{11} + \sigma'_{33}) & \sigma'_{23} \\ \sigma'_{13} & \sigma'_{23} & \sigma'_{33} \end{pmatrix}. \quad [\text{5 D.O.F. for a symmetric, deviatoric stress tensor}] \tag{3.5}$$

Recognizing that a symmetric, full stress tensor has six degrees of freedom and a symmetric, deviatoric stress tensor has five degrees of freedom, the question arises, "How does one filter a tensor with five or six degrees of freedom?" At first glance we might wish to simply filter σ_{11}, σ_{22}, σ_{33} σ_{12}, σ_{23}, and σ_{13} as six independent scalar quantities for the full stress tensor or filter σ'_{11}, σ'_{33}, σ'_{12}, σ'_{23}, and σ'_{13} as five independent scalar quantities for the deviatoric stress tensor, using the strategy outlined

in Chapter 2. Unfortunately, σ_{ij} and σ'_{ij} are always defined for a particular coordinate system. If we filter in this way, then we find that the general characteristics of the filtered stress are changed when we rotate from one coordinate frame to another. To resolve this problem, we need to rethink how to write our stress tensors.

An alternative way would be to represent the five degrees of freedom of the deviatoric stress tensor in terms of two scalar invariants of the stress tensor, and three orientation angles. Likewise, we can represent the full stress tensor with three scalar invariants and three orientation angles.

Invariant Filtering

It is fairly staightforward to filter invariants, quantities that remain unchanged upon rotation of the stress tensor or coordinate system. We have many choices of invariants to choose from. For simplicity, we choose to filter the principal stresses (σ_1, σ_2, and σ_3). For the full stress tensor, we use all three of these principal stresses and for the deviatoric stress tensor we will filter σ_1, σ_2, and σ_3 then subtract out the pressure, p, so that

$$\begin{aligned} \sigma'_1 &= \sigma_1 - p \\ \sigma'_2 &= \sigma_2 - p \\ \sigma'_3 &= \sigma_3 - p. \end{aligned} \tag{3.6}$$

This reduces the independent invariant quantities from three to two because $\sigma'_1 + \sigma'_2 + \sigma'_3 = 0$.

When generating and filtering each scalar principal stress (σ_1, σ_2, or σ_3), we begin with Gaussian random noise, clip it at the three standard deviation level, and then

apply the 3D filtering described in Chapter 2 to produce 3D filtered heterogeneity with 1D spectral falloffs of some specified α. The Gaussian white noise that we start with is clipped at the three standard deviation level to remove extreme outliers because in the real Earth there is probably a limit on the amplitude of deviatoric stress, perhaps 200 MPa, beyond which the rock will begin to fail. Each scalar is given a zero mean; then the composite set of principal stresses (σ_1, σ_2, and σ_3) are given an overall size defined by $\bar{I}_2' = 1.0$, where

$$I_2' = \sigma_{11}'^{\,2} + \sigma_{22}'^{\,2} + \sigma_{33}'^{\,2} + 2\sigma_{12}'^{\,2} + 2\sigma_{23}'^{\,2} + 2\sigma_{13}'^{\,2} \tag{3.7}$$

or

$$I_2' = \sigma_1'^{\,2} + \sigma_2'^{\,2} + \sigma_3'^{\,2}. \tag{3.8}$$

We choose $\bar{\sigma}_1 = 0.0$, $\bar{\sigma}_2 = 0.0$, and $\bar{\sigma}_3 = 0.0$ when generating our heterogeneous stress tensor, $\boldsymbol{\sigma}_H'(\mathbf{x}_i)$, so that any mean values will be subsumed into the spatially homogeneous background stress tensor, $\boldsymbol{\sigma}_B'$. This means that there are times when $\sigma_3 > \sigma_2 > \sigma_1$ does not hold for the heterogeneous principal stresses. The problem can be solved by sorting the principal stresses and their associated orientations to produce degenerate principal stress orientations. However, we will visualize the principal stresses in Figures 3.1–3.2 without sorting.

Figure 3.1 shows σ_1 and σ_1' for 10,000 Gaussian random points along a 1D length, filtered with $\alpha = 0.0$, $\alpha = 0.5$, $\alpha = 1.0$, and $\alpha = 1.5$. The left-hand plots display the filtered principal stresses, and the right-hand plots display the Fourier transform of the principal stresses as a function of spatial frequency. Additionally, on the right-hand plots, a straight, thick black line shows the expected α spectral falloff. Since σ_1, σ_2,

and σ_3 are generated using the identical process, it is only necessary to plot one of the principal stresses to show the filtered properties. The main point of the plots in Figure 3.1 is to show that indeed our principal stresses, σ_1, σ_2, and σ_3, and deviatoric principal stresses, σ_1', σ_2', and σ_3', have the correct spectral falloff. They should because it is a simple application of the principle already demonstrated in Chapter 2. It is not unexpected that our deviatoric principal stresses also have the correct spectral falloff. Deviatoric stresses are the principal stresses with the pressure subtracted, where the pressure is described by equation (3.1). We know that for filtered random processes, the linear sum of filtered random processes have the same spectral properties as the two individual processes if the same filter is used. Specifically, if $R_1(x)$ and $R_2(x)$ are two Gaussian processes, then if

$$R(x) = R_1(x) + R_2(x) \tag{3.9}$$

and if $F(x)$ is a spatial filter,

$$\begin{aligned} F(x) * R(x) &= F(x) * \left[R_1(x) + R_2(x) \right] \\ &= F(x) * R_1(x) + F(x) * R_2(x). \end{aligned} \tag{3.10}$$

Figure 3.2 shows plots of 2D cross sections through 3D grids of 201x201x201 points. The principal stress, σ_1, the deviatoric principal stress, σ_1', and the pressure, p, are shown for $\alpha = 0.0$, $\alpha = 0.5$, $\alpha = 1.0$, and $\alpha = 1.5$. For each α, the 2D cross section of stress is visualized two different ways: 1) On the left, are surface plots where the vertical amplitude and color corresponds to the amplitude of the scalar principal stress. 2) On the right, are map view plots, where only the color corresponds to the amplitude of the scalar principal stress. The 2D cross sections are taken from the same location in each 3D grid, about halfway along the $\hat{z}$ axis.

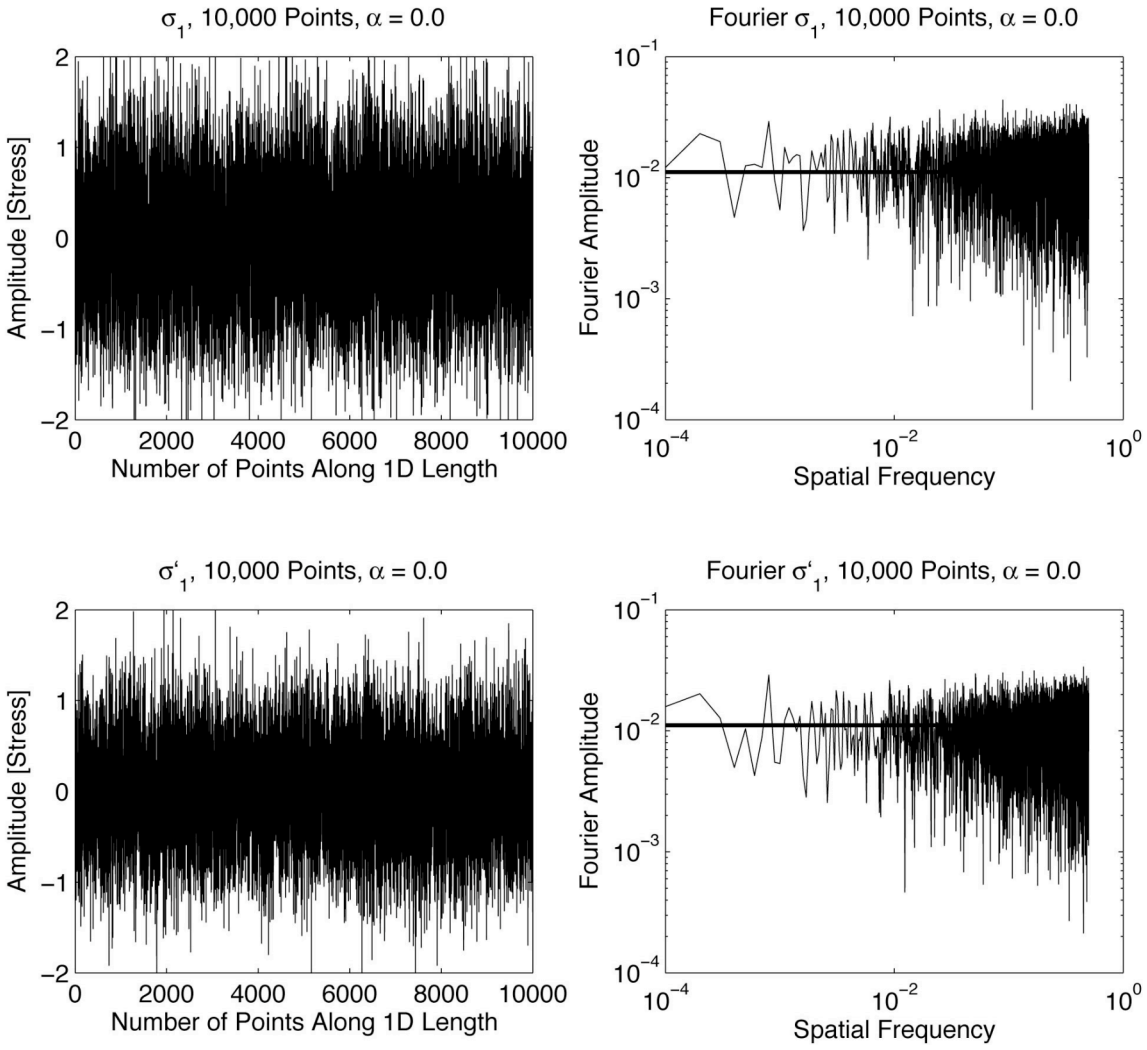
σ1, 10,000 Points, α = 0.0
Amplitude [Stress]
Number of Points Along 1D Length
Fourier σ1, 10,000 Points, α = 0.0
Fourier Amplitude
Spatial Frequency
σ'1, 10,000 Points, α = 0.0
Amplitude [Stress]
Number of Points Along 1D Length
Fourier σ'1, 10,000 Points, α = 0.0
Fourier Amplitude
Spatial Frequency

Figure 3.1 a)

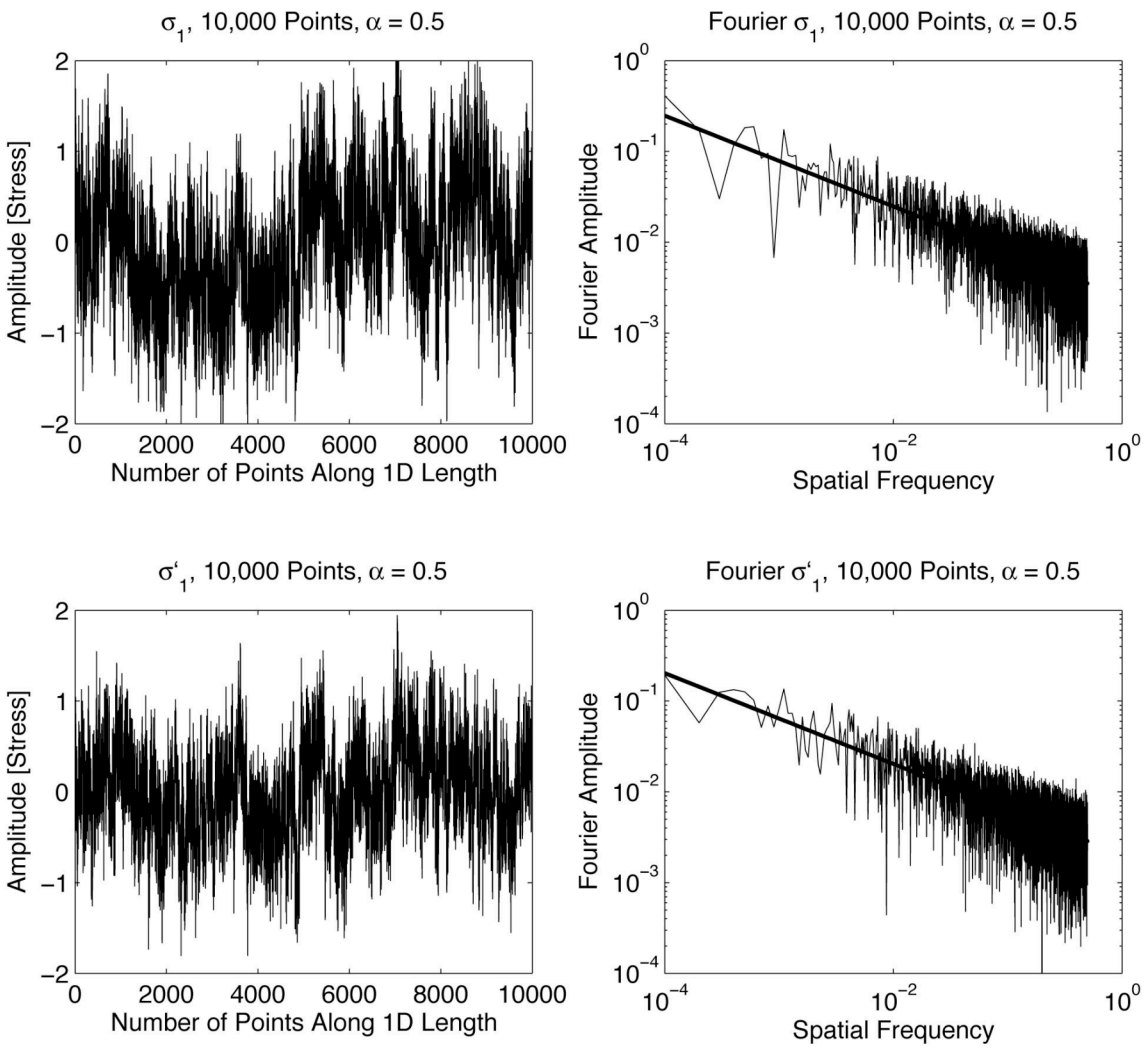
σ1, 10,000 Points, α = 0.5
Amplitude [Stress]
Number of Points Along 1D Length
Fourier σ1, 10,000 Points, α = 0.5
Fourier Amplitude
Spatial Frequency
σ'1, 10,000 Points, α = 0.5
Amplitude [Stress]
Number of Points Along 1D Length
Fourier σ'1, 10,000 Points, α = 0.5
Fourier Amplitude
Spatial Frequency

Figure 3.1 b)

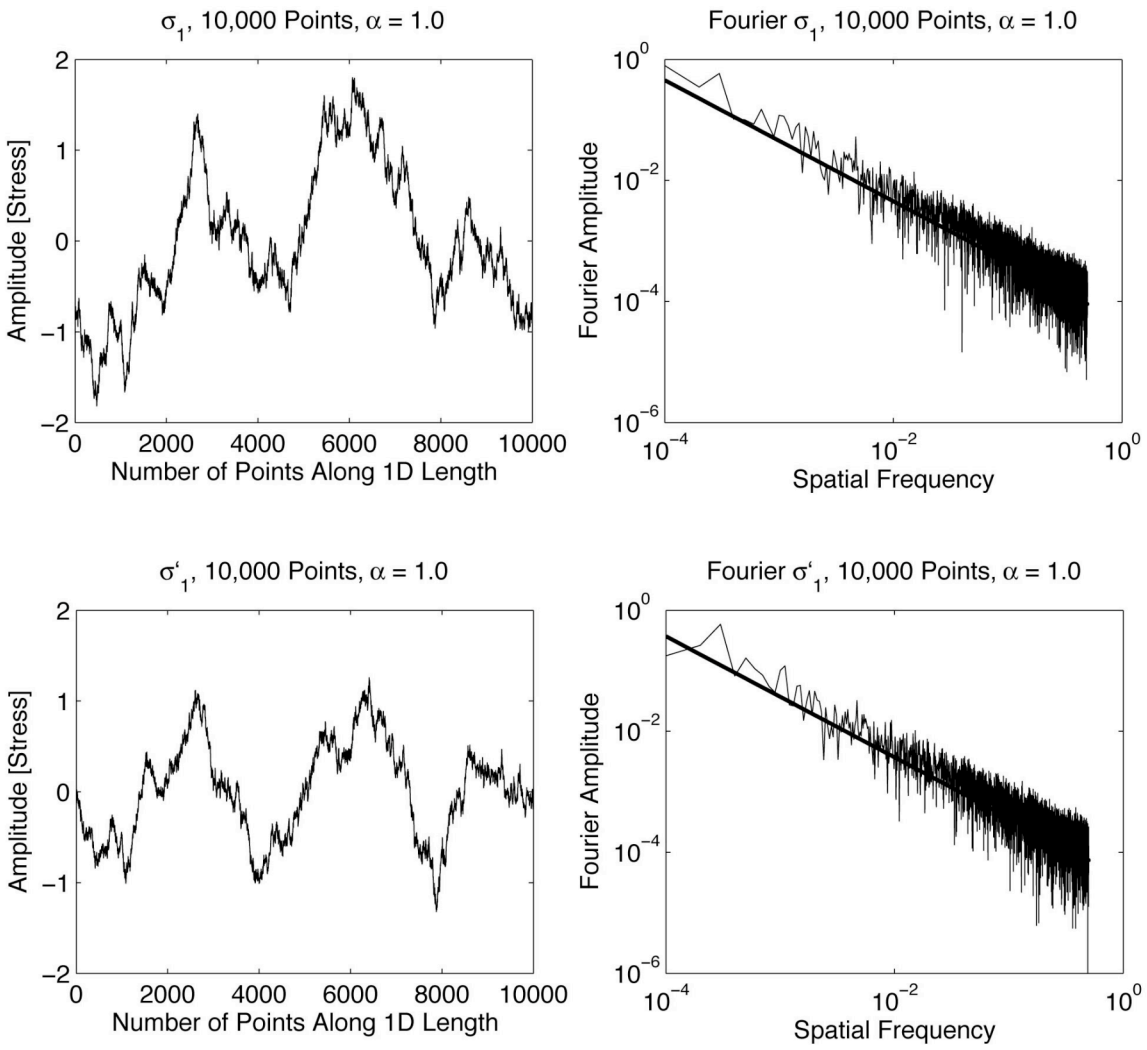
σ1, 10,000 Points, α = 1.0
Amplitude [Stress]
Number of Points Along 1D Length
Fourier σ1, 10,000 Points, α = 1.0
Fourier Amplitude
Spatial Frequency
σ'1, 10,000 Points, α = 1.0
Amplitude [Stress]
Number of Points Along 1D Length
Fourier σ'1, 10,000 Points, α = 1.0
Fourier Amplitude
Spatial Frequency

Figure 3.1 c)

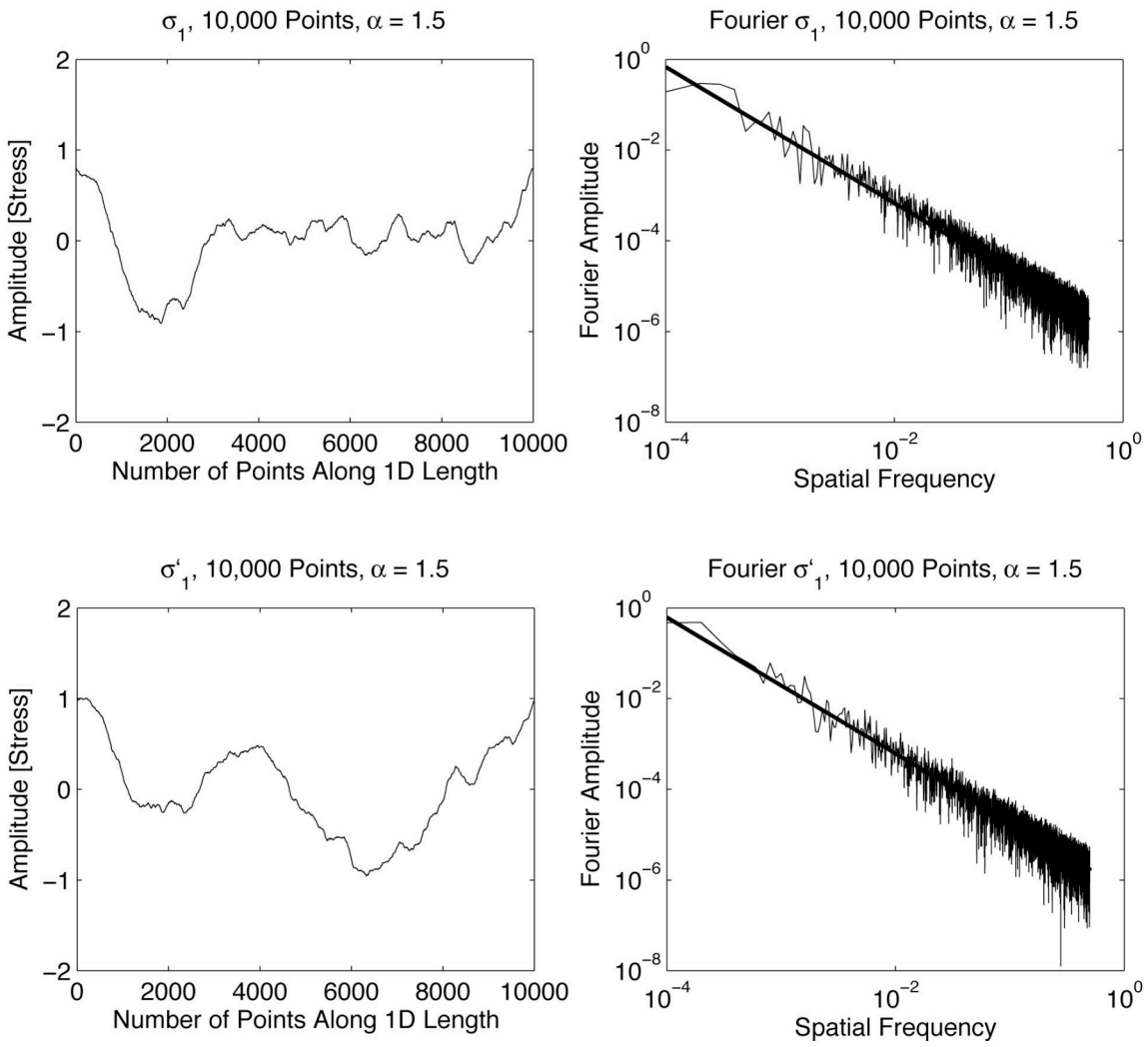
σ1, 10,000 Points, α = 1.5
Amplitude [Stress]
Number of Points Along 1D Length
Fourier σ1, 10,000 Points, α = 1.5
Fourier Amplitude
Spatial Frequency
σ'1, 10,000 Points, α = 1.5
Amplitude [Stress]
Number of Points Along 1D Length
Fourier σ'1, 10,000 Points, α = 1.5
Fourier Amplitude
Spatial Frequency

Figure 3.1 d)

Figure 3.1. *Filtered scalar invariants, σ_1 and σ_1', for 10,000 points in 1D. We start with Gaussian white noise and apply the filtering strategy from Chapter 2 to produce σ_1 with spectral 1D falloffs of α. In* ***a)*** $\alpha = 0.0$ *is applied, which means no filtering of the Gaussian white noise,* ***b)*** $\alpha = 0.5$ *is applied,* ***c)*** $\alpha = 1.0$ *is applied, and* ***d)*** $\alpha = 1.5$ *is applied. Then we subtract out the pressure, $p = (1/3)(\sigma_1 + \sigma_2 + \sigma_3)$ to produce σ_1' with the same spectral 1D falloff as σ_1. On the left are plots of the filtered stresses as a function of 1D length, and on the right are the Fourier transforms of the stresses plotted as a function of spectral frequency. The desired α spectral falloff is represented by a thick black line, and we find that indeed the spectral falloff of the filtered principal stresses closely follows the desired falloff represented by the thick line.*

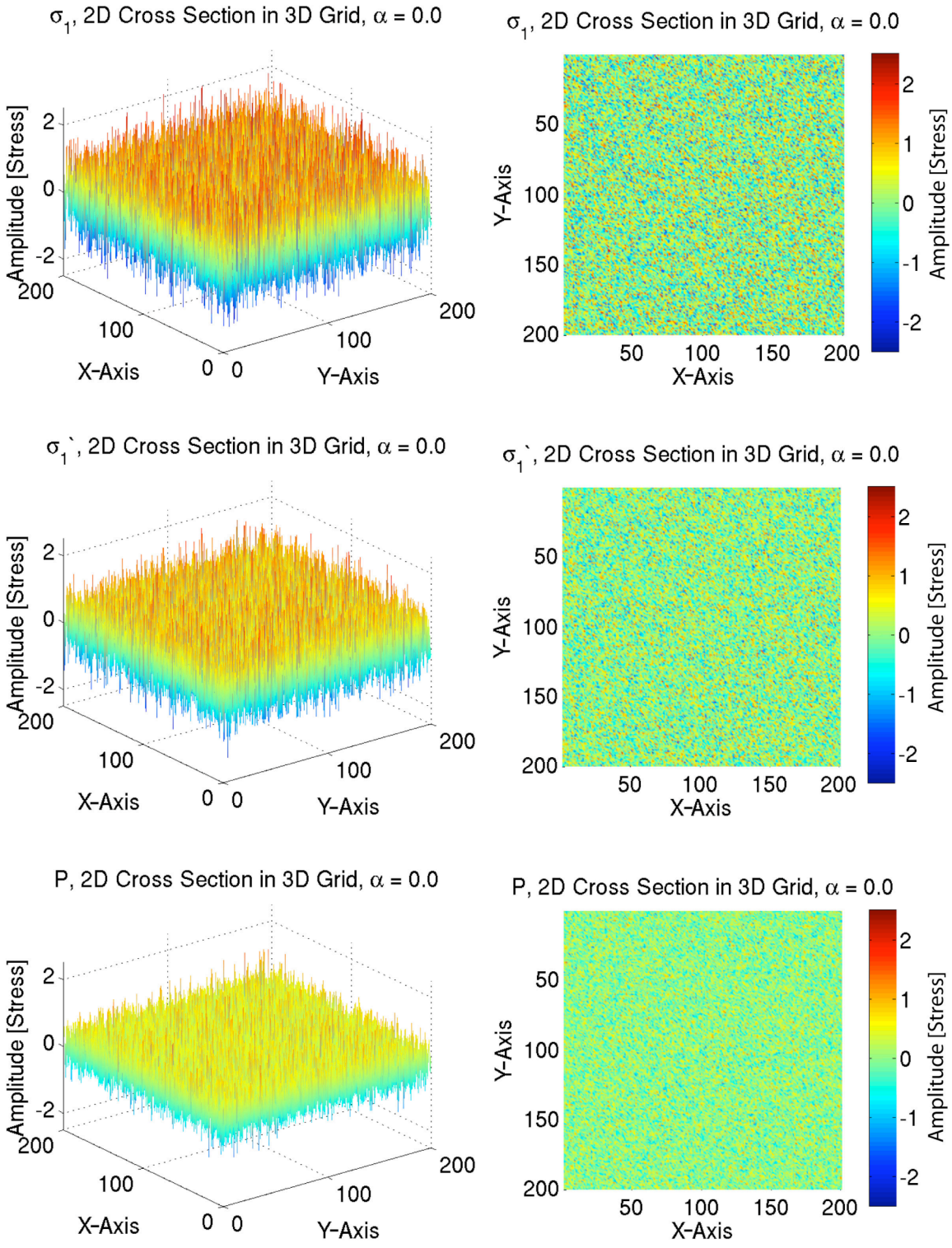
σ1, 2D Cross Section in 3D Grid, α = 0.0
Amplitude [Stress]
X-Axis
Y-Axis
σ1, 2D Cross Section in 3D Grid, α = 0.0
Y-Axis
X-Axis
Amplitude [Stress]
σ1`, 2D Cross Section in 3D Grid, α = 0.0
Amplitude [Stress]
X-Axis
Y-Axis
σ1`, 2D Cross Section in 3D Grid, α = 0.0
Y-Axis
X-Axis
Amplitude [Stress]
P, 2D Cross Section in 3D Grid, α = 0.0
Amplitude [Stress]
X-Axis
Y-Axis
P, 2D Cross Section in 3D Grid, α = 0.0
Y-Axis
X-Axis
Amplitude [Stress]

Figure 3.2 a)

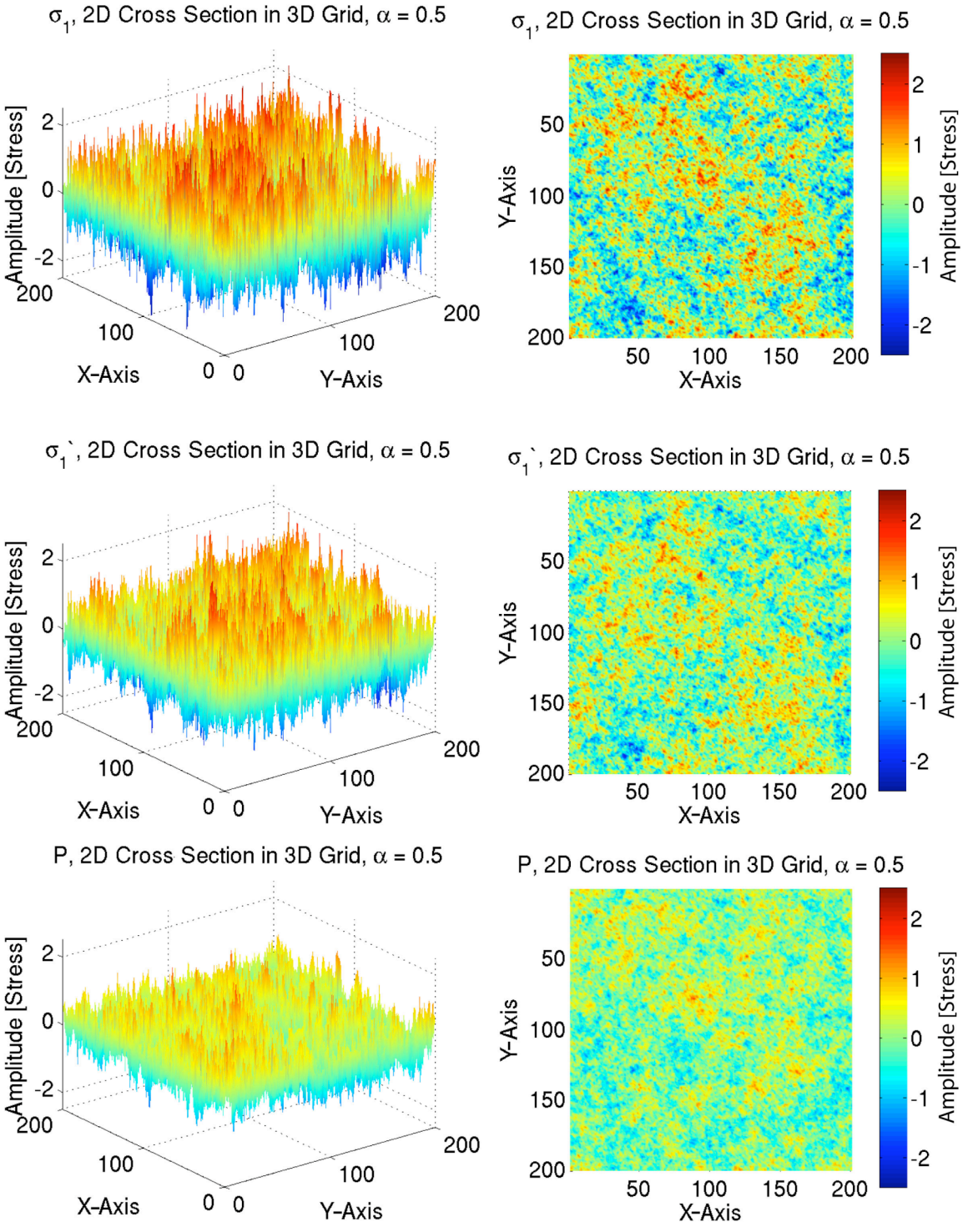
σ1, 2D Cross Section in 3D Grid, α = 0.5
Amplitude [Stress]
X-Axis
Y-Axis
σ1, 2D Cross Section in 3D Grid, α = 0.5
Y-Axis
X-Axis
Amplitude [Stress]
σ1`, 2D Cross Section in 3D Grid, α = 0.5
Amplitude [Stress]
X-Axis
Y-Axis
σ1`, 2D Cross Section in 3D Grid, α = 0.5
Y-Axis
X-Axis
Amplitude [Stress]
P, 2D Cross Section in 3D Grid, α = 0.5
Amplitude [Stress]
X-Axis
Y-Axis
P, 2D Cross Section in 3D Grid, α = 0.5
Y-Axis
X-Axis
Amplitude [Stress]

Figure 3.2 b)

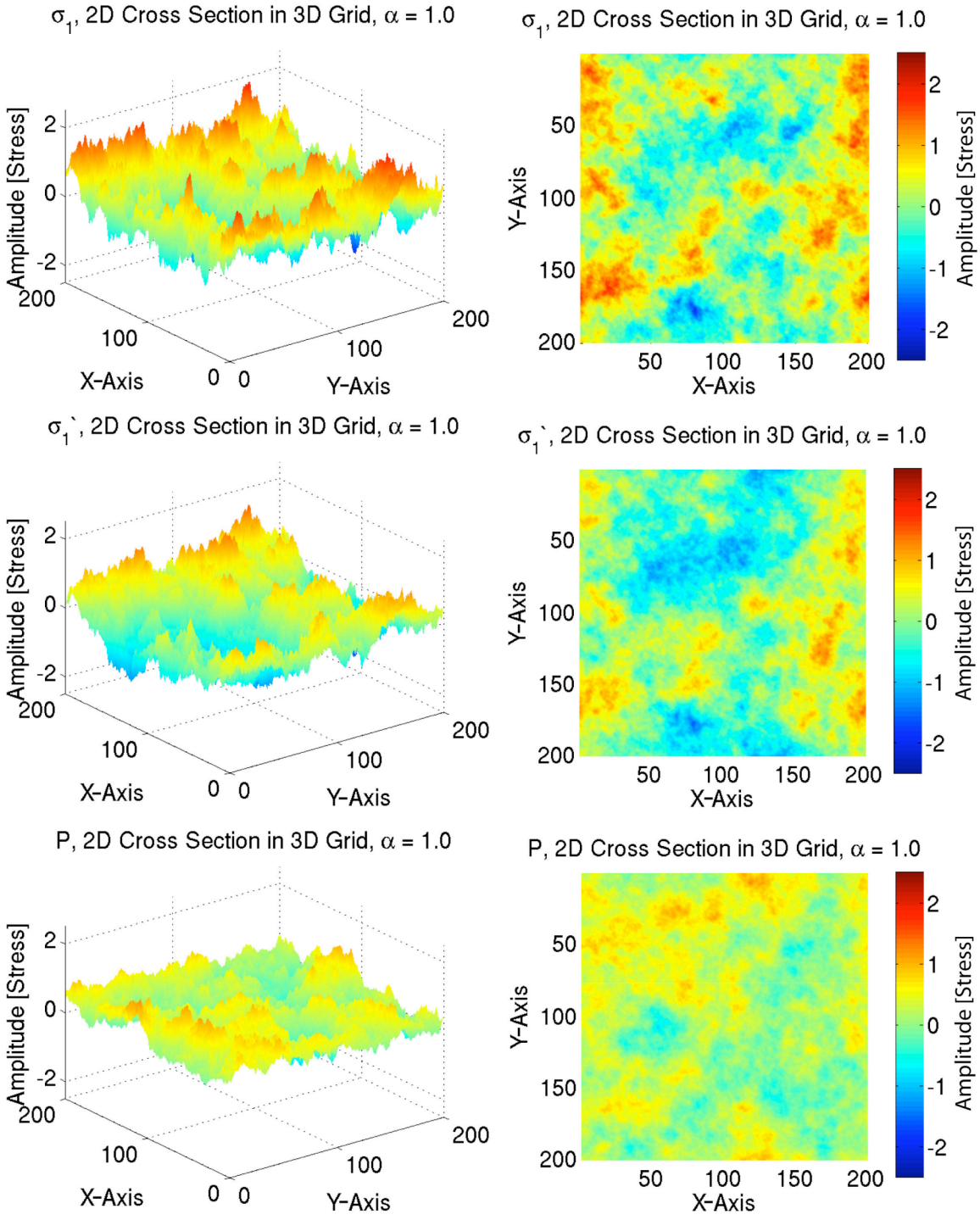
σ1, 2D Cross Section in 3D Grid, α = 1.0
Amplitude [Stress]
X-Axis
Y-Axis
σ1, 2D Cross Section in 3D Grid, α = 1.0
Y-Axis
X-Axis
Amplitude [Stress]
σ1`, 2D Cross Section in 3D Grid, α = 1.0
Amplitude [Stress]
X-Axis
Y-Axis
σ1`, 2D Cross Section in 3D Grid, α = 1.0
Y-Axis
X-Axis
Amplitude [Stress]
P, 2D Cross Section in 3D Grid, α = 1.0
Amplitude [Stress]
X-Axis
Y-Axis
P, 2D Cross Section in 3D Grid, α = 1.0
Y-Axis
X-Axis
Amplitude [Stress]

Figure 3.2 c)

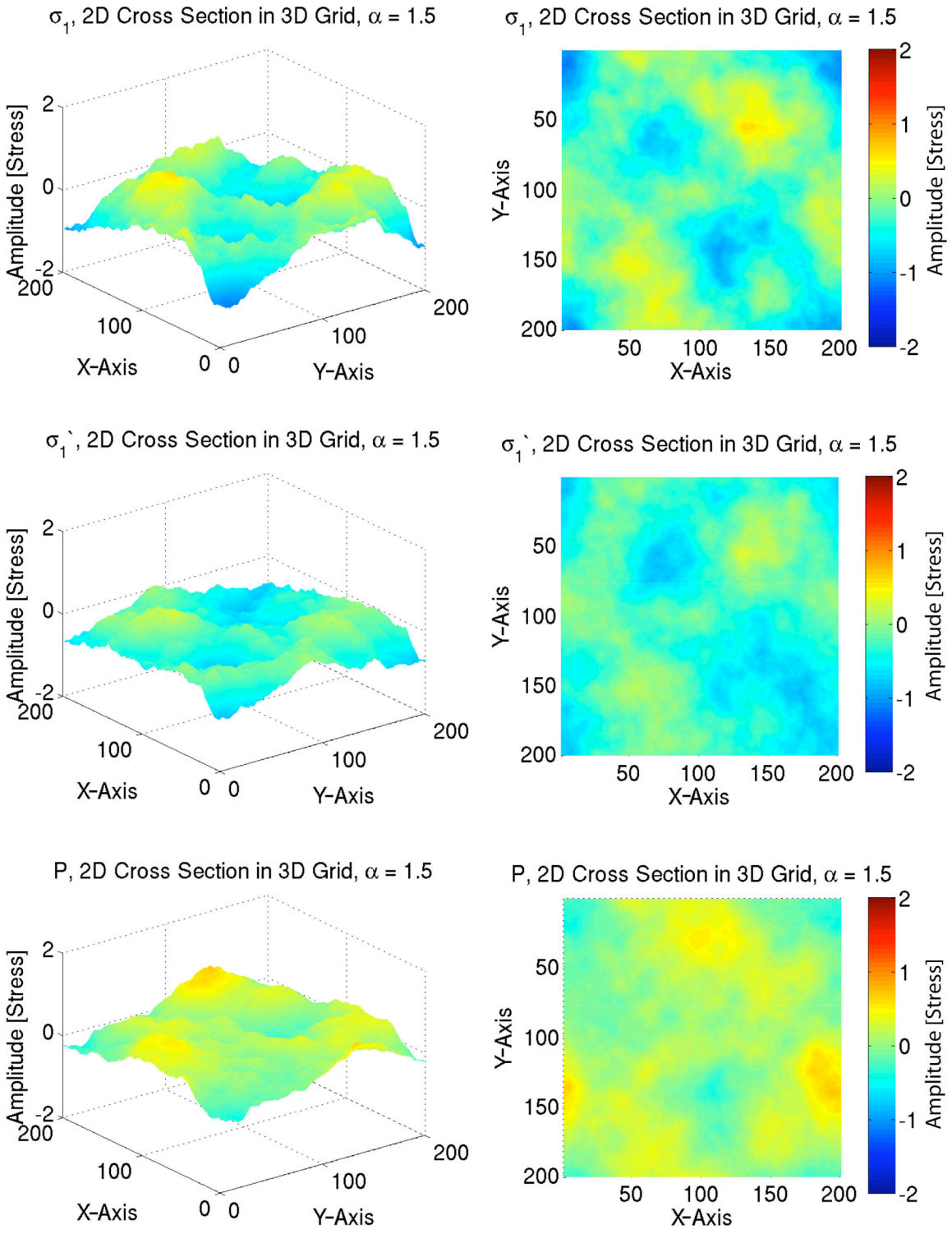
σ1, 2D Cross Section in 3D Grid, α = 1.5
Amplitude [Stress]
X-Axis
Y-Axis
σ1, 2D Cross Section in 3D Grid, α = 1.5
Y-Axis
X-Axis
Amplitude [Stress]
σ1`, 2D Cross Section in 3D Grid, α = 1.5
Amplitude [Stress]
X-Axis
Y-Axis
σ1`, 2D Cross Section in 3D Grid, α = 1.5
Y-Axis
X-Axis
Amplitude [Stress]
P, 2D Cross Section in 3D Grid, α = 1.5
Amplitude [Stress]
X-Axis
Y-Axis
P, 2D Cross Section in 3D Grid, α = 1.5
Y-Axis
X-Axis
Amplitude [Stress]

Figure 3.2 d)

Figure 3.2. *Plots of filtered scalar invariants,* σ_1, σ_1', *and* p *for 2D cross sections of 3D grids. The original 3D grids are 201x201x201; therefore, the 2D cross sections are 201x201 points. The cross sections are x-y planes at* $z = 101$, *approximately the center of the grid. We start with Gaussian white noise and apply the filtering strategy from Chapter 2 to produce filtered scalar invariants with spectral 1D falloffs of* α. *In* ***a)*** $\alpha = 0.0$ *is applied, which means no filtering of the Gaussian white noise,* ***b)*** $\alpha = 0.5$ *is applied,* ***c)*** $\alpha = 1.0$ *is applied, and* ***d)*** $\alpha = 1.5$ *is applied. On the left are surface plots of the filtered scalars where the 2 spatial dimensions of the 2D cross section are represented by the x and y axes and the amplitude of the scalar quantities is represented by the vertical height and color. On the right, are map view plots of the same 2D cross sections where the scalar amplitude is represented by color. The same color scale is used for the left and right hand plots, which goes from -2.5 to 2.5 for* $\alpha = 0.0$, $\alpha = 0.5$, *and* $\alpha = 1.0$ *and from -2.0 to 2.0 for* $\alpha = 1.5$.

Upon inspection one can notice a few features. The principal stress, σ_1, tends to have a larger amplitude than the deviatoric principal stress, σ_1', but similar spatial smoothing. By design as the value of α increases so does the spatial smoothing. Since Figure 3.2 shows only 2D cross sections through a 3D grid, and the mean is set to zero for the entire 3D grid, the means of the 2D cross sections are not necessarily zero; in fact, the means of the 2D cross sections are often non-zero.

Orientation Filtering

The next three quantities we wish to consider filtering are the three angles describing the orientation of the stress tensor. There are several sets of three angles we could choose. We could choose

- Three Euler angles that describe the rotation of a stress tensor relative to a reference orientation. This would be analogous to the strike, dip, and rake of slip vector on a fault plane.
- Azimuth and plunge of the P axis plus an angle describing the orientation of the T axis about the P axis
- A total rotation angle, ω, about a rotation axis, $[\theta,\phi]$ that represents a single rotation from a reference stress orientation to our desired point stress orientation.

The representation we prefer to use is the third one, a total rotation angle, ω, about a rotation axis, $[\theta,\phi]$. This seems to be the most natural set of three angles to filter if our intended goal is to filter stress tensor orientations. Namely, when we filter ω, we are simply filtering the amplitude of the rotation (amplitude of the spherical linear interpolation from the reference orientation to our desired orientation). When we filter

the angles in the rotation axis, $[\theta,\phi]$, we are filtering the axis about which the rotation takes place, where $[\theta,\phi]$ describe the path of the spherical linear interpolation. So by filtering these three quantities (ω,$[\theta,\phi]$), we smooth out in space the total 3D orientation of the stress tensor. See Figures 3.3 and 3.4 for graphical explanations of this representation. Figure 3.3 explains how the rotation axis is defined; it passes from the origin through the point with colatitude, θ, and longitude, ϕ (this point is called the pole of rotation). Figure 3.4 shows how once the rotation axis is defined with $[\theta,\phi]$, we can then apply our single rotation of amplitude ω, about this axis, $[\theta,\phi]$.

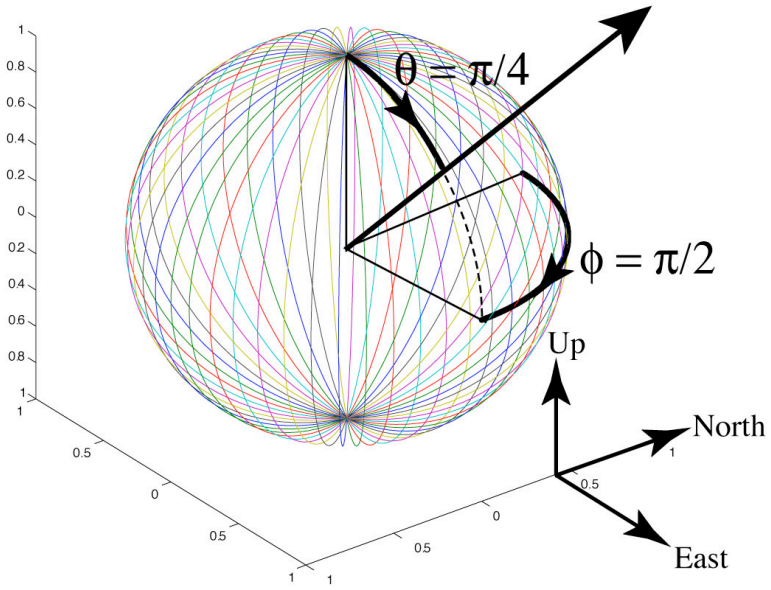

Figure 3.3. *How the rotation axis, $[\theta,\phi]$, is defined. The rotation axis, is the thick black arrow projecting out of the unit sphere. θ is the colatitude of the rotation axis, the angle between the Up vector and the rotation vector, while ϕ is the longitude of the rotation axis, the angle between the North vector and the horizontal projection of the rotation axis, in a right-hand coordinate system about the Up vector.*

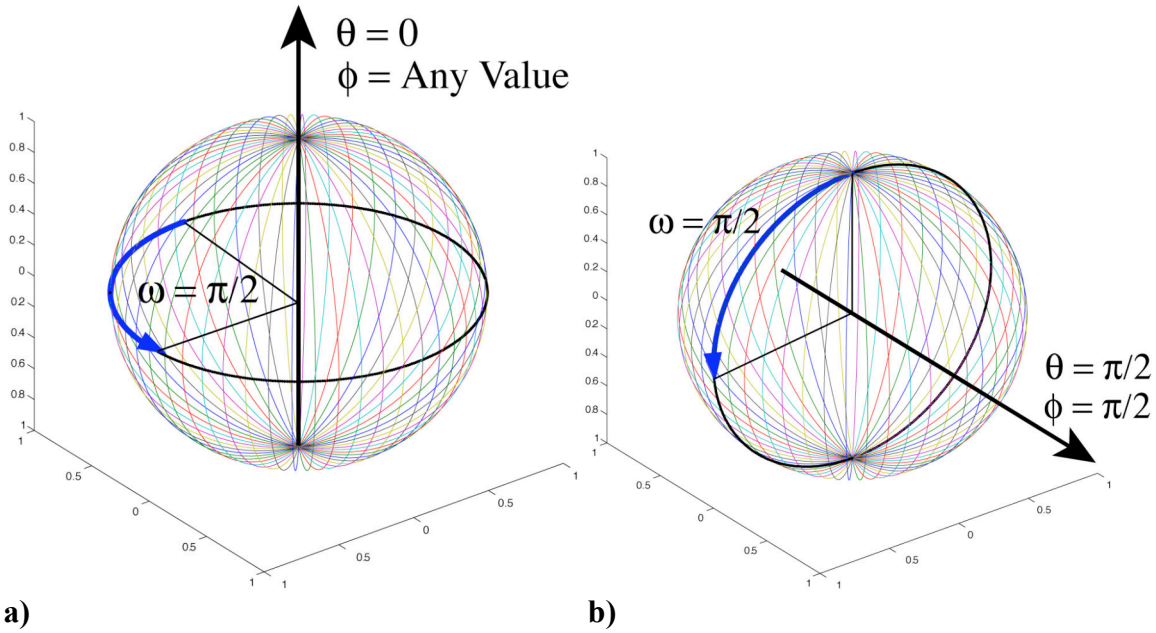

Figure 3.4. *Two examples of our* $(\omega,[\theta,\phi])$ *representation of 3D rotations. In* ***a)*** *we have* $\theta = 0$ *and* $\phi =$ *any value for the rotation axis. For* ***b)*** *we have* $\theta = \pi/2$ *and* $\phi = \pi/2$ *for the rotation axis. Both* ***a)*** *and* ***b)*** *have an* $\omega = \pi/2$ *rotation about their respective rotation axes.*

Now that we have defined the three scalar angles we wish to filter, an amplitude, ω, plus a rotation axis, $[\theta,\phi]$, how do we go about filtering them? We first wish to generate completely random sets of $(\omega,[\theta,\phi])$, then filter the three angles. Random sets of $(\omega,[\theta,\phi])$ are $(\omega,[\theta,\phi])$ such that the summation of N stress tensors as $N \to \infty$ combined with random σ_1', σ_2', and σ_3', produces an expected value of

$\boldsymbol{\sigma}' = \begin{pmatrix} 0.0 & 0.0 & 0.0 \\ 0.0 & 0.0 & 0.0 \\ 0.0 & 0.0 & 0.0 \end{pmatrix}$, i.e., $E\langle\boldsymbol{\sigma}'\rangle = 0$. This is important because when we create our filtered heterogeneous component of the stress tensor, there should be no net orientation to the deviatoric, heterogeneous term in 3D.

$$E\left\langle\boldsymbol{\sigma}'_{Heterogeneous}\right\rangle = 0 \tag{3.11}$$

To create truly random sets of $(\omega,[\theta,\phi])$, it is helpful to work in quaternion space, producing random quaternions, then transform them back to $(\omega,[\theta,\phi])$ space.

A quaternion is simply a four-component vector that represents a 3D rotation. Analogy can be used to understand this. To describe a point on a 3D unit sphere, there are two different ways to represent the position. One representation would be a three-component vector, $\vec{u} = [u_x, u_y, u_z]$, with the constraint that $|\vec{u}| = \sqrt{u_x^2 + u_y^2 + u_z^2} = 1$, so that the point lies on the surface of the 3D unit sphere. This reduces the degrees of freedom from three to two. Another representation would be in terms of two angles, θ and ϕ. In the case of a 4D unit hypersphere, we again have two possible analogous representations. We can use a four-component vector, a quaternion, $\vec{q} = [q_0, q_1, q_2, q_3]$, with the constraint that $|\vec{q}| = \sqrt{q_0^2 + q_1^2 + q_2^2 + q_3^2} = 1$, so that the point lies on the surface of the 4D unit sphere and the degrees of freedom reduce from four to three. Alternatively, we can use three angles, ω, θ, and ϕ. Thus this problem of producing random $(\omega,[\theta,\phi])$ reduces to the problem of choosing completely random points on the surface of a unit 4D hypersphere, which was solved by Marsaglia [1972].

The method of Marsaglia [1972] for picking random points on a 4D hypersphere, which produces unbiased 3D orientations, is summarized at the following web link http://mathworld.wolfram.com/HyperspherePointPicking.html [*Weisstein*]. In this method, one uses a uniform random number generator to pick pairs of points (x_1, x_2) and (x_3, x_4), keeping only those pairs that satisfy the following constraints, $x_1^2 + x_2^2 < 1$ and $x_3^2 + x_4^2 < 1$. For each set of points that are retained, one calculates the random quaternion, $\vec{q}^{\,R} = \left[q_0^R, q_1^R, q_2^R, q_3^R\right]$, as follows,

$$\begin{aligned} q_0^R &= x_4\sqrt{\frac{1-x_1^2-x_2^2}{x_3^2+x_4^2}} \\ q_1^R &= x_1 \\ q_2^R &= x_2 \\ q_3^R &= x_3\sqrt{\frac{1-x_1^2-x_2^2}{x_3^2+x_4^2}} \end{aligned} \quad . \tag{3.12}$$

Once the random unit quaternions are calculated, we then transform the four-vectors into their equivalent angles, $(\omega, [\theta, \phi])$. We use the standard relation between a quaternion, $\vec{q} = \left[q_0, q_1, q_2, q_3\right]$, and our set of angles, $(\omega, [\theta, \phi])$

$$\begin{aligned} q_0 &= \cos(\omega/2) \\ q_1 &= \sin(\omega/2)\sin(\theta)\cos(\phi) \\ q_2 &= \sin(\omega/2)\sin(\theta)\sin(\phi) \\ q_3 &= \sin(\omega/2)\cos(\theta) \end{aligned} \tag{3.13}$$

where

$$|\vec{q}| = \sqrt{q_0^2 + q_1^2 + q_2^2 + q_3^2} = 1.$$

Conversely, we can turn the quaternions into our three angles, ω, θ, and ϕ.

$$\begin{aligned}\omega &= 2\cos^{-1}\left(q_0\right)\\ \theta &= \cos^{-1}\left(q_3 / \sin\left(\omega/2\right)\right)\\ \phi &= \tan^{-1}\left(q_2/q_1\right)\end{aligned} \tag{3.14}$$

where $0° \le \omega \le 360°$, $0° \le \theta \le 180°$, and $0° \le \phi \le 360°$.

After generating random points on the 4D hypersphere (quaternions) and transforming these points into our orientation representation, $\left(\omega,[\theta,\phi]\right)$, we can now filter these three angles separately using the scalar filtering technique outlined in the previous chapter. As we will show in Figures 3.11, the filtering process introduces an orientation bias. We remove this bias by stacking at least 10–20 simulations where a random rotation has been added to the orientations in each simulation. Any orientation bias cancels out in the stacking process also seen in Figure 3.11.

To add a random rotation to our stress orientations, we again employ quaternions. Quaternions allow rotations to be added algebraically. For example, if we have a stress tensor orientation represented by the quaternion $\vec{q}^{\,A} = \left[q_0^A, q_1^A, q_2^A, q_3^A\right]$ and we wish to add on the 3D rotation represented by quaternion $\vec{q}^{\,B} = \left[q_0^B, q_1^B, q_2^B, q_3^B\right]$ to produce a final orientation represented by quaternion $\vec{q}^{\,C} = \left[q_0^C, q_1^C, q_2^C, q_3^C\right]$, the algebra would simply be (adapted from http://www.mathworks.com/access/helpdesk/help/toolbox/aeroblks/aeroblks.html, Quaternion Multiplication) [*Mathworks*, 1994-2006],

$$\begin{aligned}q_0^C &= q_0^B q_0^A - q_1^B q_1^A - q_2^B q_2^A - q_3^B q_3^A\\ q_1^C &= q_0^B q_1^A + q_1^B q_0^A - q_2^B q_3^A + q_3^B q_2^A\\ q_2^C &= q_0^B q_2^A + q_1^B q_3^A + q_2^B q_0^A - q_3^B q_1^A\\ q_3^C &= q_0^B q_3^A - q_1^B q_2^A + q_2^B q_1^A + q_3^B q_0^A.\end{aligned} \tag{3.15}$$

As expected, the order of rotations is important, i.e., rotations are noncommutative.

Figure 3.6 shows 1D plots of our filtered orientation angles, $(\omega,[\theta,\phi])$, before and after random rotations have been added. The amplitude angles, ω, are plotted on the left as a function of 1D linear distance, and the rotation axes, $[\theta,\phi]$, are plotted on the right as points on an equal area plot where $0° < \omega < 360°$, $0° < \theta < 180°$, and $0° < \phi < 360°$. The longitude, ϕ, is represented by the azimuthal angle about the circular, equal area plot as shown in Figure 3.5, and θ is represented by the radial distance from the center of the circle. $\theta = 0°$ at the center, and $\theta = 180°$ at the circumference. At first this may seem like an odd representation until one thinks about the plot in terms of latitude, $\lambda = 90° - \theta$, instead of the colatitude, θ. In terms of the latitude, λ, $\lambda = 90°$ at the center and $\lambda = –90°$ at the circumference, which is similar to an equal area P-T plot that shows the full plunge range of $\pm\ 90°$.

The top and bottom rows show $(\omega,[\theta,\phi])$, where random orientations have been filtered with an α then multiplied with a reference quaternion. The top row shows the unrotated $(\omega,[\theta,\phi])$, and the bottom row shows the rotated $(\omega,[\theta,\phi])$. When the reference quaternion is $[q_0 = 1, q_1 = 0, q_2 = 0, q_3 = 0]$, as seen in the top row, $(\omega,[\theta,\phi])$ is unchanged upon multiplication, because $[q_0 = 1, q_1 = 0, q_2 = 0, q_3 = 0]$ produces no rotation; $\omega = 2\cos^{-1}(q_0) = 2\cos^{-1}(1.0) = 0°$. When the reference quaternion is something other than $[q_0 = 1, q_1 = 0, q_2 = 0, q_3 = 0]$, as seen in the bottom row, $(\omega,[\theta,\phi])$ is rotated upon quaternion multiplication.

If there is no filtering, $\alpha = 0.0$, then our $(\omega,[\theta,\phi])$s are produced using the random unit quaternion generator, and the rotation axes, $[\theta,\phi]$, are uniformly distributed on the equal area plot as seen in Figure 3.6 a). As the filtering constant, α, increases, the spatial smoothing of $(\omega,[\theta,\phi])$ increases: 1) ω becomes smoother as a function of distance. 2) The rotation axes, $[\theta,\phi]$, at first clump for $\alpha = 0.5$ and $\alpha = 1.0$, then track a clearly distinguishable linear path on the equal area plot for $\alpha = 1.5$. The rotated and unrotated cases have fairly similar properties (degree of spatial smoothing, clumping, etc.); therefore, we should be able to stack the filtered and randomly rotated $(\omega,[\theta,\phi])$s to produce no net orientation, while maintaining to first order, the α-filtered properties of each individual run.

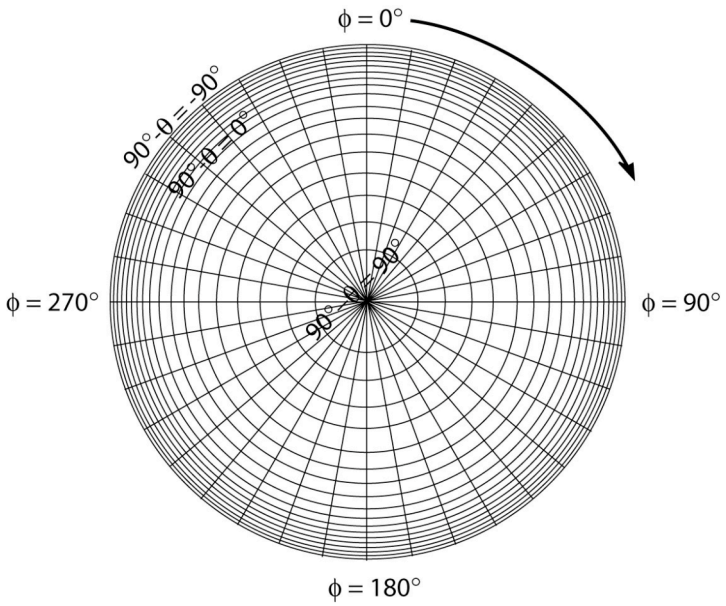

Figure 3.5. *A cartoon of the equal area plots used in Figure 3.6 for the rotation axes,* $[\theta,\phi]$. *The longitude,* ϕ*, is the azimuth of the circle, and latitude,* $\lambda = 90° - \theta$*, is plotted as a function of radial distance where,* $\lambda = 90° - \theta = 90°$ *at the center and* $\lambda = 90° - \theta = -90°$*, at the circumference. Note the cartoon is not necessarily to scale.*

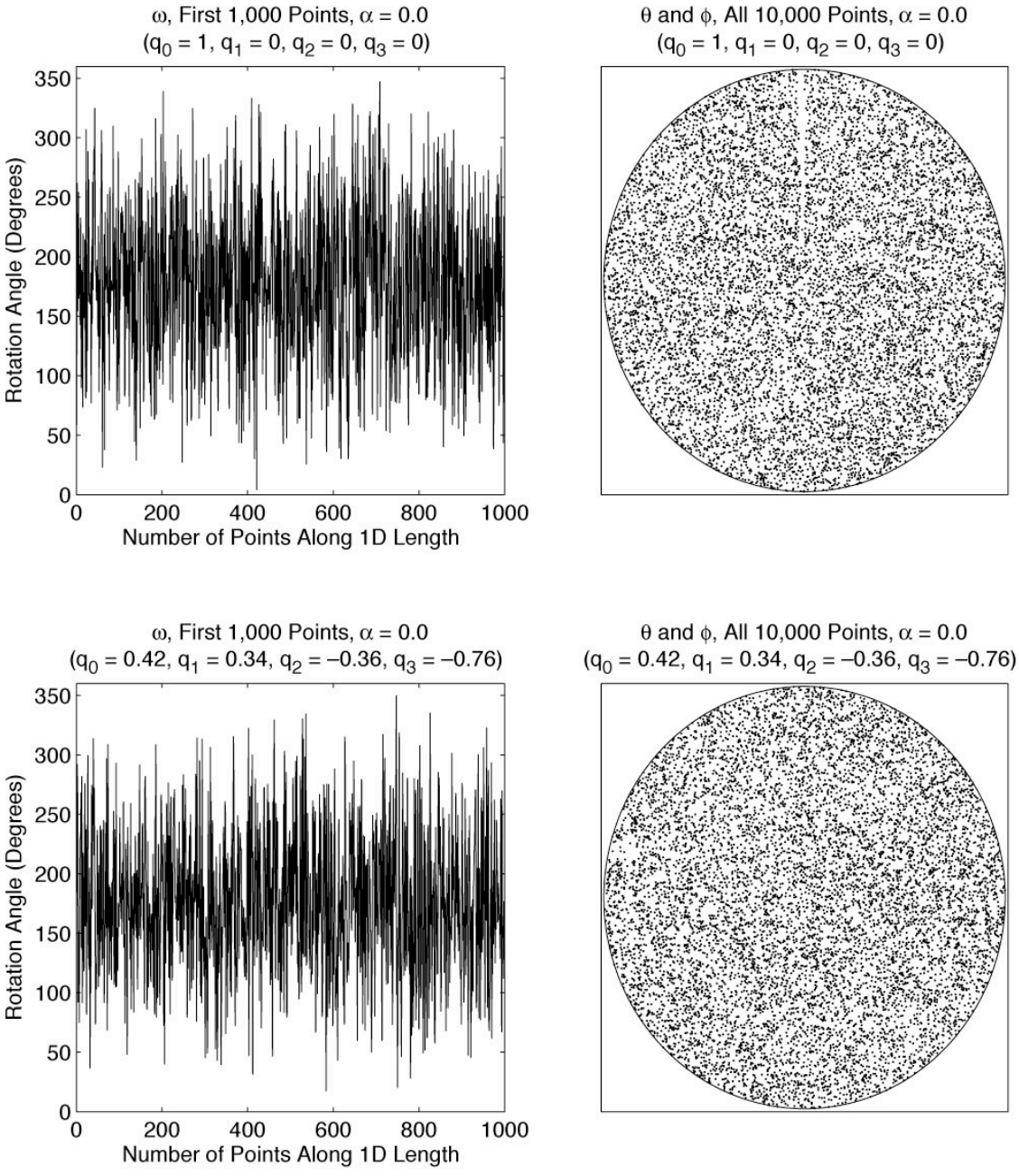
ω, First 1,000 Points, α = 0.0
(q0 = 1, q1 = 0, q2 = 0, q3 = 0)
θ and ϕ, All 10,000 Points, α = 0.0
(q0 = 1, q1 = 0, q2 = 0, q3 = 0)
Rotation Angle (Degrees)
Number of Points Along 1D Length
ω, First 1,000 Points, α = 0.0
(q0 = 0.42, q1 = 0.34, q2 = −0.36, q3 = −0.76)
θ and ϕ, All 10,000 Points, α = 0.0
(q0 = 0.42, q1 = 0.34, q2 = −0.36, q3 = −0.76)
Rotation Angle (Degrees)
Number of Points Along 1D Length

Figure 3.6 a)

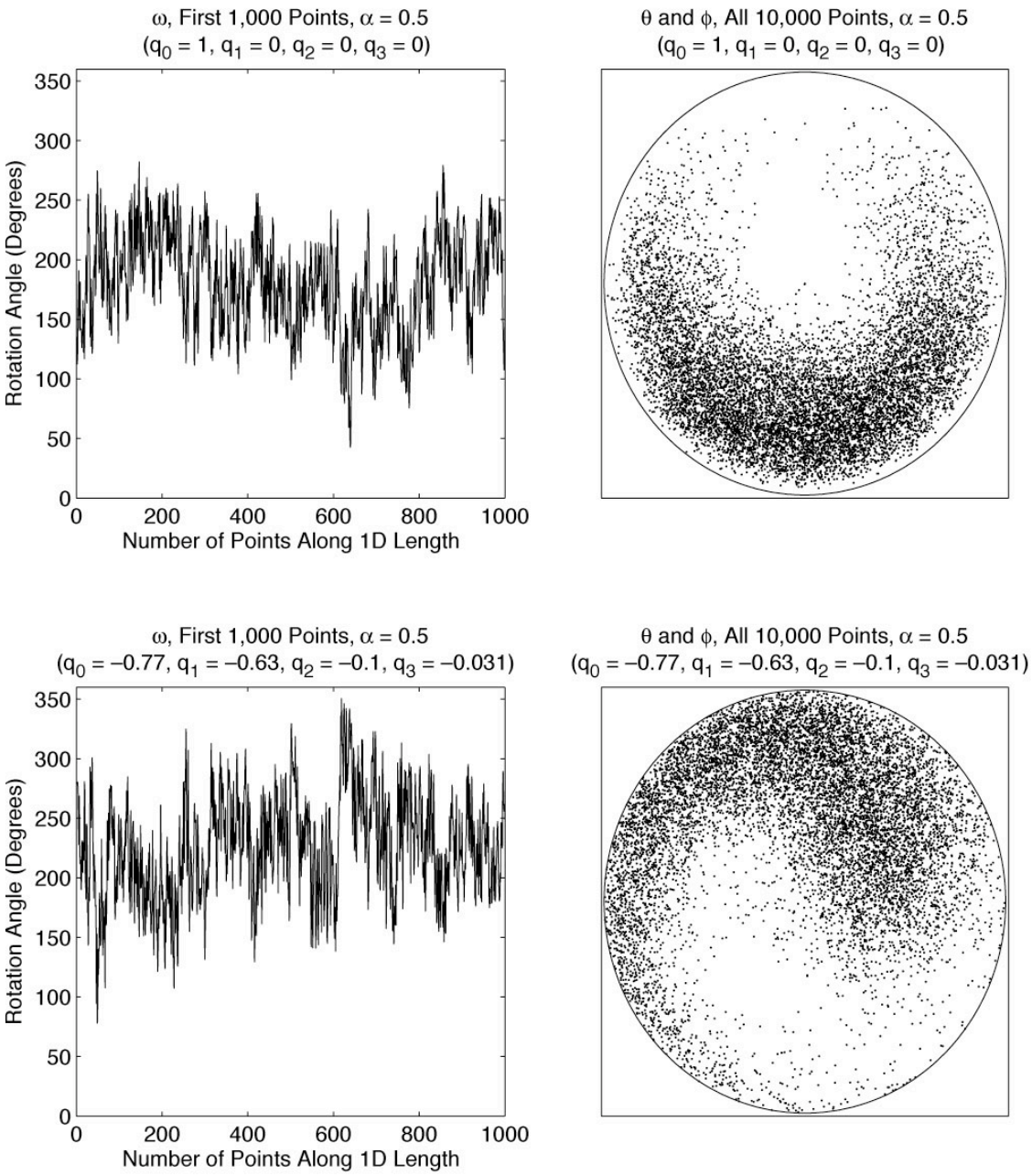
ω, First 1,000 Points, α = 0.5
(q0 = 1, q1 = 0, q2 = 0, q3 = 0)
θ and ϕ, All 10,000 Points, α = 0.5
(q0 = 1, q1 = 0, q2 = 0, q3 = 0)
Rotation Angle (Degrees)
Number of Points Along 1D Length
ω, First 1,000 Points, α = 0.5
(q0 = −0.77, q1 = −0.63, q2 = −0.1, q3 = −0.031)
θ and ϕ, All 10,000 Points, α = 0.5
(q0 = −0.77, q1 = −0.63, q2 = −0.1, q3 = −0.031)
Rotation Angle (Degrees)
Number of Points Along 1D Length

Figure 3.6 b)

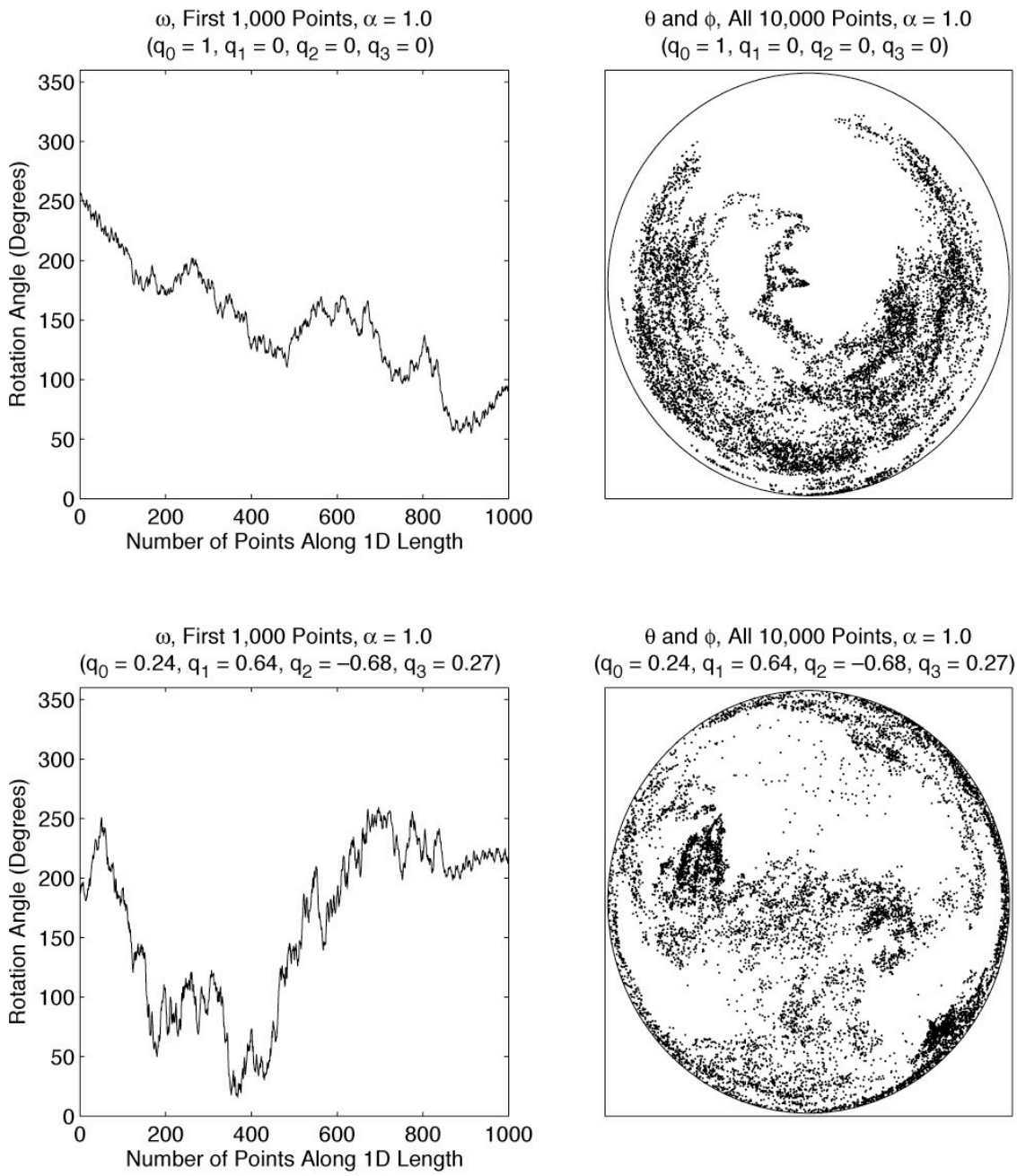
ω, First 1,000 Points, α = 1.0
(q0 = 1, q1 = 0, q2 = 0, q3 = 0)
θ and ϕ, All 10,000 Points, α = 1.0
(q0 = 1, q1 = 0, q2 = 0, q3 = 0)
Rotation Angle (Degrees)
Number of Points Along 1D Length
ω, First 1,000 Points, α = 1.0
(q0 = 0.24, q1 = 0.64, q2 = −0.68, q3 = 0.27)
θ and ϕ, All 10,000 Points, α = 1.0
(q0 = 0.24, q1 = 0.64, q2 = −0.68, q3 = 0.27)
Rotation Angle (Degrees)
Number of Points Along 1D Length

Figure 3.6 c)

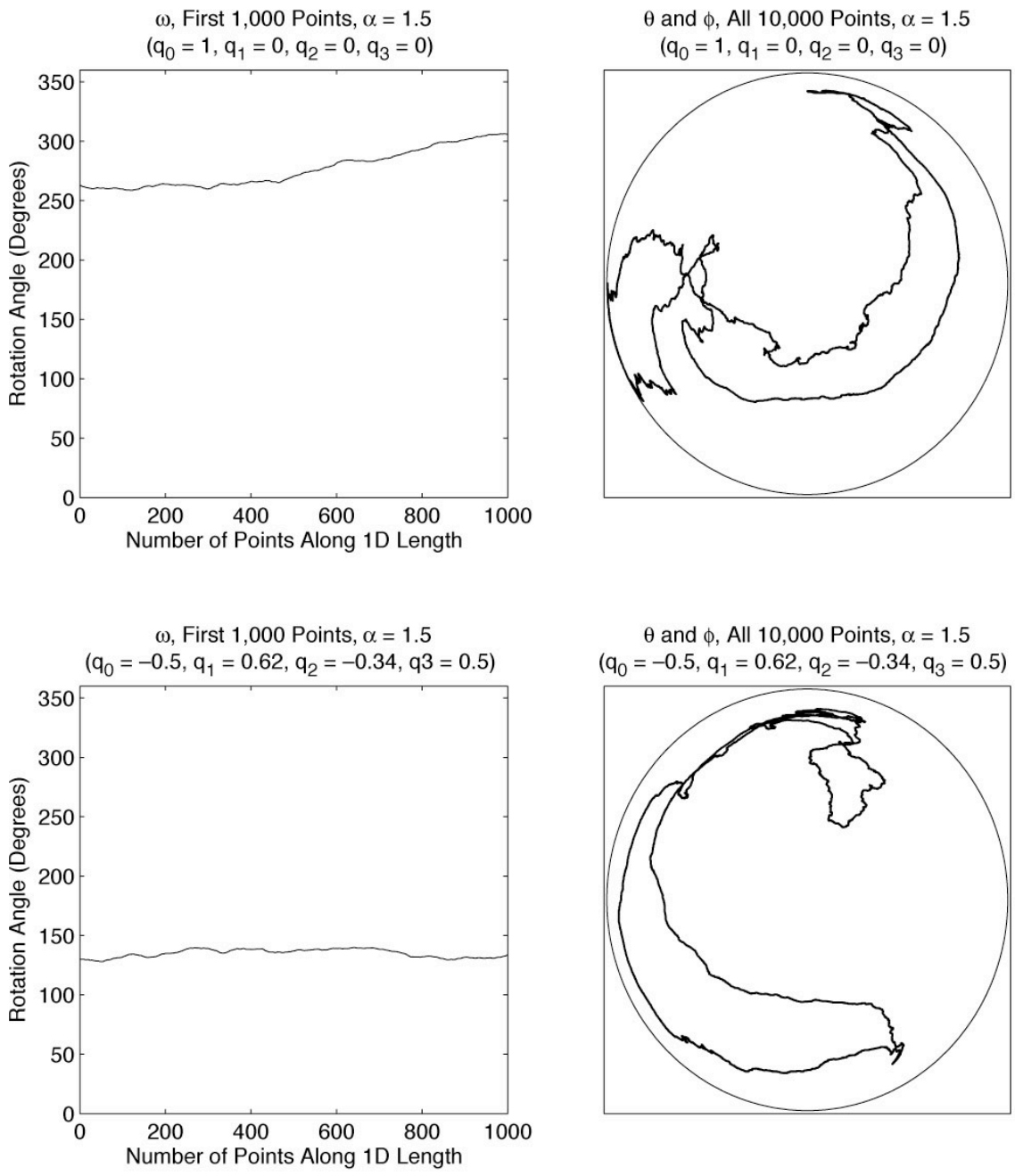
ω, First 1,000 Points, α = 1.5
(q0 = 1, q1 = 0, q2 = 0, q3 = 0)
θ and ϕ, All 10,000 Points, α = 1.5
(q0 = 1, q1 = 0, q2 = 0, q3 = 0)
Rotation Angle (Degrees)
Number of Points Along 1D Length
ω, First 1,000 Points, α = 1.5
(q0 = –0.5, q1 = 0.62, q2 = –0.34, q3 = 0.5)
θ and ϕ, All 10,000 Points, α = 1.5
(q0 = –0.5, q1 = 0.62, q2 = –0.34, q3 = 0.5)
Rotation Angle (Degrees)
Number of Points Along 1D Length

Figure 3.6 d)

Figure 3.6. *A series of 1D simulations are shown with different degrees of smoothing, α, applied where* ***a)*** $\alpha = 0.0$, ***b)*** $\alpha = 0.5$, ***c)*** $\alpha = 1.0$, *and* ***d)*** $\alpha = 1.5$. *Each simulation is approximately 10,000 points. For each α, there are a total of four subplots. On the top left is a 1,000-points-long segment of the filtered rotation angle, ω. As expected, as α increases, the spatial smoothness of the rotation angle, ω, increases. On the bottom left is again ω, but after a random rotation has been applied to the orientation angles. It appears to maintain its filtered properties to first order upon inspection. See Figure 3.8 for a more thorough evaluation of what happens to the spectral properties upon rotation of coordinate system. On the top right is an equal area plot with the rotation axes, $[\theta,\phi]$, plotted as black dots. On the bottom right is another equal area plot of the rotation poles, $[\theta,\phi]$, after a random rotation has been applied. Again the spatially smoothed rotation poles maintain their spectral properties to first order.*

For $\alpha = 0.0$, no spatial smoothing or completely random orientations produce completely random rotation poles on our equal area plot. This unbiased distribution remains unchanged upon rotation of coordinate systems. As α increases, the rotation poles begin clumping together until they form 1D lines, representing the wander of the 1D data set.

In Figure 3.7, our three orientation angles, $(\omega,[\theta,\phi])$, for 1D simulations are visualized in a different way. 3D unit spheres have been plotted with a wire mesh, then the position of the rotation axes, $[\theta,\phi]$, are plotted as points on the sphere. Last, the color of the points represents the amplitude angle, ω according to the horizontal color bars underneath. On the left, are the unrotated, $(\omega,[\theta,\phi])$, and on the right are the rotated, $(\omega,[\theta,\phi])$. When there is no filtering, $\alpha = 0.0$, the rotation axes, $[\theta,\phi]$, are uniformly distributed over the sphere, and the color, which represents the amplitude, ω, is random. Additionally, when $\alpha = 0.0$ the angles, $(\omega,[\theta,\phi])$, appear to be unchanged upon rotation. There is the same random pattern after rotation as before. As the filtering, α, increases, the spatial smoothing of the points on the sphere increases, and the spatial smoothing of the colors increases, representing the smoothing of the three angles, $(\omega,[\theta,\phi])$, until at $\alpha = 1.5$ the data form clear demarcated linear tracks. The rotated data on the right have similar smoothness as the unrotated data to first order.

The spectral properties of the unrotated and rotated ω are plotted in Figure 3.8 to examine how closely our filtered angles approach the desired α spectral falloff. While not shown, the rotation axes, $[\theta,\phi]$, have similar properties, but ϕ is more difficult to plot because one needs to wrap the phase appropriately before calculating the spectral properties. The plots on the left in Figure 3.8 show the angle ω as a function of 1D length, and the plots on the right in Figure 3.8 show the Fourier transform of the angle ω as a function of spatial frequency. The right-hand plots also have a thick black line, which shows the desired α spectral falloff. To first order, ω, follows the desired α spectral falloff for both the rotated and unrotated cases with the lowest frequencies

sometimes a little underrepresented. The exact spectral falloff for our three orientation angles, $(\omega,[\theta,\phi])$, is calculated in Table 3.1, where the spectral falloffs for 200 1D simulations, approximately 10,000 points each is averaged for different values of α. Then the results of Table 3.1 are plotted in Figure 3.9. We find that indeed the unrotated, $(\omega,[\theta,\phi])$, has exactly the spectral falloff we want, α, but the rotated angles, are slightly rougher for $\alpha < 0.6$.

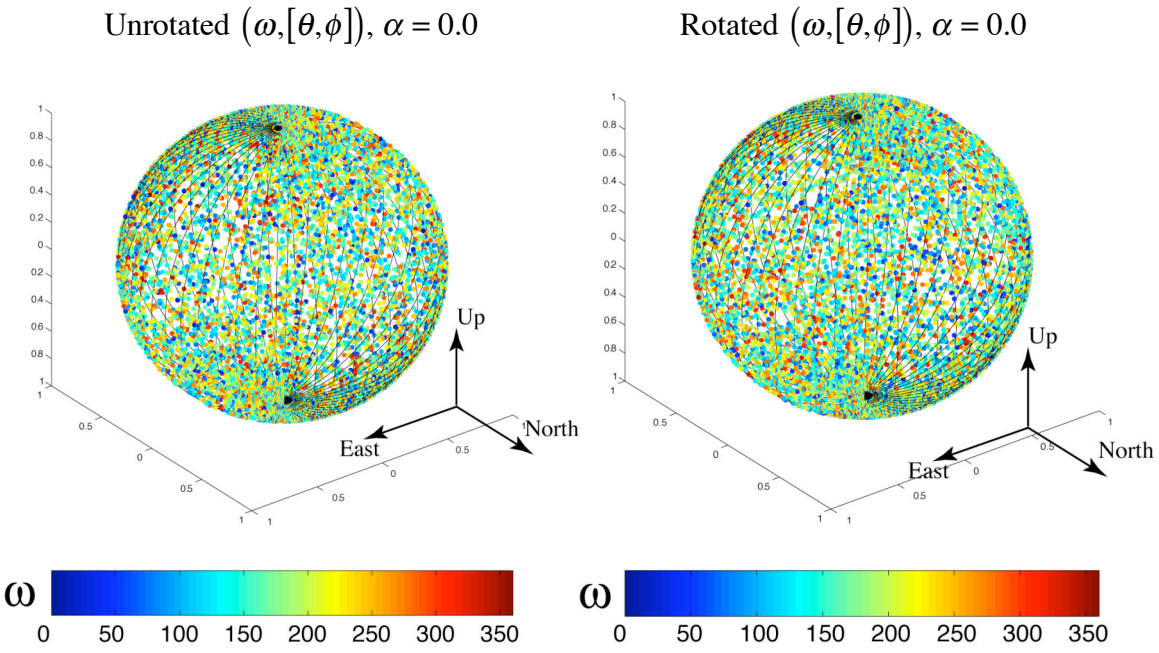

Figure 3.7 a)

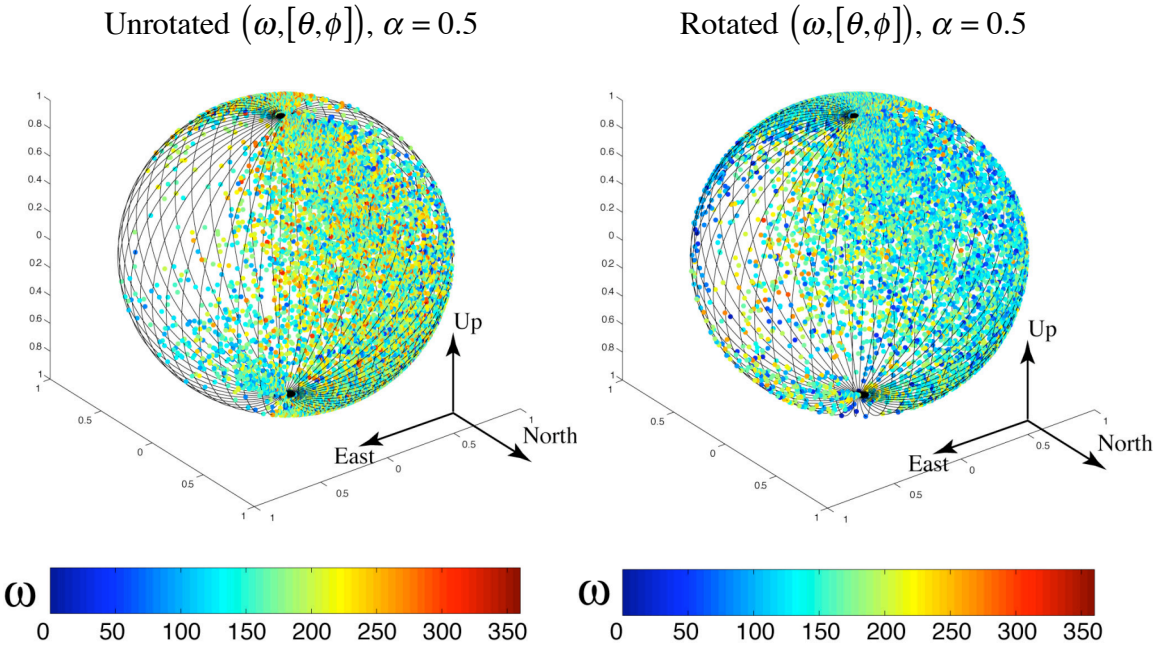

Figure 3.7 b)

Unrotated $(\omega,[\theta,\phi])$, $\alpha = 1.0$ Rotated $(\omega,[\theta,\phi])$, $\alpha = 1.0$

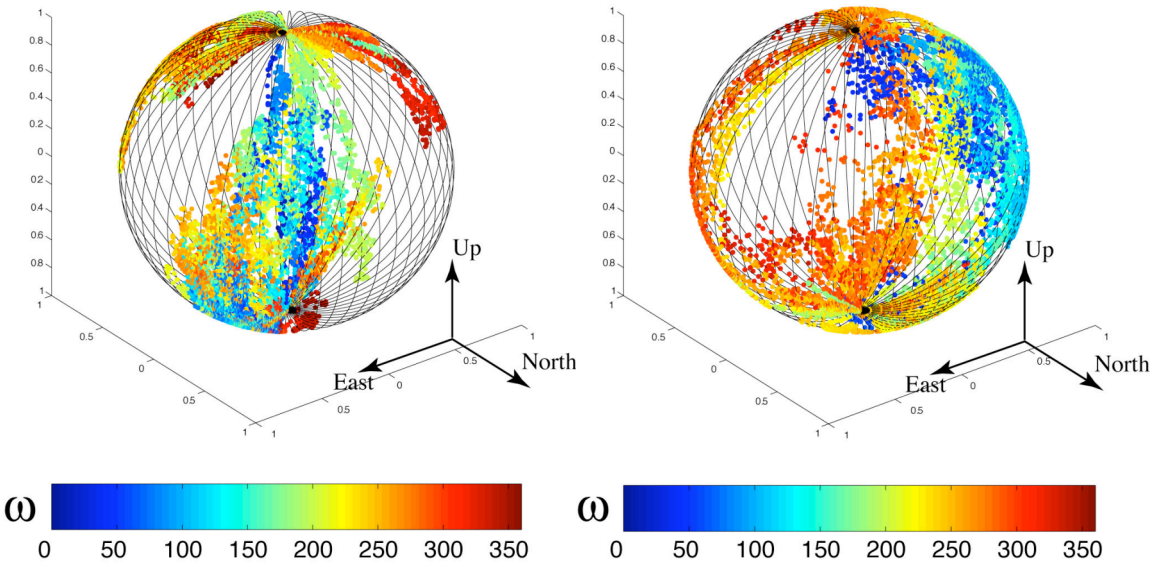

Figure 3.7 c)

Unrotated $(\omega,[\theta,\phi])$, $\alpha = 1.5$ Rotated $(\omega,[\theta,\phi])$, $\alpha = 1.5$

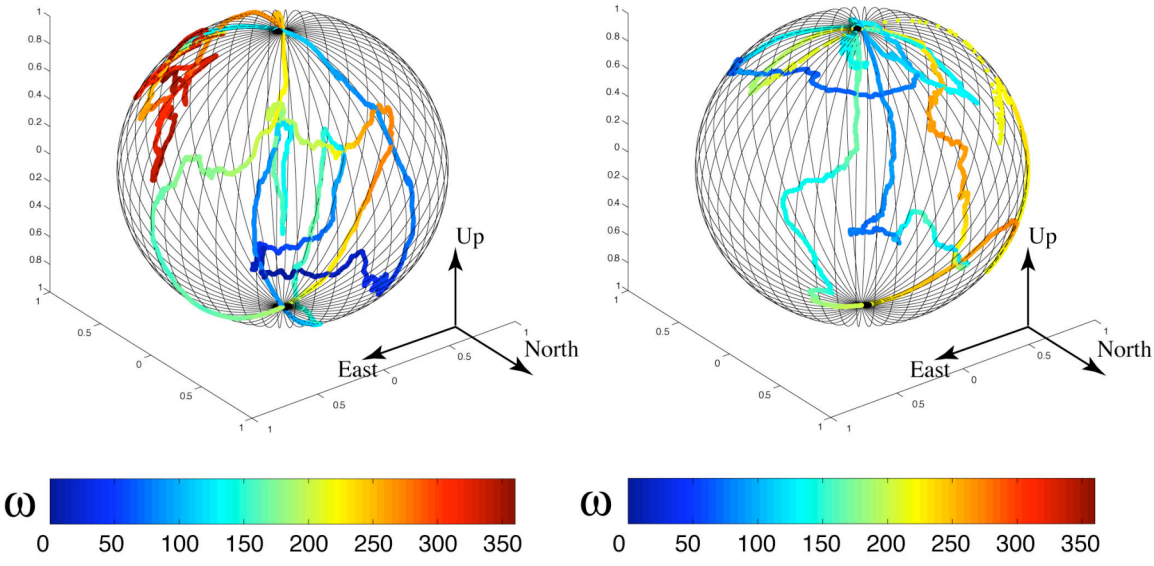

Figure 3.7 d)

Figure 3.7. *This is another way to visualize our filtered orientation data. The position of the plotted points on the 3D spheres represents the rotation axes* $[\theta,\phi]$*, and the color represents the rotation about the poles,* ω*, where* $blue = 0°$ *and* $red = 360°$*. Of course, for* $\alpha = 0.0$*, there are random positions of the points and random colors, representing the random 3D orientations,* $(\omega,[\theta,\phi])$*. As* α *increases, the spatial smoothing of point locations increases until there are linear tracks. Concurrently, as* α *increases, the spatial smoothing of color increases until the color changes smoothly from one to another along the 1D lines for* $\alpha = 1.5$*. This demonstrates that we have successfully smoothed the three orientation angles,* $(\omega,[\theta,\phi])$*, together. On the left, we plot* $(\omega,[\theta,\phi])$ *without the random rotation added, and on the right, we plot* $(\omega,[\theta,\phi])$ *with the random rotation added. These show that* $(\omega,[\theta,\phi])$ *still has similar properties regardless of the random rotation added.*

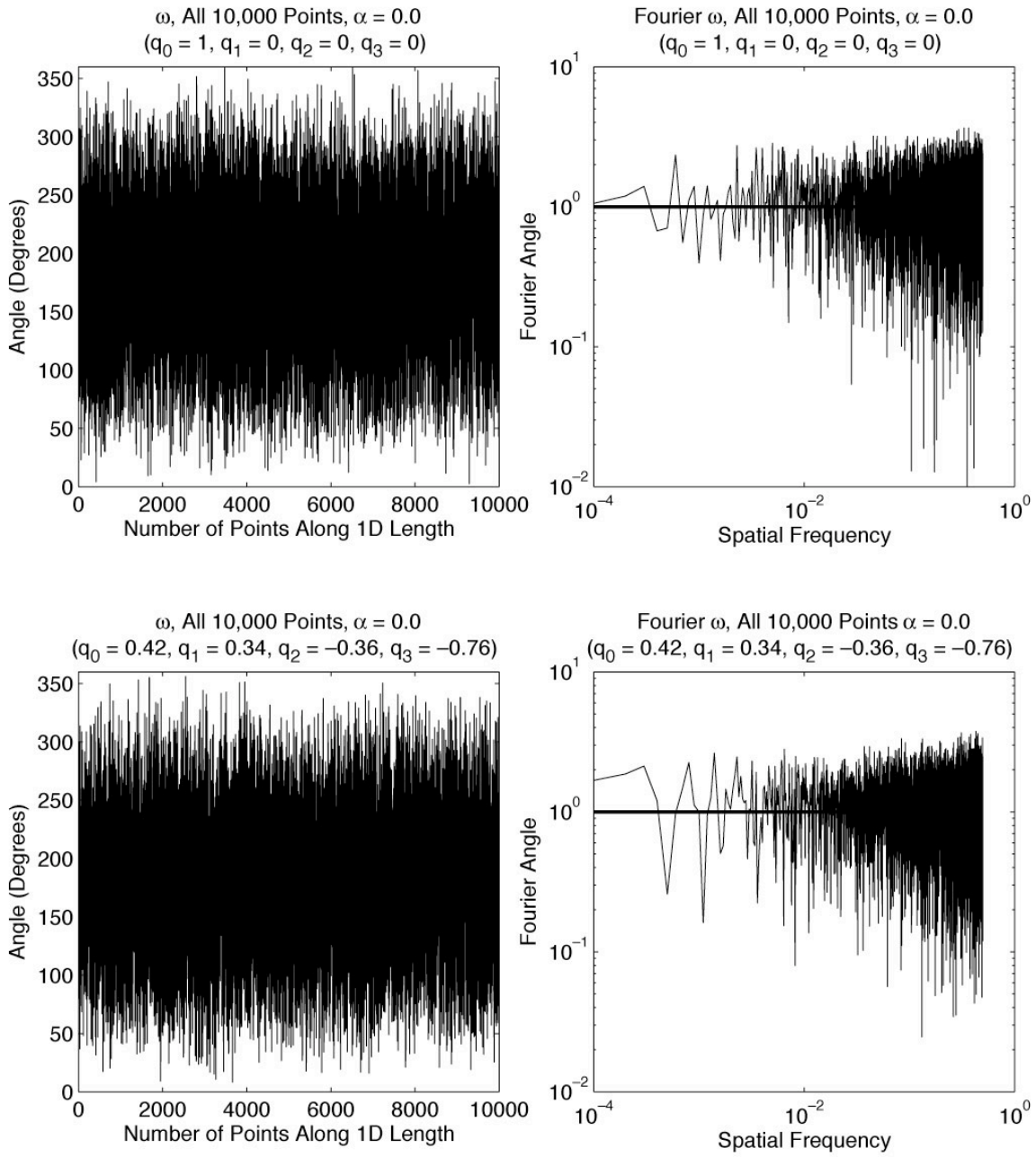
ω, All 10,000 Points, α = 0.0
(q0 = 1, q1 = 0, q2 = 0, q3 = 0)
Angle (Degrees)
Number of Points Along 1D Length
Fourier ω, All 10,000 Points, α = 0.0
(q0 = 1, q1 = 0, q2 = 0, q3 = 0)
Fourier Angle
Spatial Frequency
ω, All 10,000 Points, α = 0.0
(q0 = 0.42, q1 = 0.34, q2 = −0.36, q3 = −0.76)
Angle (Degrees)
Number of Points Along 1D Length
Fourier ω, All 10,000 Points α = 0.0
(q0 = 0.42, q1 = 0.34, q2 = −0.36, q3 = −0.76)
Fourier Angle
Spatial Frequency

Figure 3.8 a)

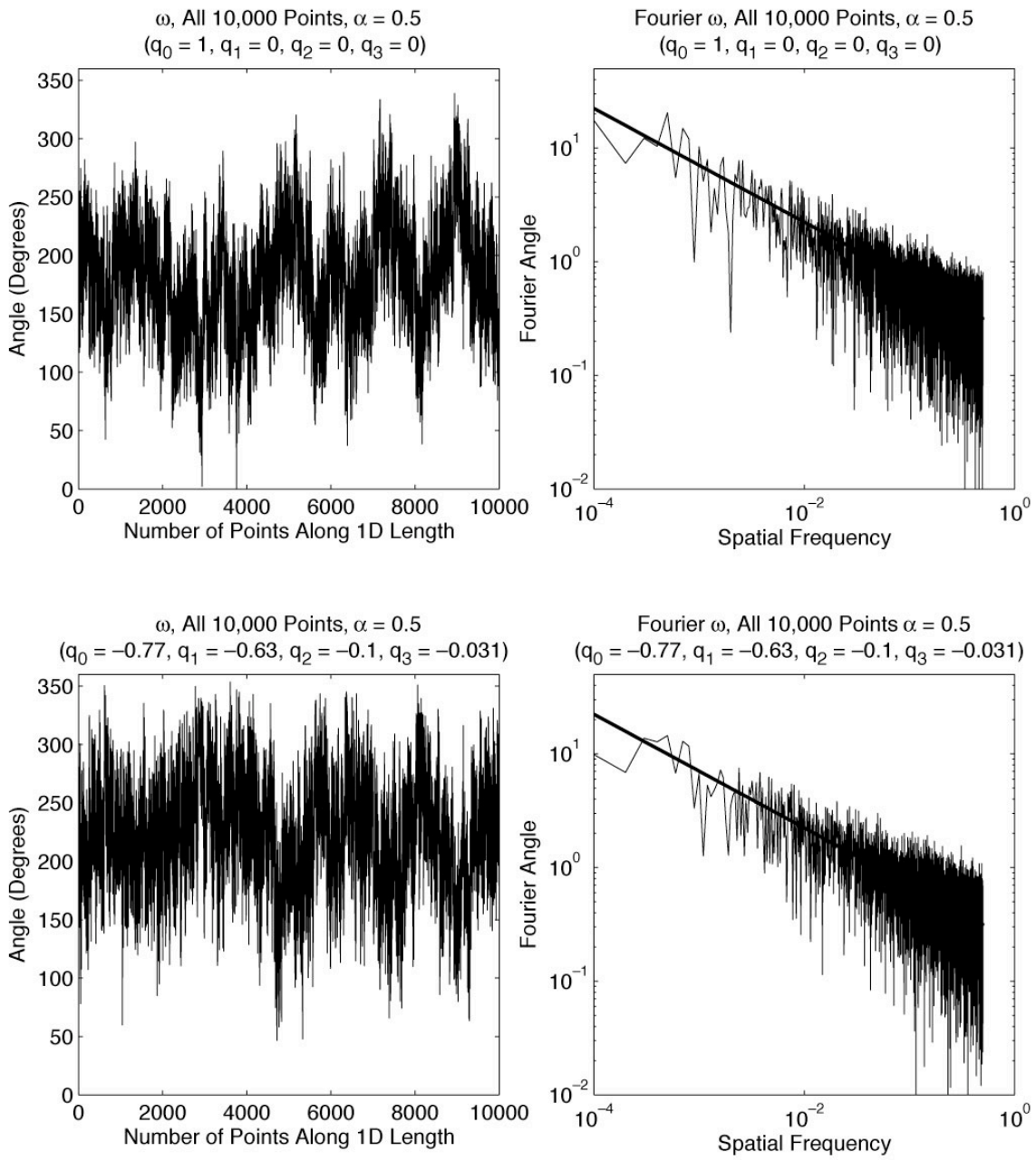
ω, All 10,000 Points, α = 0.5
(q0 = 1, q1 = 0, q2 = 0, q3 = 0)
Angle (Degrees)
Number of Points Along 1D Length
Fourier ω, All 10,000 Points, α = 0.5
(q0 = 1, q1 = 0, q2 = 0, q3 = 0)
Fourier Angle
Spatial Frequency
ω, All 10,000 Points, α = 0.5
(q0 = −0.77, q1 = −0.63, q2 = −0.1, q3 = −0.031)
Angle (Degrees)
Number of Points Along 1D Length
Fourier ω, All 10,000 Points α = 0.5
(q0 = −0.77, q1 = −0.63, q2 = −0.1, q3 = −0.031)
Fourier Angle
Spatial Frequency

Figure 3.8 b)

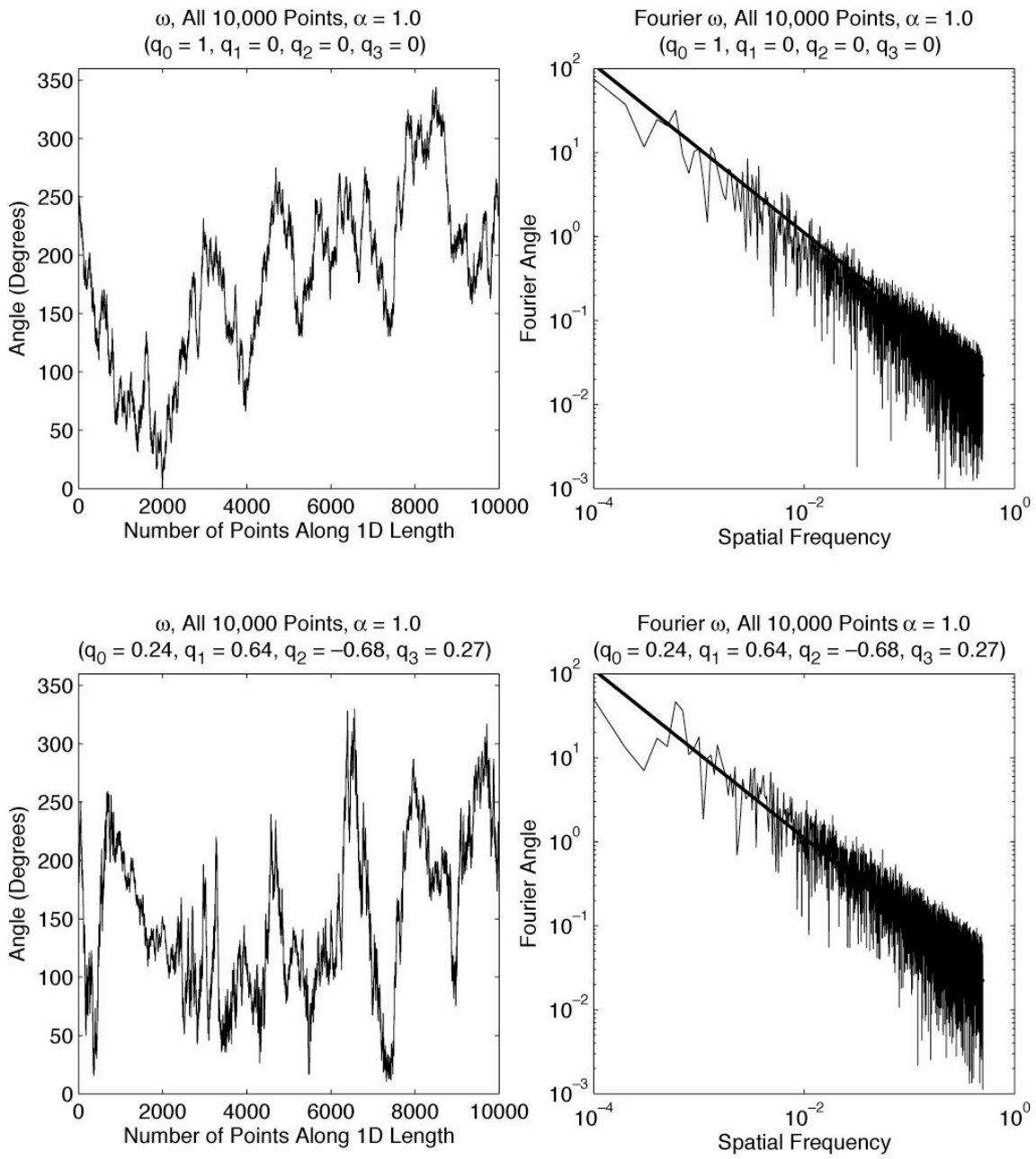
ω, All 10,000 Points, α = 1.0
(q0 = 1, q1 = 0, q2 = 0, q3 = 0)
Angle (Degrees)
Number of Points Along 1D Length
Fourier ω, All 10,000 Points, α = 1.0
(q0 = 1, q1 = 0, q2 = 0, q3 = 0)
Fourier Angle
Spatial Frequency
ω, All 10,000 Points, α = 1.0
(q0 = 0.24, q1 = 0.64, q2 = –0.68, q3 = 0.27)
Angle (Degrees)
Number of Points Along 1D Length
Fourier ω, All 10,000 Points α = 1.0
(q0 = 0.24, q1 = 0.64, q2 = –0.68, q3 = 0.27)
Fourier Angle
Spatial Frequency

Figure 3.8 c)

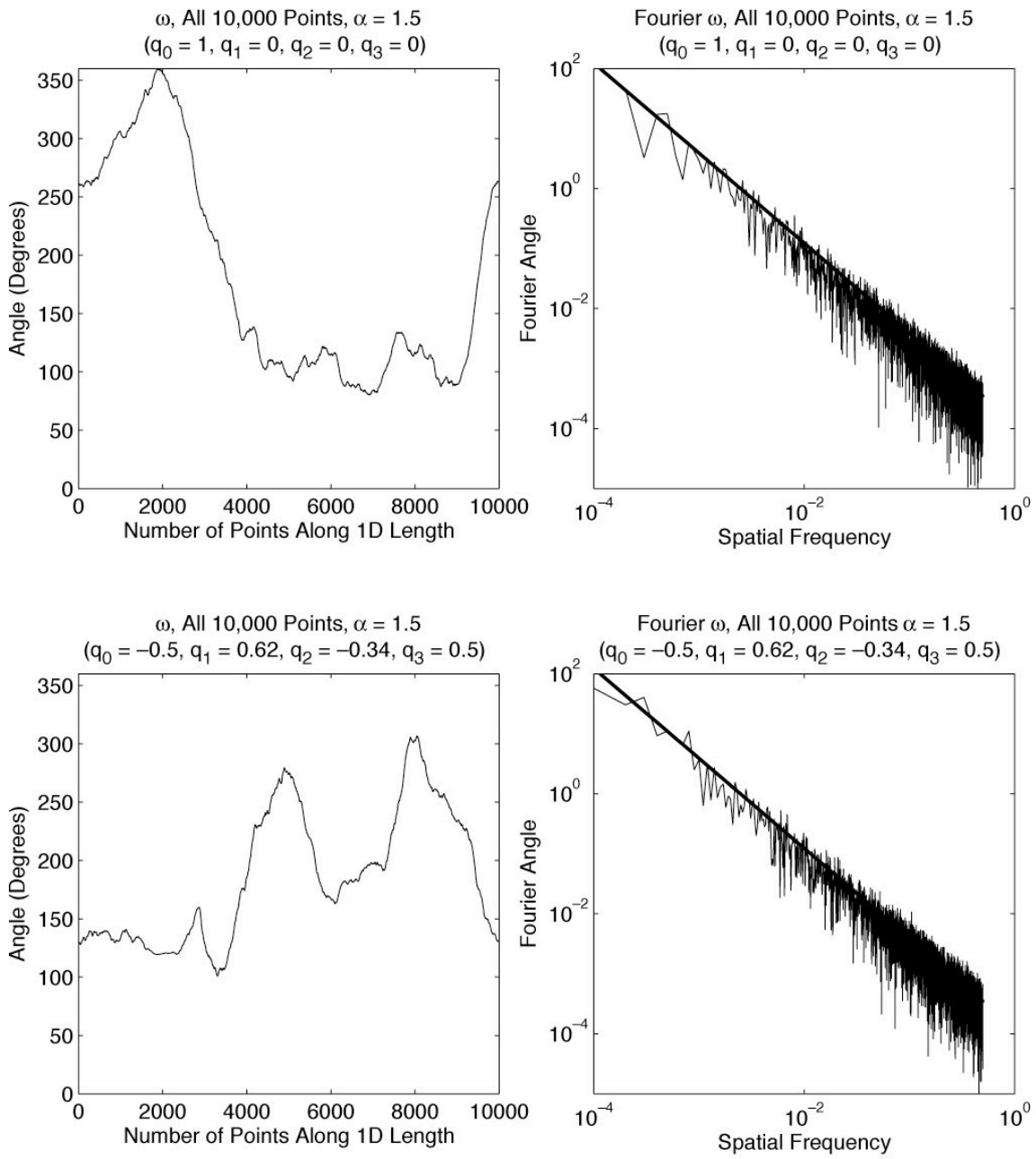
ω, All 10,000 Points, α = 1.5
(q0 = 1, q1 = 0, q2 = 0, q3 = 0)
Angle (Degrees)
Number of Points Along 1D Length
Fourier ω, All 10,000 Points, α = 1.5
(q0 = 1, q1 = 0, q2 = 0, q3 = 0)
Fourier Angle
Spatial Frequency
ω, All 10,000 Points, α = 1.5
(q0 = −0.5, q1 = 0.62, q2 = −0.34, q3 = 0.5)
Angle (Degrees)
Number of Points Along 1D Length
Fourier ω, All 10,000 Points α = 1.5
(q0 = −0.5, q1 = 0.62, q2 = −0.34, q3 = 0.5)
Fourier Angle
Spatial Frequency

Figure 3.8 d)

Figure 3.8. *A series of 1D simulations are shown with different degrees of smoothing,* α*, applied where* ***a)*** $\alpha = 0.0$*,* ***b)*** $\alpha = 0.5$*,* ***c)*** $\alpha = 1.0$*, and* ***d)*** $\alpha = 1.5$*. Each simulation is approximately 10,000 points. In this figure,* ω *is plotted for all 10,000 points on the left, and its spectral falloff is plotted on the right. The top plots represent* ω *before the random rotation is added, and the bottom plots represent* ω *after the random rotation is added. The main feature to notice is that* ω *does indeed have the approximately the appropriate spectral falloff both before and after the random rotation. The thick black line represents the expected* α *falloff, and the smoothed* ω *data for all the cases we tried between* $0.0 < \alpha < 1.5$ *approximately follows this expected thick black line. Sometimes, the very low frequencies are a little underrepresented, but overall this works quite well.*

Table 3.1. The Spectral Falloff Calculated for Each Filtered Angle as a Function of α

α	ω **Unrotated Falloff**	θ **Unrotated Falloff**	ϕ **Unrotated Falloff**	ω **Rotated Falloff**	θ **Rotated Falloff**
0	-4.16E-03	-2.79E-03	-1.62E-03	-4.85E-03	1.19E-03
0.1	0.1020	0.1016	0.0978	0.0548	0.0489
0.2	0.2010	0.2016	0.2008	0.1358	0.1317
0.3	0.2985	0.2951	0.3039	0.2299	0.2211
0.35	0.3480	0.3525	0.3461	0.2796	0.2645
0.4	0.4011	0.4003	0.4019	0.3459	0.3301
0.5	0.5003	0.5008	0.5021	0.4623	0.4352
0.6	0.6001	0.6006	0.6007	0.5841	0.5475
0.7	0.7016	0.7006	0.7005	0.6872	0.6609
0.8	0.8008	0.7987	0.8066	0.8009	0.7778
0.9	0.8999	0.8999	0.8970	0.8987	0.8822
1	1.0000	1.0051	1.0030	1.0023	1.0028
1.1	1.0986	1.0980	1.0969	1.0924	1.1060
1.2	1.2026	1.1982	1.1961	1.2031	1.2030
1.3	1.2963	1.3026	1.2996	1.2984	1.2964
1.4	1.3960	1.4012	1.4020	1.4002	1.3977
1.5	1.5033	1.4986	1.4989	1.4980	1.4944

If everything is working properly, the spectral falloff should $\approx \alpha$. *For each* α, *we*

- *generate 200 1D simulations, approximately 10,000 points each,*
- *determine the spectral falloff for the log-log plots of the data,*
- *then average the slopes for all 200 simulations.*

As expected, the spectral falloff of the unrotated angles, ω, θ, *and* ϕ *equals* α *for* $0.0 \le \alpha \le 1.5$. *The rotated simulations have spectral falloffs close to* α, *but tend to be a little spatially rougher, especially for* $\alpha < 0.6$ *(Figure 3.9). We calculate the spectral falloff of only the* ω *and* θ *rotated angles because the jumps in* ϕ *for a rotated simulation make it difficult to accurately assess a new spatial roughness.*

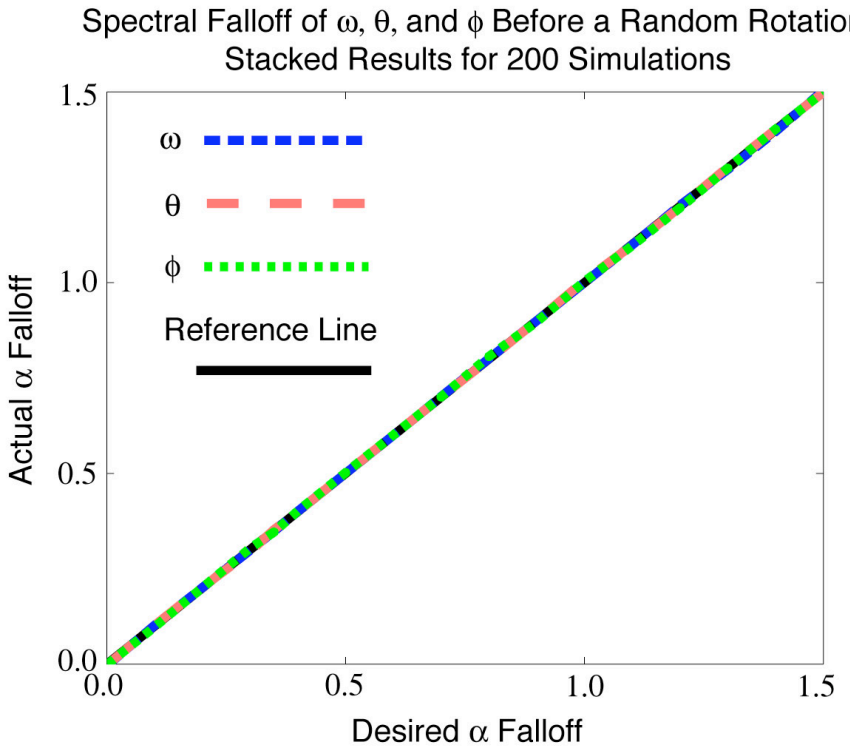
Spectral Falloff of ω, θ, and ϕ Before a Random Rotation
Stacked Results for 200 Simulations
ω
θ
ϕ
Reference Line
Actual α Falloff
Desired α Falloff
0.0
0.5
1.0
1.5

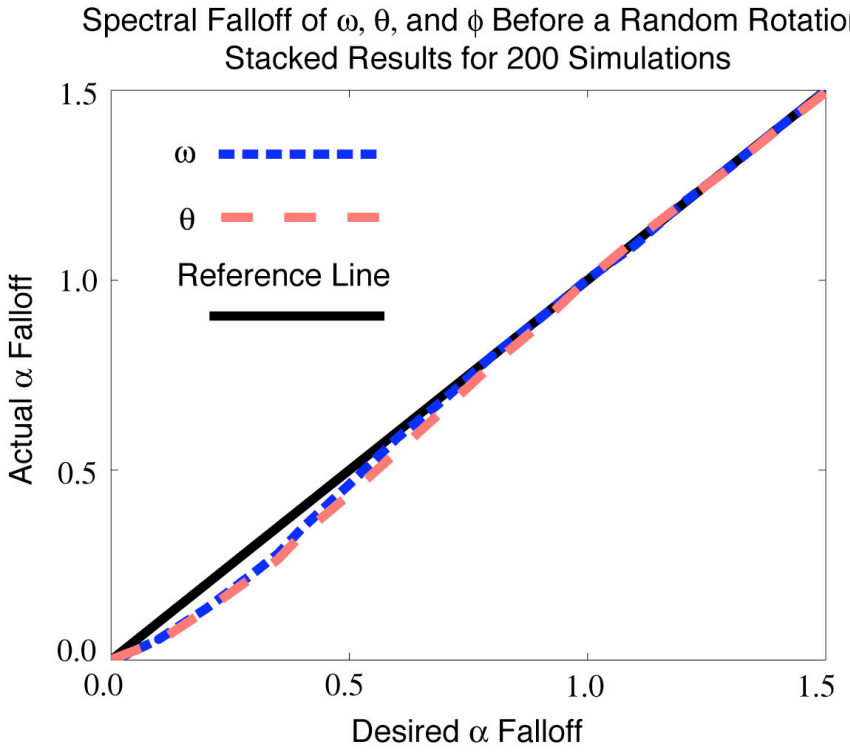
Spectral Falloff of ω, θ, and ϕ Before a Random Rotation
Stacked Results for 200 Simulations
ω
θ
Reference Line
Actual α Falloff
Desired α Falloff
0.0
0.5
1.0
1.5

Figure 3.9. *Plots of Table 3.1 data. The top plot shows spectral falloff as a function of* α *for the unrotated data, and the bottom plot shows the spectral falloff as a function of* α *for the rotated data. In both cases, the desired relationship is a linear line with a slope of 1.0 and an intercept of 0.0, indicated by a thick black line. In the top plot, the unrotated,* ω *(in blue),* θ *(in red), and* ϕ *(in green) plot directly on top of the desired black line. In the bottom plot, the rotated* ω *(in blue) and* θ *(in red) tend to be slightly rougher spatially for* $\alpha < 0.6$*, which produces spectral falloff values (negative slopes on a log-log plot) that are slightly less than* α*.*

Now that we have determined how to create filtered, approximately random, heterogeneous stress tensor orientations in terms of our three angles $(\omega,[\theta,\phi])$ and thoroughly examined their spectral properties, we can convert $(\omega,[\theta,\phi])$ into strike, dip, and rake, (Θ,δ,λ). Last, we will combine (Θ,δ,λ) with filtered σ_1, σ_2, and σ_3 to produce our full-filtered heterogeneous stress tensor. Technically, in the code used for this thesis, once $(\omega,[\theta,\phi])$ has been filtered, we convert it first into the associated quaternion vectors, $\vec{q}^{\,F} = \left[q_0^F, q_1^F, q_2^F, q_3^F\right]$, where F stands for filtered, then calculate (Θ,δ,λ). Using the derived equations in Appendix B, we have,

$$\tan\lambda = \frac{q_0^F\ q_1^F + q_2^F\ q_3^F}{q_0^F\ q_2^F - q_1^F\ q_3^F} \tag{3.16}$$

$$\tan\Theta = \frac{q_0^F\ q_1^F - q_2^F\ q_3^F}{q_0^F\ q_2^F + q_1^F\ q_3^F} \tag{3.17}$$

$$\tan\delta = \frac{2\left(q_0^F\ q_1^F + q_2^F\ q_3^F\right)/\sin\lambda}{q_0^F\ q_0^F - q_1^F\ q_1^F - q_2^F\ q_2^F + q_3^F\ q_3^F}\ . \tag{3.18}$$

Appendix A describes how to combine (Θ,δ,λ) with σ_1, σ_2, and σ_3 to produce the full heterogeneous stress tensor. It also explains how to convert (Θ,δ,λ) into the azimuth and plunge of the P-T axes, (θ_P,δ_P) and (θ_T,δ_T).

Plots of (θ_P,δ_P) and (θ_T,δ_T) from filtered 1D heterogeneous orientations, $(\omega,[\theta,\phi])$, are shown in Figure 3.11 for four different levels of smoothing, $\alpha = 0.0$, 0.5, 1.0, and 1.5. (θ_P,δ_P) and (θ_T,δ_T) are plotted on equal area plots for a plunge range of $\pm\ 90°$ as diagrammed in Figure 3.10. Typically, P-T equal area plots only have a plunge range of $0° - 90°$, because if for example, $\delta_P < 0$, then one can just apply the following transformation, $\delta_P' = -\delta_P$ and $\theta_P' = \theta_P + \pi$, to create a vector with a non-negative plunge that produces the same stress tensor. However, in our simulations, when $\alpha = 1.5$, it is interesting to see the unbroken linear track of the 1D simulation in P-T space, and this can only be seen if we use the full range of $\pm\ 90°$. In the top row, the P-T angles, (θ_P,δ_P) and (θ_T,δ_T), are plotted for filtered, unrotated $(\omega,[\theta,\phi])$, and in the bottom row the same data are plotted after a rotation. The quaternion vector listed for each plot is the quaternion that is multiplied with $(\omega,[\theta,\phi])$, where, $[q_0 = 1, q_1 = 0, q_2 = 0, q_3 = 0]$ produces no rotation, and $\vec{q} \neq [q_0 = 1, q_1 = 0, q_2 = 0, q_3 = 0]$ produces a rotation. For $\alpha = 0.0$, the points in P-T space on the equal area plots are uniformly distributed. This means that indeed, the random quaternion generator does

produce random orientations in 3D. Last, as the spatial smoothing, α, increases, the smoothing in P-T space increases. Thus, it would appear that the spatial smoothing of our orientations $(\omega,[\theta,\phi])$ translates well into (θ_P,δ_P) and (θ_T,δ_T).

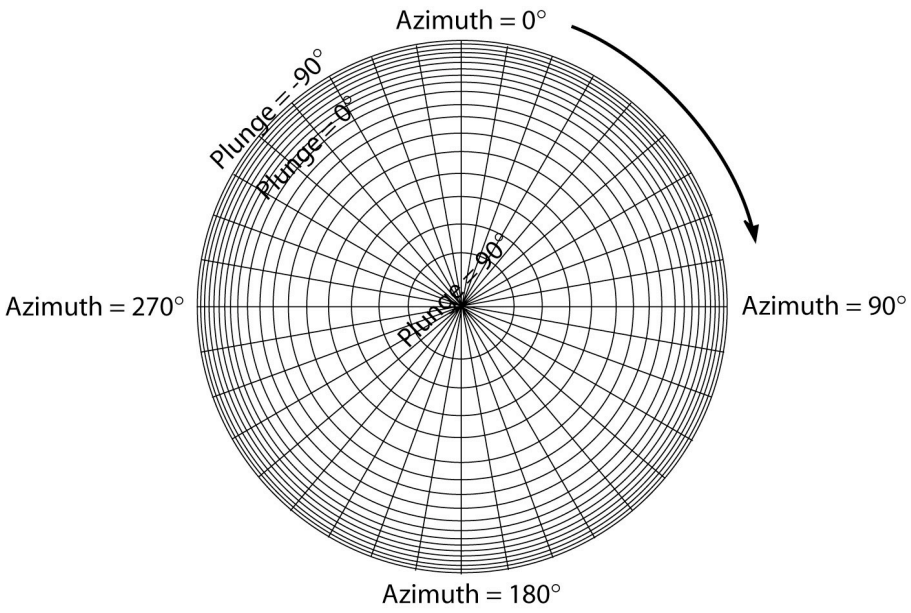

Figure 3.10. *A cartoon of the equal area plots used in Figure 3.11 for the P-T azimuths and plunges,* (θ_P,δ_P) and (θ_T,δ_T). *The longitude,* θ, *is the azimuth of the circle, and plunge,* δ, *is plotted as a function of radial distance where,* $\delta = 90°$ *at the center, and* $\delta = -90°$ *at the circumference. Note the radial lines are not necessarily to scale.*

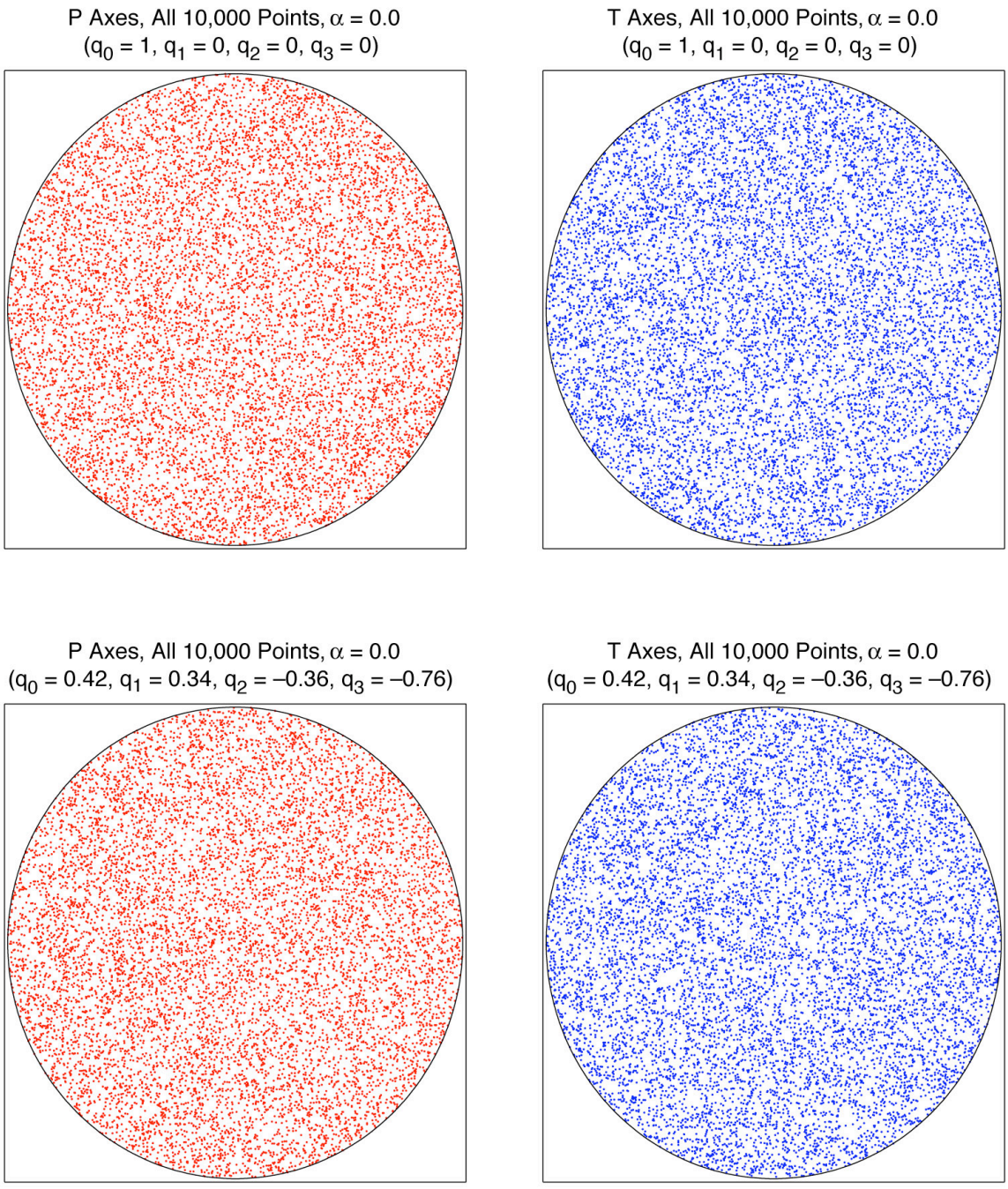
P Axes, All 10,000 Points, α = 0.0
(q0 = 1, q1 = 0, q2 = 0, q3 = 0)
T Axes, All 10,000 Points, α = 0.0
(q0 = 1, q1 = 0, q2 = 0, q3 = 0)
P Axes, All 10,000 Points, α = 0.0
(q0 = 0.42, q1 = 0.34, q2 = –0.36, q3 = –0.76)
T Axes, All 10,000 Points, α = 0.0
(q0 = 0.42, q1 = 0.34, q2 = –0.36, q3 = –0.76)

Figure 3.11 a)

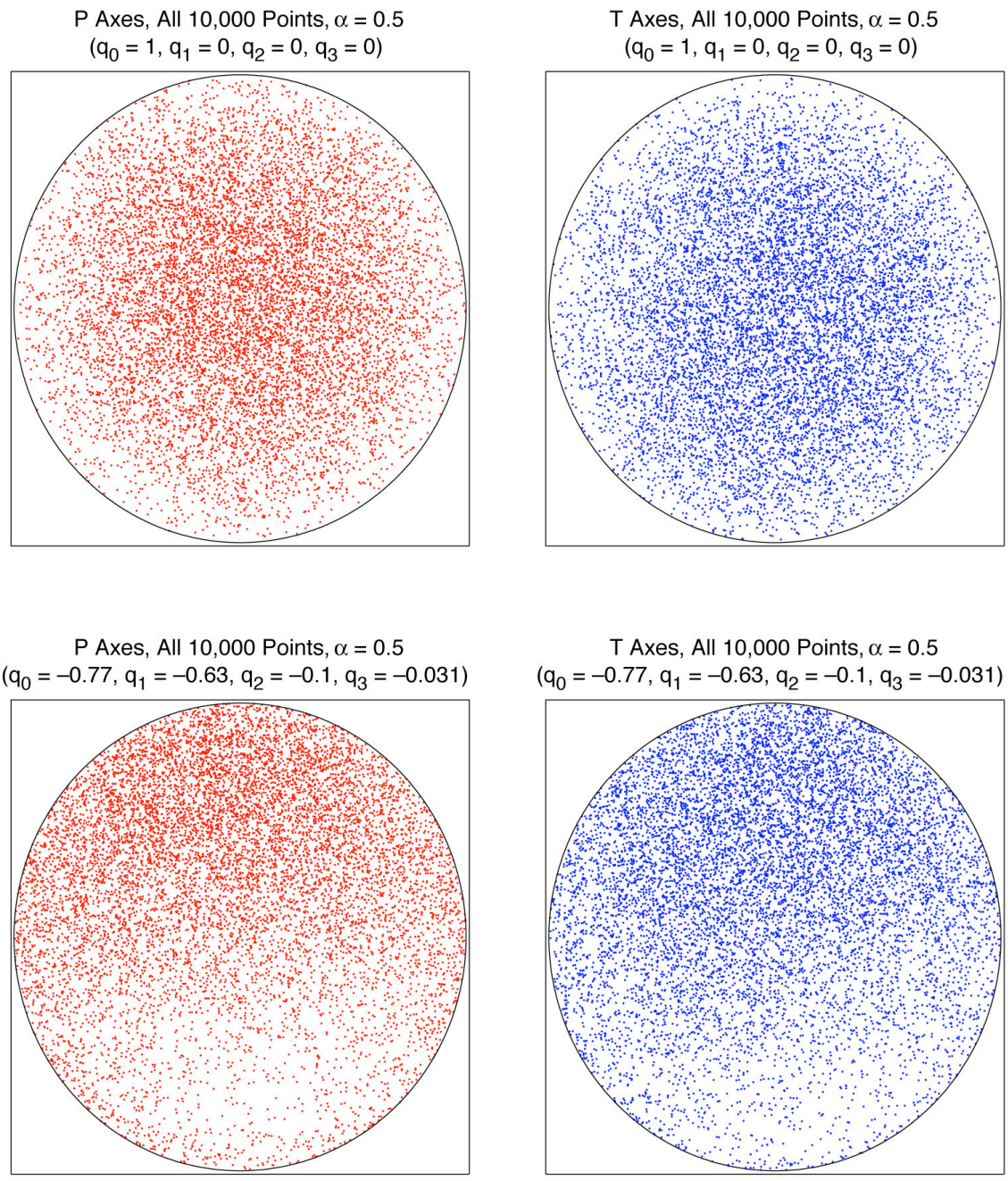
P Axes, All 10,000 Points, α = 0.5
(q0 = 1, q1 = 0, q2 = 0, q3 = 0)
T Axes, All 10,000 Points, α = 0.5
(q0 = 1, q1 = 0, q2 = 0, q3 = 0)
P Axes, All 10,000 Points, α = 0.5
(q0 = –0.77, q1 = –0.63, q2 = –0.1, q3 = –0.031)
T Axes, All 10,000 Points, α = 0.5
(q0 = –0.77, q1 = –0.63, q2 = –0.1, q3 = –0.031)

Figure 3.11 b)

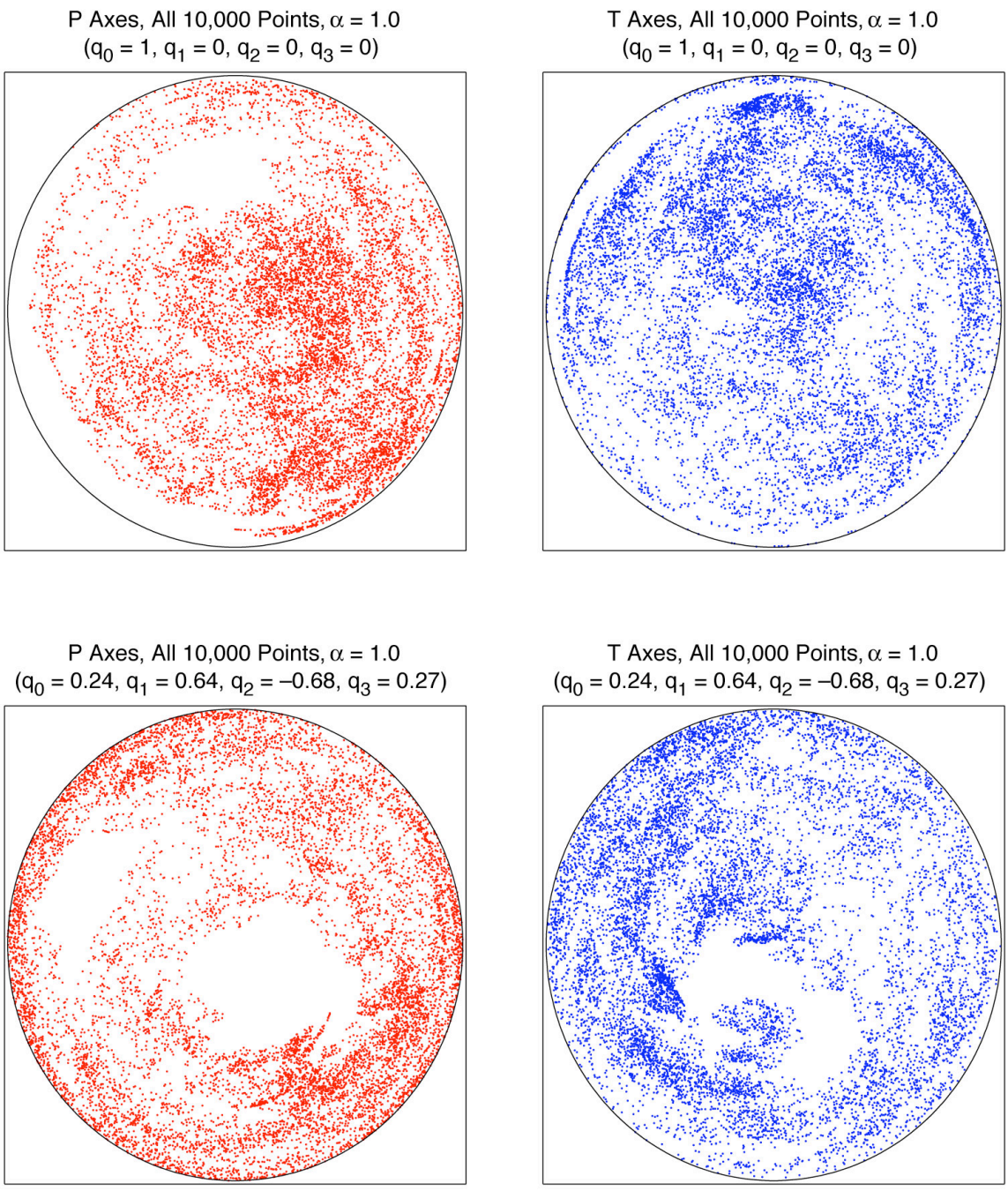
P Axes, All 10,000 Points, α = 1.0
(q0 = 1, q1 = 0, q2 = 0, q3 = 0)
T Axes, All 10,000 Points, α = 1.0
(q0 = 1, q1 = 0, q2 = 0, q3 = 0)
P Axes, All 10,000 Points, α = 1.0
(q0 = 0.24, q1 = 0.64, q2 = –0.68, q3 = 0.27)
T Axes, All 10,000 Points, α = 1.0
(q0 = 0.24, q1 = 0.64, q2 = –0.68, q3 = 0.27)

Figure 3.11 c)

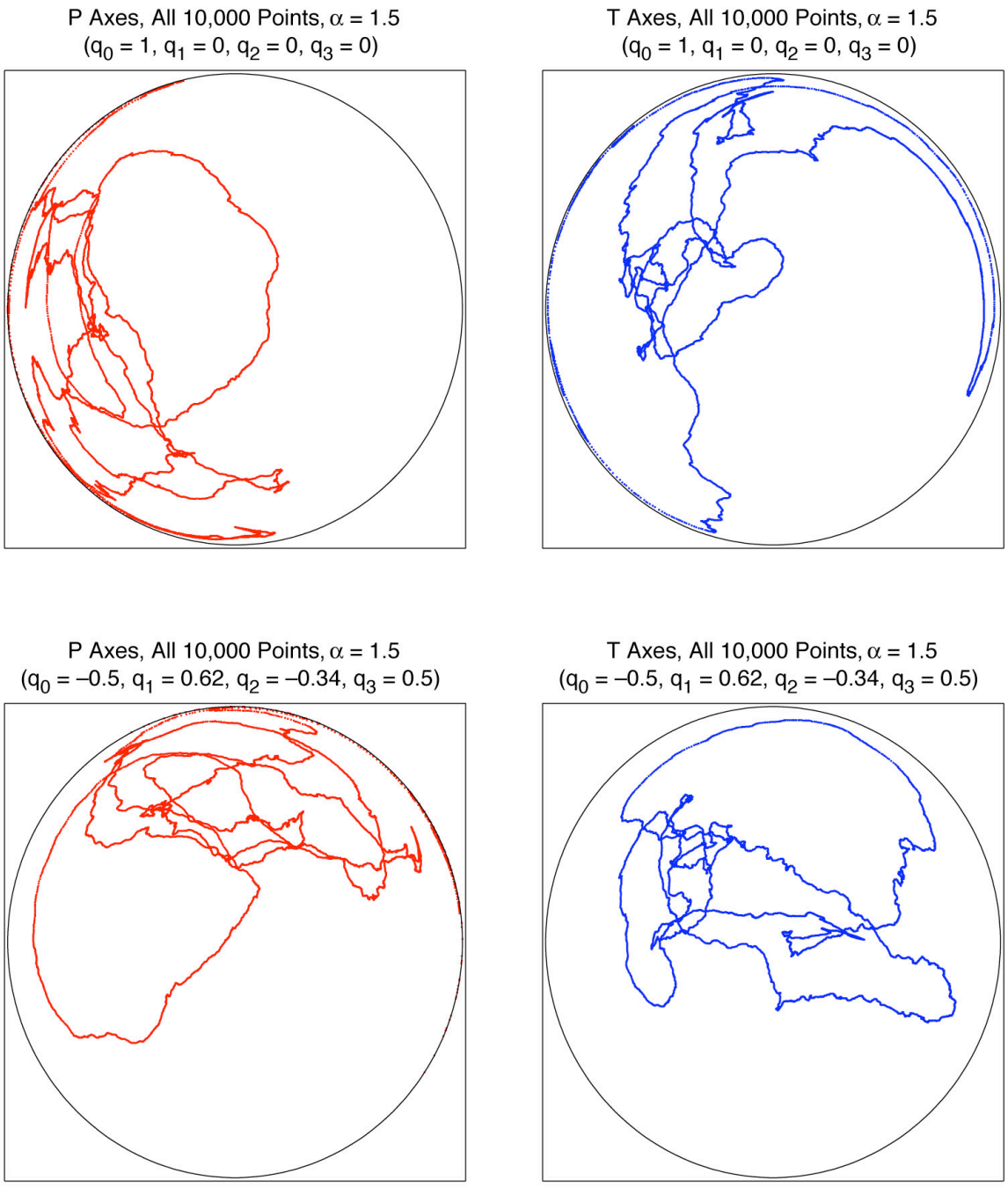
P Axes, All 10,000 Points, α = 1.5
(q0 = 1, q1 = 0, q2 = 0, q3 = 0)
T Axes, All 10,000 Points, α = 1.5
(q0 = 1, q1 = 0, q2 = 0, q3 = 0)
P Axes, All 10,000 Points, α = 1.5
(q0 = –0.5, q1 = 0.62, q2 = –0.34, q3 = 0.5)
T Axes, All 10,000 Points, α = 1.5
(q0 = –0.5, q1 = 0.62, q2 = –0.34, q3 = 0.5)

Figure 3.11 d)

Figure 3.11. *The Principal Compression Axes (P axes) and Principal Tension Axes (T axes) are plotted as on equal area plots for a series of simulations. The P axes are red on the left, and the T axes are blue on the right. The plunge range is* $\pm 90°$ *on the equal area plots instead of the usual* $0° - 90°$*, so that when* $\alpha = 1.5$ *one can more easily track the linear track of the data in P-T space. The top rows show P-T angles,* (θ_P, δ_P) *and* (θ_T, δ_T)*, for the filtered and unrotated,* $(\omega, [\theta, \phi])$*, and the bottom row shows the same data except that* $(\omega, [\theta, \phi])$ *were rotated. The quaternion by which the data* $(\omega, [\theta, \phi])$ *were multiplied is listed on each plot, where* $[q_0 = 1, q_1 = 0, q_2 = 0, q_3 = 0]$ *produces no rotation, and* $\vec{q} \neq [q_0 = 1, q_1 = 0, q_2 = 0, q_3 = 0]$ *produces a rotation.*

Note that for ***a)*** $\alpha = 0.0$ *the P-T axes are evenly and randomly distributed on the equal area plots for both the unrotated and rotated cases. This indicates there is no orientation bias for* $\alpha = 0.0$*, which is not surprising since our unfiltered orientations were by design generated randomly. For* ***b)*** $\alpha = 0.5$ *one can see that the axes are still somewhat randomly distributed, but there is a slight radial clumping for the unrotated P-T plots, and this clumping of orientations is rotated for the bottom P-T plots. As* α *increases further, to* ***c)*** $\alpha = 1.0$*, more fine-scale structure and orientational clumping arises, and it still has some orientational bias. Last, when* ***d)*** $\alpha = 1.5$*, the orientations smoothly vary from one point to another such that it forms a continuous, wandering line in P-T space. One can see that for* $\alpha > 0.0$*, a single filtered simulation may not generate randomly orientated data; hence, this is why we wish to stack many simulations where each data set has been given a random rotation. Figure 3.13 shows the efficacy of this approach.*

While the filtering of the orientation angles, $(\omega,[\theta,\phi])$, works quite well in producing filtered, P-T axes angles, (θ_P,δ_P) and (θ_T,δ_T), it also produces an orientation bias. Since we wish to generate heterogeneous stress with no orientation bias, we employ the strategy mentioned previously. Generate at least 10–20 filtered data sets, add a random rotation to each data set, then stack the data sets. Figure 3.13 compares the stacking of multiple data sets with and without the random rotations to demonstrate the necessity of randomly rotating the data sets before stacking them. P-T axes are plotted in Figure 3.13, using the typical $0° - 90°$ plunge range for P-T equal area plots. This typical plunge range is diagrammed in the Figure 3.12 cartoon. In Figure 3.13, the top row of P-T equal area plots for each α has stacked 200 1D simulations, each 1,001 points long, without any random rotations applied to $(\omega,[\theta,\phi])$. The bottom row of P-T equal area plots for each α has stacked 200 1D simulations, each 1,001 points long, with a random rotation applied to $(\omega,[\theta,\phi])$ for each simulation.

One finds that stacking the data alone (top rows), without any random rotations applied, helps, but still produces an average bias in the P-T orientations; one can visually see this in Figure 3.13 with the uneven coverage of the equal area plots especially for $\alpha = 1.5$. When one adds a random rotation to each simulation and then stacks multiple simulations (bottom rows), the P-T orientations begin to average out until the equal area plots are fairly uniformly covered, and there is little to no orientation bias.

Underneath each set of P-T plots, we have also listed the component-wise mean heterogeneous stress tensor, that is calculated as follows:

$$\boldsymbol{\sigma}'_{HeterogeneousMean} = \frac{1}{N1\ N2}\sum_{j=1}^{N2}\sum_{i=1}^{N1}\boldsymbol{\sigma}'^{ij}_{Heterogeneous}\left(\sigma_1'^{ij},\sigma_2'^{ij},\sigma_3'^{ij},\omega^{ij},\theta^{ij},\phi^{ij}\right) \qquad (3.19)$$

where $N1$ is the number of points in each simulation and $N2$ is the number of simulations. Note, filtered deviatoric principal stresses, σ_1', σ_2', and σ_3' have been combined with our orientation angles $(\omega,[\theta,\phi])$, to generate $\boldsymbol{\sigma}'_{Heterogeneous}$ for each simulation; then the above component-wise mean equation above is applied. Last, the square root of the second invariant of the deviatoric stress tensor, $\sqrt{I_2'}$, is calculated for the component-wise mean heterogeneous stress tensor. In Chapter 4, we will see why $I_2' = \sigma_{11}'^{\,2} + \sigma_{22}'^{\,2} + \sigma_{33}'^{\,2} + 2\sigma_{12}'^{\,2} + 2\sigma_{23}'^{\,2} + 2\sigma_{13}'^{\,2}$, is so important; I_2' is an invariant measure of the maximum shear stress and is the quantity used to determine when points fail for our grid. Also, as mentioned in Chapter 1, $\sqrt{I_2'}$ is used in calculating the ratio of heterogeneous stress to background stress. Therefore, $\sqrt{I'_{2\ HeterogeneousMean}}$ is a natural way of measuring the size of the residual average stress tensor. The smaller the $\sqrt{I'_{2\ HeterogeneousMean}}$ the better when attempting to produce heterogeneous deviatoric stress tensors with an approximately zero component-wise mean. We find that in Figure 3.13 indeed, stacking the data alone is insufficient to produce approximately zero mean stress tensors; adding a rotation to each simulation then stacking is necessary if one wishes to have a zero mean stress tensor for any filtering power, α.

Our last figure with filtered 1D data, is Figure 3.14, which shows one component of the filtered deviatoric stress tensor, σ_{11}', and its spectral properties. The other components of the deviatoric stress tensor, σ_{22}', σ_{33}', σ_{12}', σ_{23}', and σ_{13}', have similar spectral properties and are not shown. The main point of Figure 3.14 is to show that even if the orientations $(\omega,[\theta,\phi])$ and the principal stresses, σ_1', σ_2', and σ_3' are all filtered

with an $\alpha > 0.0$, the components of the stress tensor in a Cartesian coordinate system, σ'_{11}, σ'_{22}, σ'_{33}, σ'_{12}, σ'_{23}, and σ'_{13} do not have the α spectral falloff. To create our stress tensor, we have rotated principal stresses at each point into their specified reference frames. The simple act of rotating principal stresses into different reference frames, even using smoothed rotations, causes the symmetric stress tensor to not have the same α smoothing as the principal stresses. Even if one started with a Cartesian stress tensor and smoothed each component separately, then rotated to another reference frame, one loses all the α smoothing spectral properties. So Figure 3.14 helps demonstrate why we choose not to filter the components of a stress tensor for a particular reference frame but instead choose to filter the principal stresses and orientation angles.

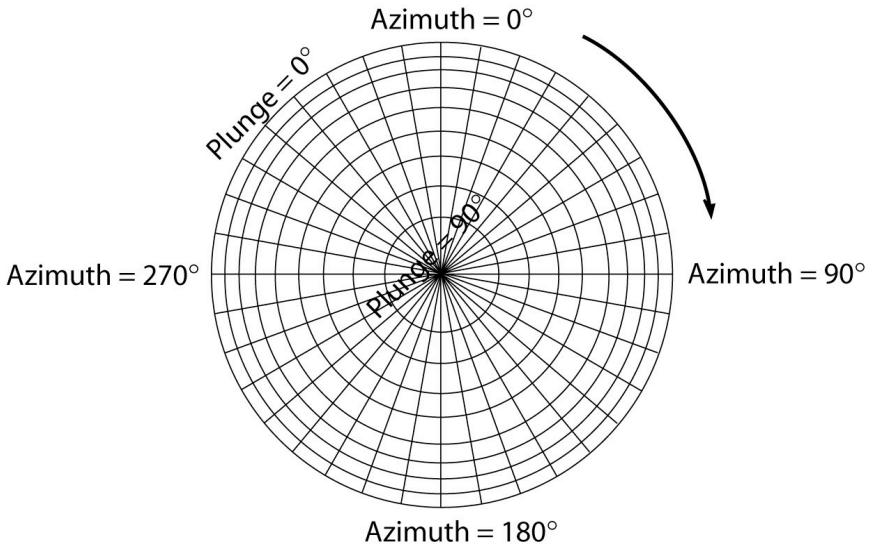

Figure 3.12. *A cartoon of the equal area plots used in Figure 3.13 for the P-T azimuths and plunges,* (θ_P, δ_P) and (θ_T, δ_T). *The longitude,* θ, *is the azimuth of the circle, and plunge,* δ, *is plotted as a function of radial distance where* $\delta = 90°$ *at the center, and* $\delta = 0°$ *at the circumference. Note the radial lines are not necessarily to scale.*

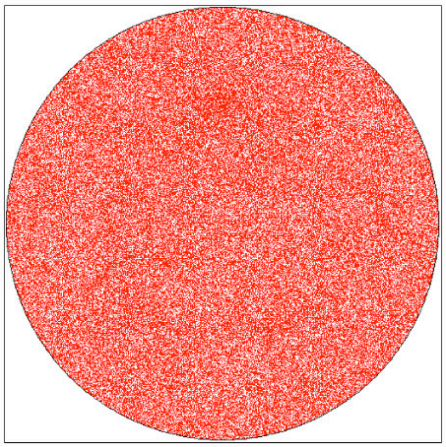

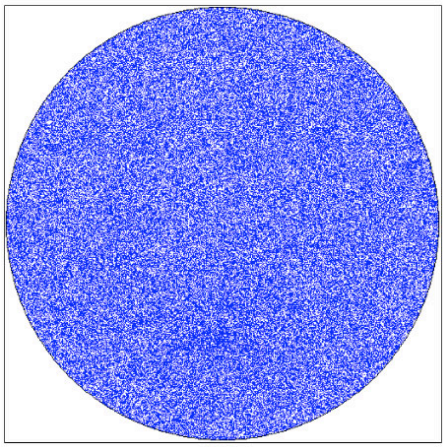

$$\boldsymbol{\sigma}'_{HeterogeneousMean} = \begin{pmatrix} 0.0009 & 0.0006 & -0.0007 \\ 0.0006 & -0.0013 & 0.0081 \\ -0.0007 & 0.0081 & 0.0004 \end{pmatrix} \text{ for 200 runs, 1,001 points each}$$

$$\sqrt{I'_{2\ HeterogeneousMean}} = 0.0117$$

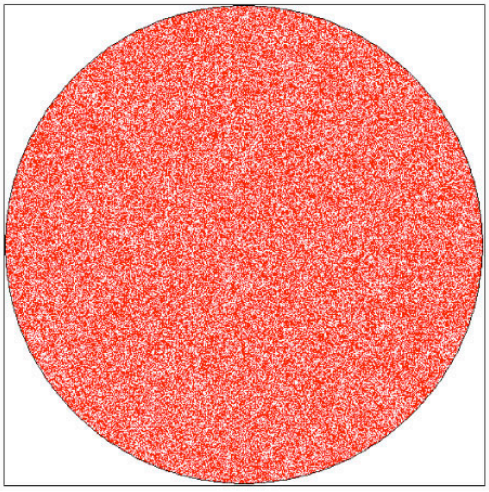

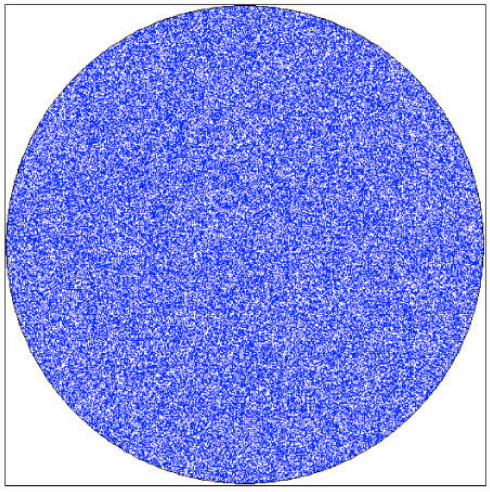

$$\boldsymbol{\sigma}'_{HeterogeneousMean} = \begin{pmatrix} -0.0010 & 0.0001 & -0.0002 \\ 0.0001 & 0.0013 & -0.0011 \\ -0.0002 & -0.0011 & -0.0003 \end{pmatrix} \text{ for 200 runs, 1,001 points each}$$

$$\sqrt{I'_{2\ HeterogeneousMean}} = 0.0023$$

Figure 3.13 a)

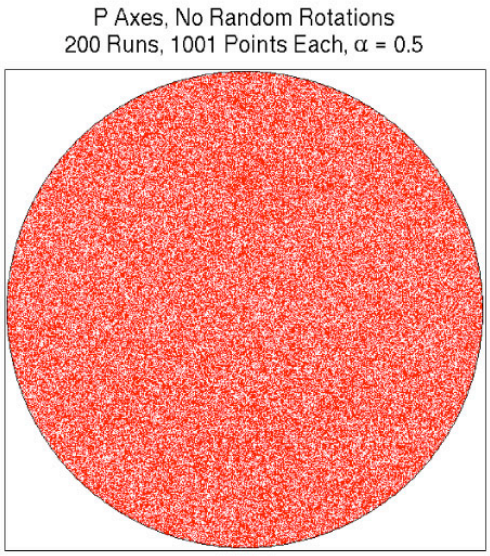

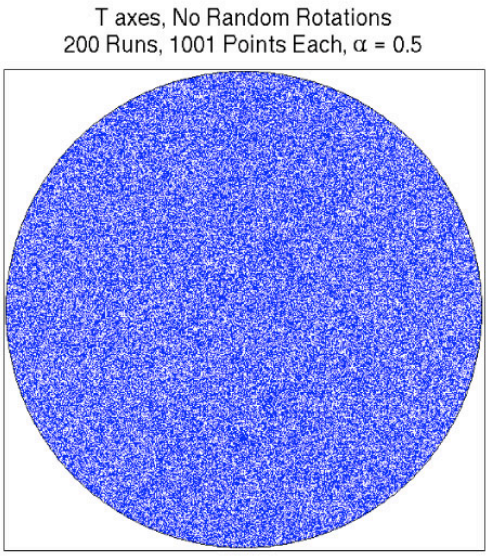

$$\boldsymbol{\sigma}'_{HeterogeneousMean} = \begin{pmatrix} -0.0013 & 0.0001 & -0.0008 \\ 0.0001 & -0.0002 & -0.0013 \\ -0.0008 & -0.0013 & 0.0015 \end{pmatrix}$$ for 200 runs, 1,001 points each

$$\sqrt{I'_{2\ HeterogeneousMean}} = 0.0030$$

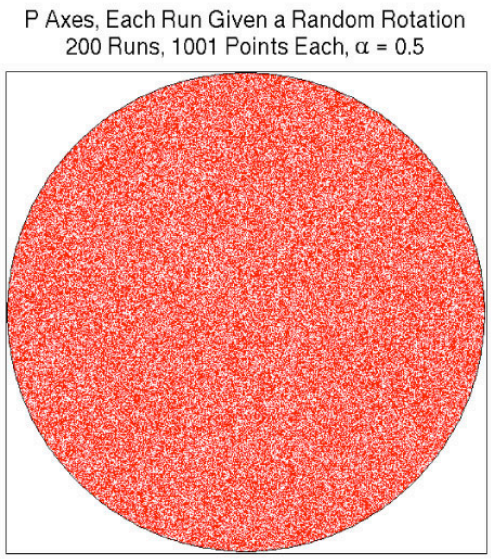

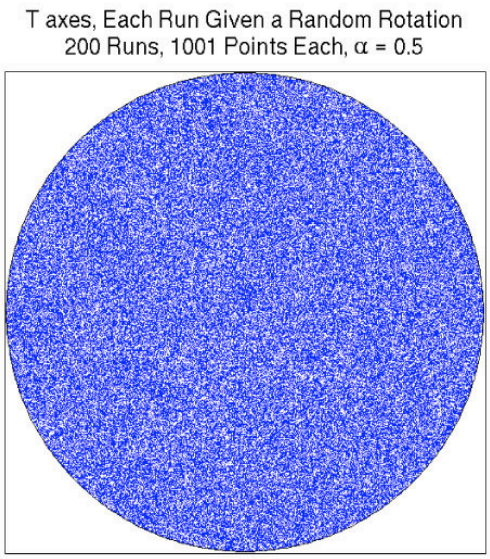

$$\boldsymbol{\sigma}'_{HeterogeneousMean} = \begin{pmatrix} 0.0003 & -0.0000 & 0.0007 \\ -0.0000 & -0.0016 & 0.0001 \\ 0.0007 & 0.0001 & 0.0013 \end{pmatrix}$$ for 200 runs, 1,001 points each

$$\sqrt{I'_{2\ HeterogeneousMean}} = 0.0023$$

Figure 3.13 b)

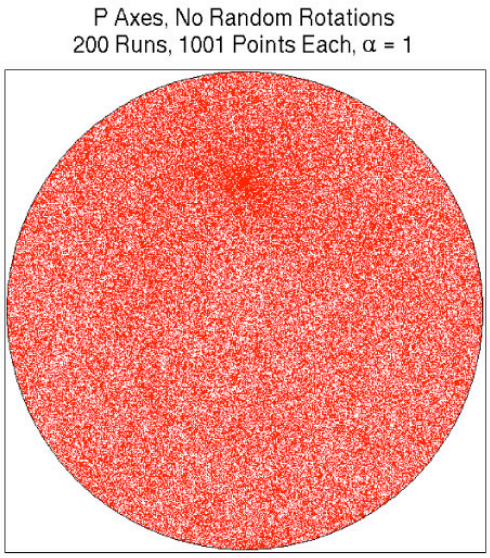

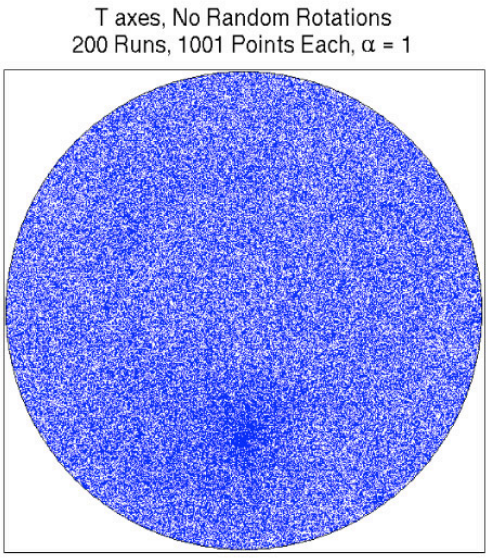

$$\boldsymbol{\sigma}'_{HeterogeneousMean} = \begin{pmatrix} -0.0011 & 0.0022 & 0.0006 \\ 0.0022 & -0.0036 & 0.0216 \\ 0.0006 & 0.0216 & 0.0047 \end{pmatrix} \text{ for 200 runs, 1,001 points each}$$

$$\sqrt{I'_{2\ HeterogeneousMean}} = 0.0314$$

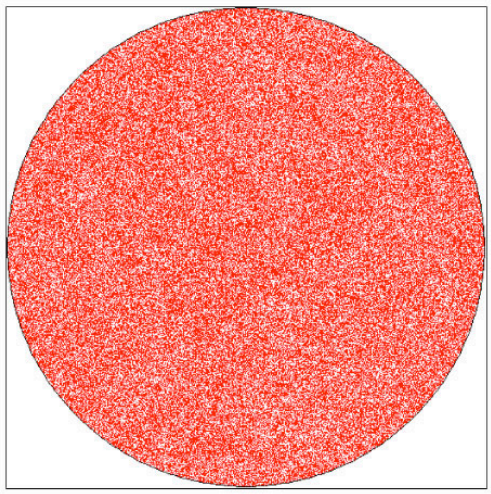

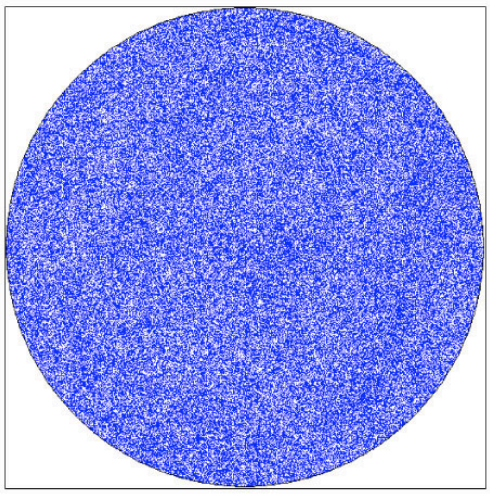

$$\boldsymbol{\sigma}'_{HeterogeneousMean} = \begin{pmatrix} 0.0022 & -0.0012 & 0.0003 \\ -0.0012 & -0.0019 & -0.0024 \\ 0.0003 & -0.0024 & -0.0004 \end{pmatrix} \text{ for 200 runs, 1,001 points each}$$

$$\sqrt{I'_{2\ HeterogeneousMean}} = 0.0048$$

Figure 3.13 c)

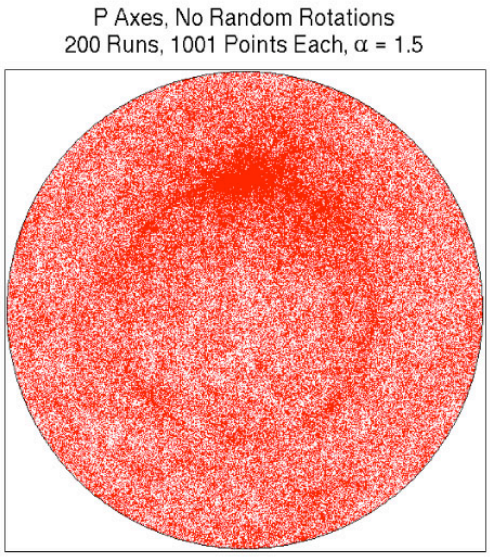

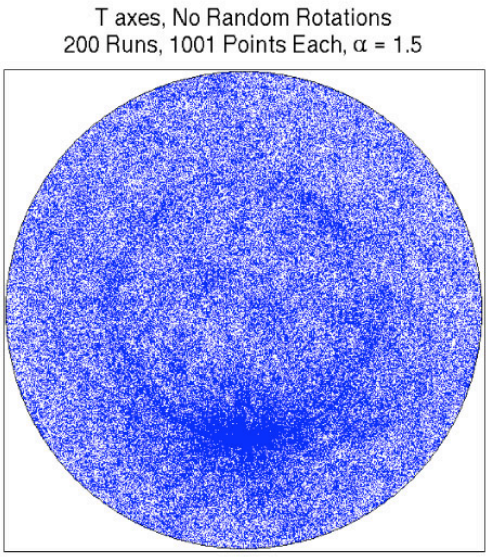

$$\boldsymbol{\sigma}'_{HeterogeneousMean} = \begin{pmatrix} -0.0009 & -0.0060 & 0.0035 \\ -0.0060 & -0.0128 & 0.0753 \\ 0.0035 & 0.0753 & 0.0137 \end{pmatrix} \text{ for 200 runs, 1,001 points each}$$

$$\sqrt{I'_{2\ HeterogeneousMean}} = 0.1086$$

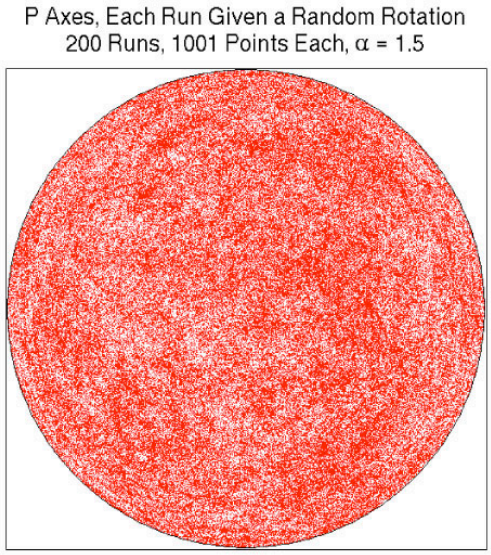

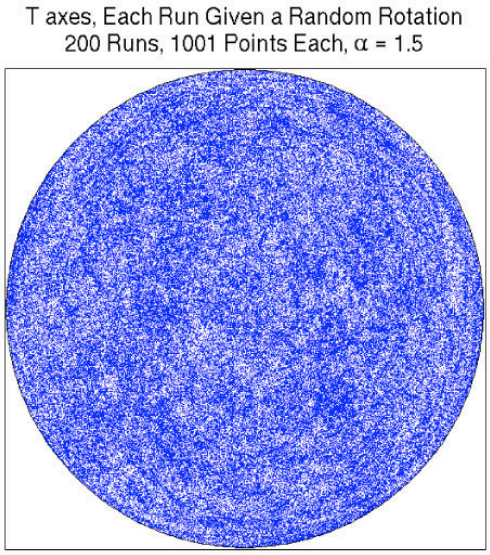

$$\boldsymbol{\sigma}'_{HeterogeneousMean} = \begin{pmatrix} 0.0022 & -0.0021 & 0.0081 \\ -0.0021 & -0.0023 & 0.0053 \\ 0.0081 & 0.0053 & 0.0001 \end{pmatrix} \text{ for 200 runs, 1,001 points each}$$

$$\sqrt{I'_{2\ HeterogeneousMean}} = 0.0117$$

Figure 3.13 d)

Figure 3.13. *For 4 different levels of smoothing,* ***a)*** $\alpha = 0.0$, ***b)*** $\alpha = 0.5$, ***c)*** $\alpha = 1.0$, *and* ***d)*** $\alpha = 1.5$**,** *we stack the results of 200 simulations, 1D length of 1,001 points each, and inspect whether or not there still is an orientation bias. In the top row, each simulation's three orientation angles,* $(\omega,[\theta,\phi])$, *are filtered, converted to the P-T angles,* (θ_P,δ_P) *and* (θ_T,δ_T), *then stacked. In the top row each simulation's three orientation angles,* $(\omega,[\theta,\phi])$, *are filtered, given a random rotation, converted to the P-T angles,* (θ_P,δ_P) *and* (θ_T,δ_T), *then stacked. Below each set of P-T equal area plots is an associated* $\boldsymbol{\sigma}'_{HeterogeneousMean}$ *stress tensor. This is calculated as follows. For each simulation, filtered principal stresses,* σ'_1, σ'_2, *and* σ'_3 *with* $\sqrt{I'_2} = 1.0$, *are combined with the unrotated or rotated angles,* $(\omega,[\theta,\phi])$, *to produce filtered heterogeneous stress tensors. Then all the stress tensors from all the simulations are averaged component-wise to create,* $\boldsymbol{\sigma}'_{HeterogeneousMean}$. *Last,* $\sqrt{I'_{2\ HeterogeneousMean}}$, *is shown as a measure of the size of* $\boldsymbol{\sigma}'_{HeterogeneousMean}$. *It shows the extent to which the components of* $\boldsymbol{\sigma}'_{HeterogeneousMean}$ *have not canceled out in the stacked simulations, and there is still a bias in the heterogeneous stress. Ideally, we want stacked simulations that have the following properties: 1) P and T equal area plots with uniform distributions of points (indicating no orientation bias) 2)* $\boldsymbol{\sigma}'_{HeterogeneousMean}$ *with each component approaching zero; therefore,* $\sqrt{I'_{2\ HeterogeneousMean}} \to 0$ *as the number of stacked runs* $\to \infty$. *We find that stacking filtered data alone is insufficient (the top row), that one needs to both randomly rotate each simulation and then stack the data to produce heterogeneous stress with no orientation bias and a* $\sqrt{I'_{2\ HeterogeneousMean}} \approx 0$ *for all* α.

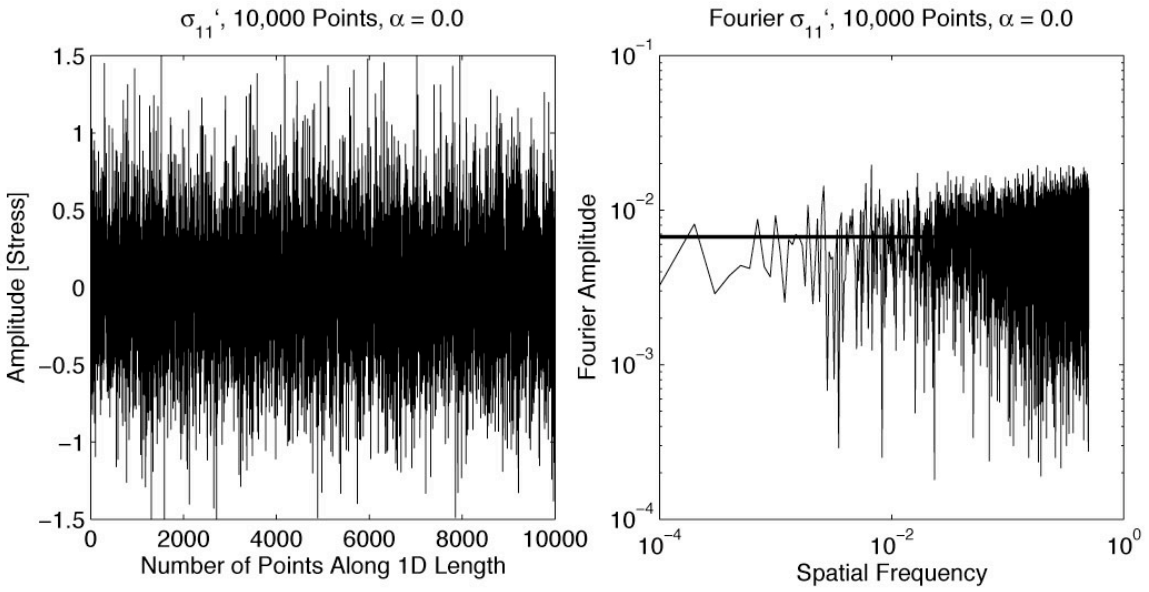

Figure 3.14 a)

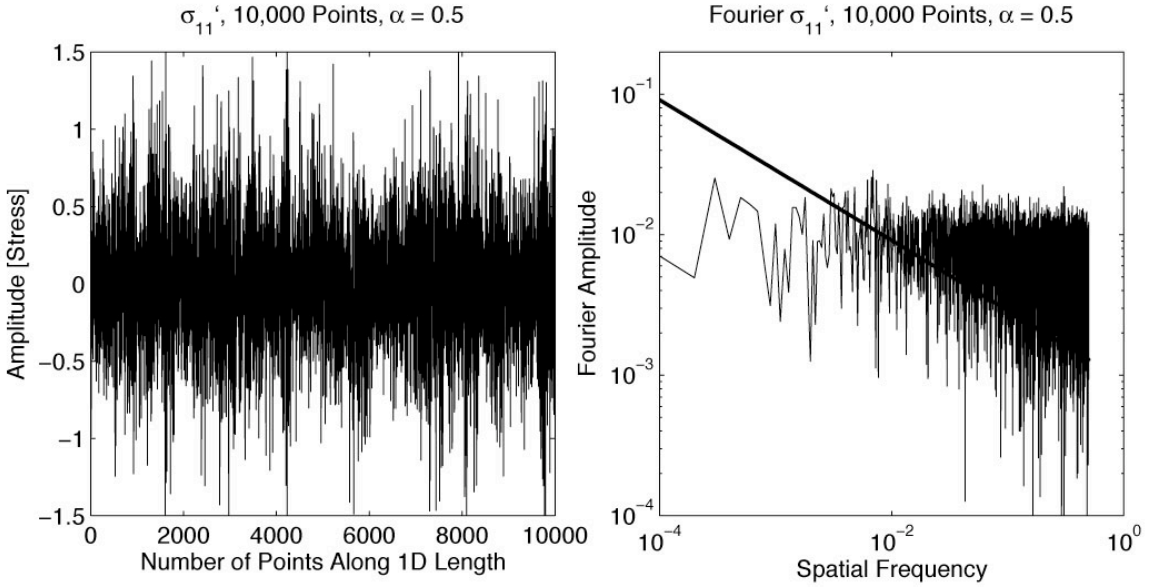

Figure 3.14 b)

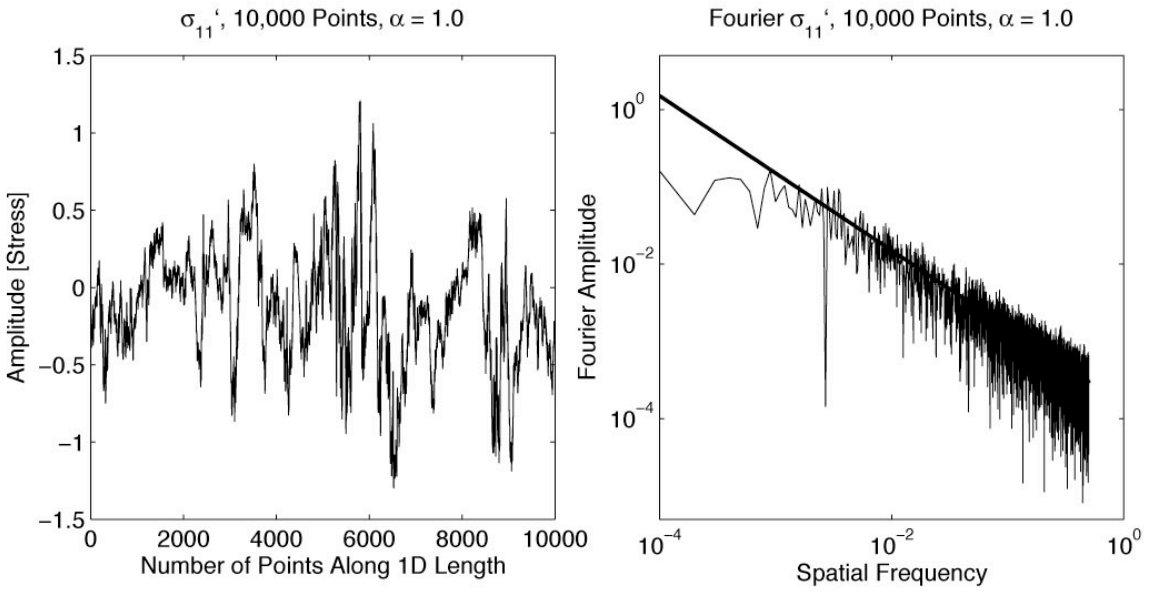

Figure 3.14 c)

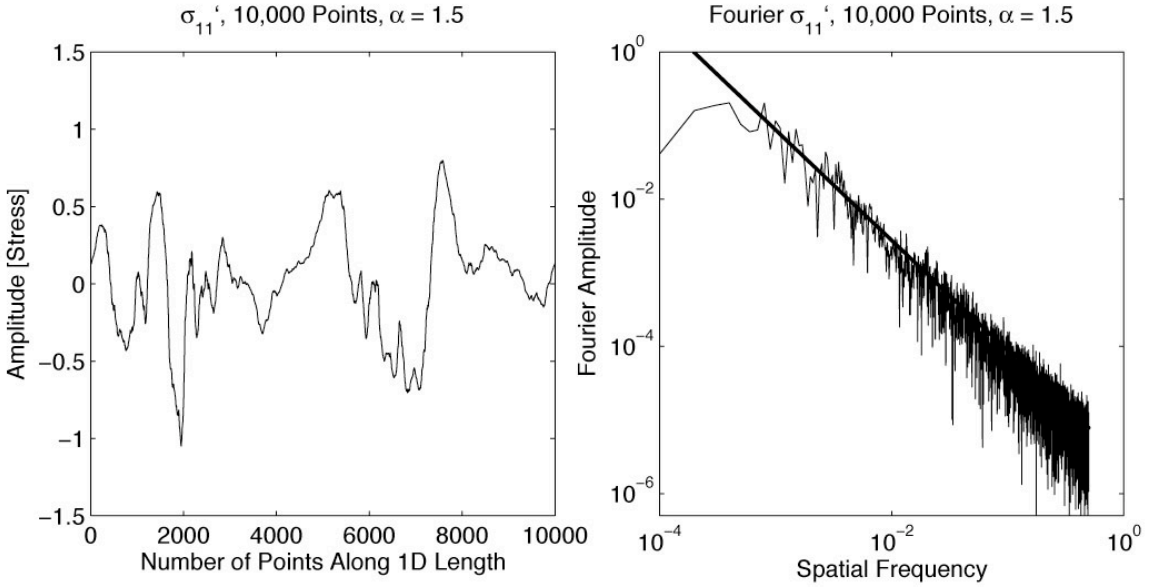

Figure 3.14 d)

Figure 3.14. *We plot the one component of a stress tensor for different levels of* α *smoothing. The other components of the stress tensor have similar spectral properties. Smoothed orientation angles,* $(\omega,[\theta,\phi])$*, and smoothed principal stresses,* σ_1'*,* σ_2'*, and* σ_3'*, are combined together to produce a symmetric stress tensor in a particular reference frame. Note that the independent components of the stress tensor are much rougher than the smoothed orientation angles and principal stresses. When the smoothed principal stresses,* σ_1'*,* σ_2'*, and* σ_3'*, are rotated into their respective reference frames using the smoothed angles,* $(\omega,[\theta,\phi])$*, to produce the Cartesian stress tensor components, much of the* α *smoothing is lost. This occurs because the symmetric stress tensor is defined for a Cartesian coordinate system in a particular reference frame, and stress components can lose their spectral properties upon rotation. This property is the reason we chose to filter the principal stresses and orientation angles rather than components of the Cartesian stress tensor in a particular reference frame.*

The last few plots show results for our 201x201x201 3D grids. Figures 3.15–3.18 show 2D slices through our filtered 3D grids at the $Z = 100$ height, midway through the 3D grids. The quantities shown in Figures 3.15–3.18 are shown for four different levels of smoothing, $\alpha = 0.0$, 0.5, 1.0, and 1.5 . In Figures 3.15–3.17, we find plots of the filtered and rotated 3D orientation angles, $\left(\omega[\theta,\phi]\right)$. Note for each α , a different random seed is used to create the 3D grid prior to filtering, and a different random rotation is applied to each grid. Random rotations can change the mean values of $\left(\omega[\theta,\phi]\right)$; hence, the 2D slices of $\left(\omega[\theta,\phi]\right)$, shown in Figures 3.15–3.17, have different mean levels for different α . This has nothing to do with the filtering. It is simply a function of the different random rotations that are applied.

In Figure 3.18 we have plots of σ'_{11}, the first diagonal component of the deviatoric stress tensor. The 3D deviatoric stress tensor is calculated by combining the filtered, and rotated 3D orientation angles, $\left(\omega[\theta,\phi]\right)$ with filtered 3D principal stresses, σ'_1, σ'_2, and σ'_3. We only show one component of the filtered 3D deviatoric stress tensor because the other components are similar. Again the components of the deviatoric stress tensor are not as spatially smooth as the orientation angles or principal stresses as we saw in the 1D. The only pattern we find within the filtered deviatoric stress tensor is that the standard deviations of the off-diagonal components tend to be ≈14% smaller than the standard deviations of the diagonal components.

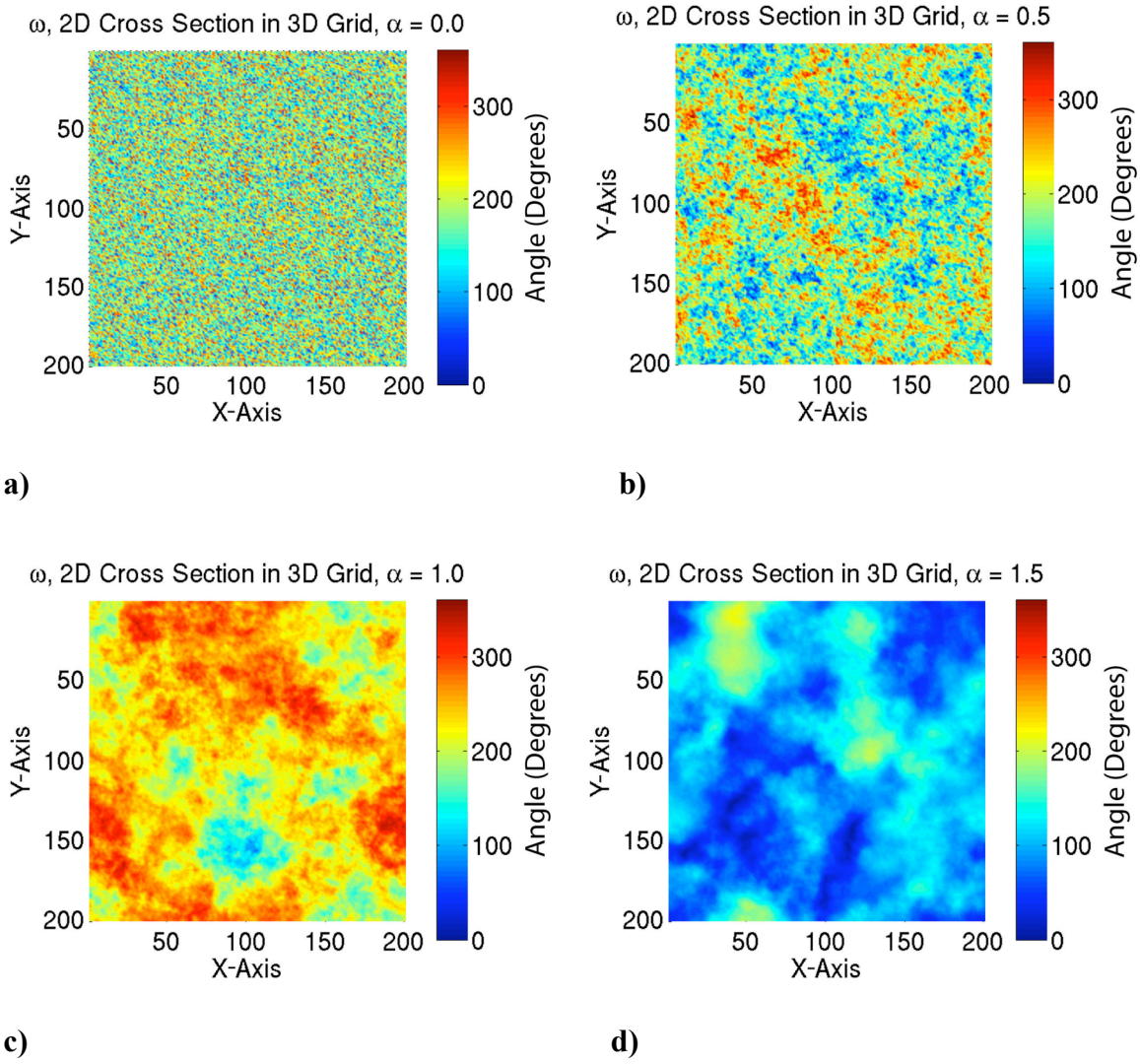

Figure 3.15. *2D slices of the angle, ω, through a 3D grid for four different levels of smoothing,* ***a)*** $\alpha = 0.0$, ***b)*** $\alpha = 0.5$, ***c)*** $\alpha = 1.0$, *and* ***d)*** $\alpha = 1.5$. *Each grid is 201x201x201 points, for a total of over 8 million grid points. The 2D slices shown are in the x-y plane approximately halfway through the grid at z = 100. All the planes exhibit similar spatial smoothing. Since it is a different simulation for each α, with a different random rotation of the angles $(\omega,[\theta,\phi])$ for each simulation, the mean value of the angle, ω, is different from simulation to simulation.*

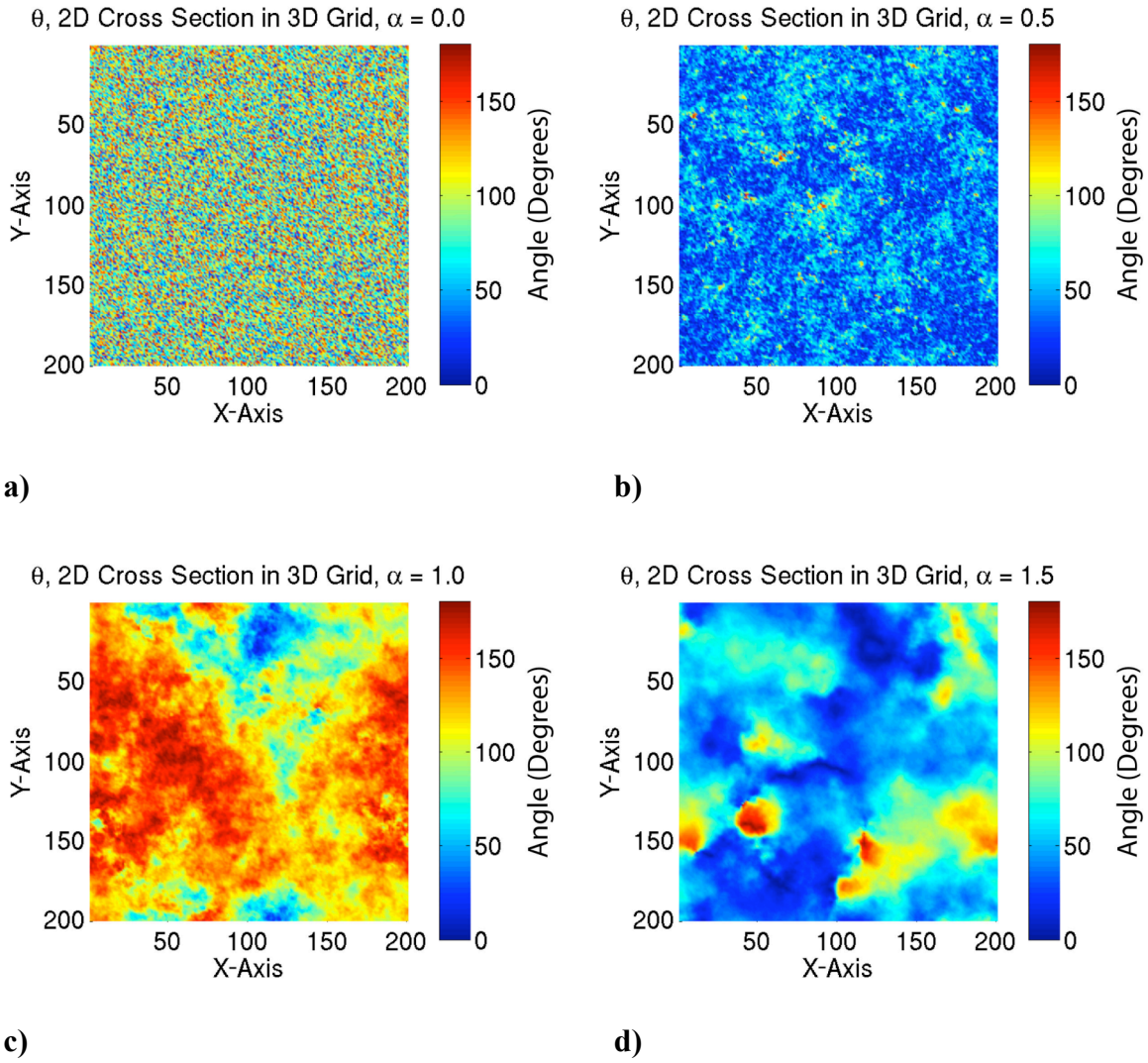

Figure 3.16. *2D slices of the angle, θ, through a 3D grid for four different levels of smoothing,* ***a)*** $\alpha = 0.0$, ***b)*** $\alpha = 0.5$, ***c)*** $\alpha = 1.0$, *and* ***d)*** $\alpha = 1.5$. *The 2D slices shown are in the x-y plane approximately halfway through the grid at z = 100. All the planes exhibit similar spatial smoothing. Since it is a different simulation for each α, with a different random rotation of the angles $(\omega,[\theta,\phi])$ for each simulation, the mean value of the angle, θ, is different from simulation to simulation.*

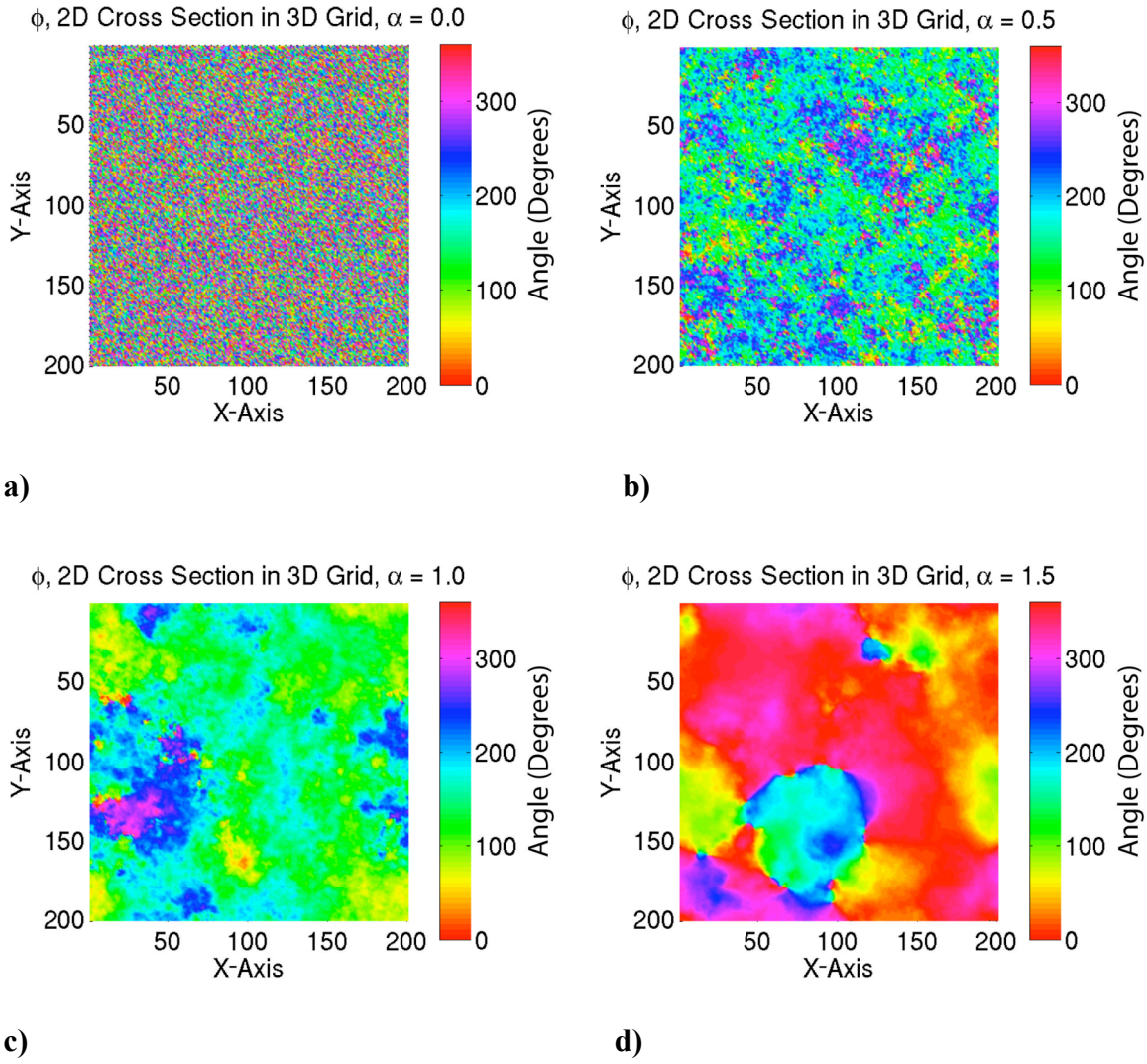

Figure 3.17. *2D slices of the angle, ϕ, through a 3D grid for four different levels of smoothing,* ***a)*** $\alpha = 0.0$, ***b)*** $\alpha = 0.5$, ***c)*** $\alpha = 1.0$, *and* ***d)*** $\alpha = 1.5$. *The 2D slices shown are in the x-y plane approximately halfway through the grid at z = 100. All the planes exhibit similar spatial smoothing. Since it is a different simulation for each α, with a different random rotation of the angles $(\omega,[\theta,\phi])$ for each simulation, the mean value of the angle, ϕ, is different from simulation to simulation.*

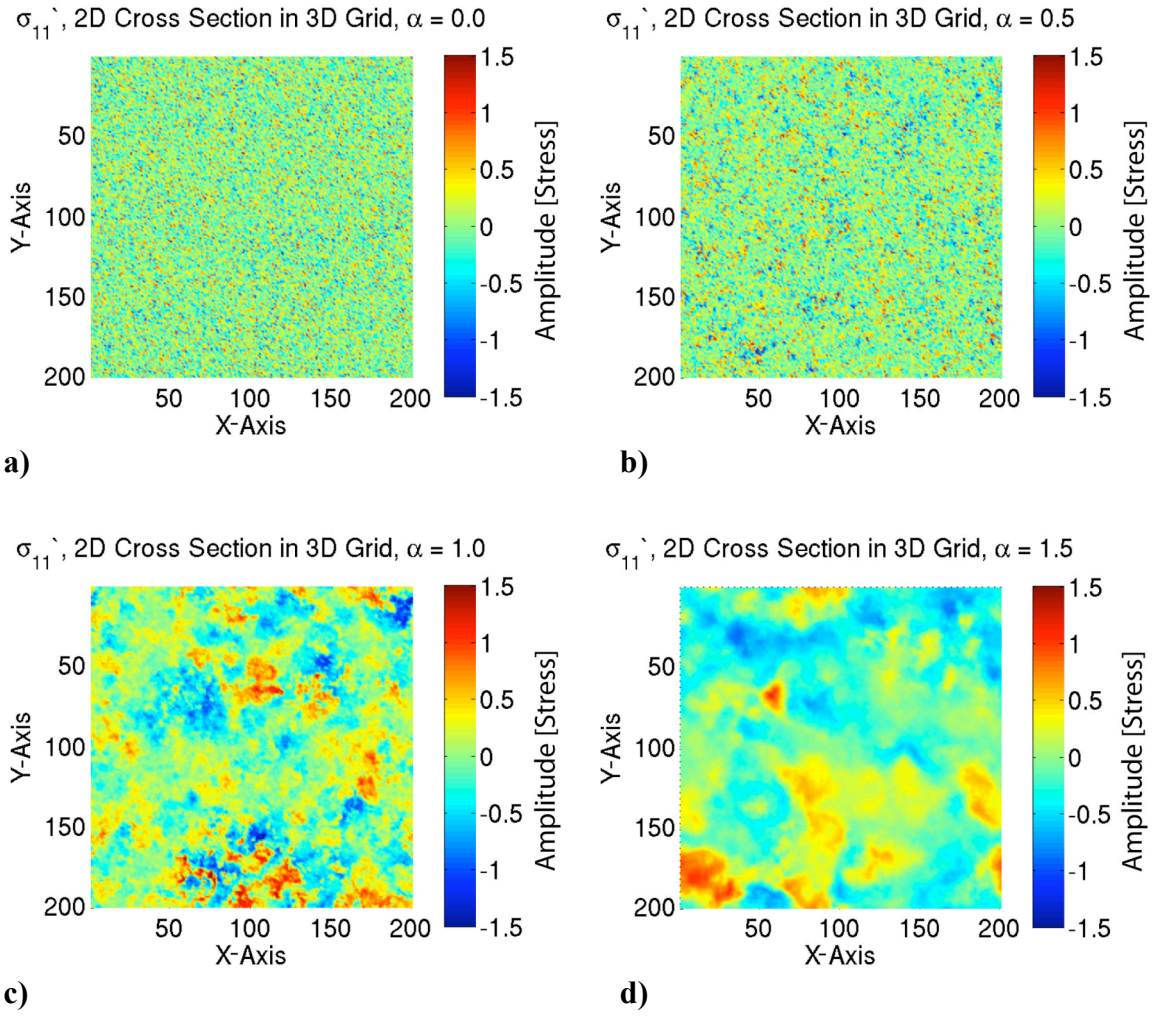

Figure 3.18. *2D slices of the first diagonal component of the deviatoric stress tensor,* σ'_{11}*, through a 3D grid for four different levels of smoothing,* ***a)*** $\alpha = 0.0$*,* ***b)*** $\alpha = 0.5$*,* ***c)*** $\alpha = 1.0$*, and* ***d)*** $\alpha = 1.5$*. The 2D slices shown are in the x-y plane approximately halfway through the grid at z = 100.* σ'_{11} *is rougher than the smoothed principal stresses,* σ'_1*,* σ'_2*,* and σ'_3*, or smoothed orientation angles* $(\omega,[\theta,\phi])$*. See Figure 3.14, the 1D example, for an explanation. The other components of the deviatoric stress tensor show similar spectral properties, i.e., degree of spatial smoothing.*

The next question we ask is how random are our 3D grids for different levels of spatial smoothing, α. Figure 3.19 explores this. Using the azimuth and plunge ranges illustrated in the Figure 3.12 cartoon, Figure 3.19 plots the P-T axes from randomly selected points within our 3D grids for four different levels of α. For each α, 100,000 points are randomly selected and plotted, a component-wise mean stress tensor, $\boldsymbol{\sigma}'_{HeterogeneousMean}$, is calculated, and its associated $\sqrt{I'_{2\ HeterogeneousMean}}$ (a measure of the size of $\boldsymbol{\sigma}'_{HeterogeneousMean}$) is shown. If the 3D grid has unbiased orientations, we would expect to see a uniform coverage of the equal area P-T plots as we see in Figure 3.19 a) and if the stress heterogeneity has a zero mean (which is what we are trying to design), we would expect the components of $\boldsymbol{\sigma}'_{HeterogeneousMean}$ to be close to zero and $\sqrt{I'_{2\ HeterogeneousMean}}$ to be very small. For comparison, the deviatoric principal stresses used in creating the stress tensor, have an $\sqrt{I'_2} = 1.0$. We find that for the $\alpha = 0.0$ case, Figure 3.19 a), the P-T equal area plots are uniformly covered with points as one might expect for no filtering. As α increases, the spatial clumping of data on the P-T plots increases. Interestingly, $\sqrt{I'_{2\ HeterogeneousMean}}$ is quite small for both $\alpha = 0.0$ and $\alpha = 0.5$, less than 1% when compared to the size of the input principal stresses, $\sqrt{I'_2} = 1.0$. As α increases, eventually, $\sqrt{I'_{2\ HeterogeneousMean}}$ increases to $\approx 2\%$ for $\alpha = 1.0$ and $\sqrt{I'_{2\ HeterogeneousMean}} \approx 8\%$ for $\alpha = 1.5$. Consequently, if one remains within the range of $0.0 \le \alpha < 1.0$, there will be less than 2% bias within the heterogeneity stress tensor for our 3D grids.

For first order calculations, a single filtered 3D heterogeneous stress grid should be sufficient to approximate heterogeneous stress with zero mean for $0.0 \le \alpha < 1.0$ if one averages over the entire grid. For $1.0 \le \alpha \le 1.5$, other issues will arise. Namely, as α

increases and the heterogeneous stress is increasingly smoothed, there will develop regions within the grid that will be more likely to fail than others (large I_2'), which can produce an average orientation bias in simulations that generate synthetic focal mechanisms. Again the answer will be to stack results from simulations with different 3D heterogeneous stress grids. See Chapter 4 for an explanation as to why regions with large I_2' are more likely to fail.

Figure 3.19 demonstrates that there is little to no bias when one averages over our entire 3D grids, but what happens if one averages over only a subregion of our 3D grids? This is another subject unto itself [*Heaton*, 2006, in preparation], but for now we just want to show that as the spatial smoothing, α, increases, there is increased clustering of orientations in P-T space, and the stress tensor has a significant non-zero mean for subregions. Also some subregions will be more likely to fail than others, those with larger I_2'. Figure 3.20 diagrams how we divide our grid into subregions (with the unprimed numbers) and the subdivide into sub-subregions (with the primed numbers). Figure 3.21 shows P-T plots, $\boldsymbol{\sigma}'_{HeterogeneousMean}$, and $\sqrt{I'_{2\ HeterogeneousMean}}$ for sample subregions and sub-subregions. The azimuthal and plunge ranges are the same as in Figure 3.19. For each α, one subregion, (1,1,1), containing 100,000 points and one sub-subregion, (1',1',1'), containing 1,000 points are plotted. As expected, for $\alpha = 0.0$, it is still uniform, random, even in the subdivisions of the grid. For $\alpha = 0.5$, a little spatial clumping begins. It is for $\alpha = 1.0$ and $\alpha = 1.5$, that we begin to notice marked differences between the average orientations of subdivisions and the entire grid. For example, $\alpha = 1.0$, (1,1,1) has a $\sqrt{I'_{2\ HeterogeneousMean}} \approx 18\%$, and the sub-subregion (1',1',1')

has an $\sqrt{I'^2_{HeterogeneousMean}} \approx 43\%$. Compare that to the $\sqrt{I'^2_{HeterogeneousMean}} \approx 2\%$ for randomly selected points from the entire 3D grid in Figure 3.19. When $\alpha = 1.5$, the effect can become even more extreme. (1,1,1) has a $\sqrt{I'^2_{HeterogeneousMean}} \approx 29\%$, and the sub-subregion (1',1',1') has a $\sqrt{I'^2_{HeterogeneousMean}} \approx 160\%$ whereas $\sqrt{I'^2_{HeterogeneousMean}} \approx 8\%$ for randomly selected points in Figure 3.19.

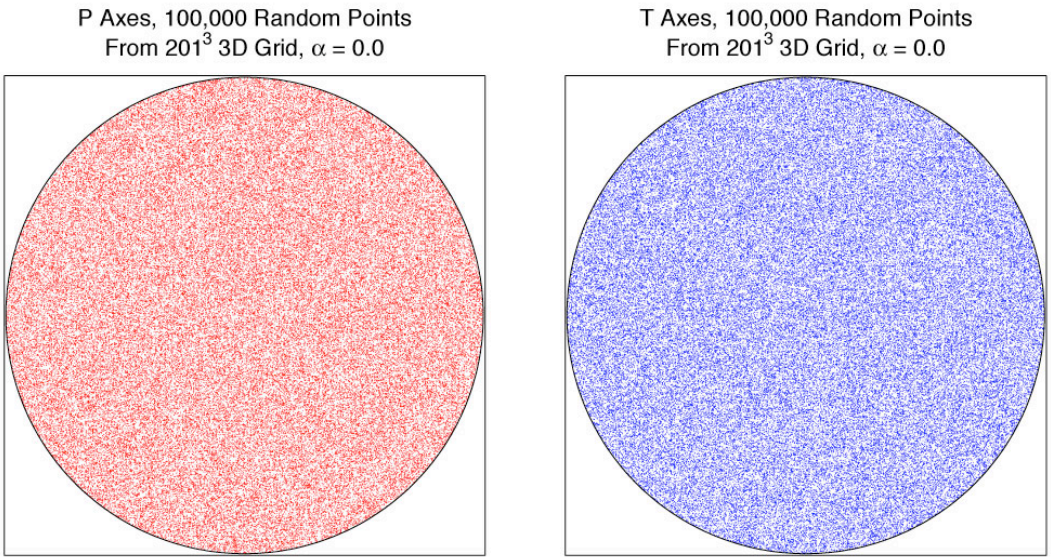

$$\boldsymbol{\sigma}'_{HeterogeneousMean} = \begin{pmatrix} -0.0012 & -0.0010 & -0.0016 \\ -0.0010 & -0.0004 & 0.0000 \\ -0.0016 & 0.0000 & 0.0016 \end{pmatrix} \text{ for 100,000 Random Points}$$

$$\sqrt{I'_{2\ HeterogeneousMean}} = 0.0033$$

Figure 3.19 a)

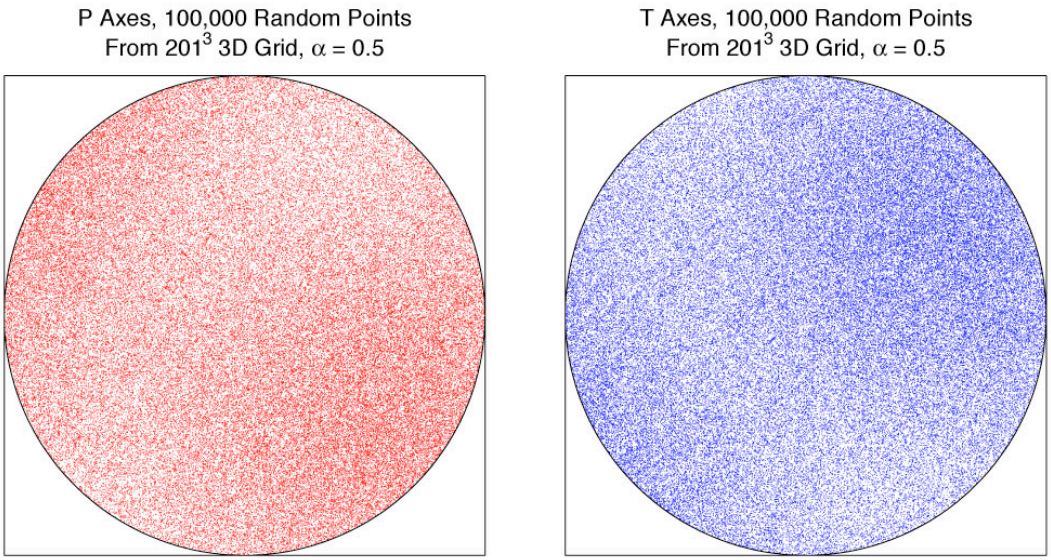

$$\boldsymbol{\sigma}'_{HeterogeneousMean} = \begin{pmatrix} 0.0015 & -0.0013 & 0.0006 \\ -0.0013 & -0.0011 & -0.0013 \\ 0.0006 & -0.0013 & -0.0004 \end{pmatrix} \text{ for 100,000 Random Points}$$

$$\sqrt{I'_{2\ HeterogeneousMean}} = 0.0033$$

Figure 3.19 b)

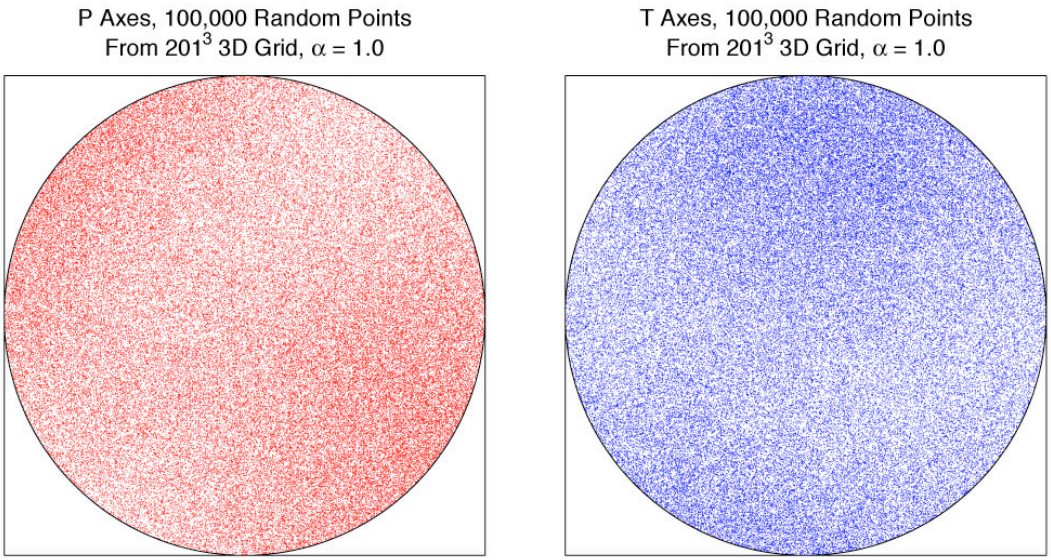

$$\boldsymbol{\sigma}'_{HeterogeneousMean} = \begin{pmatrix} 0.0110 & 0.0037 & 0.0042 \\ 0.0037 & -0.0107 & -0.0031 \\ 0.0042 & -0.0031 & -0.0003 \end{pmatrix} \text{ for 100,000 Random Points}$$

$$\sqrt{I'_{2\ HeterogeneousMean}} = 0.0178$$

Figure 3.19 c)

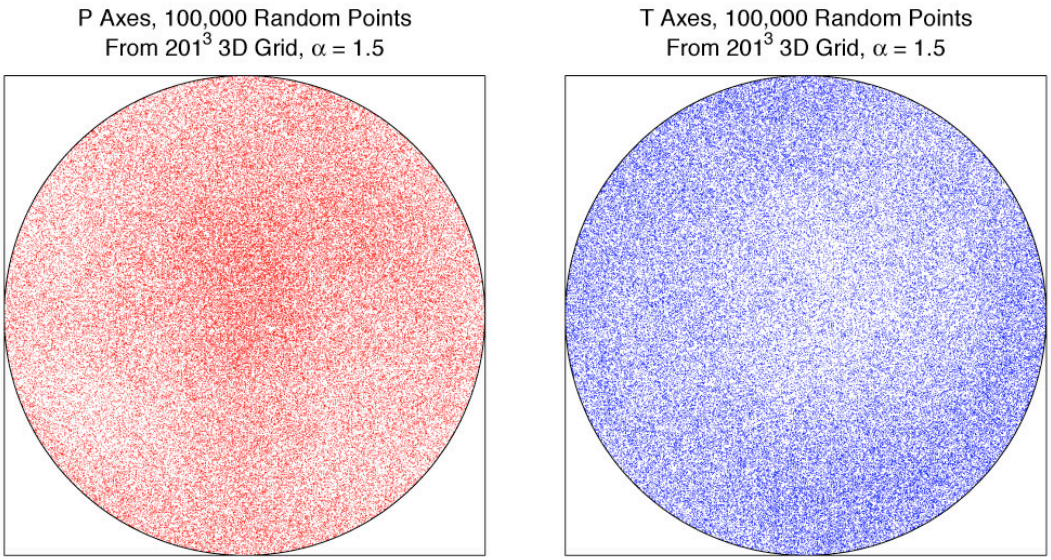

$$\boldsymbol{\sigma}'_{HeterogeneousMean} = \begin{pmatrix} -0.0241 & 0.0166 & -0.0151 \\ 0.0166 & 0.0515 & 0.0236 \\ -0.0151 & 0.0236 & -0.0274 \end{pmatrix} \text{ for 100,000 Random Points}$$

$$\sqrt{I'_{2\ HeterogeneousMean}} = 0.0781$$

Figure 3.19 d)

Figure 3.19. *We have P (Principal Compression Axis in red) and T (Principal Tension Axis in blue) plots for 3D, filtered, heterogeneous grids at four different levels of smoothing,* ***a)*** $\alpha = 0.0$, ***b)*** $\alpha = 0.5$, ***c)*** $\alpha = 1.0$, *and* ***d)*** $\alpha = 1.5$. *Each grid is 201x201x201 points for a total of over 8 million grid points. We randomly choose 100,000 points from the over 8 million possible points and plot their P and T Axes axes on equal area plots. For these P-T plots, we choose the conventional plunge range shown in Figure 3.12. For each* α, *we calculate the component-wise mean tensor for the 100,000 randomly selected points,* $\boldsymbol{\sigma}'_{HeterogeneousMean}$ *and its associated* $\sqrt{I'_{2\ HeterogeneousMean}}$, *which has units of stress. For comparison, the principal stresses that are used in creating, the stress tensors have a* $\sqrt{I'_2} = 1.0$. *In* ***a)*** $\alpha = 0.0$, *there is no clumping of the points on the P-T plots indicating that the heterogeneous stress is without any appreciable orientation bias and is uniformly distributed over orientation space. Also* $\sqrt{I'_{2\ HeterogeneousMean}}$, *a measure of the size of the stress bias, is quite small for* $\alpha = 0.0$, *less than 1%. As* α *increases, the spatial clumping of the points begins to appear to a small degree. In 3D simulations, this is a much smaller effect than in 1D if the entire 3D grid is being sampled. As* α *increases ,* $\sqrt{I'_{2\ HeterogeneousMean}}$ *also begins to increase to* $\approx 2\%$ *for* $\alpha = 1.0$ *and* $\approx 8\%$ *for* $\alpha = 1.5$.

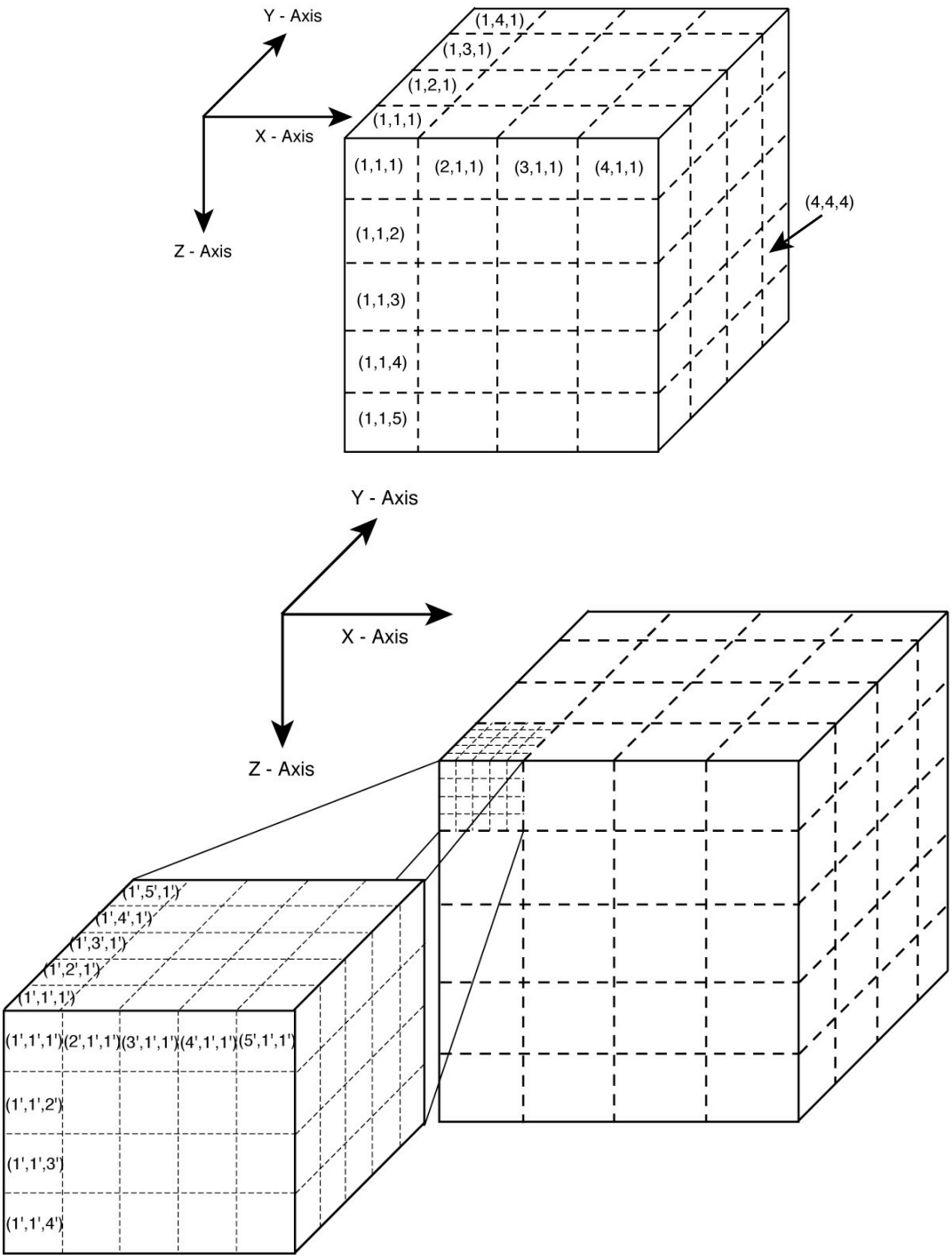

Figure 3.20. *A diagram of how we divide, then subdivide the 3D grid. The first division, produces subregions, approximately 100,000 points each. The second division produces sub-subregions, approximately 1,000 points each.*

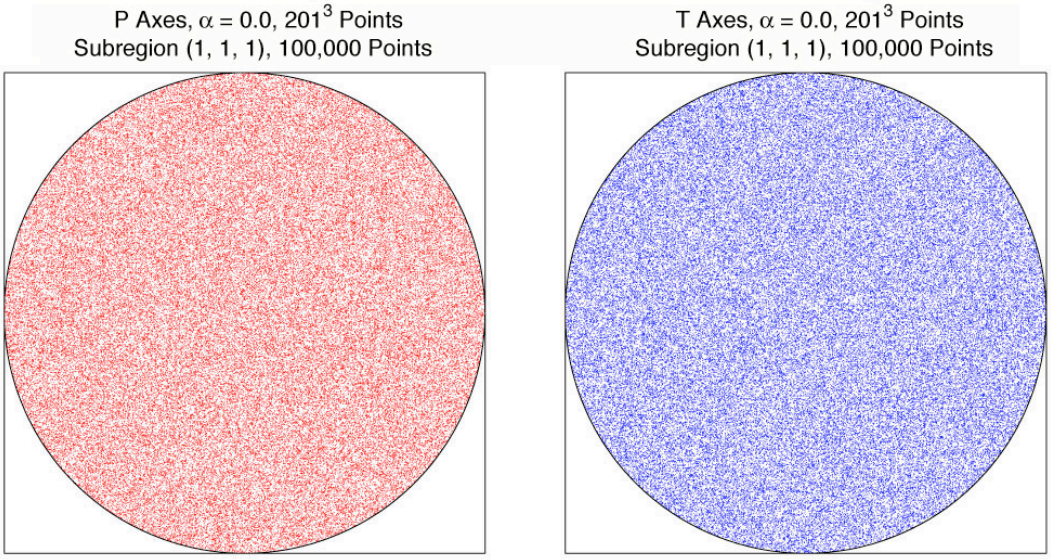

$$\boldsymbol{\sigma}'_{HeterogeneousMean} = \begin{pmatrix} -0.0011 & 0.0007 & -0.0012 \\ 0.0007 & 0.0013 & -0.0006 \\ -0.0012 & -0.0006 & -0.0002 \end{pmatrix} \text{ for 100,000 Points}$$

$$\sqrt{I'_{2\ HeterogeneousMean}} = 0.0027$$

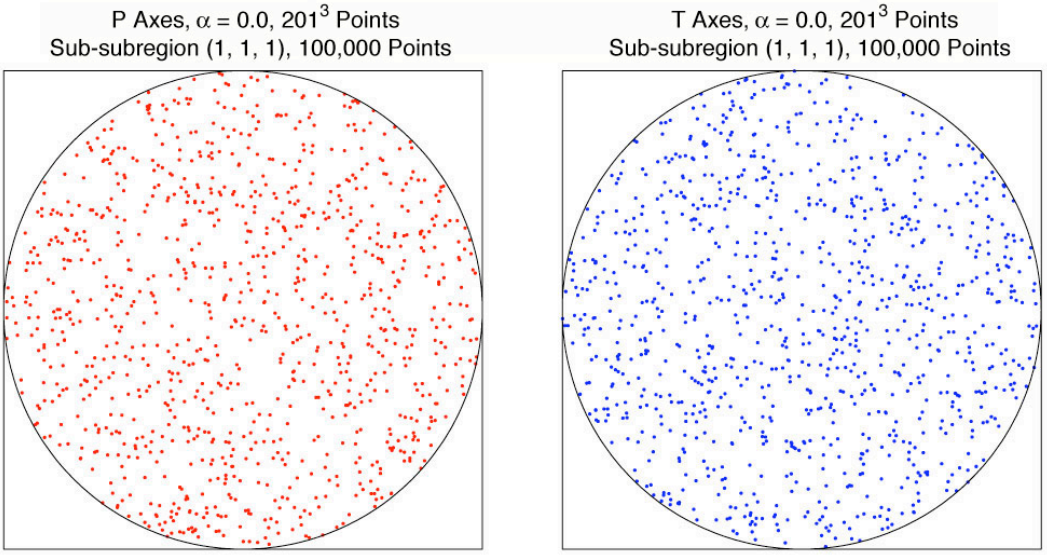

$$\boldsymbol{\sigma}'_{HeterogeneousMean} = \begin{pmatrix} 0.0023 & 0.0093 & -0.0079 \\ 0.0093 & -0.0236 & 0.0066 \\ -0.0079 & 0.0066 & 0.0213 \end{pmatrix} \text{ for 1,000 Points}$$

$$\sqrt{I'_{2\ HeterogeneousMean}} = 0.0374$$

Figure 3.21 a)

$$\boldsymbol{\sigma}'_{HeterogeneousMean} = \begin{pmatrix} -0.0220 & -0.0163 & 0.0169 \\ -0.0163 & 0.0175 & 0.0057 \\ 0.0169 & 0.0057 & 0.0045 \end{pmatrix} \text{ for 100,000 Points}$$

$$\sqrt{I'_{2\ HeterogeneousMean}} = 0.0447$$

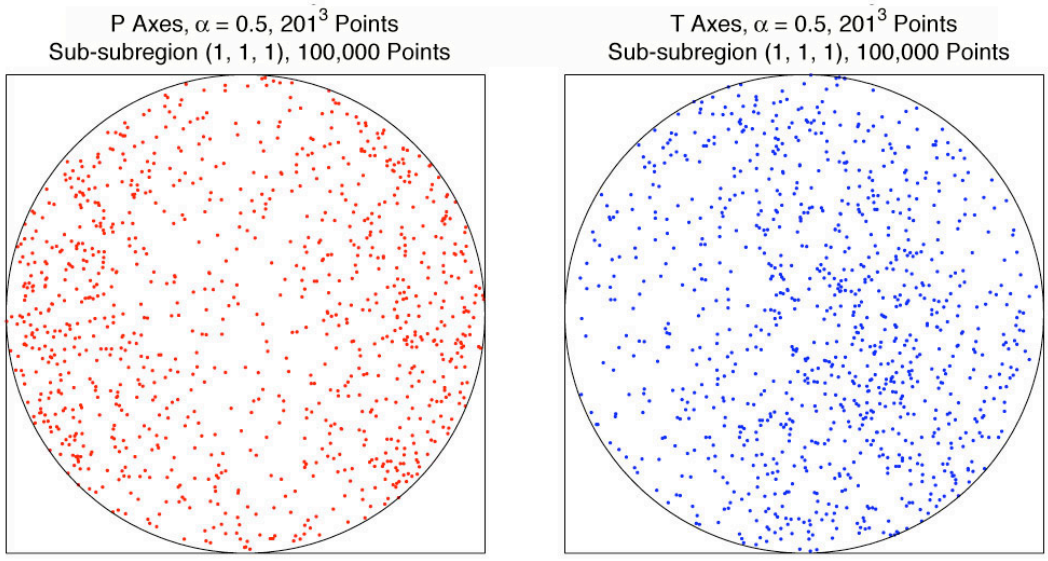

$$\boldsymbol{\sigma}'_{HeterogeneousMean} = \begin{pmatrix} 0.0398 & 0.0081 & 0.0167 \\ 0.0081 & -0.0094 & -0.0089 \\ 0.0167 & -0.0089 & -0.0304 \end{pmatrix} \text{ for 1,000 Points}$$

$$\sqrt{I'_{2\ HeterogeneousMean}} = 0.0592$$

Figure 3.21 b)

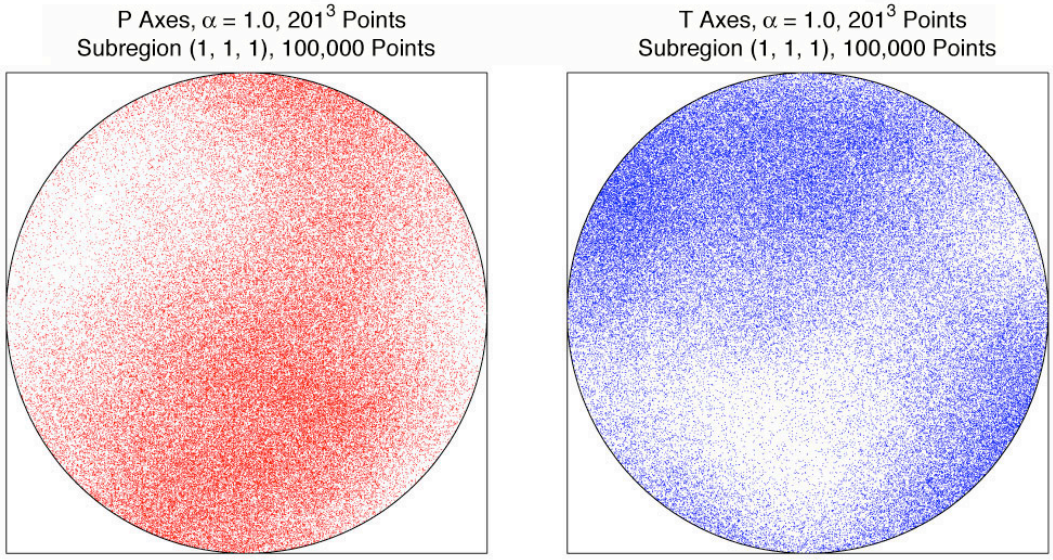

$$\boldsymbol{\sigma}'_{HeterogeneousMean} = \begin{pmatrix} 0.0696 & -0.0584 & 0.0259 \\ -0.0584 & -0.0212 & -0.0948 \\ 0.0259 & -0.0948 & -0.0483 \end{pmatrix} \text{ for 100,000 Points}$$

$$\sqrt{I'_{2\ HeterogeneousMean}} = 0.1836$$

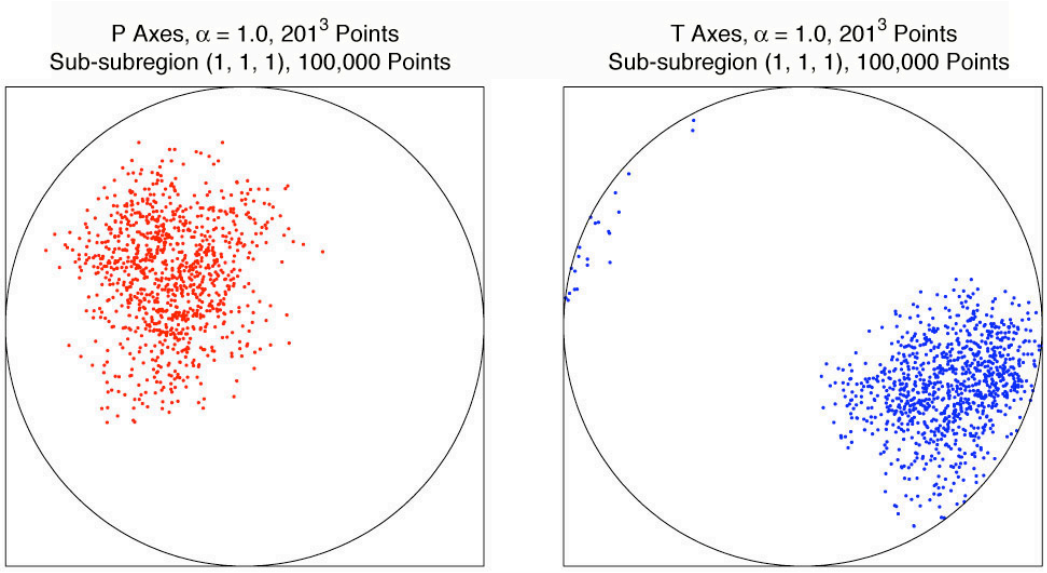

$$\boldsymbol{\sigma}'_{HeterogeneousMean} = \begin{pmatrix} 0.0887 & -0.1720 & -0.0753 \\ -0.1720 & -0.2653 & -0.0388 \\ -0.0753 & -0.0388 & 0.1766 \end{pmatrix} \text{ for 1,000 Points}$$

$$\sqrt{I'_{2\ HeterogeneousMean}} = 0.4277$$

Figure 3.21 c)

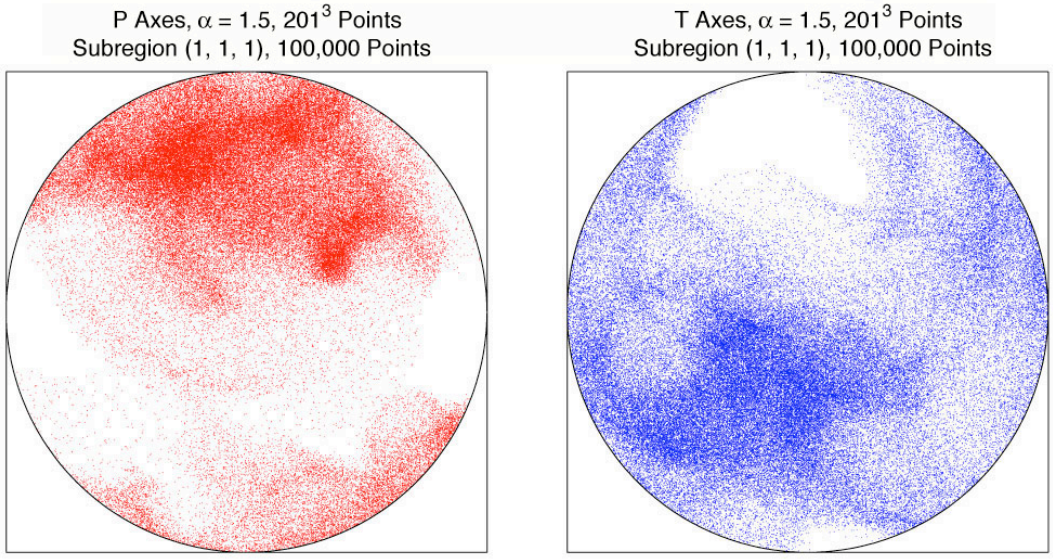

$$\boldsymbol{\sigma}'_{HeterogeneousMean} = \begin{pmatrix} -0.1565 & -0.0763 & -0.0053 \\ -0.0763 & 0.0753 & -0.1371 \\ -0.0053 & -0.1371 & 0.0811 \end{pmatrix} \text{ for 100,000 Points}$$

$$\sqrt{I'_{2\ HeterogeneousMean}} = 0.2933$$

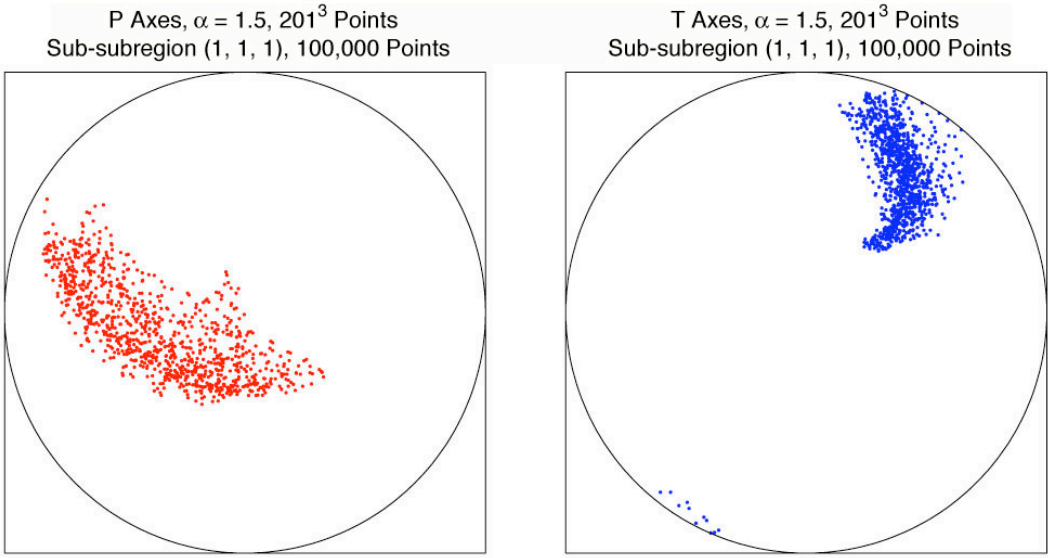

$$\boldsymbol{\sigma}'_{HeterogeneousMean} = \begin{pmatrix} 0.0746 & -0.4324 & 0.6902 \\ -0.4324 & -0.5582 & 0.5851 \\ 0.6902 & 0.5851 & 0.4836 \end{pmatrix} \text{ for 1,000 Points}$$

$$\sqrt{I'_{2\ HeterogeneousMean}} = 1.6007$$

Figure 3.21 d)

Figure 3.21. *This is similar to Figure 3.19, except that we plot the P and T axes for all the points within different subregions. The grid is first divided into 4x4x5 subregions of approximately 100,000 points each. Then the (1,1,1) subregion is subdivided into 5x5x4 sub-subregions, of approximately 1,000 points each. The purpose of this exercise is to show that as the spatial smoothing increases, subregions develop coherent orientation patterns. Therefore, even if the entire grid has little to no orientation bias, a subregion might have a significant orientation bias due to the long spatial wavelength coherence of orientations. We plot one sample subregion, (1,1,1), and one sample sub-subregion (1',1',1'), for each level of smoothing,* ***a)*** $\alpha = 0.0$, ***b)*** $\alpha = 0.5$, ***c)*** $\alpha = 1.0$, *and* ***d)*** $\alpha = 1.5$. *We find that for no smoothing,* ***a)*** $\alpha = 0.0$, *it does not matter whether we are looking at a subregion or the entire grid as in Figure 4.17. The subregions have random, uniform distributions of P and T axes on equal area plots. There is no appreciable clumping and* $\sqrt{I'_{2\ HeterogeneousMean}} \approx 0.0$ *for each subregion. Now as* α *increases so does the spatial clumping in P-T space and the value of* $\sqrt{I'_{2\ HeterogeneousMean}}$. *In fact, for* $\alpha = 1.5$, $\sqrt{I'_{2\ HeterogeneousMean}} \approx 1.6$, *for (1',1',1'), the same order magnitude as* $I'_2 = 1.0$, *the value of* I'_2 *for the input principal stresses. This indicates a very strong orientation bias in the sub-subregion. Therefore, as* α *increases the differential between subregion orientation bias and the entire grid orientation, grid bias increases. This is interesting, because as we will see in later chapters, this orientation clustering in space reproduces some of the clustering statistics seen in the real Earth.*

Summary of How to Create a Filtered 3D Heterogeneous Stress Tensor with Approximately Zero Mean

Now that we have explored some of the characteristics of our filtered principal stresses, orientation angles, and stress matrices in both 1D and 3D, let us summarize how to create our full heterogeneous stress matrices:

- Spatially filter three or two invariants of the stress tensor. We choose to filter the principal stresses for simplicity.
    - Generate 3D grids with Gaussian random noise for σ_1, σ_2, and σ_3 independently.
    - Filter each principal stress in 3D using the Chapter 2 methodology.
    - Use all three filtered, independent principal stresses, σ_1, σ_2, and σ_3, to create the full stress tensor with six independent quantities.
    - Or use the deviatoric principal stresses, σ_1', σ_2', and σ_3', where

      $\sigma_1' = \sigma_1 - p$
      $\sigma_2' = \sigma_2 - p$ and $p = (1/3)(\sigma_{11} + \sigma_{22} + \sigma_{33})$, so that the constraint
      $\sigma_3' = \sigma_3 - p$

      $\sigma_1' + \sigma_2' + \sigma_3' = 0$ is satisfied, to create the deviatoric stress tensor with five independent quantities.
- Create approximately random, spatially filtered orientations:
    - Generate a set of completely random orientations using a random unit quaternion generator.
    - Convert the quaternions into three angles, a rotation axis, $[\theta, \phi]$, and a rotation ω about the rotation axis.

- Spatially filter these three angles, $(\omega,[\theta,\phi])$.
- Resize the angles so that their spatial means have the following values, $\bar{\omega} = 180°$, $\bar{\theta} = 90°$, and $\bar{\phi} = 180°$, and their possible ranges fall within, $0° \le \omega \le 360°$, $0° \le \theta \le 180°$, and $0° \le \phi \le 360°$.
- Convert the spatially filtered $(\omega,[\theta,\phi])$, back into its associated filtered quaternion, $\vec{q}^{\,F} = \left[q_0^F, q_1^F, q_2^F, q_3^F\right]$.
- Add a random rotation to this filtered quaternion, using algebraic quaternion multiplication.
- Then convert this filtered, randomly rotated quaternion into strike, dip, and rake, (Θ,δ,λ).

- Combine the spatially filtered fault parameters, (Θ,δ,λ), with the spatially filtered principal stresses, to produce an approximately randomly oriented, spatially filtered, heterogeneous stress matrix.
- Use the heterogeneous stress matrix in simulations that produce synthetic focal mechanisms.
- Repeat the above steps at least ten times and stack the results to produce data that have no substantial orientation bias in the heterogeneity.

References

Heaton, T. H. (2006, in preparation), Scale dependence of the strength of the Earth's crust.

Marsaglia, G. (1972), Choosing a Point from the Surface of a Sphere, *Annual Mathematical Statistics*, *43*, 645–646.

Mathworks, I. (1994–2006), Aerospace Block Set - Quaternion Multiplication, *http://www.mathworks.com/access/helpdesk/help/toolbox/aeroblks/aeroblks.html*.

Weisstein, E. W. Hypersphere Point Picking, in *MathWorld -- A Wolfram Web Resource.* *http://mathworld.wolfram.com/HyperspherePointPicking.html*, edited.

Chapter 4. Plastic Yield Criterion (Hencky-Mises Failure Criterion) and How Its Interaction with Spatially Heterogeneous Stress Biases Earthquake Failures Toward the Stress Rate Tensor, $\dot{\boldsymbol{\sigma}}'_T$

Overview of Why Understanding the Fracture Criterion Is Important

In this chapter we wish to demonstrate that as the amplitude of the heterogeneity increases, the orientations of the failures in our simulations become increasingly biased toward the stress rate tensor, $\dot{\boldsymbol{\sigma}}'_T$. We will do this by 1) analyzing the fracture criterion used to bring points to failure as synthetic earthquakes and 2) examining P-T plots of synthetic focal mechanisms from our simulations.

If the real Earth has significant spatially heterogeneous stress, which we have reason to believe it does, our observation of bias toward the stress rate, $\dot{\boldsymbol{\sigma}}'_T$, has important implications for interpreting stress inversion studies. Currently, it is assumed that the popularly used stress inversion schemes [*Angelier*, 1975; 1984; *Carey and Brunier*, 1974; *Etchecopar, et al.*, 1981; *Gephart*, 1990; *Gephart and Forsyth*, 1984; *Mercier and Carey-Gailhardis*, 1989; *Michael*, 1984; 1987] measure the spatially uniform component of the tectonic stress tensor, which we call $\boldsymbol{\sigma}'_B$ (the background stress). If the Earth also experiences a bias toward the $\dot{\boldsymbol{\sigma}}'_T$ in the presence of spatially heterogeneous stress as seen in our simulations, then this bias must be subtracted to correctly estimate $\boldsymbol{\sigma}'_B$. If the heterogeneity has too large of an amplitude, the correction may be possible, and one will not be able to determine $\boldsymbol{\sigma}'_B$. An outline of how one might begin to subtract out this $\dot{\boldsymbol{\sigma}}'_T$ bias and determine $\boldsymbol{\sigma}'_B$ is presented in Chapter 5. In any case, our simulation results imply that one must be very careful in interpreting stress inversion results, as they may be more complicated than commonly assumed.

In the real Earth, stress inversion schemes are commonly used to infer deviatoric stress information from focal mechanism orientations. In particular, the three principal deviatoric stress axes orientations are calculated along with a dimensionless quantity that relates the magnitudes of the principal stresses, the stress ratio, $R = \left(\frac{\sigma_2 - \sigma_3}{\sigma_1 - \sigma_3} \right)$ [e.g., *Rivera and Kanamori*, 2002]. In this study we are not addressing whether or not the stress inversion schemes accurately invert the given focal mechanism data. Instead, we are questioning an assumption that goes into the interpretation of the results. The implicit assumption we question is, "Focal mechanisms are a good uniform random measurement of stress in the Earth's crust." In other words, "the points which fail and produce earthquake focal mechanisms uniformly sample the actual stress field, and upon inversion, yield the spatial mean stress tensor, $\boldsymbol{\sigma}'_B$." In our simulations, we show that the interaction of the failure criterion with spatially heterogeneous stress produces a bias to which orientations and stress ratios, R, are most likely to fail, a bias toward our stress rate tensor, $\dot{\boldsymbol{\sigma}}'_T$. If this is indicative of the real Earth, then the answer to our question would be no, focal mechanism data sets are not a good uniform random sampler of stress. Not all points fail in the real Earth as earthquakes in a regional stress study, only a minute fraction. The points that are most likely to fail will be those aligned with $\dot{\boldsymbol{\sigma}}'_T$; hence, the set of focal mechanisms included in inversion studies will produce an inverted stress tensor biased toward $\dot{\boldsymbol{\sigma}}'_T$. See Figure 4.1 for a simple scalar example of bias to visually demonstrate this concept.

In Figure 4.1 we show a scalar quantity represented by the length of the vertical bars. Set A represents the entire data set and Set B is the first half of the data. The scalar

quantities have been arranged so that the larger values happen first and cluster in Set B. Because the larger values occur first, estimates of the scalar value will be biased if they use only the first half of the data set, Set B. Similarly, we ask, could the focal mechanisms used in standard stress inversions be a biased sampling of stress in the real Earth? Only a small fraction of all the possible points in a study region fail within the study window when applying stress inversions, and there is the possibility that this small subset of all possible points could have a biased average orientation. If so, interpretations of stress inversions may need to be revised. This is a difficult question to answer by observation alone, which is why we numerically investigate this problem.

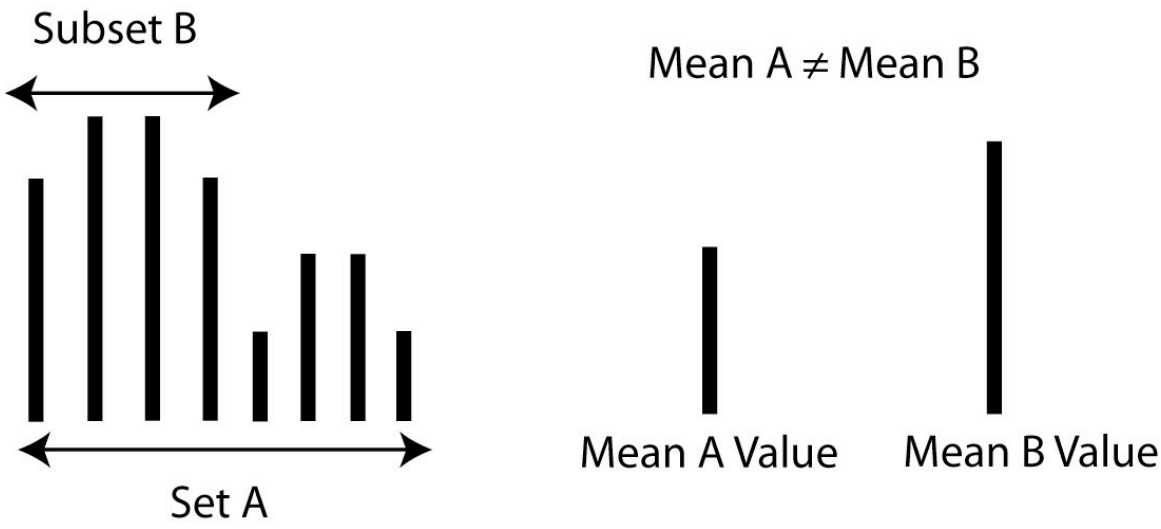

Figure 4.1. *This is a simple scalar example of bias. The entire data set is represented by Set A. The first half of the data set is represented by Set B. In this case, the larger values happen first and cluster in Set B. One cannot estimate the mean of Set A by measuring only Set B, because of the bias towards larger scalar values in Set B. Similarly, if there is a bias in which points fail as earthquakes, produce focal mechanisms, and are included in stress inversion studies, then the results of stress inversion studies may also be biased; consequently, stress inversion studies may not reflect the spatial mean stress as commonly assumed.*

Fracture Criterion Used to Produce Earthquakes—Hencky-Mises Plastic Yield

The Hencky-Mises plastic yield condition [*Housner and Vreeland*, 1965] is the preferred fracture criterion for this thesis because of its simplicity. It predicts failure when the maximum shear stress is greater than a threshold value. The measure used is an invariant quantity so this failure criterion works regardless of the coordinate system or orientation of the individual stress tensors. The coefficient of friction is essentially zero (optimally oriented planes) and pressure does not enter into the equation. (If one wishes to investigate non-zero pressures and coefficients of friction see Appendix C, Coulomb Fracture Criterion.) Last, because we are dealing with optimally oriented planes, the conjugate planes become mathematically indistinguishable. The equation for this plastic yield is

$$I_2' = \frac{2}{3}\tau_0^2 \tag{4.1}$$

[*Housner and Vreeland*, 1965] where τ_0 is the uniaxial yield stress and I_2' is the second invariant of the deviatoric stress tensor, $\boldsymbol{\sigma}'$, where

$$I_2' = \sigma_{11}'^2 + \sigma_{22}'^2 + \sigma_{33}'^2 + 2\left[\sigma_{12}'^2 + \sigma_{23}'^2 + \sigma_{13}'^2\right]. \tag{4.2}$$

At this point it is useful to introduce the tensor scalar product to aid us in our equation derivations. The scalar product of two tensors, A and B, can be defined as

$$A : B = \sum_{i=1}^{3}\sum_{j=1}^{3} A_{ij}B_{ij}. \tag{4.3}$$

In this notation the second invariant of the deviatoric stress tensor can now be written as,

$$I_2' = \boldsymbol{\sigma}' : \boldsymbol{\sigma}', \tag{4.4}$$

which is a much more compact notation.

In our simulations, we wish to determine when each individual point in the 3D grid fails; hence, we are interested in examining the failure equation for each single spatial grid point, $\mathbf{x}_i$, where $\mathbf{x}_i$ is the 3D coordinate of the *i*th point in the grid. The equation for a single point is

$$I_2'(\mathbf{x}_i,t) = \boldsymbol{\sigma}'(\mathbf{x}_i,t) : \boldsymbol{\sigma}'(\mathbf{x}_i,t). \tag{4.5}$$

It is the summation of the squared deviatoric stress matrix elements. If our deviatoric stress tensor at any point in the grid is

$$\boldsymbol{\sigma}'(\mathbf{x}_i,t) = \boldsymbol{\sigma}'_H(\mathbf{x}_i) + \boldsymbol{\sigma}'_B + \dot{\boldsymbol{\sigma}}'_T\ t \tag{4.6}$$

where $\boldsymbol{\sigma}'_H(\mathbf{x}_i)$ is the spatially heterogeneous stress, $\boldsymbol{\sigma}'_B$ is the spatially and temporally uniform background tectonic stress, and $\dot{\boldsymbol{\sigma}}'_T\ t$ is the linearly increasing secular component of tectonic stress from plate motion, then our failure criterion can be rewritten as

$$I_2'(\mathbf{x}_i,t) = \left(\boldsymbol{\sigma}'_H(\mathbf{x}_i) + \boldsymbol{\sigma}'_B + \dot{\boldsymbol{\sigma}}'_T\ t\right) : \left(\boldsymbol{\sigma}'_H(\mathbf{x}_i) + \boldsymbol{\sigma}'_B + \dot{\boldsymbol{\sigma}}'_T\ t\right). \tag{4.7}$$

Multiplying through, we have

$$\begin{aligned} I_2'(\mathbf{x}_i,t) = {} & \boldsymbol{\sigma}'_H(\mathbf{x}_i) : \boldsymbol{\sigma}'_H(\mathbf{x}_i) + \boldsymbol{\sigma}'_B : \boldsymbol{\sigma}'_B + \left(\dot{\boldsymbol{\sigma}}'_T : \dot{\boldsymbol{\sigma}}'_T\right) t^2 \\ & + 2\boldsymbol{\sigma}'_H(\mathbf{x}_i) : \boldsymbol{\sigma}'_B + 2\boldsymbol{\sigma}'_H(\mathbf{x}_i) : \dot{\boldsymbol{\sigma}}'_T\ t + 2\boldsymbol{\sigma}'_B : \dot{\boldsymbol{\sigma}}'_T\ t. \end{aligned} \tag{4.8}$$

Note that

$$\left(\boldsymbol{\sigma}'_H(\mathbf{x}_i) + \boldsymbol{\sigma}'_B\right) : \left(\boldsymbol{\sigma}'_H(\mathbf{x}_i) + \boldsymbol{\sigma}'_B\right) = \boldsymbol{\sigma}'_H(\mathbf{x}_i) : \boldsymbol{\sigma}'_H(\mathbf{x}_i) + 2\boldsymbol{\sigma}'_H(\mathbf{x}_i) : \boldsymbol{\sigma}'_B + \boldsymbol{\sigma}'_B : \boldsymbol{\sigma}'_B \tag{4.9}$$

and

$$2\left(\boldsymbol{\sigma}'_H(\mathbf{x}_i) + \boldsymbol{\sigma}'_B\right) : \dot{\boldsymbol{\sigma}}'_T\ t = 2\boldsymbol{\sigma}'_H(\mathbf{x}_i) : \dot{\boldsymbol{\sigma}}'_T\ t + 2\boldsymbol{\sigma}'_B : \dot{\boldsymbol{\sigma}}'_T\ t. \tag{4.10}$$

Therefore, we can rewrite our second invariant as

$$I_2'(\mathbf{x}_i,t) = \left(\boldsymbol{\sigma}_H'(\mathbf{x}_i) + \boldsymbol{\sigma}_B'\right) : \left(\boldsymbol{\sigma}_H'(\mathbf{x}_i) + \boldsymbol{\sigma}_B'\right) + \left(\dot{\boldsymbol{\sigma}}_T' : \dot{\boldsymbol{\sigma}}_T'\right)t^2 + 2\left(\boldsymbol{\sigma}_H'(\mathbf{x}_i) + \boldsymbol{\sigma}_B'\right) : \dot{\boldsymbol{\sigma}}_T'\ t. \tag{4.11}$$

Interestingly, the first term is simply the second invariant of the deviatoric stress tensor at time $t = 0$. This means we can write our equation as

$$I_2'(\mathbf{x}_i,t) = I_2'(\mathbf{x}_i,0) + \left(\dot{\boldsymbol{\sigma}}_T' : \dot{\boldsymbol{\sigma}}_T'\right)t^2 + 2\left(\boldsymbol{\sigma}_H'(\mathbf{x}_i) + \boldsymbol{\sigma}_B'\right) : \dot{\boldsymbol{\sigma}}_T'\ t \tag{4.12}$$

where

$$I_2'(\mathbf{x}_i,0) = \left(\boldsymbol{\sigma}_H'(\mathbf{x}_i) + \boldsymbol{\sigma}_B'\right) : \left(\boldsymbol{\sigma}_H'(\mathbf{x}_i) + \boldsymbol{\sigma}_B'\right). \tag{4.13}$$

We now ask, at what time, t_F, does $I_2' = \frac{2}{3}\tau_0^2$, for each point $\mathbf{x}_i$, where t_F is the time of failure? To address this question conceptually, we can divide $I_2'(\mathbf{x}_i,t)$ into three components,

$$I_2'(\mathbf{x}_i,t) = I_2'(\mathbf{x}_i,0) + \frac{dI_2'(\mathbf{x}_i,t)}{dt}t - \left(\dot{\boldsymbol{\sigma}}_T' : \dot{\boldsymbol{\sigma}}_T'\right)t^2 \tag{4.14}$$

where

$$\frac{dI_2'(\mathbf{x}_i,t)}{dt} = 2\left(\dot{\boldsymbol{\sigma}}_T' : \dot{\boldsymbol{\sigma}}_T'\right)t + 2\left(\boldsymbol{\sigma}_H'(\mathbf{x}_i) + \boldsymbol{\sigma}_B'\right) : \dot{\boldsymbol{\sigma}}_T'. \tag{4.15}$$

For small stressing rates, $\dot{\boldsymbol{\sigma}}_T'$, and small times, t (which will be true for the simulations shown), all the $\left(\dot{\boldsymbol{\sigma}}_T' : \dot{\boldsymbol{\sigma}}_T'\right)t$ terms are ≈ 0.

Therefore, we have two main terms,

$$I_2'(\mathbf{x}_i,t) \approx I_2'(\mathbf{x}_i,0) + \frac{dI_2'(\mathbf{x}_i,t)}{dt}t \tag{4.16}$$

where

$$I_2'(\mathbf{x}_i,0) = \left(\boldsymbol{\sigma}_H'(\mathbf{x}_i) + \boldsymbol{\sigma}_B'\right) : \left(\boldsymbol{\sigma}_H'(\mathbf{x}_i) + \boldsymbol{\sigma}_B'\right) \tag{4.17}$$

and

$$\frac{dI_2'(\mathbf{x}_i,t)}{dt} \approx 2\left(\boldsymbol{\sigma}_H'(\mathbf{x}_i) + \boldsymbol{\sigma}_B'\right) : \dot{\boldsymbol{\sigma}}_T'. \tag{4.18}$$

The first term of equation (4.16), $I_2'(\mathbf{x}_i,0)$, shows the state of the system at $t = 0$ and the heterogeneity of the system. The second term, $\frac{dI_2'(\mathbf{x}_i,t)}{dt}$, describes how quickly points are either increasing or decreasing their maximum deviatoric shear stress. For a point to fail quickly, it generally needs to satisfy the following three criteria.

- $I_2'(\mathbf{x}_i,0) < \frac{2}{3}\tau_0^2$. In other words, the point $\mathbf{x}_i$, at $t = 0$, must have an I_2' less than the the failure threshold of $\frac{2}{3}\tau_0^2$, to be considered in the simulation. We find that the placement of the failure threshold, $\frac{2}{3}\tau_0^2$, determines what part of the heterogeneity we sample; i.e., do we place $\frac{2}{3}\tau_0^2$ above the maximum $I_2'(\mathbf{x}_i,0)$ and sample extreme outliers that would have already plastically yielded, or do we place the failure threshold at the 1.5–2.0 standard deviation level within $I_2'(\mathbf{x}_i,0)$ and exclude the top 5–15% of the points as outliers?

- $\dfrac{\frac{2}{3}\tau_0^2 - I_2'(\mathbf{x}_i,0)}{\frac{2}{3}\tau_0^2} \ll 1$. For a point $\mathbf{x}_i$ to fail quickly and be considered in the first 2,000 failures of the simulations, it needs to start with a value of $I_2'(\mathbf{x}_i,0)$ quite close to the failure threshold, $\frac{2}{3}\tau_0^2$, at $t = 0$.

- $\dfrac{dI_2'(\mathbf{x}_i,t)}{dt} > 0$, and preferably maximized. The time derivative of $I_2'(\mathbf{x}_i,t)$ must be greater than zero if there is to be any failure at all. If $I_2'(\mathbf{x}_i,0) < \frac{2}{3}\tau_0^2$ and $\dfrac{dI_2'(\mathbf{x}_i,t)}{dt} > 0$ then the point $\mathbf{x}_i$ is progressing toward the failure threshold $\frac{2}{3}\tau_0^2$. If $I_2'(\mathbf{x}_i,0) < \frac{2}{3}\tau_0^2$ and $\dfrac{dI_2'(\mathbf{x}_i,t)}{dt} < 0$ the point $\mathbf{x}_i$ is moving further away from the failure threshold $\frac{2}{3}\tau_0^2$. Obviously, the larger the positive rate of change, $\dfrac{dI_2'(\mathbf{x}_i,t)}{dt}$, the more quickly $\mathbf{x}_i$ progesses toward failure.

Placement of the Failure Threshold

We opt to normalize $I_2'(\mathbf{x}_i,0)$ so that the failure threshold $\frac{2}{3}\tau_0^2$ falls somewhat below the maximum $I_2'(\mathbf{x}_i,0)$ value to avoid outliers for several reasons: 1) The points with largest values of $I_2'(\mathbf{x}_i,0)$ would already have plastically failed. 2) Sampling the extreme outliers in the simulations results in non-steady earthquake rates. There are very few events at first, as one samples the extreme outliers, then the rate rapidly accelerates

as one begins to sample the rest of the heterogeneity. Normalizing $I_2'(\mathbf{x}_i,0)$ so that $\frac{2}{3}\tau_0^2$ falls at 1.5 or 2.0 standard deviations produces relatively constant earthquake rates over 4 orders of magnitude in time. 3) The distribution of tensors present in the family of heterogeneous stress tensors, $\boldsymbol{\sigma}_H'(\mathbf{x}_i)$, with values of $I_2'(\mathbf{x}_i,0)$ close to the failure threshold, $\frac{2}{3}\tau_0^2$, partially depends on where the failure threshold falls within the $I_2'(\mathbf{x}_i,0)$ distribution. If $\frac{2}{3}\tau_0^2$ = *Maximum* $I_2'(\mathbf{x}_i,0)$, then all the points close to $\frac{2}{3}\tau_0^2$ will have $\boldsymbol{\sigma}_H'(\mathbf{x}_i) \approx \boldsymbol{\sigma}_B'$. If $\frac{2}{3}\tau_0^2$ falls at the 1.5 or 2.0 standard deviation level for $I_2'(\mathbf{x}_i,0)$ (i.e. excluding the top ~ 15% or ~ 5% points in $I_2'(\mathbf{x}_i,0)$ respectively), there is still bias toward $\boldsymbol{\sigma}_B'$, but there is generally a greater variety of $\boldsymbol{\sigma}_H'(\mathbf{x}_i)$ that produce $\frac{\frac{2}{3}\tau_0^2 - I_2'(\mathbf{x}_i,0)}{\frac{2}{3}\tau_0^2} \ll 1$. If $\frac{2}{3}\tau_0^2$ falls at the 1.5 standard deviations level for $I_2'(\mathbf{x}_i,0)$ or less, we start throwing out too many points associated with the $\boldsymbol{\sigma}_B'$ orientation, and a hole appears right at the $\boldsymbol{\sigma}_B'$ orientation in our P-T plots.

On the other hand, if $I_2'(\mathbf{x}_i,0)$ is normalized so that $\frac{2}{3}\tau_0^2$ falls at the 2.0 standard deviation level for $I_2'(\mathbf{x}_i,0)$, with 95% of the points in $I_2'(\mathbf{x}_i,0)$ below the failure threshold, we find a satisfactory tradeoff. Simulations with this normalization of $I_2'(\mathbf{x}_i,0)$ have fairly steady earthquake rates over several orders of magnitude in time and still provide a good variety of $\boldsymbol{\sigma}_H'(\mathbf{x}_i)$ close to and aligned with $\boldsymbol{\sigma}_B'$.

Plots of $I_2'(x_i,0)$ with units of $\left[Stress^2\right]$ and the failure threshold, $\frac{2}{3}\tau_0^2$, in 1D are shown in Figure 4.2 for four different values of spatial smoothing, $\alpha = 0.0, 0.5, 1.0,$ and 1.5. Within each plot, $I_2'(x_i,0)$ is shown for three different values of the Heterogeneity Ratio, $HR = \frac{\sqrt{Mean\left[\ \boldsymbol{\sigma}'_H(\mathbf{x}_i) : \boldsymbol{\sigma}'_H(\mathbf{x}_i)\right]}}{\sqrt{\boldsymbol{\sigma}'_B : \boldsymbol{\sigma}'_B}}$, where $\boldsymbol{\sigma}'_H(\mathbf{x}_i) : \boldsymbol{\sigma}'_H(\mathbf{x}_i)$ is the second invariant of the heterogeneous stress tensor, $\boldsymbol{\sigma}'_H(\mathbf{x}_i)$, and $\boldsymbol{\sigma}'_B : \boldsymbol{\sigma}'_B$ is the second invariant of the spatially homogeneous, background stress tensor, $\boldsymbol{\sigma}'_B$. In order of increasing heterogeneity amplitude, we have $HR = 0.1$ plotted in red, $HR = 0.3$ plotted in green, and $HR = 1.0$ plotted in blue. They have been normalized so that 95% of the points fall below the same failure threshold level, $\frac{2}{3}\tau_0^2$, the $I_2'(x_i,0)$ 2.0 standard deviation level. $\frac{2}{3}\tau_0^2$ is plotted with the thick, horizontal, dashed, black line. The main points we wish to show are simply that 1) as HR increases, the heterogeneous amplitude $I_2'(x_i,0)$ increases, 2) as α increases, the spatial smoothing of $I_2'(x_i,0)$ increases.

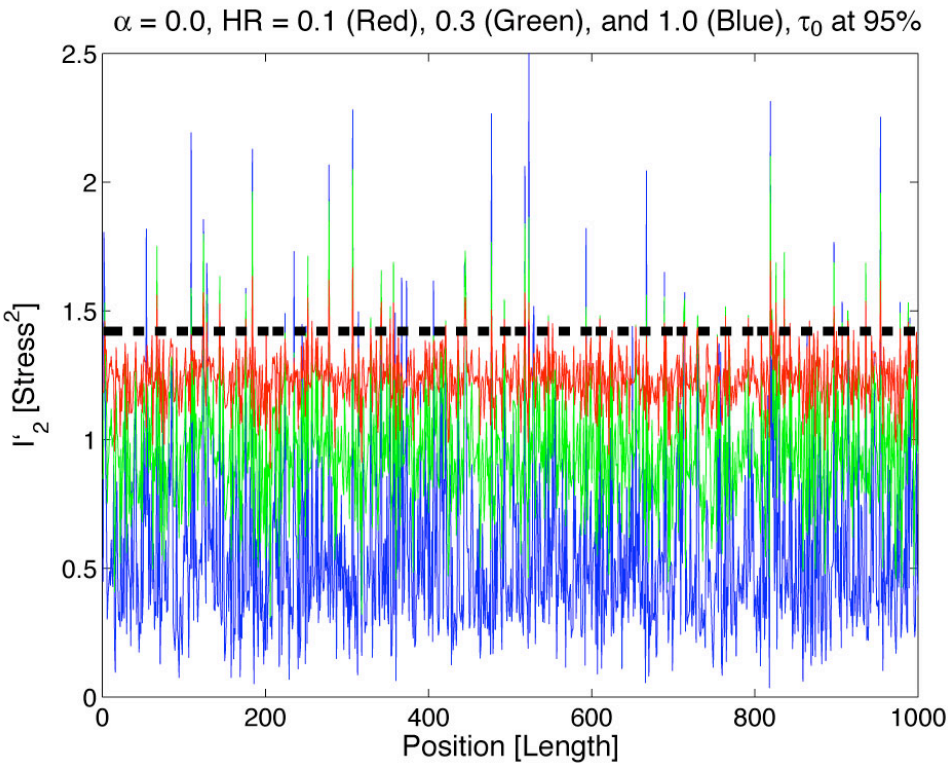

Figure 4.2 a)

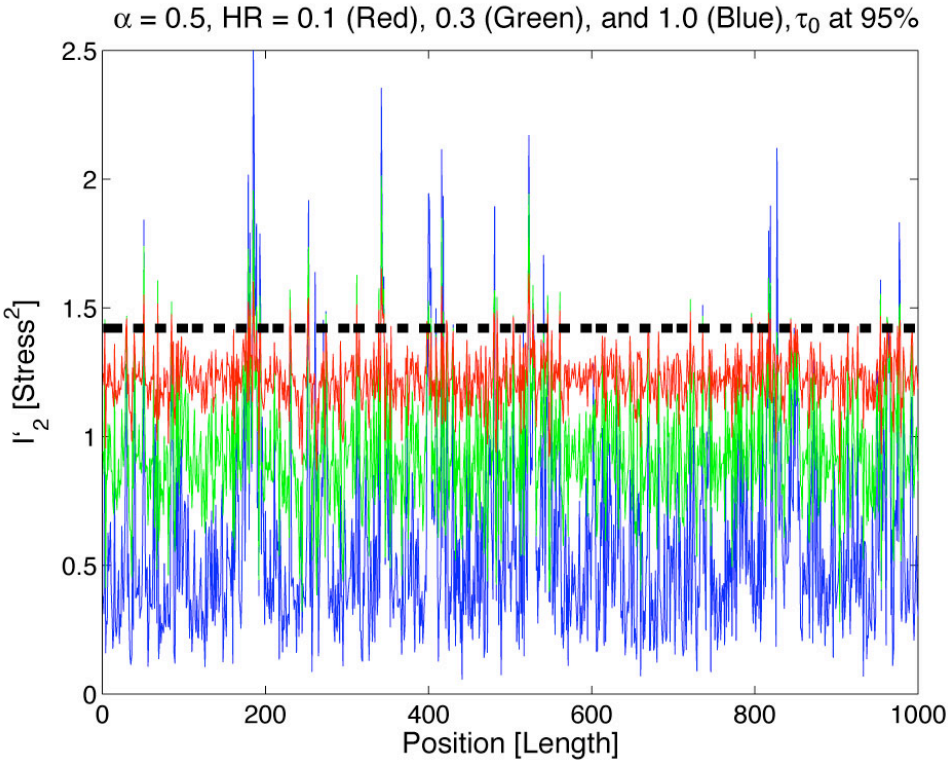

Figure 4.2 b)

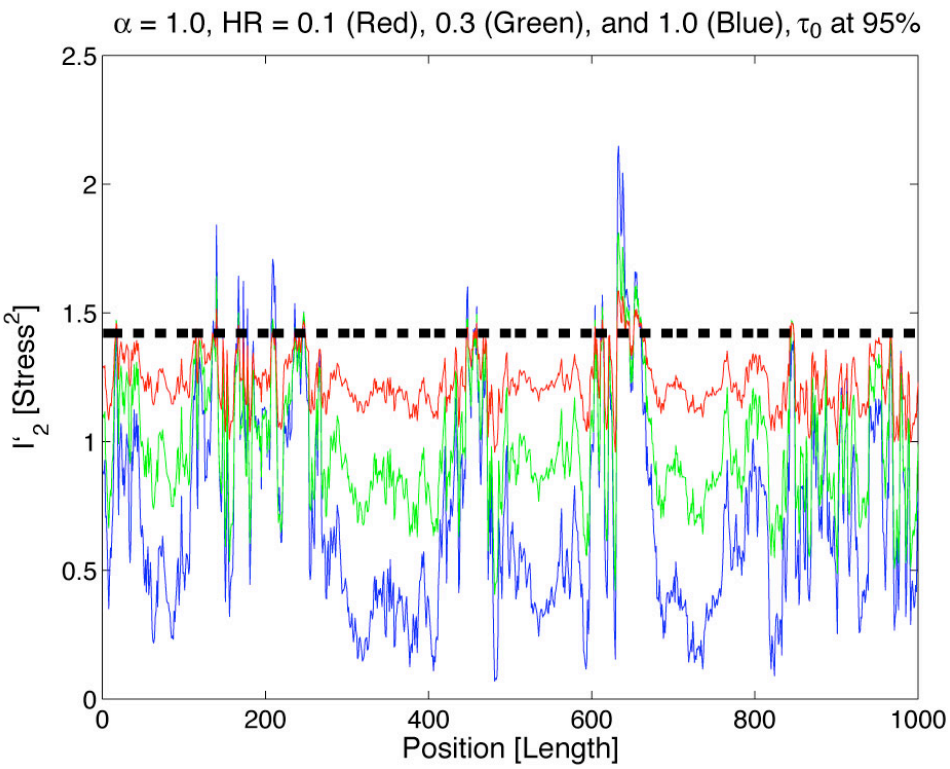

Figure 4.2 c)

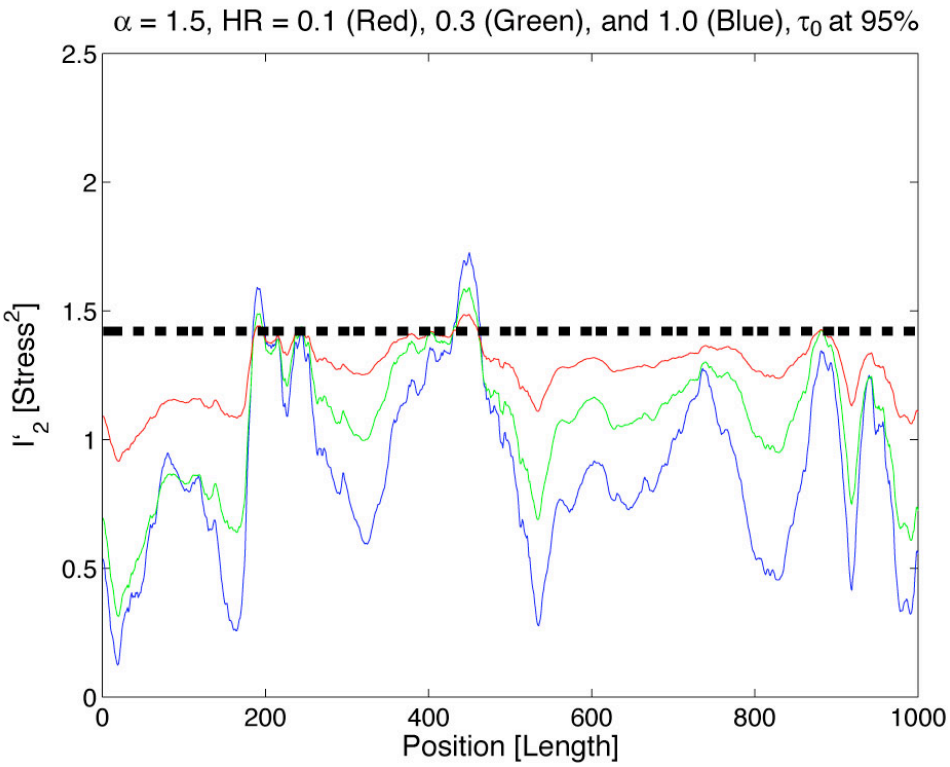

Figure 4.2 d)

Figure 4.2. *Plots of* $I_2'(x_i,0)$ *for 1,001 points in 1D, to show what the maximum shear stress looks like at* $t=0.0$. *To create* $I_2'(x_i,0)$, *we generate* $\boldsymbol{\sigma}'_H(x_i)$ *with different levels of spatial filtering,* ***a)*** $\alpha=0.0$, ***b)*** $\alpha=0.5$, ***c)*** $\alpha=1.0$, *and* ***d)*** $\alpha=1.5$, *and add it component-wise to a background stress tensor,* $\boldsymbol{\sigma}'_B$, *using three different heterogeneous amplitudes within each plot. Within each plot, we have* $HR=0.1$ *in red,* $HR=0.3$ *in green, and* $HR=1.0$ *in blue.* $I_2'(x_i,0)$ *is normalized so that the failure threshold,* $\frac{2}{3}\tau_0^2$, *the thick, dashed, black line, falls at the 2.0 standard deviation level of* $I_2'(x_i,0)$ *values. This means approximately 95% of the values of* $I_2'(x_i,0)$ *are below* $\frac{2}{3}\tau_0^2$. *Any points below* $\frac{2}{3}\tau_0^2$ *can be counted as failures in the simulation, and any points above* $\frac{2}{3}\tau_0^2$ *at time* $t=0$ *are considered outliers that have previously plastically failed. The points that are most likely to fail first are those that have* $I_2'(x_i,0)$ *close to the failure threshold,* $\frac{2}{3}\tau_0^2$, *i.e.,* $\frac{\frac{2}{3}\tau_0^2 - I_2'(\mathbf{x}_i,0)}{\frac{2}{3}\tau_0^2} \ll 1$, *and are quickly moving toward failure, i.e.,* $\frac{dI_2'(\mathbf{x}_i,t)}{dt}$ *large and positive.*

Why the Most Likely Points to Fail Are Biased Toward $\dot{\boldsymbol{\sigma}}'_T$, When the Heterogeneity Ratio, *HR*, Is Large

To understand why we have an increasing bias toward $\dot{\boldsymbol{\sigma}}'_T$ as the heterogeneous ratio, HR (a measure of the heterogeneity amplitude), increases, we once more look at equation (4.16), $I'_2(\mathbf{x}_i,t) \approx I'_2(\mathbf{x}_i,0) + \dfrac{dI'_2(\mathbf{x}_i,t)}{dt}t$. We rewrite the first and second terms. The first term on the right hand side, $I'_2(\mathbf{x}_i,0)$, which describes the initial stress state, can be rewritten as

$$I'_2(x_i,0) = \boldsymbol{\sigma}'_H(\mathbf{x}_i) : \boldsymbol{\sigma}'_H(\mathbf{x}_i) + 2\boldsymbol{\sigma}'_H(\mathbf{x}_i) : \boldsymbol{\sigma}'_B + \boldsymbol{\sigma}'_B : \boldsymbol{\sigma}'_B \tag{4.19}$$

or

$$I'_2(x_i,0) = \boldsymbol{\sigma}'_H(\mathbf{x}_i) : \boldsymbol{\sigma}'_H(\mathbf{x}_i) + 2\boldsymbol{\sigma}'_H(\mathbf{x}_i) : \boldsymbol{\sigma}'_B + C_0 \tag{4.20}$$

where the constant

$$C_0 = \boldsymbol{\sigma}'_B : \boldsymbol{\sigma}'_B. \tag{4.21}$$

The second term on the right hand side of equation (4.16), $\dfrac{dI'_2(\mathbf{x}_i,t)}{dt}$, which describes whether or not the points are going toward failure, can be rewritten as,

$$\frac{dI'_2(\mathbf{x}_i,t)}{dt} \approx 2\boldsymbol{\sigma}'_H(\mathbf{x}_i) : \dot{\boldsymbol{\sigma}}'_T + 2\boldsymbol{\sigma}'_B : \dot{\boldsymbol{\sigma}}'_T \tag{4.22}$$

or

$$\frac{dI'_2(\mathbf{x}_i,t)}{dt} \approx 2\boldsymbol{\sigma}'_H(\mathbf{x}_i) : \dot{\boldsymbol{\sigma}}'_T + C_1 \tag{4.23}$$

where the constant is

$$C_1 = 2\boldsymbol{\sigma}'_B : \dot{\boldsymbol{\sigma}}'_T. \tag{4.24}$$

Since C_1 is a constant, it has the same value at every point $\mathbf{x}_i$ and C_1 simply determines when $\frac{dI_2'(\mathbf{x}_i,t)}{dt} > 0$. For example, if $\dot{\boldsymbol{\sigma}}_T' = -c\,\boldsymbol{\sigma}_B'$, where c is a constant, we will have $C_1 < 0$, and a number of points will now go away from failure instead of toward it. If the heterogeneity is sufficiently small, $HR << 1$, and $C_1 < 0$, we may find there are no failures right away. Determining the set of points that have $\frac{dI_2'(\mathbf{x}_i,t)}{dt} > 0$ is the main effect of C_1, but because it is a constant, we can ignore it when assessing which points are more likely to fail than others; instead, we need to primarily look at the terms that are a function of $\mathbf{x}_i$, to determine why the failures are biased toward $\dot{\boldsymbol{\sigma}}_T'$.

The term that is a function of $\mathbf{x}_i$ in $\frac{dI_2'(\mathbf{x}_i,t)}{dt}$ is $2\boldsymbol{\sigma}_H'(\mathbf{x}_i) : \dot{\boldsymbol{\sigma}}_T'$. Because it involves component-wise cross-terms of the heterogeneous stress tensor, $\boldsymbol{\sigma}_H'(\mathbf{x}_i)$, and the stress rate tensor, $\dot{\boldsymbol{\sigma}}_T'$, we predict that the points that have the largest, positive $\frac{dI_2'(\mathbf{x}_i,t)}{dt}$ will be those where $\boldsymbol{\sigma}_H'(\mathbf{x}_i)$ is on average aligned component-wise with $\dot{\boldsymbol{\sigma}}_T'$.

What about $I_2'(x_i,0)$? How does this affect which points are most likely to fail? Examining equations (4.20) and (4.21), we see that the value of the constant C_0 simply raises or lowers all the points in $I_2'(x_i,0)$; it has no bearing on which points are most likely to fail, because we normalize the overall size of $I_2'(x_i,0)$, so that the 95% level is at the failure threshold, $\frac{2}{3}\tau_0^2$. Now the other two terms in equation (4.20) are more interesting because they do have different values as a function of $\mathbf{x}_i$. $2\boldsymbol{\sigma}_H'(\mathbf{x}_i) : \boldsymbol{\sigma}_B'$

involves component-wise cross terms between the heterogeneous stress, $\boldsymbol{\sigma}'_H(\mathbf{x}_i)$, and the background stress, $\boldsymbol{\sigma}'_B$; therefore, this term will tend to promote points with $\boldsymbol{\sigma}'_H(\mathbf{x}_i)$ on average aligned with $\boldsymbol{\sigma}'_B$ to be near the failure threshold. However, there is one more term to consider, $\boldsymbol{\sigma}'_H(\mathbf{x}_i):\boldsymbol{\sigma}'_H(\mathbf{x}_i)$, which is simply the second invariant of $\boldsymbol{\sigma}'_H(\mathbf{x}_i)$. $\boldsymbol{\sigma}'_H(\mathbf{x}_i):\boldsymbol{\sigma}'_H(\mathbf{x}_i)$ promotes points to be near the failure criterion if the overall size of $\boldsymbol{\sigma}'_H(\mathbf{x}_i)$ is large irrespective of orientation. Consequently, if $\boldsymbol{\sigma}'_H(\mathbf{x}_i):\boldsymbol{\sigma}'_H(\mathbf{x}_i) >> 2\boldsymbol{\sigma}'_H(\mathbf{x}_i):\boldsymbol{\sigma}'_B$, then there will be little to no bias to which $\boldsymbol{\sigma}'_H(\mathbf{x}_i)$ orientations are close to the threshold, and the $2\boldsymbol{\sigma}'_H(\mathbf{x}_i):\dot{\boldsymbol{\sigma}}'_T$ term will primarily choose points to fail where $\boldsymbol{\sigma}'_H(\mathbf{x}_i)$ is on average aligned with $\dot{\boldsymbol{\sigma}}'_T$. Now if $\boldsymbol{\sigma}'_H(\mathbf{x}_i):\boldsymbol{\sigma}'_H(\mathbf{x}_i) << 2\boldsymbol{\sigma}'_H(\mathbf{x}_i):\boldsymbol{\sigma}'_B$, we expect the bias in $\boldsymbol{\sigma}'_H(\mathbf{x}_i)$ toward $\boldsymbol{\sigma}'_B$ to be significant for points near the failure threshold.

Another way to quantify this is in terms of the Heterogeneity Ratio, $HR = \dfrac{\sqrt{Mean\left[\ \boldsymbol{\sigma}'_H(\mathbf{x}_i):\boldsymbol{\sigma}'_H(\mathbf{x}_i)\right]}}{\sqrt{\boldsymbol{\sigma}'_B:\boldsymbol{\sigma}'_B}}$, where if $HR << 1$, $\boldsymbol{\sigma}'_H(\mathbf{x}_i):\boldsymbol{\sigma}'_H(\mathbf{x}_i) << 2\boldsymbol{\sigma}'_H(\mathbf{x}_i):\boldsymbol{\sigma}'_B$, and the $\boldsymbol{\sigma}'_{H_{Failure}}\left(\mathbf{x}_{i_{Failure}}\right)$ (the heterogeneous stress of those points that fail) will be biased toward the $\boldsymbol{\sigma}'_B$. As HR increases, $\boldsymbol{\sigma}'_{H_{Failure}}\left(\mathbf{x}_{i_{Failure}}\right)$ will be decreasingly biased toward $\boldsymbol{\sigma}'_B$ and increasingly biased toward $\dot{\boldsymbol{\sigma}}'_T$, until as $HR >> 1$, $\boldsymbol{\sigma}'_H(\mathbf{x}_i):\boldsymbol{\sigma}'_H(\mathbf{x}_i) >> 2\boldsymbol{\sigma}'_H(\mathbf{x}_i):\boldsymbol{\sigma}'_B$, and $\bar{\boldsymbol{\sigma}}'_{H_{Failure}}\left(\mathbf{x}_{i_{Failure}}\right) \approx \dot{\boldsymbol{\sigma}}'_T$.

Now that we have examined how the failure criterion, $I'_2(\mathbf{x}_i,t) = \dfrac{2}{3}\tau_0^2$, affects the selection of $\boldsymbol{\sigma}'_{H_{Failure}}\left(\mathbf{x}_{i_{Failure}}\right)$, biasing it toward $\boldsymbol{\sigma}'_B$ for $HR << 1$ and toward $\dot{\boldsymbol{\sigma}}'_T$ for

$HR >> 1$, keep in mind that the final stress tensor at failure is a summation of three terms, $\boldsymbol{\sigma}'_{Failure}\left(\mathbf{x}_{i_{Failure}}, t_{Failure}\right) = \boldsymbol{\sigma}'_{H_{Failure}}\left(\mathbf{x}_{i_{Failure}}\right) + \boldsymbol{\sigma}'_B + \dot{\boldsymbol{\sigma}}'_T \; t$. For small, $\dot{\boldsymbol{\sigma}}'_T \; t$, the orientation of our failure stress tensors are primarily a tradeoff between $\boldsymbol{\sigma}'_{H_{Failure}}\left(\mathbf{x}_{i_{Failure}}\right)$ and $\boldsymbol{\sigma}'_B$. If $HR << 1$, $\boldsymbol{\sigma}'_{Failure}\left(\mathbf{x}_{i_{Failure}}, t_{Failure}\right) \approx \boldsymbol{\sigma}'_B$, and if $HR >> 1$, $\boldsymbol{\sigma}'_{Failure}\left(\mathbf{x}_{i_{Failure}}, t_{Failure}\right) \approx \boldsymbol{\sigma}'_{H_{Failure}}\left(\mathbf{x}_{i_{Failure}}\right)$.

In summary:

- If $HR << 1$
  - $\bar{\boldsymbol{\sigma}}'_{H_{Failure}}\left(\mathbf{x}_{i_{Failure}}\right)$ biased toward $\boldsymbol{\sigma}'_B$.
  - $\boldsymbol{\sigma}'_{Failure}\left(\mathbf{x}_{i_{Failure}}, t_{Failure}\right) \approx \boldsymbol{\sigma}'_B$
- If $HR >> 1$
  - $\bar{\boldsymbol{\sigma}}'_{H_{Failure}}\left(\mathbf{x}_{i_{Failure}}\right) \approx \dot{\boldsymbol{\sigma}}'_T$
  - $\boldsymbol{\sigma}'_{Failure}\left(\mathbf{x}_{i_{Failure}}, t_{Failure}\right) \approx \boldsymbol{\sigma}'_{H_{Failure}}\left(\mathbf{x}_{i_{Failure}}\right)$
  - $\bar{\boldsymbol{\sigma}}'_{Failure}\left(\mathbf{x}_{i_{Failure}}, t_{Failure}\right) \approx \dot{\boldsymbol{\sigma}}'_T$
- As HR increases
  - $\bar{\boldsymbol{\sigma}}'_{H_{Failure}}\left(\mathbf{x}_{i_{Failure}}\right)$ becomes increasingly biased toward $\dot{\boldsymbol{\sigma}}'_T$ instead of $\boldsymbol{\sigma}'_B$
  - $\boldsymbol{\sigma}'_{H_{Failure}}\left(\mathbf{x}_{i_{Failure}}\right)$ becomes increasingly important in the $\boldsymbol{\sigma}'_{Failure}\left(\mathbf{x}_{i_{Failure}}, t_{Failure}\right)$ equation.
  - Therefore, $\bar{\boldsymbol{\sigma}}'_{Failure}\left(\mathbf{x}_{i_{Failure}}, t_{Failure}\right)$ rotates from $\boldsymbol{\sigma}'_B$ to $\dot{\boldsymbol{\sigma}}'_T$.
  - And the heterogeneity of $\boldsymbol{\sigma}'_{Failure}\left(\mathbf{x}_{i_{Failure}}, t_{Failure}\right)$ increases.

Demonstration of the Bias Toward $\dot{\boldsymbol{\sigma}}'_T$ as Heterogeneity Increases: Simulations of the San Gabriel Mountains and the Southern San Andreas Fault Zone

In this section we simulate two different regions, the San Gabriel Mountains, Region #1, and the Southern San Andreas Fault Zones, Region #2, which we assume to have different background stresses, $\boldsymbol{\sigma}'_{B1}$ and $\boldsymbol{\sigma}'_{B2}$ (Figures 4.3 and 4.4). The same stress rate is applied, $\dot{\boldsymbol{\sigma}}'_T$, which is simply oriented $45°$ relative to the major plate boundary, the San Andreas Fault (Figure 4.5, bottom). As spatial heterogeneity increases, the simulations rotate from their respective background orientations ($\boldsymbol{\sigma}'_{B1}$ and $\boldsymbol{\sigma}'_{B2}$) to the stress rate orientation, $\dot{\boldsymbol{\sigma}}'_T$ (Figure 4.5). We run a series of simulations for each region with 32 different heterogeneity ratios, HR, spanning $0.1 \le HR \le 100$ and for $\alpha = 0.0, 0.5, 1.0,$ and 1.5. We save the first 2,000 failures as our synthetic focal mechanisms, $\boldsymbol{\sigma}'_{Failure}\left(\mathbf{x}_{i_{Failure}}, t_{Failure}\right)$. Indeed, as HR increases, $\bar{\boldsymbol{\sigma}}'_{Failure}\left(\mathbf{x}_{i_{Failure}}, t_{Failure}\right)$ rotates from $\boldsymbol{\sigma}'_B$ to $\dot{\boldsymbol{\sigma}}'_T$ and the heterogeneity of $\boldsymbol{\sigma}'_{Failure}\left(\mathbf{x}_{i_{Failure}}, t_{Failure}\right)$ increases as seen in P-T plots of $\boldsymbol{\sigma}'_{Failure}\left(\mathbf{x}_{i_{Failure}}, t_{Failure}\right)$ (Figures 4.6–4.7). Figure 4.8 is interesting because it visually displays that the simulation failures tend to occur at the intersection of $\dfrac{dI'_2(\mathbf{x}_i, t)}{dt} > 0$ and $\dfrac{\frac{2}{3}\tau_0^2 - I'_2(\mathbf{x}_i, 0)}{\frac{2}{3}\tau_0^2} \le 5\%$ (the top 5% of the points close to the failure threshold), per our previous discussion.

One detail we need to emphasize is that since we are using a plastic yield criterion in this chapter, similar to Coulomb Failure with $\mu = 0.0$, failures occurs on maximally

orientated planes, ± 45° from the σ_1 and σ_3 axes. This means that the P axis is aligned with the σ_1 principal stress, and the T axis is aligned with the σ_3 principal stress. Generally, the P and T axes are not aligned with the principal stresses, as in the case of Coulomb Failure with $\mu > 0.0$. Appendix A explains the mathematics behind this. For this chapter, however, we use the special case of maximally oriented planes, which have P and T axes aligned with σ_1 and σ_3 respectively.

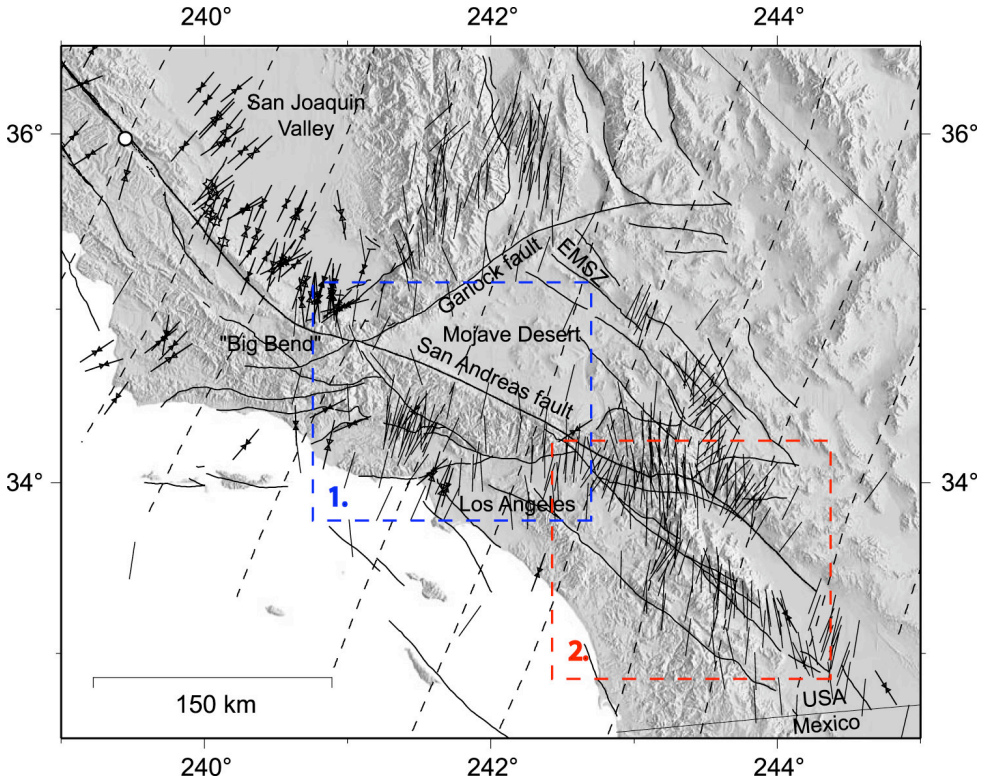

Figure 4.3. *Figure modified from Townend and Zoback [2004]. The dashed box with the #1 is magnified in Figure 4.4 a) to zoom in on the San Gabriel Mountains, our Region #1. The dashed red box with the #2 is magnified in Figure 4.4 b) to zoom in on the Southern San Andreas Fault, our Region #2. The orientations of maximum compressive stress in the Townend and Zoback figure are calculated using earthquake focal mechanism inversions, borehole breakouts, and hydraulic fracturing.*

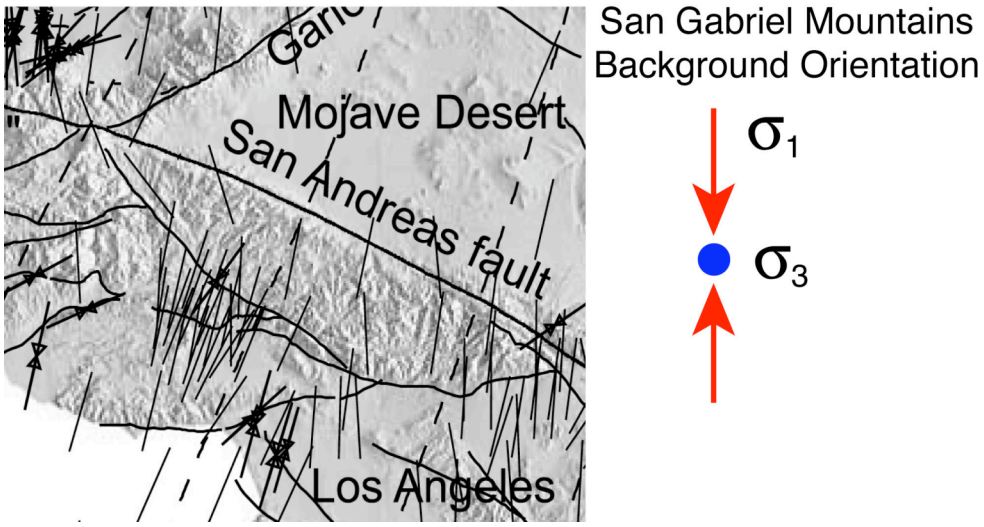

a)

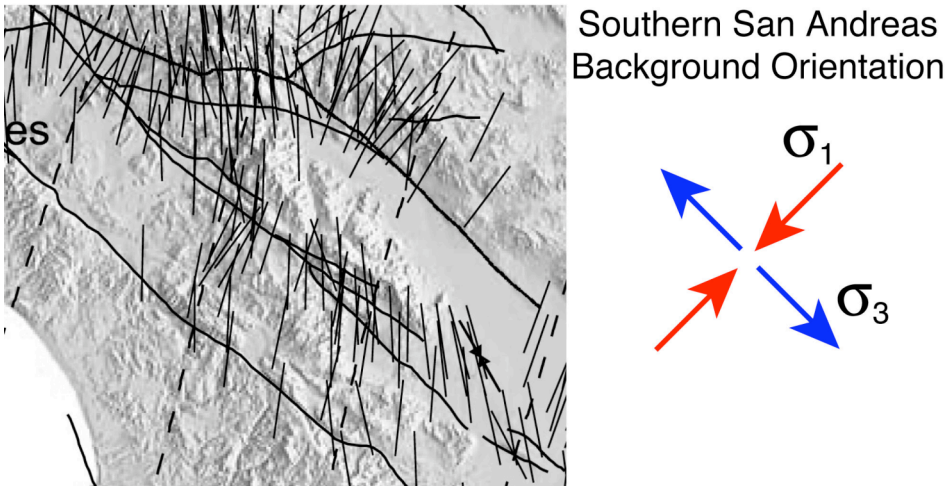

b)

Figure 4.4. *a) is a magnified inset from Figure 4.3. The diagram to the right shows the stress orientation we use for the San Gabriel Mountains background stress,* $\boldsymbol{\sigma}'_{B1}$. *We also have drawn the* σ_1 *and* σ_3 *axes next to the inset, where the inward pointing, red arrows indicate a* $N-S$ *direction of the principal compression axis, and the small blue circle indicates a vertical direction of the principal tension axis. In b) we have the second magnified inset from Figure 4.3. The diagram to the right shows the stress orientation used for our Southern San Andreas simulations background stress,* $\boldsymbol{\sigma}'_{B2}$, *with a principal compressive stress direction (red arrows) almost perpendicular to the fault.*

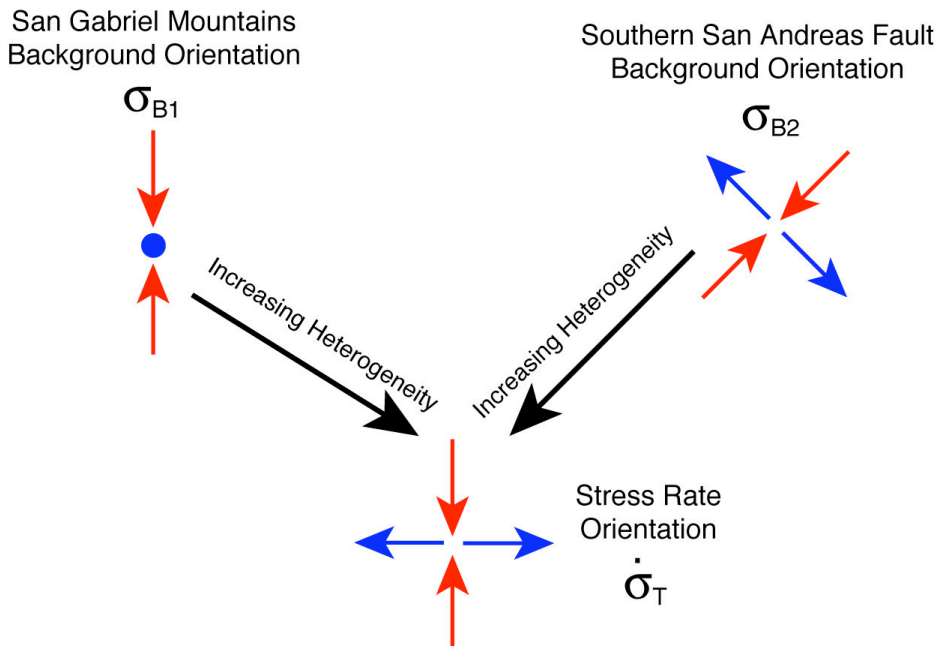

Figure 4.5. *The inward pointing red arrows for* $\boldsymbol{\sigma}_{B1}$, $\boldsymbol{\sigma}_{B2}$, *and* $\dot{\boldsymbol{\sigma}}_T$ *show the directions of their respective* σ_1 *axes. The outward pointing blue arrows for* $\boldsymbol{\sigma}_{B2}$ *and* $\dot{\boldsymbol{\sigma}}_T$ *and the upward/downward blue arrow represented by the blue circle for* $\boldsymbol{\sigma}_{B1}$ *show the directions of their respective* σ_3 *axes. As the amplitude of spatial heterogeneity,* HR, *increases, the simulation stress tensors (component-wise average of the first 2,000 points that fail in our 3D grid) increasingly rotate from the background stress to the stress rate,* $\dot{\boldsymbol{\sigma}}'_T$. *Even though our two regions, the San Gabriel Mountains and the Southern San Andreas Fault, have very different background stresses, as* HR *increases, the simulations for the two regions will become increasing similar until for* $HR \gg 1$ *they will be indistinguishable from one another and will have an average failure stress tensor,* $\bar{\boldsymbol{\sigma}}'_{Failure}\left(\mathbf{x}_{i_{Failure}}, t_{Failure}\right)$, *aligned with stress rate,* $\dot{\boldsymbol{\sigma}}'_T$. *Figures 4.6–4.7 demonstrate this effect with P-T plots of simulations for different values of* HR.

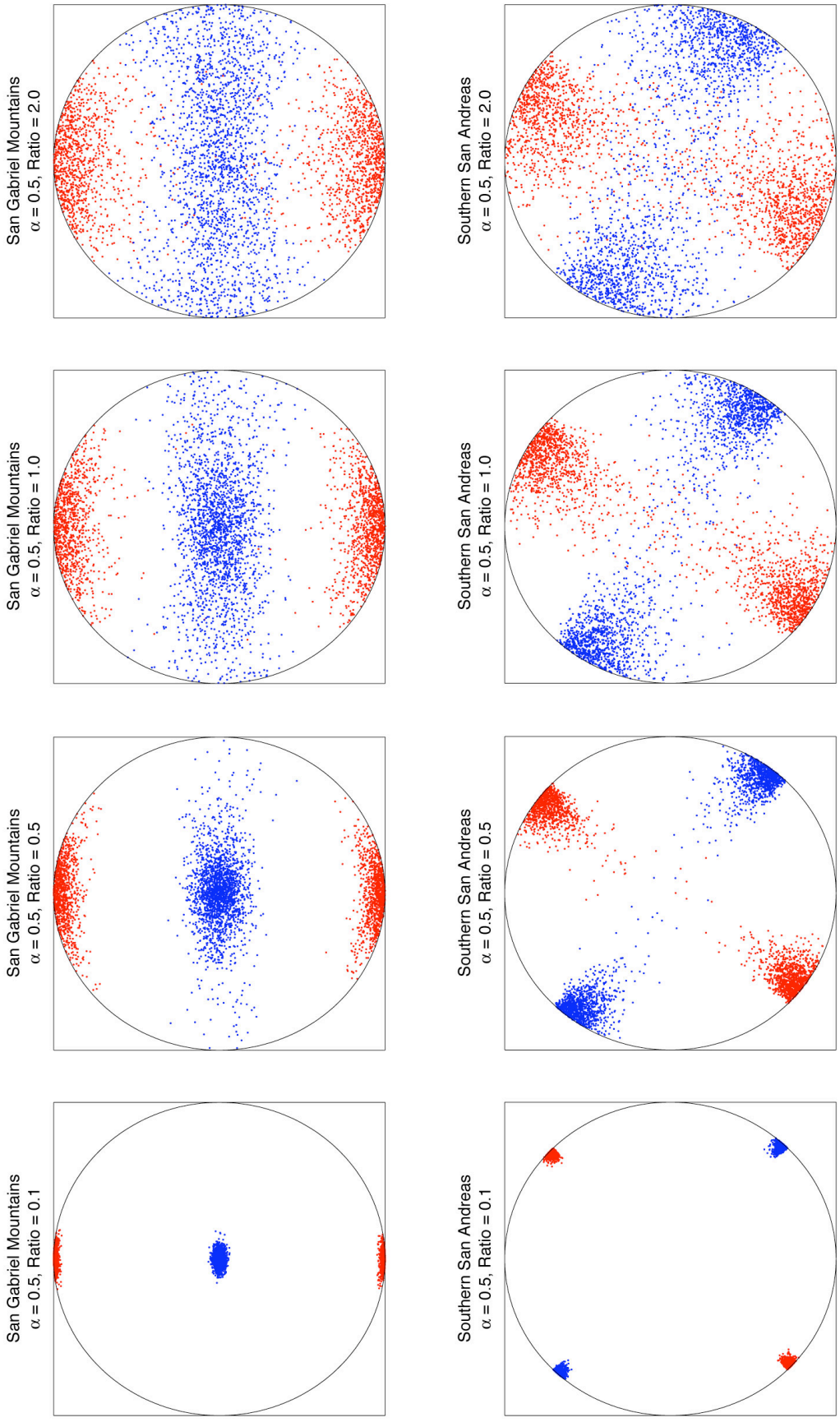
San Gabriel Mountains
α = 0.5, Ratio = 2.0
Southern San Andreas
α = 0.5, Ratio = 2.0
San Gabriel Mountains
α = 0.5, Ratio = 1.0
Southern San Andreas
α = 0.5, Ratio = 1.0
San Gabriel Mountains
α = 0.5, Ratio = 0.5
Southern San Andreas
α = 0.5, Ratio = 0.5
San Gabriel Mountains
α = 0.5, Ratio = 0.1
Southern San Andreas
α = 0.5, Ratio = 0.1

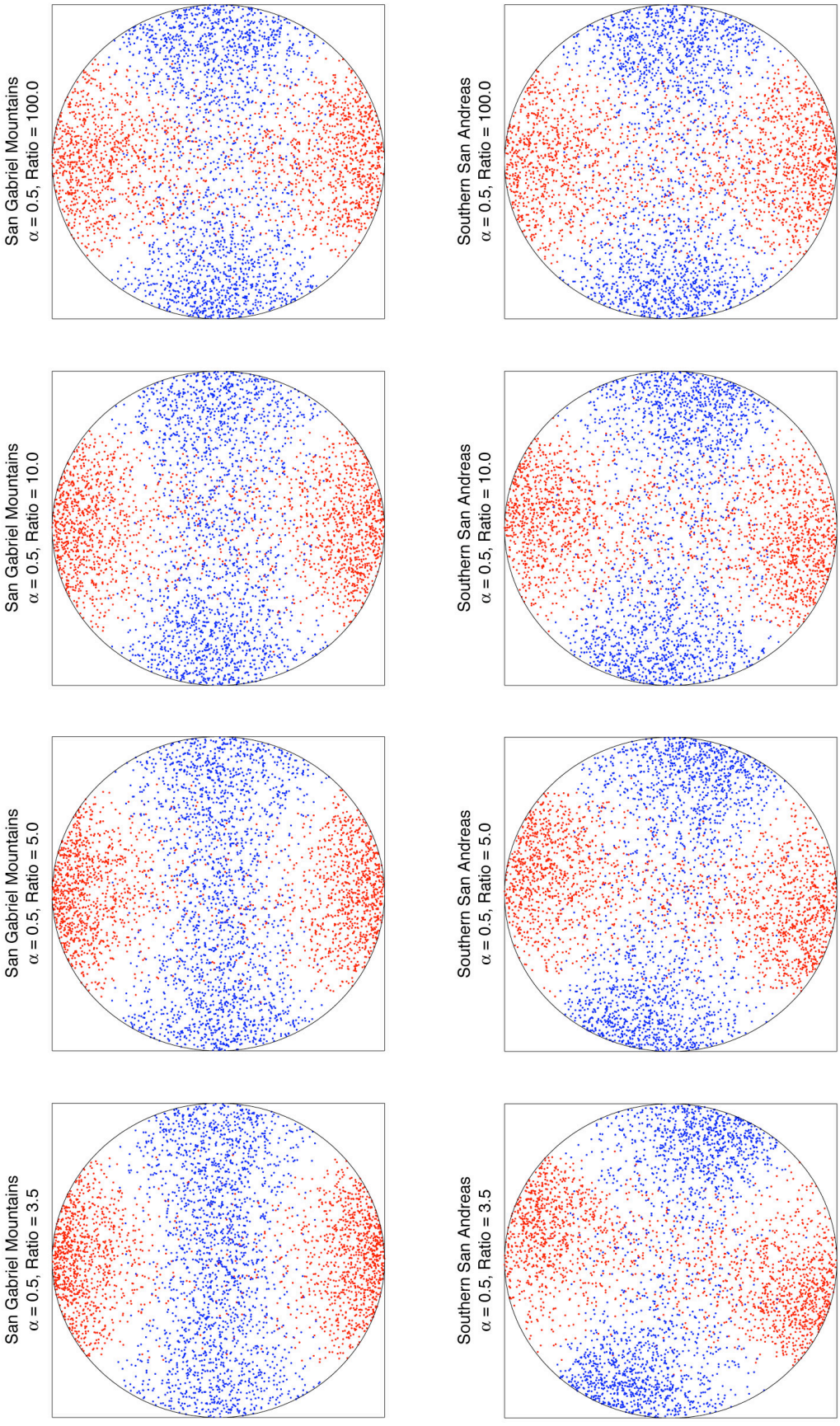
San Gabriel Mountains
α = 0.5, Ratio = 100.0
Southern San Andreas
α = 0.5, Ratio = 100.0
San Gabriel Mountains
α = 0.5, Ratio = 10.0
Southern San Andreas
α = 0.5, Ratio = 10.0
San Gabriel Mountains
α = 0.5, Ratio = 5.0
Southern San Andreas
α = 0.5, Ratio = 5.0
San Gabriel Mountains
α = 0.5, Ratio = 3.5
Southern San Andreas
α = 0.5, Ratio = 3.5

Figure 4.6. *P-T plots of Region #1 on top, the San Gabriel Mountains, and Region #2 on the bottom, the Southern San Andreas, for different levels of spatial heterogeneity,* $HR = \frac{\sqrt{Mean\left[\ \boldsymbol{\sigma}'_H(\mathbf{x}_i) : \boldsymbol{\sigma}'_H(\mathbf{x}_i)\right]}}{\sqrt{\boldsymbol{\sigma}'_B : \boldsymbol{\sigma}'_B}}$. *The spatial smoothing* α *shown here is* $\alpha = 0.5$, *and the plots for* $\alpha = 0.0$ *and* $\alpha = 1.0$ *look almost identical. The P axes are in red and the T axes are in blue.* HR, *which compares the relative size of the heterogeneous stress to the background stress, increases from* $HR = 0.1$ *(almost no heterogeneity) to* $HR = 100$ *(almost all heterogeneity). For* $HR = 0.1$, *there is little to no scatter of the P-T orientations, and they are centered on the respective background stress orientations,* $\boldsymbol{\sigma}'_{B1}$ *and* $\boldsymbol{\sigma}'_{B2}$. *As* HR *increases, the scatter of the P-T axes increases, and the average orientations of the simulations rotate toward the stress rate orientation,* $\dot{\boldsymbol{\sigma}}'_T$. *It becomes increasingly difficult to distinguish between the two regions as the spatial stress heterogeneity increases, until for* $HR = 100$, *the San Gabriel Mountains simulations and the Southern San Andreas Fault simulations look almost identical. If stress heterogeneity in the real Earth is this extreme, one could only measure the stress rate,* $\dot{\boldsymbol{\sigma}}'_T$; *there would be no information for determining the actual background stress, which could be quite different from* $\dot{\boldsymbol{\sigma}}'_T$.

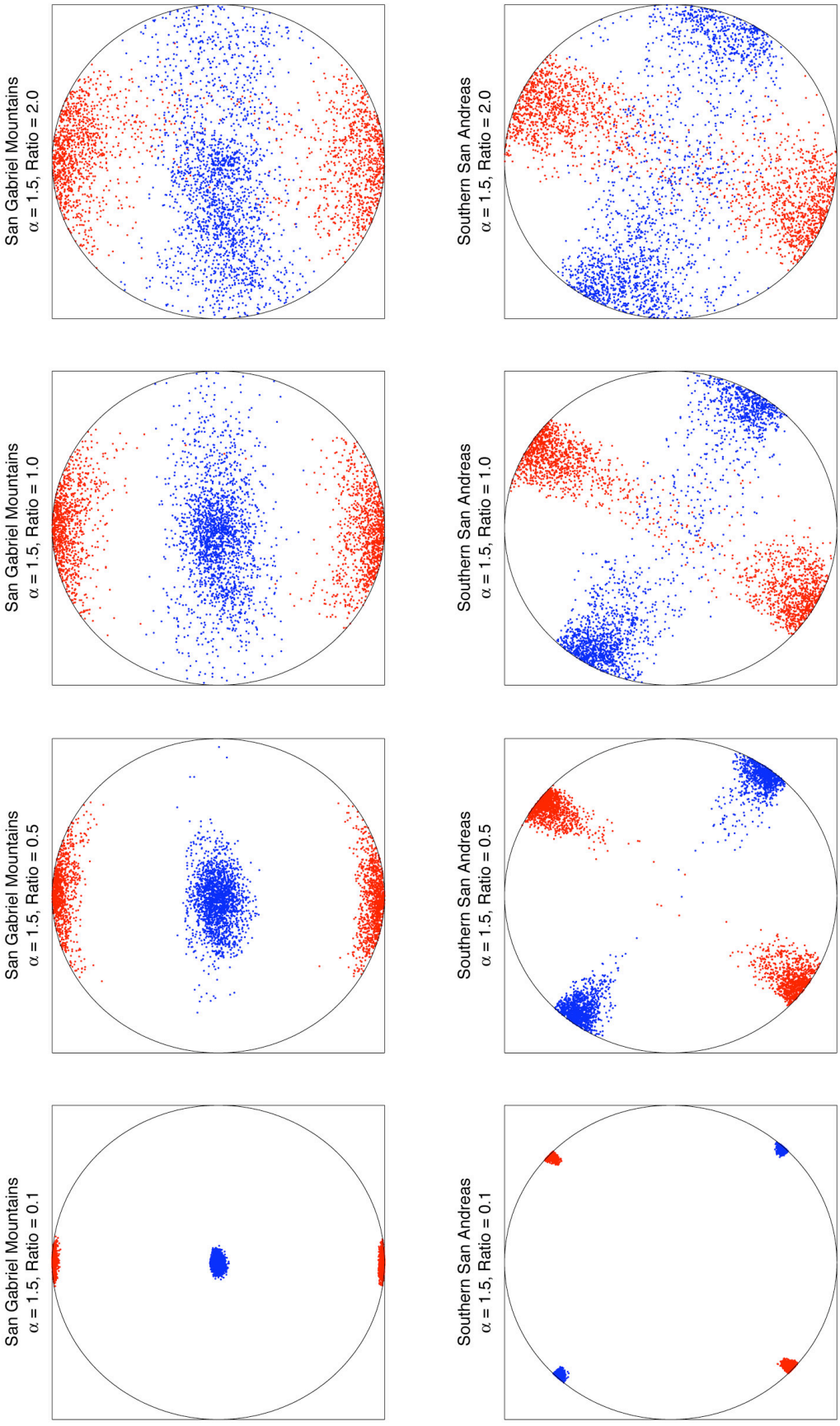
San Gabriel Mountains
α = 1.5, Ratio = 2.0
Southern San Andreas
α = 1.5, Ratio = 2.0
San Gabriel Mountains
α = 1.5, Ratio = 1.0
Southern San Andreas
α = 1.5, Ratio = 1.0
San Gabriel Mountains
α = 1.5, Ratio = 0.5
Southern San Andreas
α = 1.5, Ratio = 0.5
San Gabriel Mountains
α = 1.5, Ratio = 0.1
Southern San Andreas
α = 1.5, Ratio = 0.1

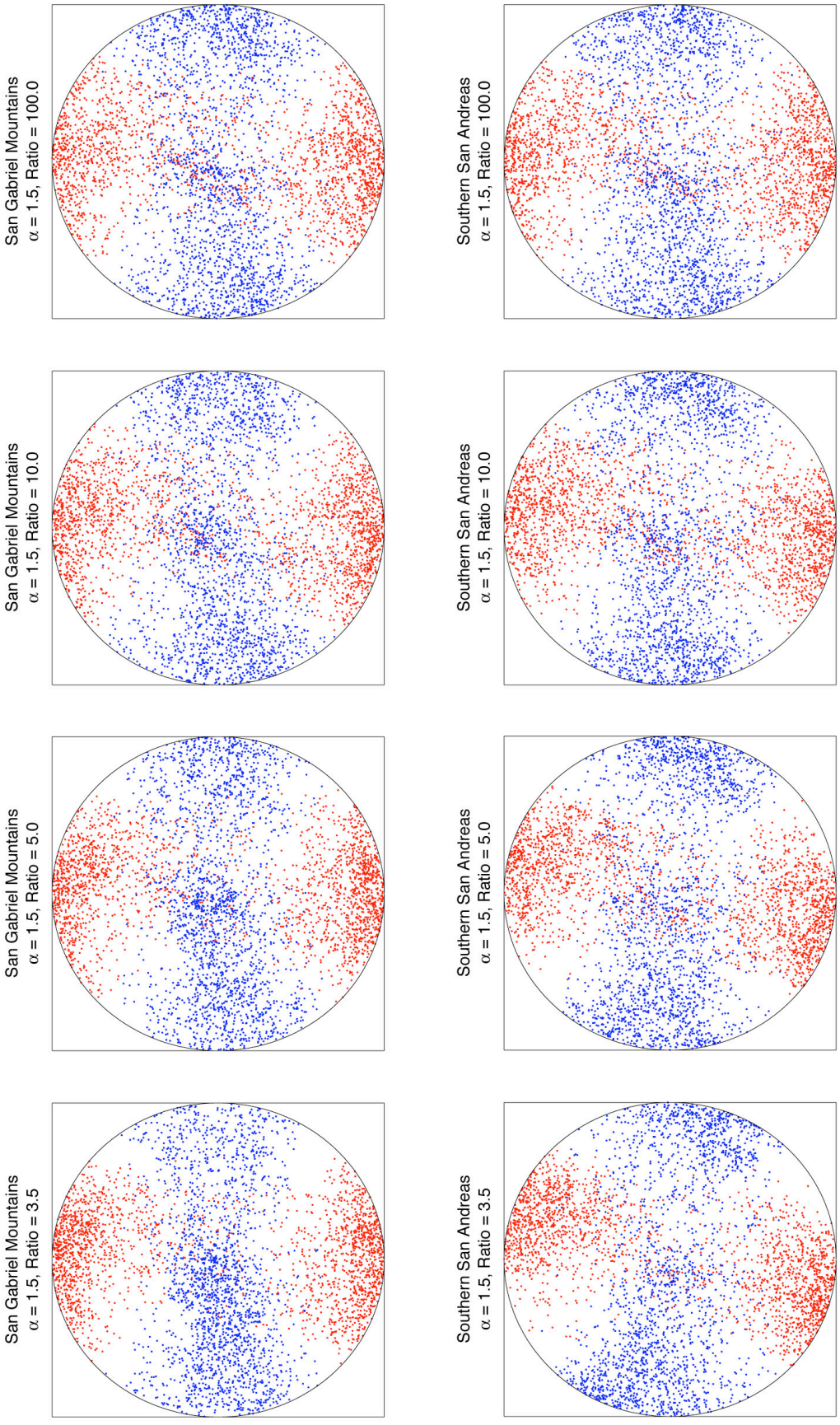
San Gabriel Mountains
α = 1.5, Ratio = 100.0
Southern San Andreas
α = 1.5, Ratio = 100.0
San Gabriel Mountains
α = 1.5, Ratio = 10.0
Southern San Andreas
α = 1.5, Ratio = 10.0
San Gabriel Mountains
α = 1.5, Ratio = 5.0
Southern San Andreas
α = 1.5, Ratio = 5.0
San Gabriel Mountains
α = 1.5, Ratio = 3.5
Southern San Andreas
α = 1.5, Ratio = 3.5

Figure 4.7. *P-T plots of Region #1 on top, the San Gabriel Mountains, and Region #2 on the bottom, the Southern San Andreas, for different levels of spatial heterogeneity,* $HR = \frac{\sqrt{Mean\left[\ \boldsymbol{\sigma}'_H(\mathbf{x}_i) : \boldsymbol{\sigma}'_H(\mathbf{x}_i)\right]}}{\sqrt{\boldsymbol{\sigma}'_B : \boldsymbol{\sigma}'_B}}$. *The spatial smoothing* α *shown here is* $\alpha = 1.5$, *and the effect of the spatial smoothing is apparent in the P-T plots. The same heterogeneous grid is used for all the simulations with* $\alpha = 1.5$ *and one can see how the spatial filtering distorts the P-T patterns seen in the simulations for* $\alpha \le 1.0$. *There is still a rotation as* HR *increases as seen in Figure 4.6 and for* $HR = 100$, *the two regions become indistinguishable as in Figure 4.6. This degree of spatial smoothing is unrealistic for the real Earth but is kept as an end-member case.*

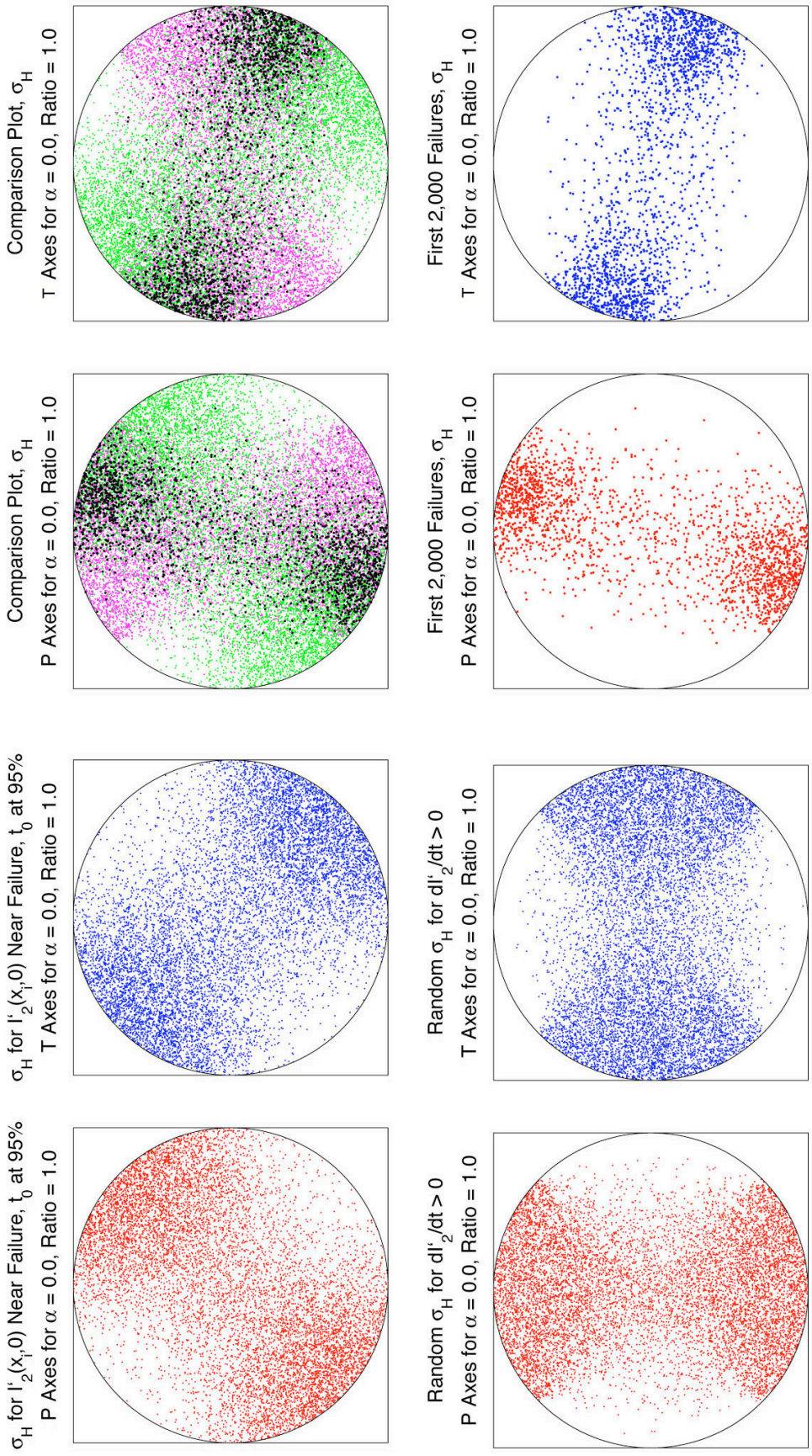
Comparison Plot, σ_H
T Axes for α = 0.0, Ratio = 1.0
First 2,000 Failures, σ_H
T Axes for α = 0.0, Ratio = 1.0
Comparison Plot, σ_H
P Axes for α = 0.0, Ratio = 1.0
First 2,000 Failures, σ_H
P Axes for α = 0.0, Ratio = 1.0
σ_H for $l'_2(x_i,0)$ Near Failure, t_0 at 95%
T Axes for α = 0.0, Ratio = 1.0
Random σ_H for $dl'_2/dt > 0$
T Axes for α = 0.0, Ratio = 1.0
σ_H for $l'_2(x_i,0)$ Near Failure, t_0 at 95%
P Axes for α = 0.0, Ratio = 1.0
Random σ_H for $dl'_2/dt > 0$
P Axes for α = 0.0, Ratio = 1.0

Figure 4.8. *This figure containing P-T plots is taken from the simulation for Region #2, the Southern San Andreas Fault, with* $\alpha = 0.0$, *and* $HR = 1.0$. *It is intended to show that simulation failures tend to occur at the intersection of* $\frac{dI_2'(\mathbf{x}_i,t)}{dt} > 0$ *and* $\frac{\frac{2}{3}\tau_0^2 - I_2'(\mathbf{x}_i,0)}{\frac{2}{3}\tau_0^2} \le 5\%$ *(the top* 5% *of the points close to the failure threshold). All the plots in this figure show the orientations of* $\boldsymbol{\sigma}'_H(\mathbf{x}_i)$, *not the full stress tensor. The top left two plots are the P axes in red and the T axes in blue for the points close to the failure threshold,* $\frac{2}{3}\tau_0^2$; *i.e., the 10,000 points plotted are a random sampling of those points within the 3D heterogeneous grid where* $\frac{\frac{2}{3}\tau_0^2 - I_2'(\mathbf{x}_i,0)}{\frac{2}{3}\tau_0^2} \le 5\%$ *is true. The bottom left two plots are the P axes and T axes for points going toward failure; i.e., the 10,000 points plotted are a random sampling of those points where* $\frac{dI_2'(\mathbf{x}_i,t)}{dt} > 0$ *is true. The bottom right two plots show the P and T axes for the first 2,000 failures within the simulation. The top right two plots compare all three quantities and show that the simulation failures do indeed occur at the intersection of* $\frac{dI_2'(\mathbf{x}_i,t)}{dt} > 0$ *and* $\frac{\frac{2}{3}\tau_0^2 - I_2'(\mathbf{x}_i,0)}{\frac{2}{3}\tau_0^2} \le 5\%$. $\frac{\frac{2}{3}\tau_0^2 - I_2'(\mathbf{x}_i,0)}{\frac{2}{3}\tau_0^2} \le 5\%$ *is plotted in green,* $\frac{dI_2'(\mathbf{x}_i,t)}{dt} > 0$ *is plotted in magenta, and the first 2,000 simulation failures are plotted in black. Note that the black points occur at the intersection of the green and magenta.*

Quantifying the Rotation from $\boldsymbol{\sigma}'_B$ to $\dot{\boldsymbol{\sigma}}'_T$ as Heterogeneity Increases

The most obvious way to quantify the rotation from $\boldsymbol{\sigma}'_B$ to $\dot{\boldsymbol{\sigma}}'_T$ as heterogeneity increases, HR increasing, would be to calculate the following: 1) The angular difference between $\bar{\boldsymbol{\sigma}}'_{Failure}\left(\mathbf{x}_{i_{Failure}}, t_{Failure}\right)$ and $\boldsymbol{\sigma}'_B$, which we call $\angle\bar{\boldsymbol{\sigma}}'_{Failure}\boldsymbol{\sigma}'_B$. 2) The angular difference between $\bar{\boldsymbol{\sigma}}'_{Failure}\left(\mathbf{x}_{i_{Failure}}, t_{Failure}\right)$ and $\dot{\boldsymbol{\sigma}}'_T$, which we call $\angle\bar{\boldsymbol{\sigma}}'_{Failure}\dot{\boldsymbol{\sigma}}'_T$. As HR increases and the average failure orientations rotate from $\boldsymbol{\sigma}'_B$ to $\dot{\boldsymbol{\sigma}}'_T$, $\angle\bar{\boldsymbol{\sigma}}'_{Failure}\boldsymbol{\sigma}'_B$ will increase and $\angle\bar{\boldsymbol{\sigma}}'_{Failure}\dot{\boldsymbol{\sigma}}'_T$ will decrease. If we wish to normalize this quantity, we can calculate $\frac{\angle\bar{\boldsymbol{\sigma}}'_{Failure}\boldsymbol{\sigma}'_B}{\angle\boldsymbol{\sigma}'_B\dot{\boldsymbol{\sigma}}'_T}$ and $\frac{\angle\bar{\boldsymbol{\sigma}}'_{Failure}\dot{\boldsymbol{\sigma}}'_T}{\angle\boldsymbol{\sigma}'_B\dot{\boldsymbol{\sigma}}'_T}$, which typically have values ranging from ≈ 0.0 to ≈ 1.0. For example, if $\frac{\angle\bar{\boldsymbol{\sigma}}'_{Failure}\boldsymbol{\sigma}'_B}{\angle\boldsymbol{\sigma}'_B\dot{\boldsymbol{\sigma}}'_T} = 0.0$, the points that have failed in the simulation are on average aligned with the background stress, $\boldsymbol{\sigma}'_B$. This is what we would expect for $HR = 0.0$. Concurrently, we would expect $\frac{\angle\bar{\boldsymbol{\sigma}}'_{Failure}\dot{\boldsymbol{\sigma}}'_T}{\angle\boldsymbol{\sigma}'_B\dot{\boldsymbol{\sigma}}'_T} \approx 1.0$ if $\frac{\angle\bar{\boldsymbol{\sigma}}'_{Failure}\boldsymbol{\sigma}'_B}{\angle\boldsymbol{\sigma}'_B\dot{\boldsymbol{\sigma}}'_T} = 0.0$. If $HR \to \infty$, then we would expect the reverse, $\frac{\angle\bar{\boldsymbol{\sigma}}'_{Failure}\dot{\boldsymbol{\sigma}}'_T}{\angle\boldsymbol{\sigma}'_B\dot{\boldsymbol{\sigma}}'_T} \approx 0.0$ and $\frac{\angle\bar{\boldsymbol{\sigma}}'_{Failure}\boldsymbol{\sigma}'_B}{\angle\boldsymbol{\sigma}'_B\dot{\boldsymbol{\sigma}}'_T} \approx 1.0$, where the points that have failed in the simulation are on average aligned with $\dot{\boldsymbol{\sigma}}'_T$.

If $\frac{\angle\bar{\boldsymbol{\sigma}}'_{Failure}\boldsymbol{\sigma}'_B}{\angle\boldsymbol{\sigma}'_B\dot{\boldsymbol{\sigma}}'_T} \approx \angle\boldsymbol{\sigma}'_B\dot{\boldsymbol{\sigma}}'_T - \frac{\angle\bar{\boldsymbol{\sigma}}'_{Failure}\dot{\boldsymbol{\sigma}}'_T}{\angle\boldsymbol{\sigma}'_B\dot{\boldsymbol{\sigma}}'_T}$, then we know that the angular difference is purely due to a tradeoff of $\boldsymbol{\sigma}'_B$ and $\dot{\boldsymbol{\sigma}}'_T$, not any other orientations (except for small fluctuations due to randomness in the grid); consequently, we can think of these as: 1) normalized angular differences in terms of the normalized bias toward the stressing rate tensor, $\dot{\boldsymbol{\sigma}}'_T$, where

$\frac{\angle\bar{\boldsymbol{\sigma}}'_{Failure}\boldsymbol{\sigma}'_B}{\angle\boldsymbol{\sigma}'_B\dot{\boldsymbol{\sigma}}'_T} \approx \angle\boldsymbol{\sigma}'_B\dot{\boldsymbol{\sigma}}'_T - \frac{\angle\bar{\boldsymbol{\sigma}}'_{Failure}\dot{\boldsymbol{\sigma}}'_T}{\angle\boldsymbol{\sigma}'_B\dot{\boldsymbol{\sigma}}'_T} \approx$ *Normalized Bias* (% rotation toward $\dot{\boldsymbol{\sigma}}'_T$) and 2) angular differences in terms of the angular bias toward the stressing rate tensor, where $\angle\bar{\boldsymbol{\sigma}}'_{Failure}\boldsymbol{\sigma}'_B \approx \angle\boldsymbol{\sigma}'_B\dot{\boldsymbol{\sigma}}'_T - \angle\bar{\boldsymbol{\sigma}}'_{Failure}\dot{\boldsymbol{\sigma}}'_T \approx$ *Bias* (angular rotation toward $\dot{\boldsymbol{\sigma}}'_T$).

The next question we have to address in quantifying the relationship between the stress heterogeneity, HR, and *Bias* / *Normalized Bias*, is how to calculate the angular difference between our average failure stress tensor, $\bar{\boldsymbol{\sigma}}'_{Failure}\left(\mathbf{x}_{i_{Failure}}, t_{Failure}\right)$, and either $\boldsymbol{\sigma}'_B$ or $\dot{\boldsymbol{\sigma}}'_T$. In the real Earth, we have limitations on the information we can glean about the stress field using earthquakes. For a single focal mechanism, we can determine only the orientations of the P, T, and B axes (three-parameters). If one assumes the Hencky-Mises failure criterion and maximally oriented planes then this also gives us the orientation of the three principal stresses (three-parameters); however, if we invert a set of focal mechanisms, we can determine both the orientations of the three principal stresses (without having to assume maximally oriented planes) and the stress ratio, $R = \left(\frac{\sigma_2 - \sigma_3}{\sigma_1 - \sigma_3}\right)$ [e.g., *Rivera and Kanamori*, 2002] (four-parameters). This means that a focal mechanism inversion can yield the relative sizes of the components within the failure deviatoric stress tensor, but not the overall size.

This leads us to two different methodologies for quantifying the angular difference between two stress tensors. The first methodology calculates the minimum angular difference when only the three orientation parameters are available. This is particularly helpful when comparing individual focal mechanism orientations. One would determine the four different possible sets of strike, dip, and rake, $(\Theta, \delta, \lambda)$, for

each focal mechanism or stress tensor, allowing for $0 \le \delta \le 180°$ (Appendix A). Then one would convert the four sets of $(\Theta, \delta, \lambda)$ into quaternions for each focal mechanism or stress tensor. Last, using quaternion algebra (see Chapter 3), one would calculate the minimum rotation between two focal mechanisms or stress tensors, by calculating the 16 possible sets of $(\omega_R, [\theta_R, \phi_R])$ and choose the minimum ω_R.

The second methodology uses the scalar product of two deviatoric stress tensors to calculate an angular difference. Since the scalar product is a scalar quantity, invariant upon rotation, we can define an angle between the rank two tensors, A and B, as

$$\angle AB = \cos^{-1}\left(\frac{A:B}{\|A\|\|B\|}\right) \tag{4.25}$$

where

$$\|A\| = \sqrt{A:A}$$

and

$$\|B\| = \sqrt{B:B}.$$

Note that this measure of angular difference yields a result different from ω_R. It isn't a physical rotation in 3D space. Instead, it is a measure of the similarity of the two tensors including information about the relative sizes of the eigenvalues.

Since a deviatoric stress tensor has five independent quantities, normalizing by $\|A\|\|B\|$ reduces the independent quantities to four in the calculation of $\angle AB$; therefore, this type of calculation of angular difference is most useful when we know both the orientations of the three principal stresses and one other quantity like the stress ratio as in

focal mechanism inversions. From the three principal stresses and stress ratio, one way to reconstruct the deviatoric stress tensor would be as follows:

- Let $\sigma_3' = 1.0$
- Combine the stress ratio equation, $R = \left(\frac{\sigma_2' - \sigma_3'}{\sigma_1' - \sigma_3'} \right)$, and the deviatoric constraint $\sigma_1' + \sigma_2' + \sigma_3' = 0$ to derive $\sigma_1' = -\left(\frac{2 - R}{1 + R} \right) \sigma_3'$.
- Then let, $\sigma_2' = -\left(\sigma_1' + \sigma_3' \right)$
- Then combine these principal stresses with principal orientations to produce the deviatoric stress tensor. See Appendix A.

As expected, the overall size of this deviatoric stress tensor is unspecified, but it does yield the relative sizes of each component.

In Figures 4.9–4.12, we apply these two different methodologies for calculating the angular difference between $\bar{\boldsymbol{\sigma}}'_{Failure}\left(\mathbf{x}_{i_{Failure}}, t_{Failure} \right)$ and $\boldsymbol{\sigma}'_B$ for our two regions, San Gabriel Mountains and the Southern San Andreas Fault. Figures 4.9 and 4.10 plot the rotation away from $\boldsymbol{\sigma}'_B$ toward $\dot{\boldsymbol{\sigma}}'_T$ as a function of heterogeneity for our two regions using our first methodology, by showing the three-parameter *Bias* in Figure 4.9 and the three-parameter *Normalized Bias* in Figure 4.10. Figures 4.11 and 4.12 plot the same quantities as 4.9 and 4.10; only this time, we use the second methodology, four-parameter *Bias* in Figure 4.11 and four parameter *Normalized Bias* in Figure 4.12. Each point on the plots is an average over three simulations with different spatial smoothness, $\alpha = 0.0$, $\alpha = 0.5$, and $\alpha = 1.0$.

Interestingly, when we use the three-parameter method of calculating *Bias* Region #2, the Southern San Andreas, rotates smoothly from the $\boldsymbol{\sigma}'_B$ orientation to the $\dot{\boldsymbol{\sigma}}'_T$ orientation as heterogeneity, HR, increases, but Region #1, the San Gabriel Mountains, does not. Region #1, plotted in blue, quickly jumps from the $\boldsymbol{\sigma}'_B$ orientation to the $\dot{\boldsymbol{\sigma}}'_T$ orientation at $HR \approx 2.0$ (Figures 4.9 and 4.10). When we use the four parameter method of calculating *Bias*, both Region #1 and Region #2 rotate smoothly from $\boldsymbol{\sigma}'_B$ to $\dot{\boldsymbol{\sigma}}'_T$ as heterogeneity, HR, increases (Figures 4.11 and 4.12). This occurs because the stress ratio $R \approx 1.0$ for all HR in Region #2, so it does not really matter which methodology we use, the three-parameter or four-parameter method of calculating angular difference, because all the information is contained in the three principal stress orientations. However, for Region #1, the stress ratio, R, is significantly changing along with the principal stress orientations, and it follows that the three-parameter method of calculating *Bias* is insufficient to fully represent the change in orientation as a function of HR. That is why we see a step function at $HR \approx 2.0$ for Region #1. Regions #1 and #2 are extreme examples of this effect; most combinations of $\boldsymbol{\sigma}'_B$ and $\dot{\boldsymbol{\sigma}}'_T$ will have behavior in between these two for the three-parameter methodology of calculating *Bias*.

At the same time, whenever possible, it is best to use the four-parameter methodology of calculating *Bias*, which uses the inner product to produce stable *Bias* and *Normalized Bias* curves as a function of HR. For example, even though Regions #1 and #2 have very different background stresses, their *Normalized Bias* curves are quite similar. Chapter 5 will expand upon this topic by generating synthetic *Bias* and *Normalized Bias* curves using the four-parameter methodology that can be compared to real data to estimate stress parameters in the real Earth.

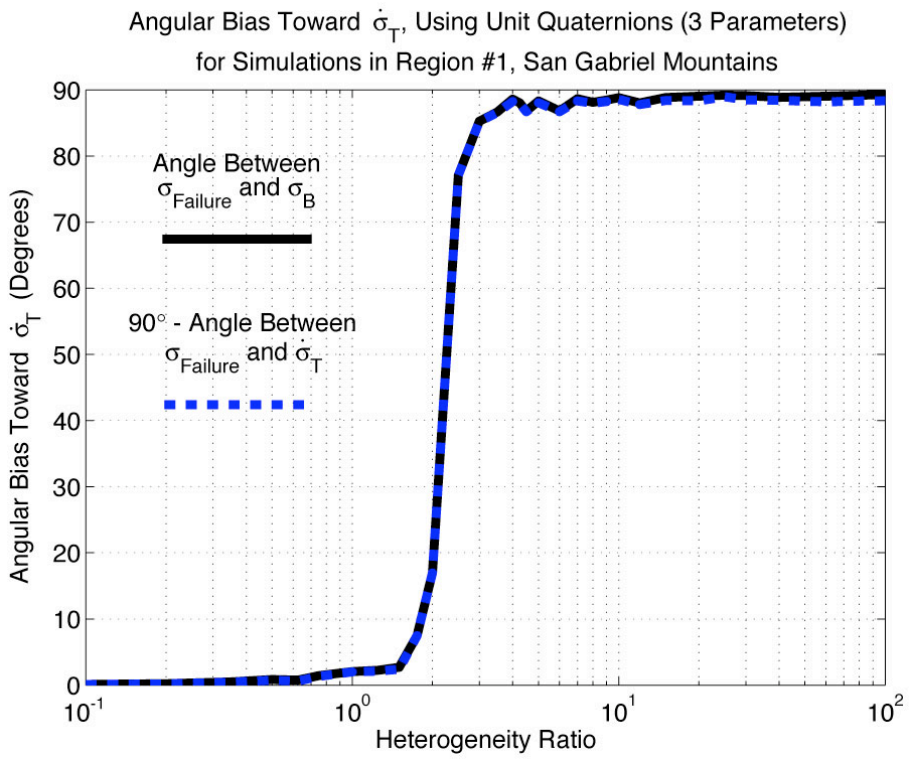

Figure 4.9 a)

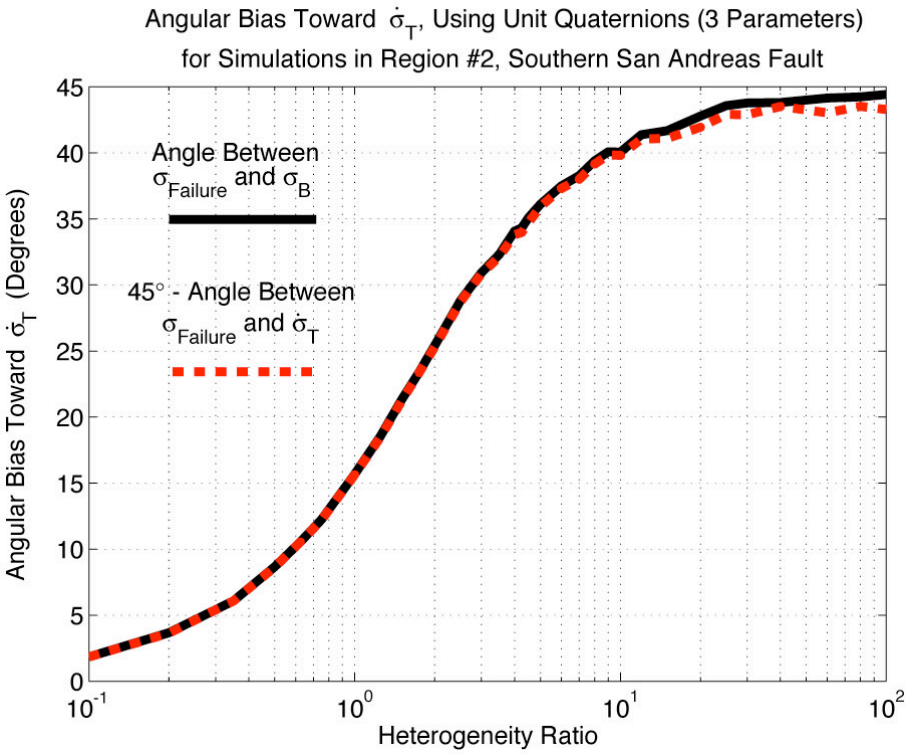

Figure 4.9 b)

Figure 4.9. *Plots of angular Bias toward the stressing rate orientation,* $\dot{\boldsymbol{\sigma}}'_T$*, as a function of heterogeneity ratio,* HR*, for the* ***a)*** *San Gabriel Mountains and the* ***b)*** *Southern San Andreas Fault. Bias is calculated two different ways in this plot. The solid black line shows the angular difference between,* $\bar{\boldsymbol{\sigma}}'_{Failure}\left(\mathbf{x}_{i_{Failure}}, t_{Failure}\right)$ *and* $\boldsymbol{\sigma}'_B$*,* $\angle\bar{\boldsymbol{\sigma}}'_{Failure}\boldsymbol{\sigma}'_B$*, and the dashed red line, which plots almost exactly on top shows* $\angle\boldsymbol{\sigma}'_B\dot{\boldsymbol{\sigma}}'_T - \angle\bar{\boldsymbol{\sigma}}'_{Failure}\dot{\boldsymbol{\sigma}}'$*. The angular difference for these two quantities,* $\angle\bar{\boldsymbol{\sigma}}'_{Failure}\boldsymbol{\sigma}'_B$ *and* $\angle\boldsymbol{\sigma}'_B\dot{\boldsymbol{\sigma}}'_T - \angle\bar{\boldsymbol{\sigma}}'_{Failure}\dot{\boldsymbol{\sigma}}'$*, is calculated using our three-parameter method. This methodology uses quaternions to determine the minimum rotation angle,* ω*, between two focal mechanisms or the principal orientations in a stress tensor. The red dashed line and the solid black lines are averages over simulations with three different levels of spatial smoothing,* $\alpha = 0.0$*,* $\alpha = 0.5$*, and* $\alpha = 1.0$*. The Southern San Andreas simulations smoothly rotate from the* $\boldsymbol{\sigma}'_B$ *orientation to the* $\dot{\boldsymbol{\sigma}}'_T$ *as* HR *increases, but the San Gabriel Mountain simulations jump abruptly from* $\boldsymbol{\sigma}'_B$ *to* $\dot{\boldsymbol{\sigma}}'_T$ *at* $HR \approx 2.0$*. This occurs because our fracture criterion is applied to the deviatoric stress tensor, not just the three orientation angles; hence, one must take into account the changes in the stress ratio,* R*, in addition to changes in the three principal orientations to adequately parameterize the rotation of* $\bar{\boldsymbol{\sigma}}'_{Failure}\left(\mathbf{x}_{i_{Failure}}, t_{Failure}\right)$ *from* $\boldsymbol{\sigma}'_B$ *to* $\dot{\boldsymbol{\sigma}}'_T$ *as* HR *increases for any pair of* $\boldsymbol{\sigma}'_B$ *and* $\dot{\boldsymbol{\sigma}}'_T$*.*

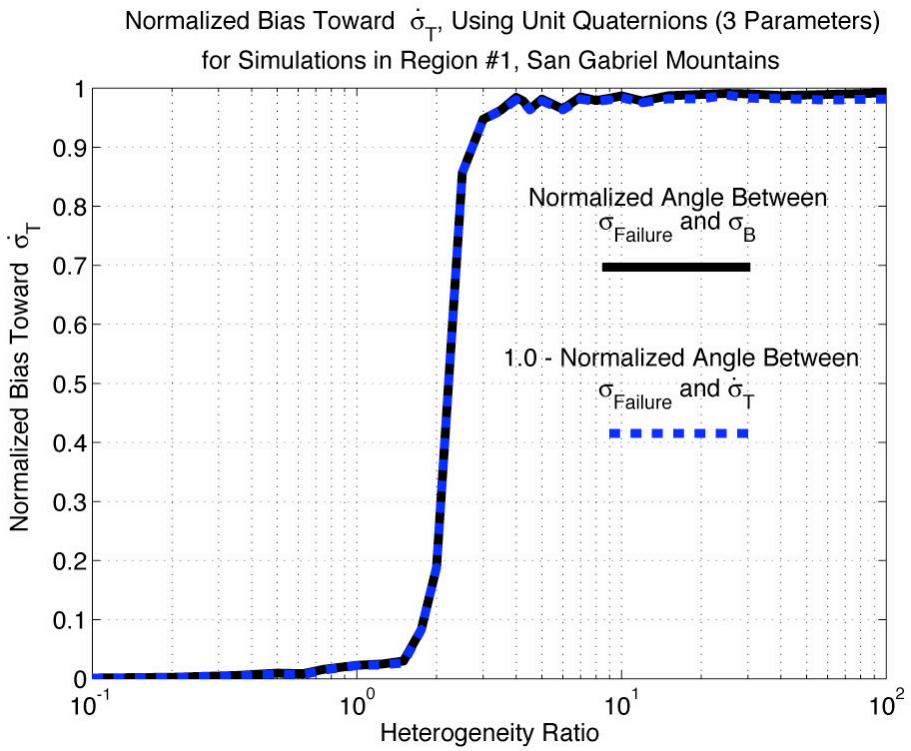

Figure 4.10 a)

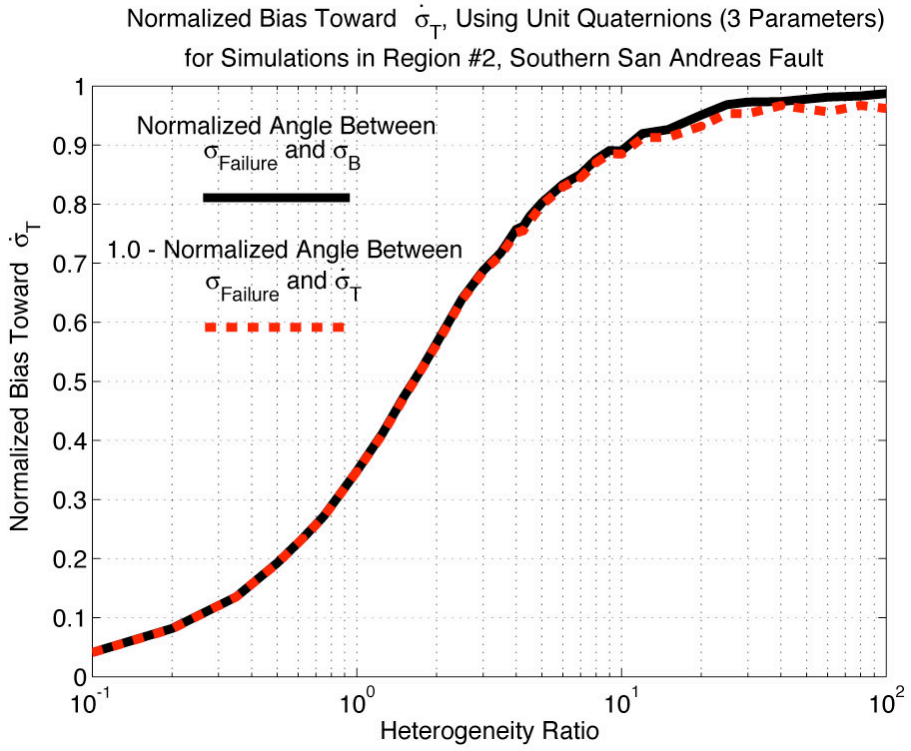

Figure 4.10 b)

Figure 4.10. *Exactly the same plots as Figure 4.9 except that the Normalized Bias is now being plotted instead of the angular Bias, where all the angles have been divided by the maximum possible angular difference,* $\angle \boldsymbol{\sigma}'_B \dot{\boldsymbol{\sigma}}'_T$. *The possible range of values is now* $0.0 \le \textit{Normalized Bias} \le 1.0$, *where the Normalized Bias is really the percent rotation toward the* $\dot{\boldsymbol{\sigma}}'_T$ *orientation.*

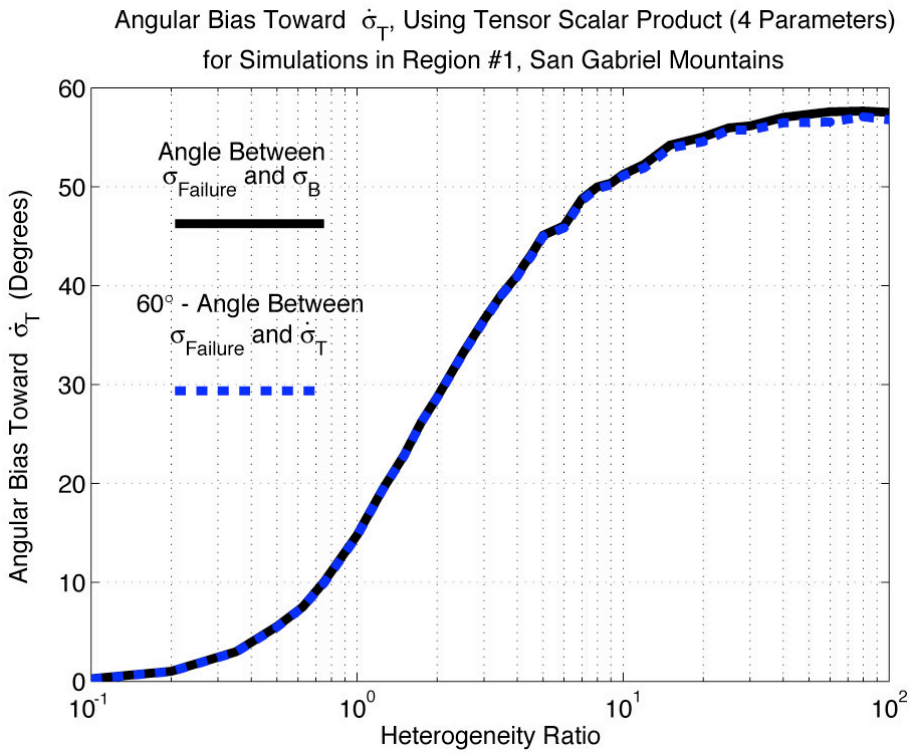

Figure 4.11 a)

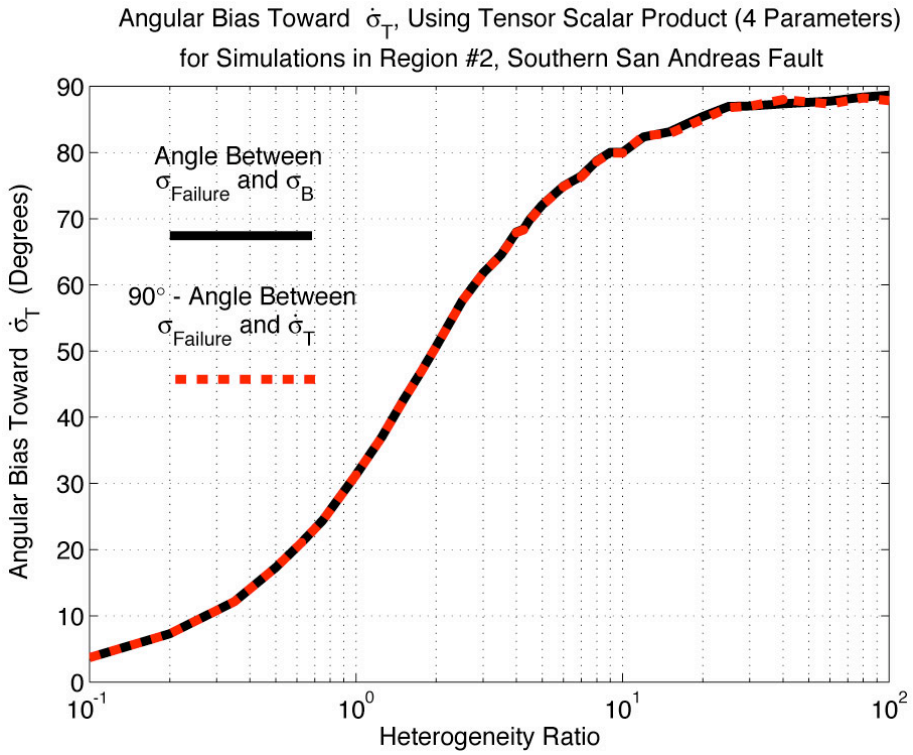

Figure 4.11 b)

Figure 4.11. *Plots of angular Bias toward the stressing rate orientation,* $\dot{\boldsymbol{\sigma}}'_T$*, as a function of heterogeneity ratio,* HR*, for the* ***a)*** *San Gabriel Mountains and the* ***b)*** *Southern San Andreas. Bias is calculated two different ways in this plot. The solid black line shows the angular difference between,* $\bar{\boldsymbol{\sigma}}'_{Failure}\left(\mathbf{x}_{i_{Failure}}, t_{Failure}\right)$ *and* $\boldsymbol{\sigma}'_B$*,* $\angle\bar{\boldsymbol{\sigma}}'_{Failure}\boldsymbol{\sigma}'_B$*, and the dashed red line, which plots almost exactly on top shows* $\angle\boldsymbol{\sigma}'_B\dot{\boldsymbol{\sigma}}'_T - \angle\bar{\boldsymbol{\sigma}}'_{Failure}\dot{\boldsymbol{\sigma}}'$*. The angular difference for these two quantities,* $\angle\bar{\boldsymbol{\sigma}}'_{Failure}\boldsymbol{\sigma}'_B$ *and* $\angle\boldsymbol{\sigma}'_B\dot{\boldsymbol{\sigma}}'_T - \angle\bar{\boldsymbol{\sigma}}'_{Failure}\dot{\boldsymbol{\sigma}}'$*, is calculated using our four-parameter method. This method takes the tensor scalar product of deviatoric stress matrices that have been calculated from the three principal stress orientations and the stress ratio,* R*, and calculates an angle. The red dashed line and the solid black lines are averages over simulations with three different levels of spatial smoothing,* $\alpha = 0.0$*,* $\alpha = 0.5$*, and* $\alpha = 1.0$*. In this figure, using the four-parameter method, both the Southern San Andreas Fault simulations and the San Gabriel Mountain simulations smoothly rotate from* $\boldsymbol{\sigma}'_B$ *to* $\dot{\boldsymbol{\sigma}}'_T$ *as* HR *increases, which is more desirable than the abrupt transition seen for the San Gabriel Mountains seen in Figure 4.9 using the three-parameter method. While the four-parameter method for calculating angular differences is by far the best, it can only be applied when one has an estimate of the stress ratio,* R*. If one has only orientation information, such as strike, dip, and rake* $(\Theta, \delta, \lambda)$ *when dealing with individual focal mechanism orientations, then one cannot use this four-parameter methodology.*

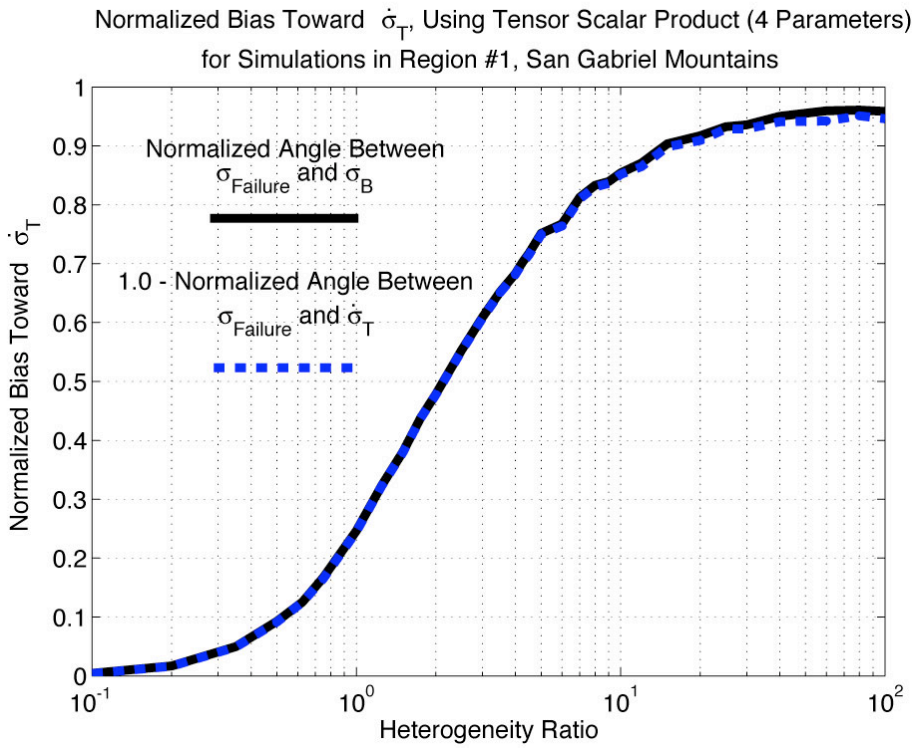

Figure 4.12 a)

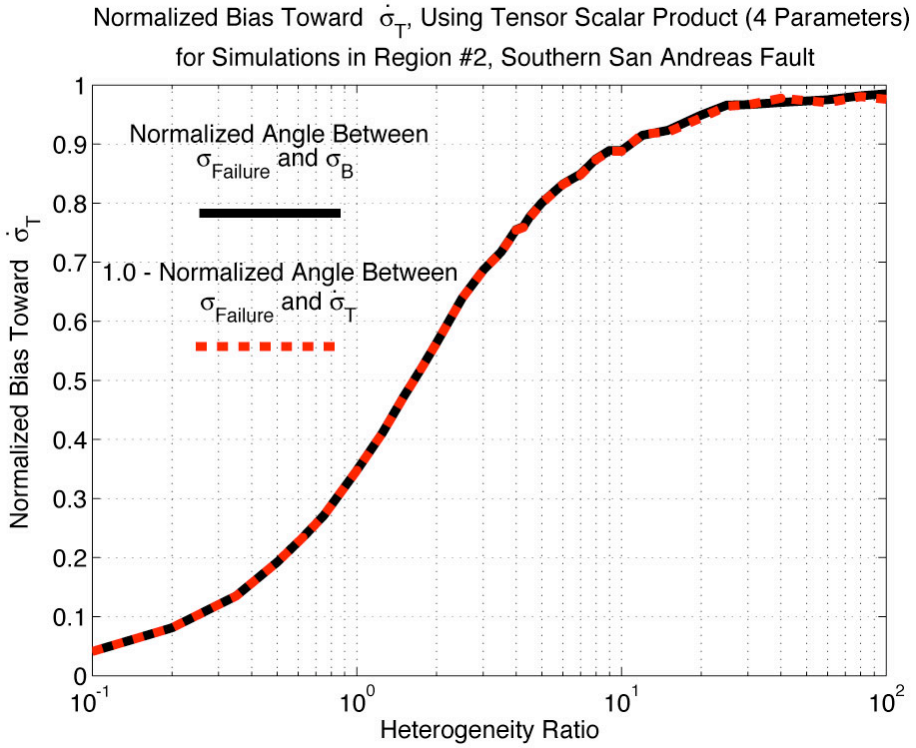

Figure 4.12 b)

Figure 4.12. *Exactly the same plots as Figure 4.11 except that the Normalized Bias is now being plotted instead of the angular Bias, where all the angles have been divided by the maximum possible angular difference,* $\angle \boldsymbol{\sigma}'_B \dot{\boldsymbol{\sigma}}'_T$. *The possible range of values is now* $0.0 \le Normalized\ Bias \le 1.0$, *where the Normalized Bias is really the percent rotation toward* $\dot{\boldsymbol{\sigma}}'_T$. *Note how similar are the Normalized Bias plots of the San Gabriel Mountains and Southern San Andreas as they both smoothly rotated toward* $\dot{\boldsymbol{\sigma}}'_T$ *using this four-parameter method of estimating angular differences.*

References

Angelier, J. (1975), Sur l'analyse de mesures recueilles dans des sites faillés: l'utilité d'une confrontation entre les méthodes dynamiques et cinématiques, *C.R. Acadamy of Science, Paris, D*, *283*, 466.

Angelier, J. (1984), Tectonic analysis of fault slip data sets, *Journal of Geophysical Research*, *89*, 5835–5848.

Carey, E., and B. Brunier (1974), Analyse théorique et numérique d'un modèle méchanique élémentaire appliqué à l'étude d'une population de failles, *C.R. Acadamy of Science, Paris, D*, *279*, 891–894.

Etchecopar, A., et al. (1981), An inverse problem in microtectonics for the determination of stress tensors from fault striation analysis, *Journal of Structrual Geology*, *3*, 51–65.
Gephart, J. W. (1990), FMSI: A Fortran program for inverting fault/slickenside and earthquake focal mechanism data to obtain the regional stress tensor, *Computers and Geosciences*, *16*, 953–989.

Gephart, J. W., and D. W. Forsyth (1984), An improved method for deteremining the regional stress tensor using earthquake focal mechanism data: Application to the San Fernando earthquake sequence, *Journal of Geophysical Research*, *89*, 9305–9320.

Housner, G. W., and T. J. Vreeland (1965), *The Analysis of Stress and Deformation*, 440 pp., Division of Engineering and Applied Science, California Institute of Technology.

Mercier, J.-L., and S. Carey-Gailhardis (1989), Regional state of stress and characteristic fault kinematics instabilities shown by aftershock sequence: the aftershock sequence of the 1978 Thessaloniki (Greece) and 1980 Campania-Lucania (Italy) earthquakes as examples, *Earth and Planetary Science Letters*, *92*, 247–264.

Michael, A. J. (1984), Determination of stress from slip data: Faults and folds, *Journal of Geophysical Research-Solid Earth*, *89*, 11517–11526.

Michael, A. J. (1987), Use of focal mechanisms to determine stress: A control study, *Journal of Geophysical Research-Solid Earth*, *92*, 357–368.

Rivera, L., and H. Kanamori (2002), Spatial heterogeneity of tectonic stress and friction in the crust, *Geophysical Research Letters*, *29*, art. no. 1088.

Townend, J., and M. D. Zoback (2004), Regional tectonic stress near the San Andreas fault in central and southern California, *Geophysical Research Letters*, *31*, L15S11, 11–15.

Chapter 5. **Estimating Stress Heterogeneity and Background Stress in the Real Earth**

Ultimately, we wish to estimate stress heterogeneity parameters in the real Earth by comparing our simulations to real focal mechanism data. Very little is known about the parameters of stress heterogeneity in the Earth, so this is an exciting topic of investigation. At the same time we have to keep in mind that there are limitations to our ability to test this, because of all the simplifying assumptions incorporated into our 3D numerical models. For example, when generating the three principal stresses (σ_1, σ_2 and σ_3), we start with Gaussian random noise in 3D and then smooth it with a fractal filter. In the real Earth, a Weibull distribution may be more appropriate. While spatial smoothing using a fractal filter may simply describe the statistics of our simulations, there is no guarantee that the real Earth's spatial stress heterogeneity varies exactly in a fractal manner. Then when we generate the actual failures, they are point failures, not finite dislocations, and we do not update the stress field. We also use a plastic yield criterion to determine failures, which means we do not allow the possibility of slip on pre-existing faults. The lack of pre-existing faults means that the spatial clustering of our focal mechanisms tends to occur in 3D clouds rather than lineations or planes; whereas, in the real Earth, seismicity often occurs on lineations or planes due to preexisting faults and fracture zones. Therefore, any conclusions derived from comparing our simulations to real data are meant to yield an initial estimate to be tested and refined by better future techniques.

The two stress heterogeneity parameters we wish to estimate are α, the degree of spatial smoothing, and HR, which describes the relative magnitudes of the spatial heterogeneity and the spatial mean. We will also have to estimate how much model noise

(as opposed to stress heterogeneity) to add to our simulated focal mechanisms to accurately compare them with real focal mechanisms; i.e., there is a mechanism uncertainty/error in the generation of real focal mechanism data that has to be taken into account if we wish to compare our simulations to real data. We will also show that the failure threshold, $\frac{2}{3}\tau_0^2$, can be an important factor as well.

To estimate α, HR, and the model noise, we compare our simulations to a plot by Hardebeck [in review, 2006], that plots the average angular difference between pairs of focal mechanisms as a function of distance between the pairs for three different regions (Figures 5.1–5.2). Figure 5.1 is a modified map from Hardebeck [in review, 2006] that shows the regions in which she computed the average angular difference between pairs of focal mechanisms and the two regions we numerically model. Figure 5.2, another modified plot from Hardebeck [in review, 2006], shows the average angular difference as a function of distance for two of the regions she studied. According to Hardebeck, for length scales < ~ 2 km the average focal mechanism variation could be explained purely by uncertainty in the focal mechanism orientations. However, as the length scale increases, the average focal mechanism variation also increases, which we will show is consistent with smoothed heterogeneous stress similar to our simulations. We will show that:

- The minimum average angular difference between focal mechanisms in Figure 5.2 can be used to estimate how much noise should be added to our simulated data. One assumes the stress is uniform at those small distances, and the minimum average angular difference is due purely to model noise.

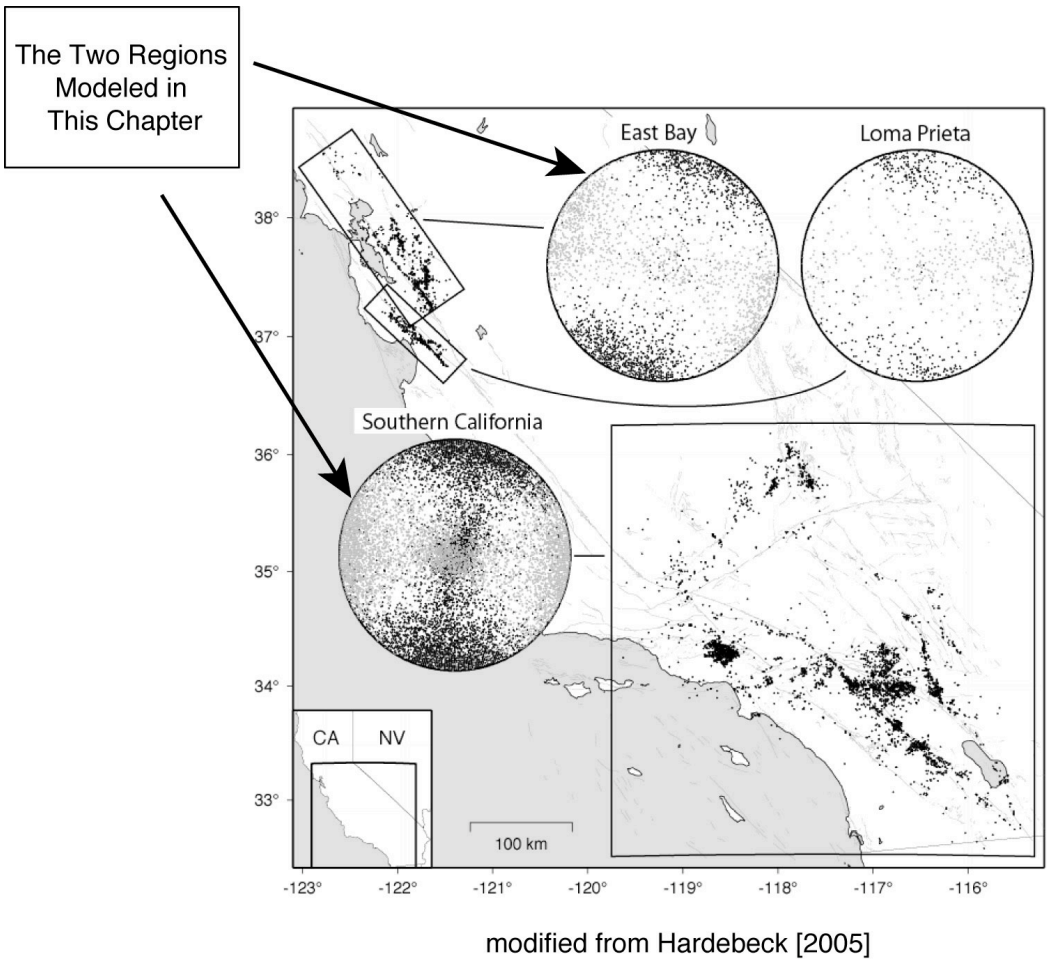

Figure 5.1. *A modified map of the three regions Hardebeck [in review, 2006] studied and P-T plots of the mechanisms used to calculate average focal mechanism difference as a function of length as seen in Figure 5.2. In this chapter we model two of the three regions, Southern California and East Bay. The P axes in the stereonet plot are the darker-shaded points. They are slightly rotated from a North-South trend. The T axes are the ligher-shaded points, slightly rotated from an East-West trend.*

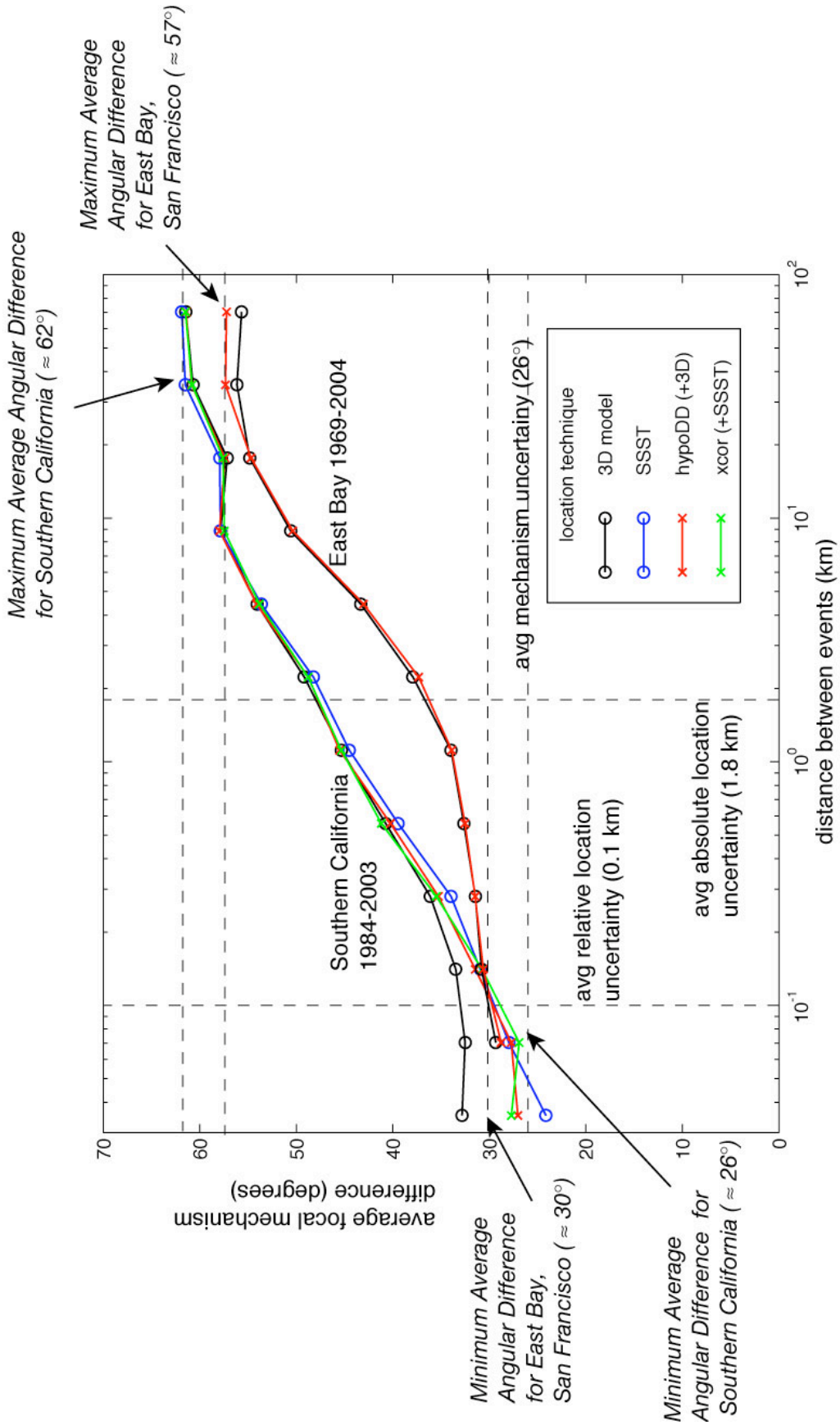
Maximum Average Angular Difference for Southern California (≈ 62°)
Maximum Average Angular Difference for East Bay, San Francisco (≈ 57°)
East Bay 1969-2004
Southern California 1984-2003
avg mechanism uncertainty (26°)
avg relative location uncertainty (0.1 km)
avg absolute location uncertainty (1.8 km)
location technique
3D model
SSST
hypoDD (+3D)
xcor (+SSST)
average focal mechanism difference (degrees)
distance between events (km)
Minimum Average Angular Difference for East Bay, San Francisco (≈ 30°)
Minimum Average Angular Difference for Southern California (≈ 26°)

Figure 5.2. *Average focal mechanism difference between pairs of focal mechanisms as a function of distance between the pairs, for two regions, Southern California and East Bay, San Francisco, modified from Hardebeck [in review, 2006]. At first glance, we can begin pulling out numbers that will help us parameterize the heterogeneity. If one assumes that the stress is approximately spatially uniform where the curve levels out for small scales on the left, then any non-zero average focal mechanism difference must be due purely to noise. When we numerically simulate the model noise, we will find how to reproduce a ~ 26° average focal mechanism difference or ~ 30° average focal mechanism difference for uniform focal mechanisms with noise added. The increasing average focal mechanism difference as a function of length is compatible with a spatially smoothed heterogeneous crust as we will show later. The maximum average focal mechanism difference should occur at the point where the points are far enough away that there is no longer significant spatial correlation due to smoothing. This curve flattens out to what one would expect for completely random, uncorrelated heterogeneous noise to produce; hence, the amplitude of this maximum will depend on the amplitude of the heterogeneity,* HR*, and of course the noise level. For Southern California, it flattens out to ~62° and for East Bay, San Francisco to ~57°. We will use these values to help us set the* HR *parameter. Last, the slope of the lines will help us set the spatial smoothing parameter,* α*. If* $\alpha = 0.0$*, Southern California would be a straight line at ~ 62°, and East Bay would be a straight line at ~ 57°. Instead, it appears that there is spatial smoothing to the heterogeneity. In general, the steeper the slope the more smoothed the heterogeneity; therefore, we would expect a larger value of* α *for East Bay, San Francisco than for Southern California.*

- Once we have an estimate of the model noise, the maximum average angular difference between focal mechanisms in Figure 5.2 can be used to estimate the heterogeneity ratio, HR. In Figure 5.2, the average angular difference increases as a function of distance then levels out at some maximum. When we produce similar plots from our numerical simulations using the three-component method from Chapter 4, we find that ratio of heterogeneity to σ'_B, HR, determines this maximum. If $HR \to \infty$, the average angular difference saturates at approximately 75°, whereas if $HR \approx 0$, the maximum is simply at the noise level because all the focal mechanisms have approximately the same orientations, and the only source of variation is noise.
- Last, the slope of the plots in Figure 5.1 will enable us to estimate the degree of spatial smoothness in the heterogeneity, the parameter, α. For example, if $\alpha = 0.0$, there is no spatial correlation between focal mechanisms, and each pair of focal mechanisms is equally uncorrelated regardless of spatial separation; hence, one would expect a flat line at the maximum angular difference associated with HR. As α increases, the slope will also increase because the stress tensors for closely spaced points are becoming increasing similar.

Estimating the Model Noise in Real Data Due to Focal Mechanism Orientation Uncertainty

In Figure 5.2, modified from Hardebeck [2006], the average angular difference reaches a minimum at ≈ 26° for the Southern California region and ≈ 30° for the East Bay region. We will assume that these minimum angular differences are purely an effect of

model noise, and that the stress itself is approximately uniform at those distances. We can simulate this by creating a set of focal mechanisms with the same orientations, adding Gaussian noise with different mean deviations, calculating the average angular difference between pairs of focal mechanisms, and eventually finding a level of Gaussian noise that duplicates the 26° and 30° minima. We add the model noise using the quaternion mathematics shown in Chapter 3, where we:

- Generate completely random unit quaternions.
- Convert them into our three rotation parameters, $(\omega,[\theta,\phi])$.
- Keep the random rotation axes, $[\theta,\phi]$, and combine them with a new ω'.
- The new ω' is generated using Gaussian white noise with a mean of zero and some specified mean deviation. The mean deviation is the parameter we need to vary to match it with the average angular difference of ≈ 26°.
- Convert $(\omega',[\theta,\phi])$ into unit quaternions and use quaternion multiplication to add these random rotations to the set of uniform focal mechanisms.
- Use these unit quaternions to transform the original focal mechanism and derive the new strike, dip, and rake, (Θ,δ,λ) or P and T axes.

Figure 5.3 shows what P-T axes would look like for different levels of model noise starting with completely homogeneous stress (all the focal mechanisms have the same orientation before adding the noise). We show a total of 2,000 focal mechanisms on each plot. On the left, we use the Southern San Andreas Fault background stress tensor, $\boldsymbol{\sigma}'_{B_1}$, that is applied to the simulations in Chapter 4, and on the right, we use the San Gabriel Mountains background stress tensor, $\boldsymbol{\sigma}'_{B_2}$, also from our simulations in

Chapter 4. We add noise onto these background stresses for ω mean deviations of 10°, 20° and 30°, where the mean noise deviation is defined as,

$$MeanDeviation = \frac{1}{N}\sum_{i=1}^{N}|\omega_i|. \tag{5.1}$$

When we try to estimate the model noise parameter for real data, we find that an ω mean deviation of ~ 17° yields an ~ 26° minimum angular difference as seen in Hardebeck [2006] for the Southern California region. For the East San Francisco Bay region, there may be a slightly larger minimum average angular difference, ~30°, which can be modeled with an ω mean deviation of ~ 20°. Figure 5.4 shows the average angular difference as a function of distance for uniform focal mechanisms that have had random Gaussian noise added with ~17° and ~ 20° mean deviations. They are approximately straight lines because we have simply added spatially uncorrelated noise to all points.

Southern San Andreas σ_B, Mean Deviaton = 10 Degrees

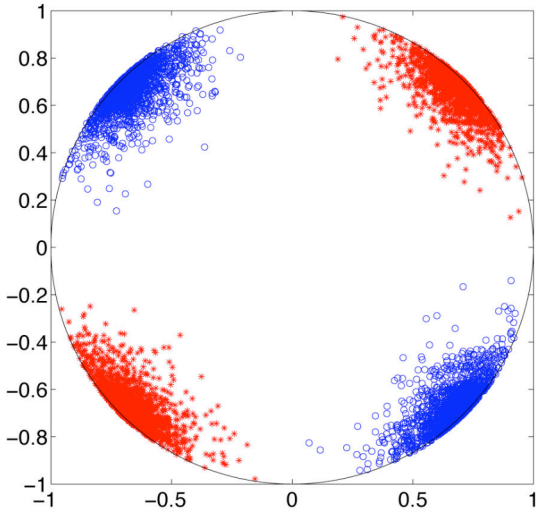

San Gabriel Mountains σ_B, Mean Deviaton = 10 Degrees

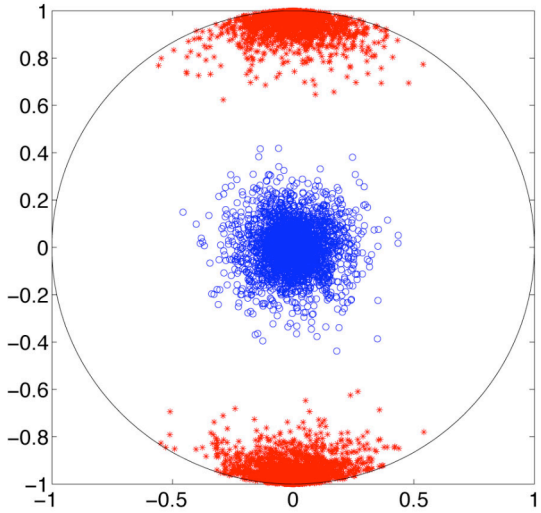

Southern San Andreas σ_B, Mean Deviaton = 20 Degrees

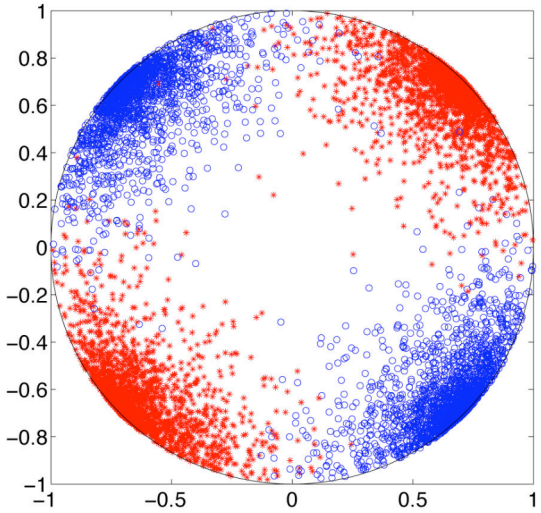

San Gabriel Mountains σ_B, Mean Deviaton = 20 Degrees

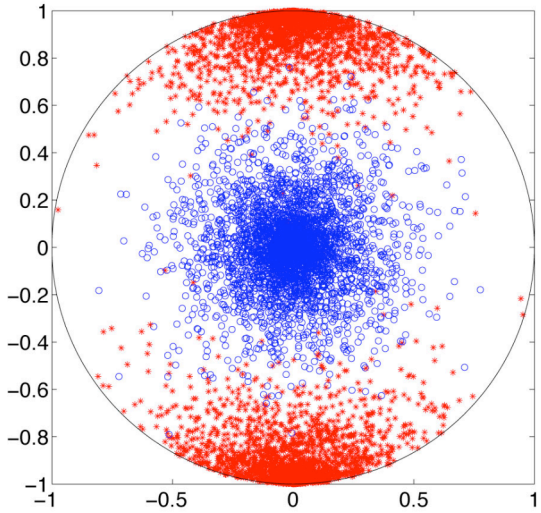

Southern San Andreas σ_B, Mean Deviaton = 30 Degrees

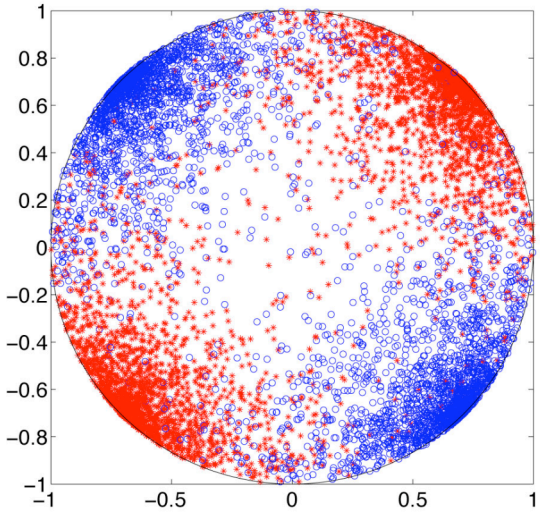

San Gabriel Mountains σ_B, Mean Deviaton = 30 Degrees

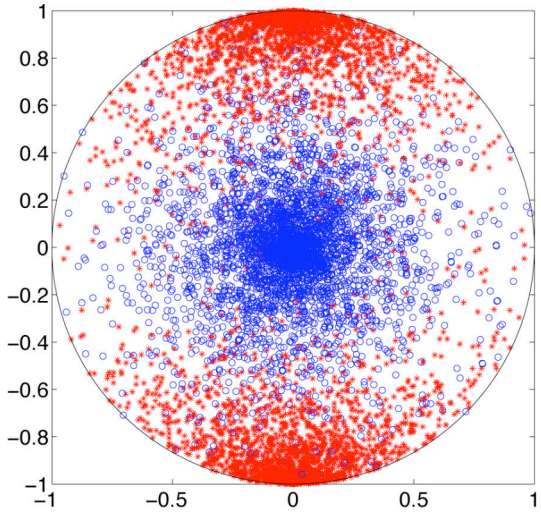

Figure 5.3. *P-T plots of noise. The P axes are plotted with red asterisks, and the T axes are plotted with blue open circles. For each plot, 2,000 focal mechanisms of the same orientation are given random rotations; therefore, any scatter in the P-T axes is due purely to model noise, not stress heterogeneity. On the left, we start with the Southern San Andreas Fault background stress tensor,* $\boldsymbol{\sigma}'_{B_1}$*, used in our simulations for Chapter 4. On the right we start with the San Gabriel Mountains background stress tensor,* $\boldsymbol{\sigma}'_{B_2}$*, also used in our Chapter 4 simulations. The top row plots the noise generated from random Gaussian angle rotations,* ω*, with mean deviation = 10°. The center row has a mean deviation of 20°, and the bottom row has a mean deviation of 30°. Mean deviations of* $\approx$ *17– 20° produce model noise that best matches real data, similar to the center row.*

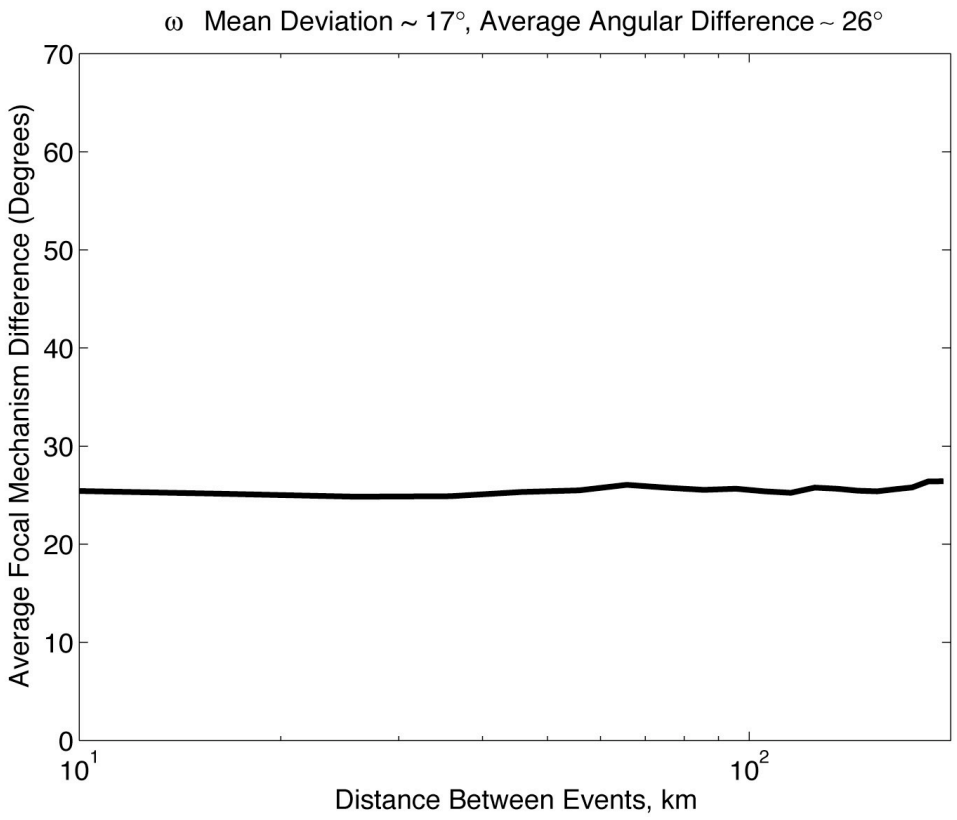
ω Mean Deviation ~ 17°, Average Angular Difference ~ 26°
Average Focal Mechanism Difference (Degrees)
0
10
20
30
40
50
60
70
10^1
10^2
Distance Between Events, km

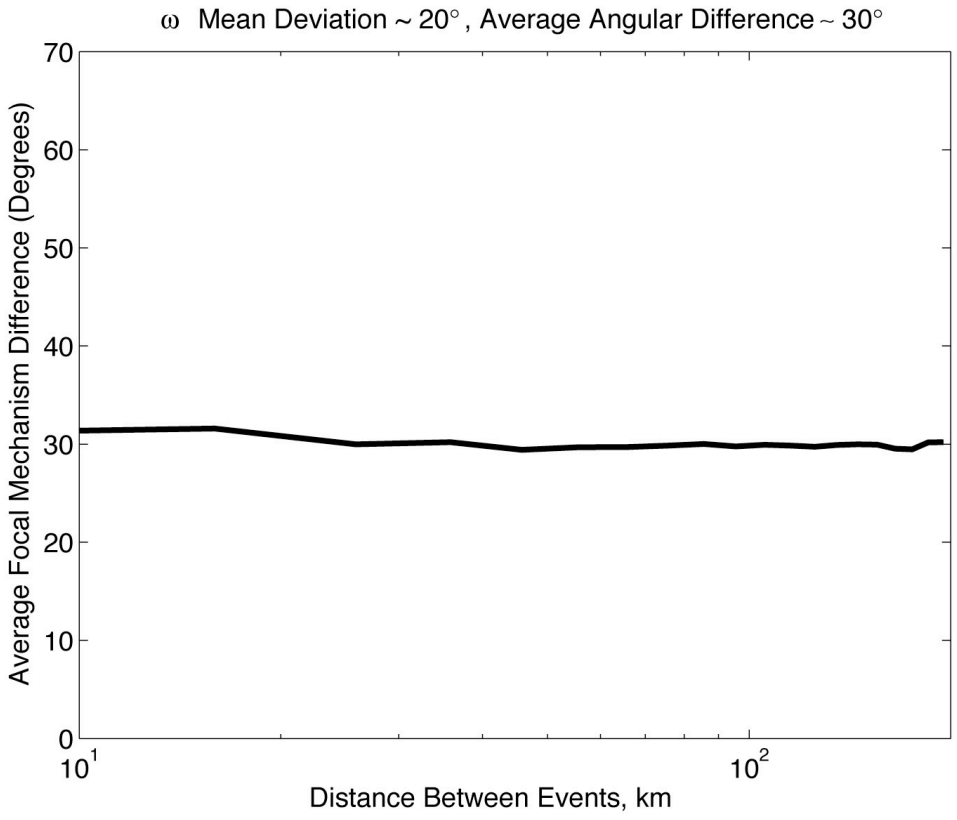
ω Mean Deviation ~ 20°, Average Angular Difference ~ 30°
Average Focal Mechanism Difference (Degrees)
0
10
20
30
40
50
60
70
10^1
10^2
Distance Between Events, km

Figure 5.4. *We start with 500 uniformly oriented focal mechanisms and add random Gaussian noise with a mean deviation of ~17° for the top plot and ~20° for the bottom plot. Then we calculate the average focal mechanism difference as a function of distance. It yields approximately straight lines at ~26° for the top plot and ~ 30° for the bottom plot. This matches the minimum values for Southern California and East Bay, San Francisco respectively in Figure 5.2; therefore, we now know how much model noise to add to our simulations to adequately represent focal mechanism uncertainties.*

Table 5.1. Misfit Statistics for Synthetic Simulations With Gaussian Noise Added

Mean Deviation for Simulations	Mean of the Misfit Angle	Standard Deviation of the Misfit Angle
Southern San Andreas, 17°	10.0944°	13.7134
San Gabriel Mountains, 17°	10.1084°	13.6266
Southern San Andreas, 20°	12.9599°	18.7245
San Gabriel Mountains, 20°	12.9816°	18.7866
Southern San Andreas, 26°	20.0672	29.0822
San Gabriel Mountains, 26°	20.0372	29.0511

For each row in the table, we generate 50 sets of 1,000 noisy uniform focal mechanisms and apply Andy Michael's program, "slick" [Michael, 1984; 1987]. Each inversion produces a mean misfit, and we average this parameter over the fifty sets. We start with two different uniform orientations, which we call the "Southern San Andreas Fault" and "San Gabriel Mountains" from Chapter 4, and apply Gaussian random noise with mean deviations of ~ 17° and ~20°. As the mean deviation of the model noise applied increases, so does the mean misfit angle from the inversions. Even though the Southern San Andreas and San Gabriel Mountains background stresses provide significantly different baseline orientations upon which model noise has been added, the mean misfit angles are nearly identical for these two types of simulations.

The relationships between mean deviation, standard deviation, and average deviation between points for a 1D Gaussian distribution in 1D Cartesian coordinates, can shed some light on our statistics. We know that for 1D Gaussians,

$$\text{Mean Deviation} = \sqrt{\frac{2}{\pi}}\ \text{Standard Deviation} \tag{5.2}$$

and

$$\text{Average Deviation Between Points} = \sqrt{2}\ \text{Standard Deviation.} \tag{5.3}$$

Consequently,

$$\text{Average Deviation Between Points} = \sqrt{\pi}\ \text{Mean Deviation.} \tag{5.4}$$

For 1D Gaussian distributions, if the Mean Deviation is 17, one would expect an Average Deviation Between Points of 30.13, and if the Mean Deviation is 20, one would expect an Average Deviation Between Points of 35.45. Our average angular differences of 26° and 30° are slightly smaller than one might expect for Mean Deviations of 17° and 20° using the above 1D statistics, but this most likely occurs because we are calculating the minimum angles between focal mechanisms using three dimensions instead of one. The statistics for 1D Cartesian Gaussians and our Gaussian angle, ω, do not have a one-to-one correspondence.

In Table 5.1 we show the statistics from applying a focal mechanism inversion program [*Michael*, 1984; 1987] to our noisy uniform focal mechanisms. For each row in the table, we generate 50 sets of 1,000 noisy uniform focal mechanisms and apply the program, "slick." The program attempts to find a best-fit spatially uniform stress field that minimizes the angular misfits between the actual slip vectors and the model slip vectors from a uniform stress field. One generated parameter is the mean angular misfit,

which we show in Table 5.1 for our homogeneous, but noisy focal mechanisms. This parameter is important because the mean angular misfit will increase as the stress heterogeneity increases. Therefore, one way of estimating the heterogeneity of a region is to

- Apply a focal mechanism inversion to the focal mechanisms in the region.
- Estimate the model noise in the focal mechanisms, due to uncertainty in focal mechanism orientations.
- Run several simulations of the region with 3D stress heterogeneity of different heterogeneous amplitudes, HR.
- Add the estimated model noise to the synthetic focal mechanisms.
- Apply the focal mechanism inversion to the noisy focal mechanisms.
- Compare the mean angular misfit from the real data in the region to the set of simulations with different levels of heterogeneity and find which HR produces a mean angular misfit that best matches the real data.

Estimating Stress Heterogeneity Parameters

We calculate the average focal mechanism difference as a function of distance for our simulations. Note, we are using the three-component method from Chapter 4 that calculates the minimum angle between focal mechanisms using only angular information. The stress ratio, R, is not taken into account. This is true for Figures 5.5–5.8. Taking the first 2,000 failures from our 3D numerical simulations we calculate the angular difference between each pair of synthetic focal mechanisms and average those values as a function of pair distance. Using the ω mean deviation levels of 17° and 20° to model

noise, we vary the two heterogeneity parameters, α and HR, until we find curves that approximately match Hardebeck's [2006] plots for Southern California and East Bay, San Francisco. In Figures 5.5–5.7, we first show the effect of varying our three parameters, α, HR, and the mean deviation of the ω noise. Then in Figure 5.8, we plot our best fits on top of Hardebeck's data for Southern California and East Bay, San Francisco.

The curves for Figures 5.5–5.7 are averaged over 4 different 3D simulations, using the same random seed for each α. Our final curves in Figure 5.8 use a minimum of five different random seeds, i.e, five different filtered 3D heterogeneous grids for each curve, and six different simulations per random seed, for a total of at least 30 different simulations for Southern California and 30 different simulations for the East Bay, San Francisco. We then plot the average focal mechanism difference as a function of length for these two sets of simulations on top of Hardebeck's data to assess our fit. The 3D simulations have a limited spatial frequency bandwidth, a little under two orders of magnitude, for several reasons: 1) The size of our grids in 3D is limited, unless we go to a supercomputer, because the number of points increases as N^3. Currently, all computations are being done on an Apple G5 computer so we limit ourselves to 201x201x201 grids. 2) The periodic boundary condition on the heterogeneity means that the average focal mechanism difference reaches a maximum at approximately 10^2 times the spacing between points, 10^2 grid spaces. 3) Distances less than 3 grid spaces produce unstable average focal mechanism differences because at that scale the discretization of the heterogeneous grid becomes important. Therefore, in Figure 5.8 our 3D results are plotted with solid lines for a bandwidth of 3 –100 grid spaces, a little under two orders of magnitude, where each grid space would approximately match 1 km in the real Earth.

To extrapolate to smaller distances and cover a greater spatial frequency bandwidth, we quickly calculate synthetic focal mechanisms, using smoothed 1D heterogeneous stress as defined in Chapters 2 and 3. We generate 1D smoothed heterogeneous stress with the same parameters as the 3D simulations, but with a greater bandwidth. Using lines of 100,001 points, we bring the first 2,000 points to failure and calculate the average focal mechanism difference as a function of distance. This produces curves with spatial frequency bandwidths of about three orders of magnitude, 1 more order of magnitude than our 3D simulations. We had hoped for four orders of magnitude, but the noise in the curves prevents this. There are some aspects of the 1D simulations we still need to study. In Figure 5.8 we just plot one simulation for Southern California and one plot for East Bay, San Francisco to give an initial idea. The 1D simulations are drawn with dashed lines and begin where the 3D simulations leave off. The 1D simulations for distances greater than 2 km become very noisy, but still generally follow the 3D numerical simulation curves and Hardebeck's [in review, 2006] data.

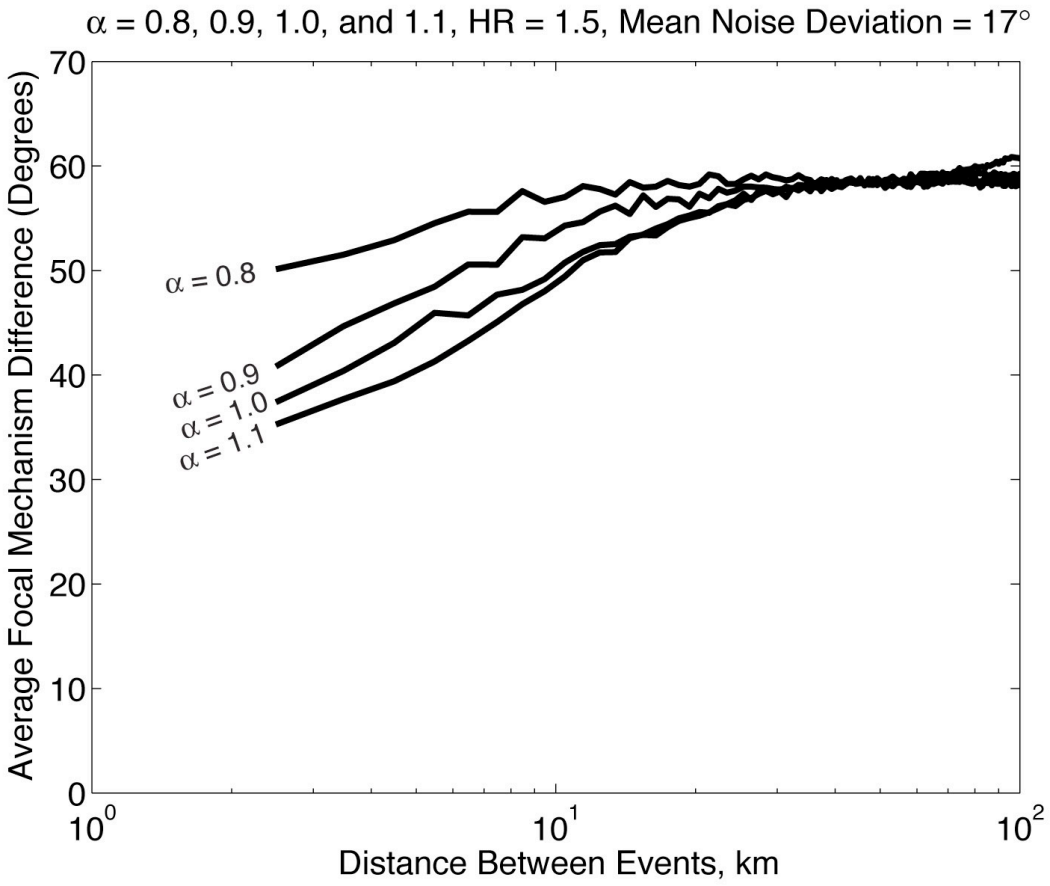

Figure 5.5. *Using the same random seed grid for each* α *, we run four different simulations for each curve and plot the average. Each curve has a heterogeneity ratio,* $HR = 1.5$ *, and an* ω *mean deviation of 17°. The spatial smoothing parameter,* α *, is varied, where* $\alpha = 0.8$ *corresponds to the most shallow curve on top, and* α *increases by 0.1 for each successive curve. As* α *increases, so does the slope of the average focal mechanism difference as a function of interevent distance. Interestingly,* α *does not appear to affect the maximum level at far interevent distances.*

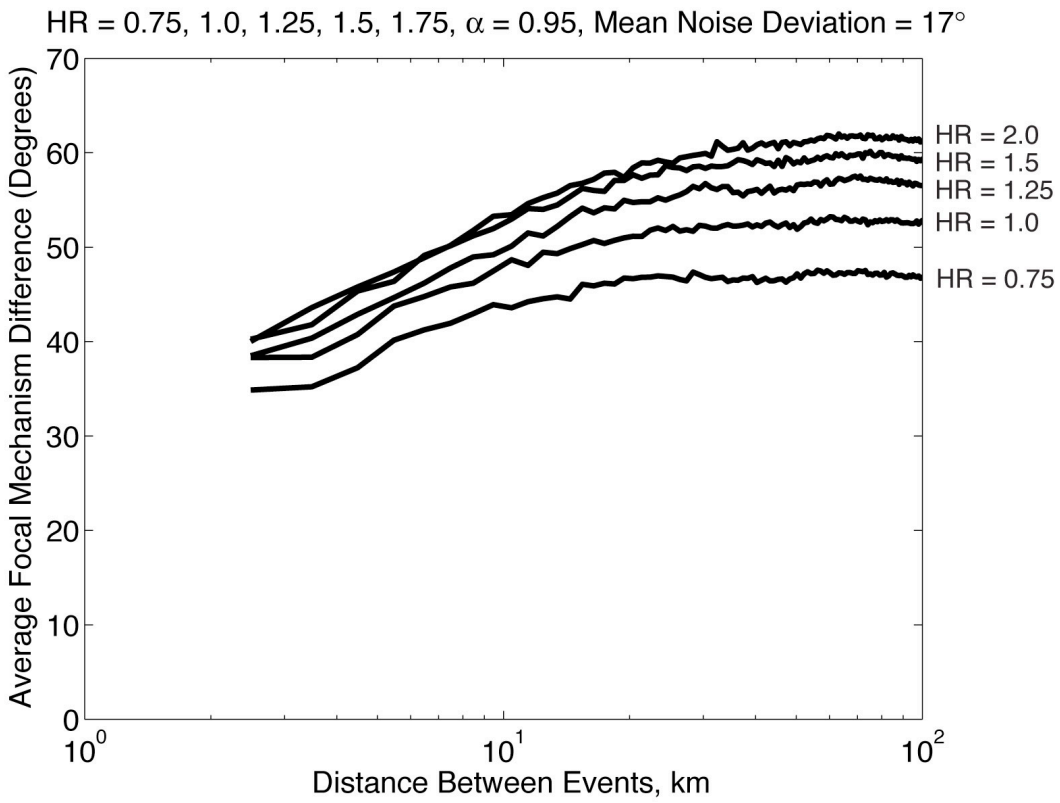

Figure 5.6. *Using the same random seed grid we run four different simulations for each curve and plot the average. Each curve has an* $\alpha = 0.95$ *and an* ω *mean deviation of 17°. The heterogeneity ratio,* HR*, is varied from* $HR = 0.75 - 2.0$*. As* HR *increases, the maximum average focal mechanism difference increases. Since* α *does not affect the maximum average focal mechanism difference and* HR *does, if we can fix the noise level, we can estimate* HR *from the maxima in Hardebeck's [in review, 2006] data.*

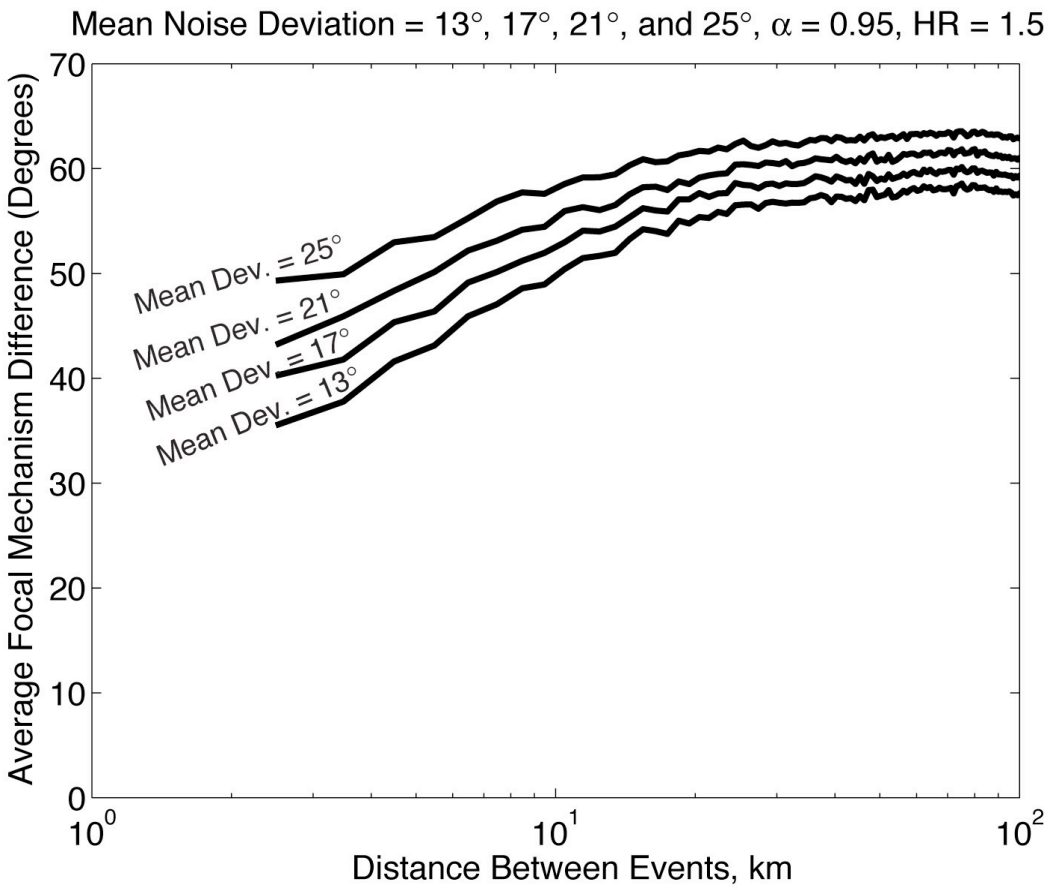

Figure 5.7. *Using the same random seed, we run four different simulations for each curve and plot the average. Each curve has an* $\alpha = 0.95$ *and an* $HR = 1.5$. *The* ω *mean deviation (focal mechanism uncertainty in real data) is varied from 13°–25° to show the effect of model noise on the simulations. As the mean deviation of the noise increases, two things happen. The curve's maximum increases, and the slope decreases. Therefore, it is important to have an accurate estimate of the model noise to parameterize both the heterogeneity ratio,* HR *and the spatial smoothing parameter,* α.

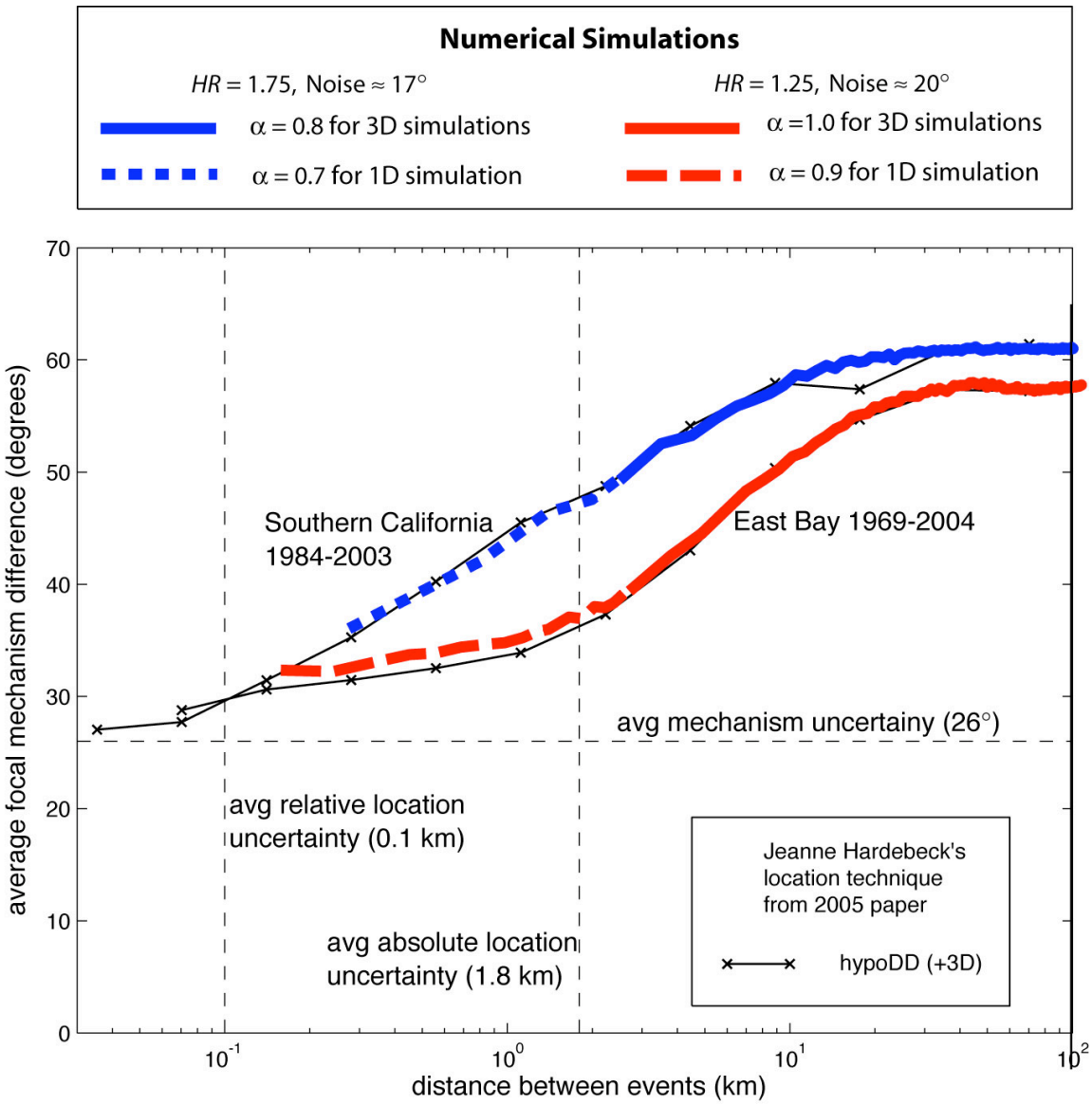

Figure 5.8. *Figure modified from Hardebeck [in review, 2006]. The thin black line for Southern California and East Bay is Hardebeck's HypoDD (+3D) solution for those two regions. The average focal mechanism difference increases with distance between focal mechanism pairs, indicating there is some type of smoothed heterogeneity. We calculate 3D and 1D simulations that seem to best fit the curves. We plot our results on top of Hardebeck's data, with solid lines for our 3D simulations and dashed lines for our 1D extrapolations. We find a heterogeneity ratio,* $HR = 1.75$ *, for Southern California in*

both our 3D and 1D simulations, and an $HR = 1.25$ *for East Bay in both our 3D and 1D simulations. The spatial smoothing parameter,* α *, estimated from these two types of simulations is slightly different. The value of* α *is approximately 0.1 lower in the 1D simulations for both Southern California and East Bay, San Francisco. Whether that is due to the reduced dimensionality or the increased bandwidth is yet to be determined. Our guess is that this is an effect of increased bandwidth in the simulation, and if we were to simulate the entire bandwidth of Hardebeck's data, almost four orders of magnitude, we might predict an* $\alpha = 0.6$ *for Southern California and an* $\alpha = 0.8$ *for East Bay, San Francisco.*

Southern California may have a larger HR and smaller α *than East Bay, San Francisco, due to the inclusion of aftershocks from moderate earthquakes such as Northridge, Landers, and Hector Mine.*

The 3D simulations give the following heterogeneity parameter estimates for Southern California, a spatial smoothing parameter, $\alpha = 0.8$, and an $HR = 1.75$ for a model noise level of 17° mean ω deviation. The initial 1D simulation uses the same $HR = 1.75$ and mean deviation of 17°, but requires a slightly smaller spatial smoothing parameter to fit the data, an $\alpha = 0.7$. From our 3D simulations of East Bay, San Francisco, we estimate an $\alpha = 1.0$ and $HR = 1.25$ with a model noise mean deviation of 20°, and from our initial 1D simulations, we estimate an $\alpha = 0.9$ and $HR = 1.25$ with a model noise mean deviation of 20°. While the 1D simulations require the same HR as the 3D simulations, the 1D simulations with the greater bandwidth require a spatially rougher stress, i.e., smaller values of α.

If we increase the bandwidth again to produce average focal mechanism difference as a function of distance to match Hardebeck's entire plots, we might predict our estimates of α to be lower once again (Table 5.2). This gives us a range of $\alpha = 0.6 - 0.8$ for Southern California and $\alpha = 0.8 - 1.0$ for East Bay, San Francisco. The heterogeneity ratios would still be $HR = 1.75$ for Southern California and $HR = 1.25$, for East Bay, San Francisco. Again these values of α are our best guess for now. What is particularly important in our parameterization is the heterogeneity ratio, HR, because this determines to what degree the focal mechanism inversion results are biased toward the stress rate tensor. Fortunately, HR appears to be a stable quantity in these parameterizations regardless of what α we use or spatial bandwidth we have.

Our guess as to why Southern California has a larger HR than East Bay, San Francisco, and smaller α, may be that Southern California includes aftershock data from moderate earthquakes such as Northridge and Landers. Initial simulations (not shown) of

aftershocks due to moderate-major earthquakes suggest that aftershocks tend to have a larger average focal mechanism difference than background seismicity because the significant static stress change accesses a greater variety of stress states, which would raise the HR estimate. Also, the mainshock may roughen the local stress state immediately after the earthquake [*Ben-Zion, et al.*, 2003] resulting in a lower estimate of the parameter α. In Figure 5.2, the curve for Southern California begins to flatten out at the same maximum angular difference as East Bay, San Francisco, about 57°, then begins to ramp up again and flattens out finally at approximately 62°. Our speculation is that the background seismicity in Southern California may actually have parameters similar to East Bay, San Francisco, an $HR = 1.25$, and predicted $\alpha = 0.8$. Adding the effects of aftershocks may produce a plot similar to Figure 5.2 for Southern California.

Table 5.2. Estimated Heterogeneous Parameters for Southern California and East Bay, San Francisco

	α Estimate for 3D simulations	α Estimate for 1D simulation	α Predicted	HR for all simulations
Southern California	0.8	0.7	0.6	1.75
East Bay, San Francisco	1.0	0.9	0.8	1.25

These are the estimated parameters from Figure 5.8. Because of the limited bandwidth of the 3D simulations, we probably overestimate the spatial smoothing parameter, α. *The 1D simulations with greater bandwidth, almost three orders of magnitude spatially, lead us to estimates of* α, *approximately 0.1 less than the 3D simulations. If we were to successfully model the entire bandwidth shown in Figure 5.8, it may lower the estimates of* α *once more. The best we can say at this point is that an* α *in the range of* $0.6 - 0.8$, *may fit the data for Southern California, and an* α *in the range of* $0.6 - 0.8$ *may fit the data for East Bay, San Francisco. Interestingly, the 1D simulations work with the same* HR, $HR = 1.75$ *for Southern California and* $HR = 1.25$ *for East Bay, San Francisco; therefore, this parameter may be insensitive to bandwidth*.

Comparing Inversions of Real Focal Mechanism Data to Inversions of Our Synthetic Focal Mechanisms

Using Hardebeck's 1984–2003 Southern California data set [*Hardebeck and Shearer*, 2003] from the web site, www.data.scec.org/research/altcatalogs.html, we apply Andy Michael's "slick" focal mechanism inversion program to A and B quality data for seven regions. We attempt to avoid aftershock zones such as Northridge, Landers, and Hector Mine. Using a type of bootstrapping for each region, we resample the region until we have 1,000 focal mechanisms, invert the data, and repeat this 50 times. We then average two of the statistics, mean misfit angle and the standard deviation of the misfit angle over the 50 inversions. See Table 5.3 and Figure 5.9 for the P-T plots of the seven regions we sample and the statistics we compute.

In order to compare our synthetic focal mechanisms to the real focal mechanisms, we apply the inversion program "slick" to our numerical simulations in the following manner. For each simulation we add model noise (to simulate focal mechanism measurement error) with a specified mean deviation, invert 1,000 noisy focal mechanisms, repeat this 50 times (adding a different random noise each time), and average the mean misfit angle and standard deviation misfit angle over the 50 sets. We create these statistics for $\alpha = 0.0, 0.5, \text{and } 1.0$, $HR = 0.1 - 100$, and mean ω deviation = 17°, 20°, and 26°, to examine the effect of each parameter. Typically, the greater the heterogeneity is, HR, the larger the mean misfit angle and the standard deviation of the misfit angle. Varying α, for $\alpha = 0.0 - 1.0$, appears to have little to no effect on the statistics. Increasing the noise, the mean ω deviation also increases the mean misfit angle and the standard deviation of the misfit angle.

Table 5.3. Seven Study Regions in Southern California from A and B Quality Focal Mechanism Data

	Latitude Range (°N)	Longitude Range (°E)	Mean Misfit Angle (Degrees)	Standard Deviation of the Misfit Angle (Degrees)	Number of Points
Test Region 1 LA Basin	33.75–34.25	241.2–241.7	18.0641	20.7630	192
Test Region 2 San Gabriel Mountains	34.25–34.5 34.4–34.7 34.5–37.5	241.75–242.25 241.5–241.75 241.25–241.5	24.7288	25.7336	64
Test Region 3	33.5–33.75	243–243.25	24.2155	25.7085	170
Test Region 4	33.75–34	243–243.25	23.6730	20.1619	260
Test Region 5	33.5–33.75	243.25–243.5	25.9741	21.6666	215
Test Region 6	33.25–33.5	243.5–243.75	22.3788	22.2544	191
Test Region 7	33.75–34	243.5–243.75	21.1410	19.6019	222

We picked seven regions to study, preferably with minimal aftershock activity. Columns 2 and 3 are the Latitudes and Longitudes that prescribe the box within which we choose focal mechanisms for the seven regions from the A and B quality data [Hardebeck and Shearer, 2003]. Using a type of bootstrapping explained in the text, we calculate the mean misfit angle and the standard deviation of the misfit angle for our three regions. These values are plotted in Figures 5.10–5.12. Then in Figure 5.13 we use the mean misfit values for each region to estimate their heterogeneity ratios, HR.

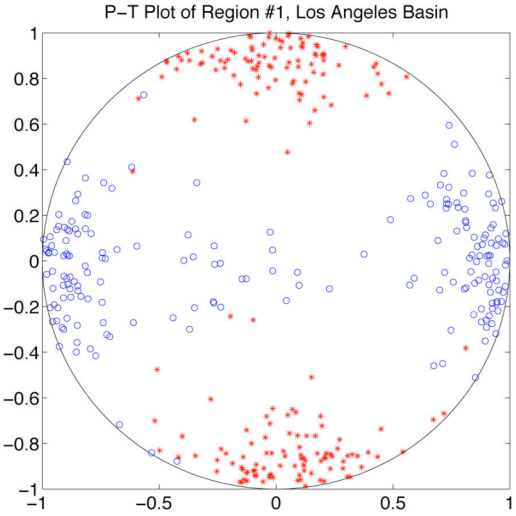
P–T Plot of Region #1, Los Angeles Basin

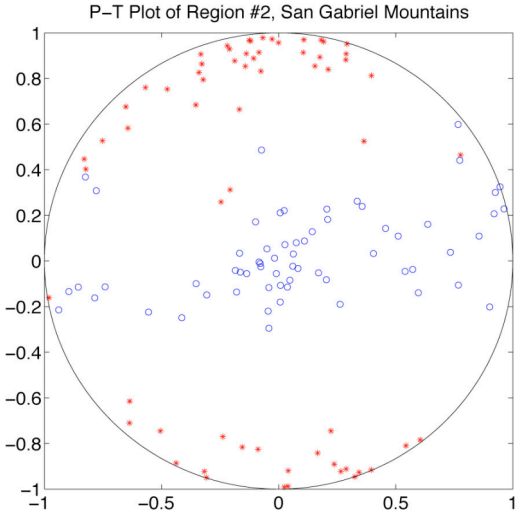
P–T Plot of Region #2, San Gabriel Mountains

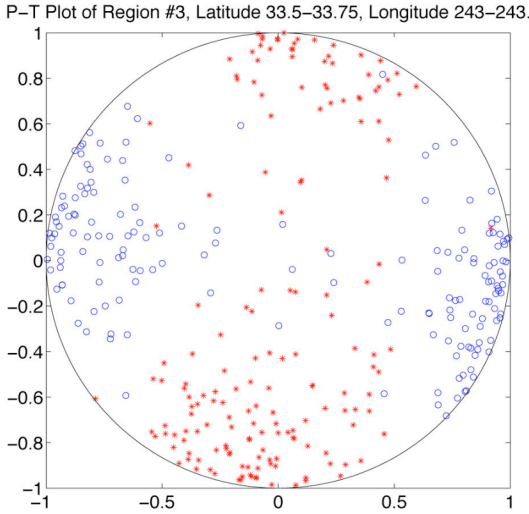
P–T Plot of Region #3, Latitude 33.5–33.75, Longitude 243–243.25

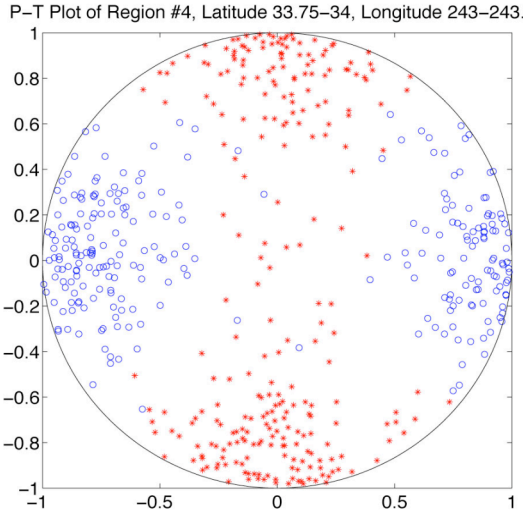
P–T Plot of Region #4, Latitude 33.75–34, Longitude 243–243.25

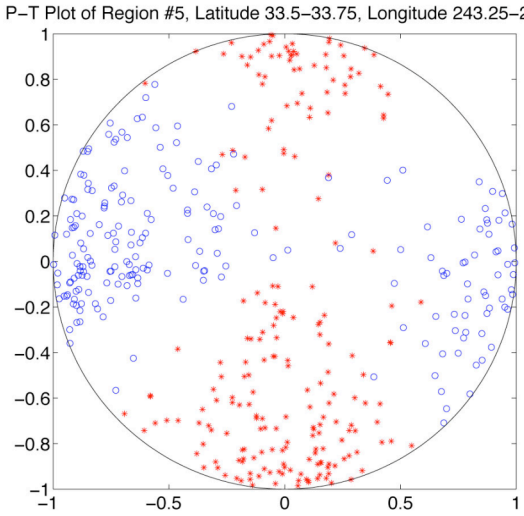
P–T Plot of Region #5, Latitude 33.5–33.75, Longitude 243.25–243.5

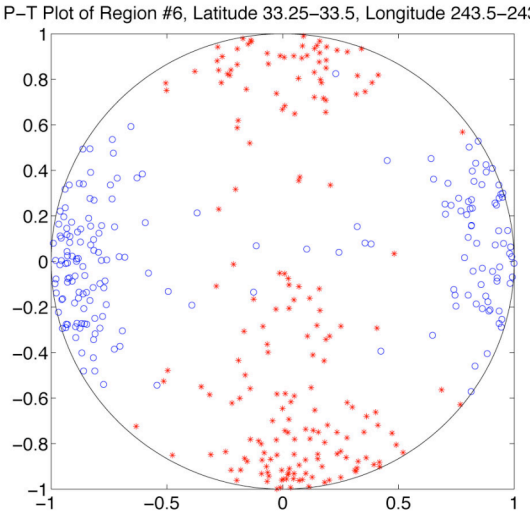
P–T Plot of Region #6, Latitude 33.25–33.5, Longitude 243.5–243.75

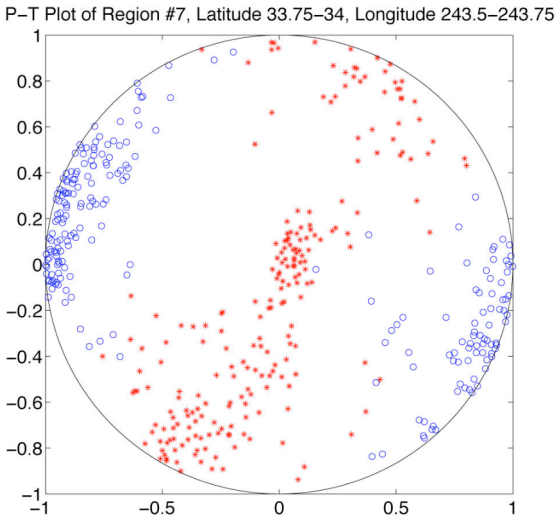

Figure 5.9. *P-T plots of the seven study regions from the A and B quality focal mechanism data. The red asterisks represent the P (compression) axes and the blue open circles represent the T (tension) axes for each focal mechanism.*

Interestingly, measurement noise and heterogeneity appear to increase these two statistics differently. Defining a new parameter, which we will call the misfit ratio,

$$MR = \frac{\text{Mean Misfit Angle}}{\text{Standard Deviation of the Misfit Angle}}, \tag{5.5}$$

we find that if there is only model noise and no stress heterogeneity one would expect a $MR \approx 0.7$. If there is no model noise and only stress heterogeneity, one could achieve a $MR \approx 1.5$. One way of assessing whether or not a mean deviation of 17° is appropriate for Southern California is to compare the mean misfit angle and the standard deviation of the misfit angle for our simulations with different α, HR, and noise to our seven regions in Table 5.3. In Figures 5.10, we explore this by plotting mean misfit angle vs. standard deviation of the misfit angle for our simulations and for our seven regions of real focal mechanism data. Generally, as HR increases (variable not shown), both the mean misfit

angle and the standard deviation of the misfit angle increase, creating the lines seen in Figure 5.10. The three red dashed lines represent α = 0.0, 0.5, and 1.0 , for the simulation background stress, "Southern San Andreas," $\boldsymbol{\sigma}'_{B_2}$, from Chapter 4 with a mean model noise deviation of 17° added to the synthetic focal mechanisms. The three solid blue lines represent α = 0.0, 0.5, and 1.0 , for the simulation background stress, "San Gabriel Mountains," $\boldsymbol{\sigma}'_{B_1}$, from Chapter 4, with a mean model noise deviation of 17° added to the synthetic focal mechanisms. The lines follow the path of increasing heterogeneity, HR , in the mean misfit angle vs. standard deviation of the misfit angle space. We plot small solid circles for the end-member, $HR = 0$, case from Table 5.1. Last, we plot the values computed for our seven regions listed in Table 5.3, with black asterisks. The point of this graph is to show that the real data, with black asterisks, are compatible with the predicted mean misfit angles and standard deviation of the misfit angles from our numerical simulations when we add a mean model noise deviation of 17° to our synthetic focal mechanisms. The real data points fall within the possible range of values. In Figure 5.11, we have the exact same graph but now a mean model noise deviation of 20° has been added to our synthetic focal mechanisms and our synthetic lines are no longer centered on the real data, indicating 20° could be an overestimate for Southern California data, at least for these seven regions. Increasing the mean model noise deviation again to 26°, we plot in Figure 5.12 the same information. The real data are completely offset from our synthetic curves, indicating that a mean noise deviation of 26° is an overestimate of noise for those regions in Southern California. These results give us increased confidence in using our mean model noise deviation of 17° when parameterizing α and HR in Southern California.

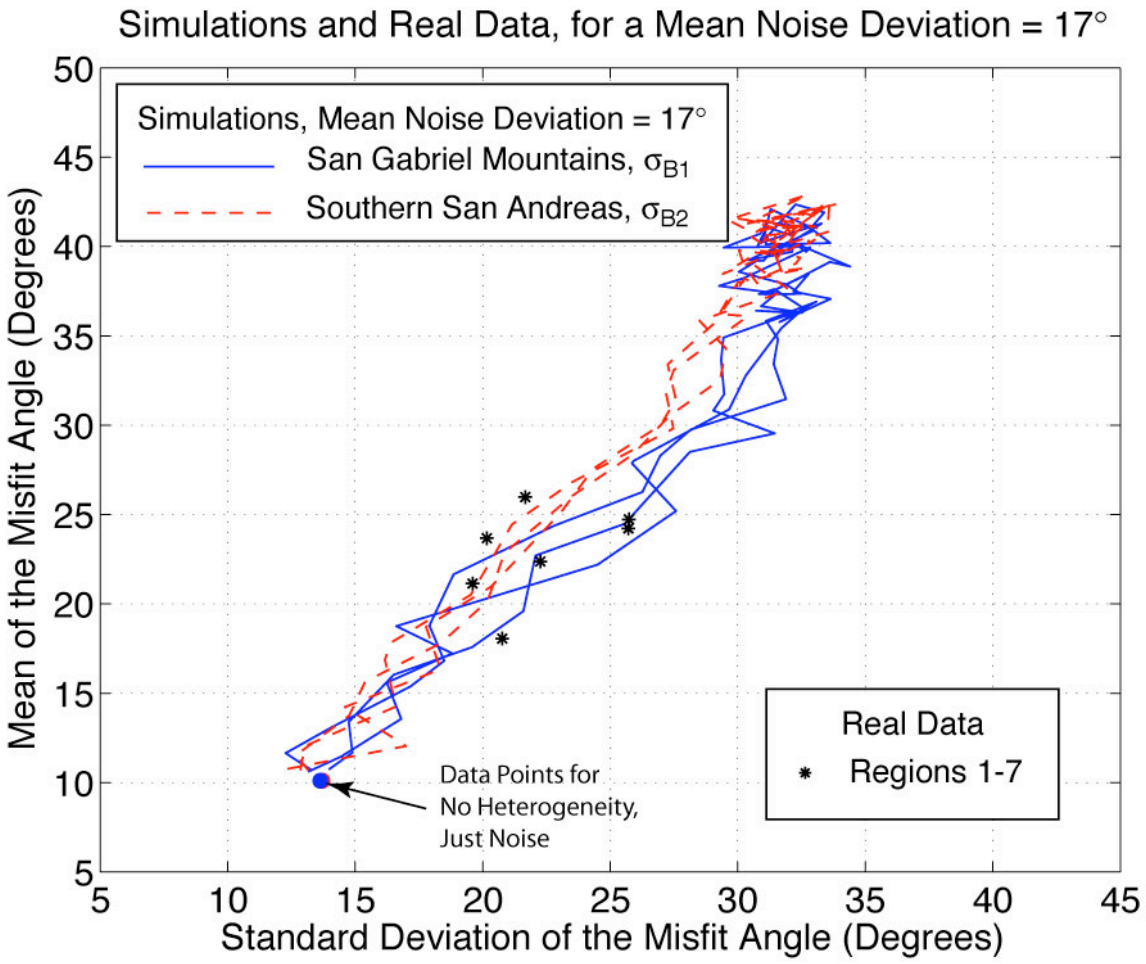

Figure 5.10. *In this Figure we compare two observables, mean misfit angle and the standard deviation of the misfit angle, for noisy simulated focal mechanisms and real data from our regions 1–7. While these two parameters should be linearly related for a Gaussian distribution, the distributions of focal mechanism orientations are not necessarily Gaussian. When we start adding model noise to our synthetic, heterogeneous focal mechanisms, we find that the ratio of mean misfit angle vs. standard deviation of the misfit angle, MR, depends on how much of the scatter comes from model noise vs. true stress heterogeneity. In this plot, we add noise with a mean model noise deviation*

of 17° (what we use when trying to parameterize Southern California in Figure 5.8) to our synthetic focal mechanisms, invert the focal mechanisms to calculate the mean misfit angle and standard deviation of the misfit angle, repeat this procedure fifty times, and average the two parameters. We do this for a range of $HR = 0.1 - 100$ *and plot the path of increasing* HR *in the mean misfit angle vs. standard deviation of the misfit angle space. The red dashed lines are for* $\alpha = 0.0, 0.5,$ and 1.0*, using the "Southern San Andreas" background stress,* $\boldsymbol{\sigma}'_{B_2}$*, from Chapter 4. The blue solid lines are for* $\alpha = 0.0, 0.5,$ and 1.0 *using the "San Gabriel Mountains" background stress,* $\boldsymbol{\sigma}'_{B_1}$*, from Chapter 4. We find that the* α *parameter has little to no effect on the calculation of the mean misfit angle or standard deviation of the misfit angle parameters. The black asterisks are the seven study regions. We find that their mean misfit angle and standard deviation of the misfit angle fall within the possible values for our noisy simulated data. The real data for seven regions in Southern California are nicely centered on the simulated curves. Therefore, it appears that the addition of a mean model noise deviation of 17° to our synthetic focal mechanisms produces statistics compatible with real data.*

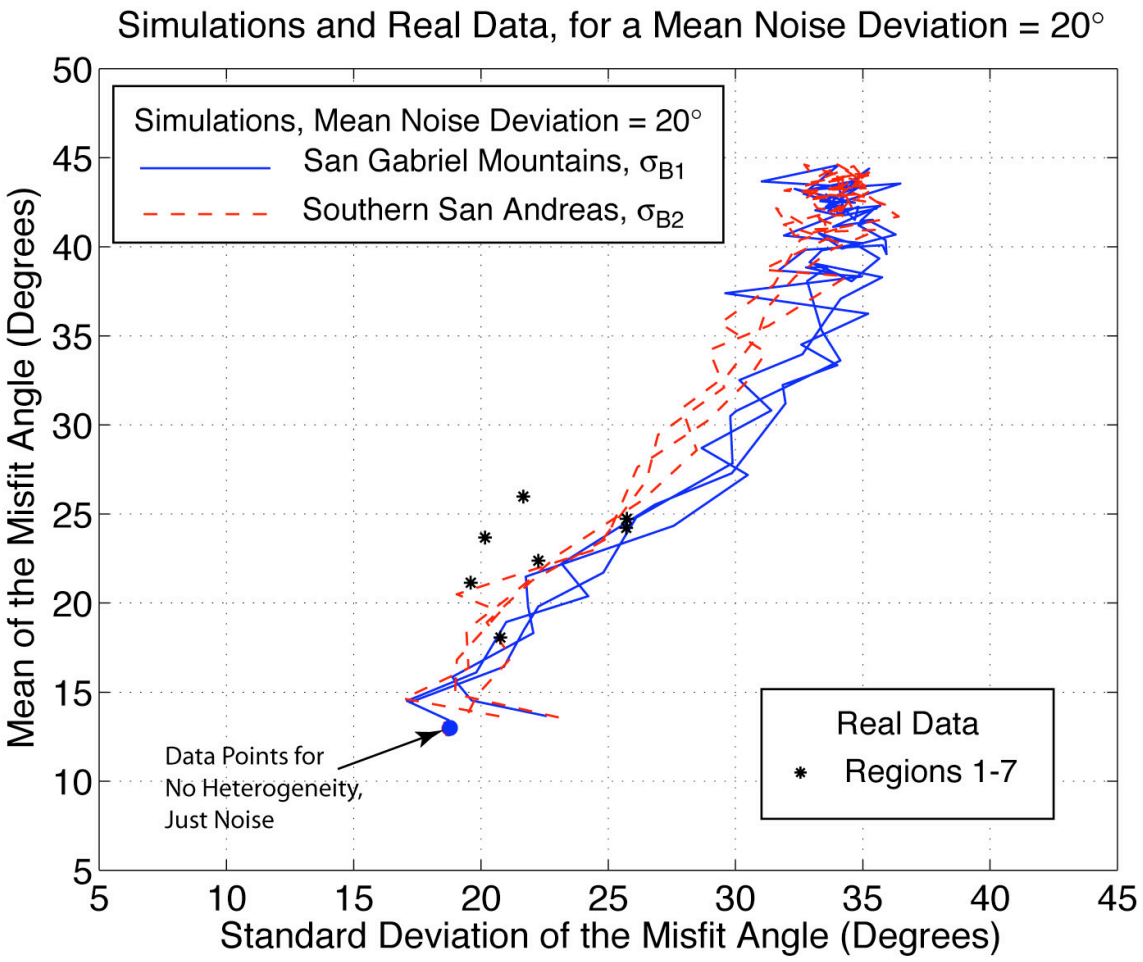

Figure 5.11. *Symbology as in Figure 5.10, with a mean model noise deviation of 20° added to the synthetic focal mechanisms. The paths of increasing heterogeneity in the mean misfit angle vs. standard deviation of the misfit angle space no longer center on the real data in black asterisks, our Southern California regions 1–7. Instead, the paths are slightly offset to the bottom right. This level of model noise is what we use for the East Bay San Francisco parameterization, but it appears that it is not as compatible as 17° for the Southern California data. This is a good check. It shows that we most likely use the correct level of model noise, mean deviation of 17°, for our parameterization of Southern California.*

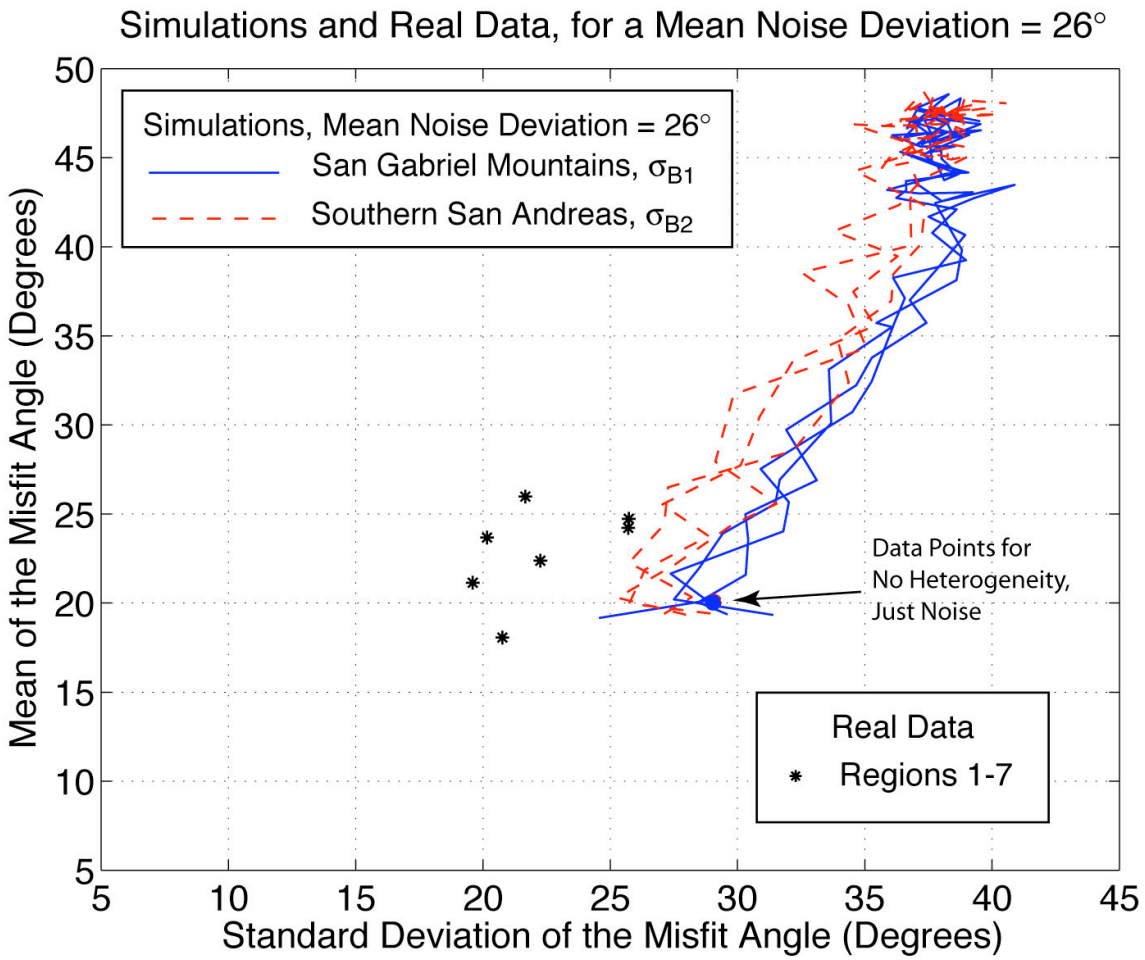

Figure 5.12. *Same type of plot as Figures 5.10 and 5.11, only we further increase the mean model noise deviation to 26°. In this case, the paths of increasing heterogeneity, the red dashed and blue solid lines, for our noisy simulated data are completely offset from the real Southern California data. This indicates that a mean deviation of 26° overestimates the model noise for background seismicity in Southern California.*

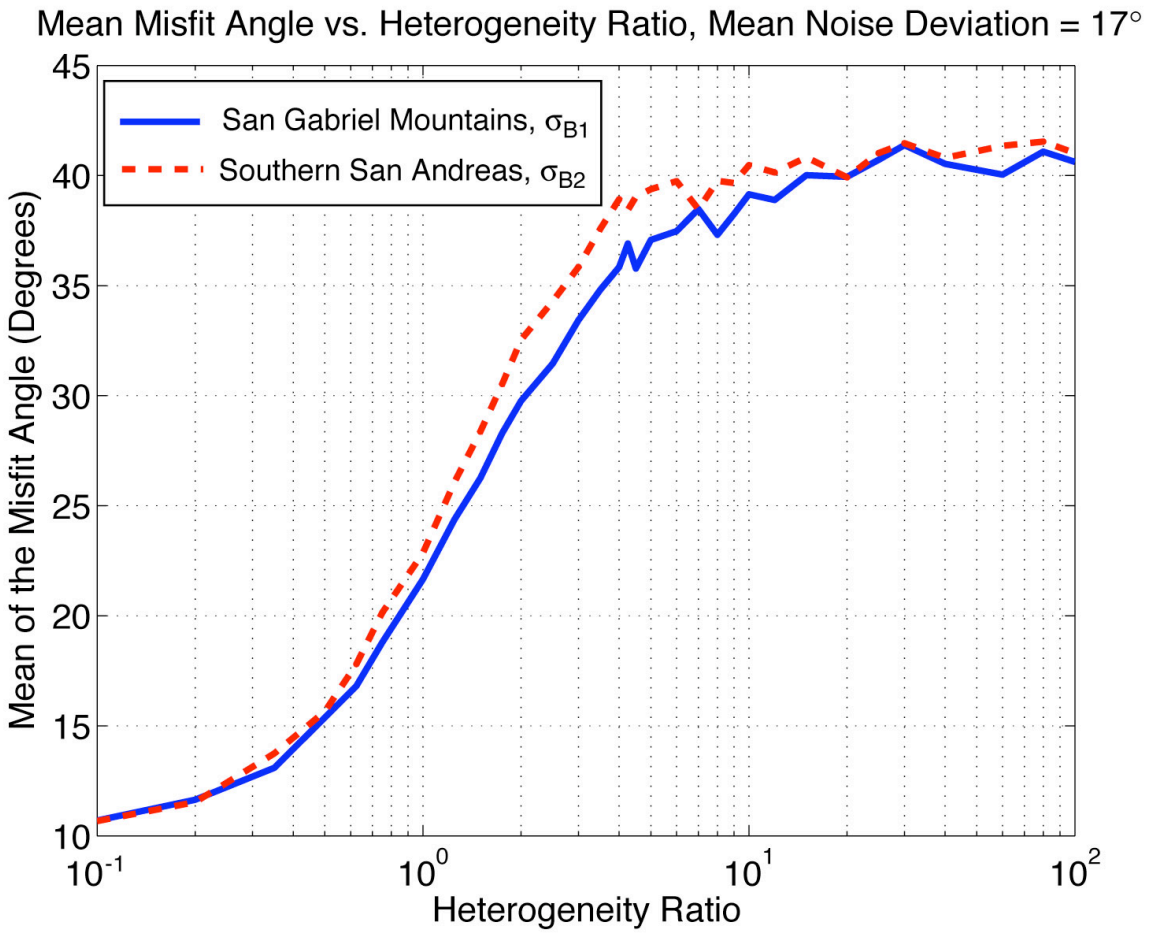

Figure 5.13. *This plot of mean misfit angle as a function of Heterogeneity Ratio, HR was constructed by adding a mean model noise deviation of 17° to our synthetic focal mechanisms for* $\alpha = 1.0$*, inverting the focal mechanisms using the program "slick" [Michael, 1984; 1987] to produce the mean misfit angle, repeating this 50 times, then averaging the mean misfit angle. The solid blue line uses the simulations with the "San Gabriel Mountains" background stress,* σ'_{B_1}*, and the dashed red line uses the simulations with the "Southern San Andreas" background stress,* σ'_{B_2}*, both introduced in Chapter 4. For these two very different background stresses, the mean misfit angle vs. HR curves are fairly similar. Of greater interest is that the increase of mean misfit angle as a function of HR has a very similar shape to the curves in Figure 4.12. In*

Figure 4.12, we plot the percent bias toward the stress rate tensor, $\dot{\boldsymbol{\sigma}}'_T$, as a function of HR. This gives us hope that there may be a linear relationship between mean misfit angle for real data and the bias toward the stress rate tensor, $\dot{\boldsymbol{\sigma}}'_T$.

It is true that the mean misfit angle and the standard deviation of the misfit angle are related by a constant for a 1D Gaussian distribution; therefore, in our attempt to vary the noise until we have an appropriate misfit ratios, MR, that matches real data, we are really varying the shape of the distribution of the focal mechanism scatter until it is similar to what is seen in the real Earth.

Now that we have confirmed that a mean model noise deviation of ≈17° is appropriate for the Southern California, we plot in Figure 5.13 the mean misfit angle as a function of heterogeneity ratio, HR for our simulated data with 17° model noise added. Presumably, we can use this relationship between mean misfit angle and heterogeneity to estimate the HR for real data. In Figure 5.13, we use a mean model noise deviation of 17° added to our synthetic focal mechanisms, and we use an $\alpha = 1.0$, which is close to our estimated α. The value of α has little to no effect on the curves in Figure 5.13 so it probably does not matter exactly what value to use in these calculations so long as it is close to our estimate. The solid blue line shows our results for simulations with a "San Gabriel Mountains" background stress, $\boldsymbol{\sigma}'_{B_1}$, and the red dashed lines shows our results for simulations with a "Southern San Andreas" background stress, $\boldsymbol{\sigma}'_{B_2}$. There are three features to note: 1) Mean misfit angle increases with heterogeneity ratio, HR. 2) The

two very different sets of simulations give similar curves. 3) The relation between mean misfit angle and HR looks very similar to the relation between the normalized bias toward our stress rate tensor, $\dot{\boldsymbol{\sigma}}'_T$, and HR as seen in Figure 4.12 in the previous chapter. This gives us hope that we can use the mean misfit angle in focal mechanism inversions for the real Earth to estimate both the heterogeneity ratio, HR, and the percent bias toward the stress rate tensor, $\dot{\boldsymbol{\sigma}}'_T$. Figure 5.14 explores this relationship, by plotting the percent bias toward $\dot{\boldsymbol{\sigma}}'_T$ from Figure 4.12 as function of mean misfit angle using the parameter, HR, to connect the two quantities; therefore, the solid lines are paths of increasing heterogeneity, HR. We plot this for our two sets of simulations, "San Gabriel Mountains," $\boldsymbol{\sigma}'_{B_1}$, and the "Southern San Andreas," $\boldsymbol{\sigma}'_{B_2}$. We find that the relationship between percent bias toward $\dot{\boldsymbol{\sigma}}'_T$ as a function of mean misfit angle is approximately a linear relationship for a mean misfit angle range of 15°–37°. The two sets of simulations produce slightly different slopes and intercepts for the linear best fits (see dashed lines in Figure 5.14), but there is some similarity. This type of relationship between percent bias and mean misfit angle needs to be studied further, and the effects of all the simulation parameters carefully dissected before we will have much confidence. At the same time, it is a starting point.

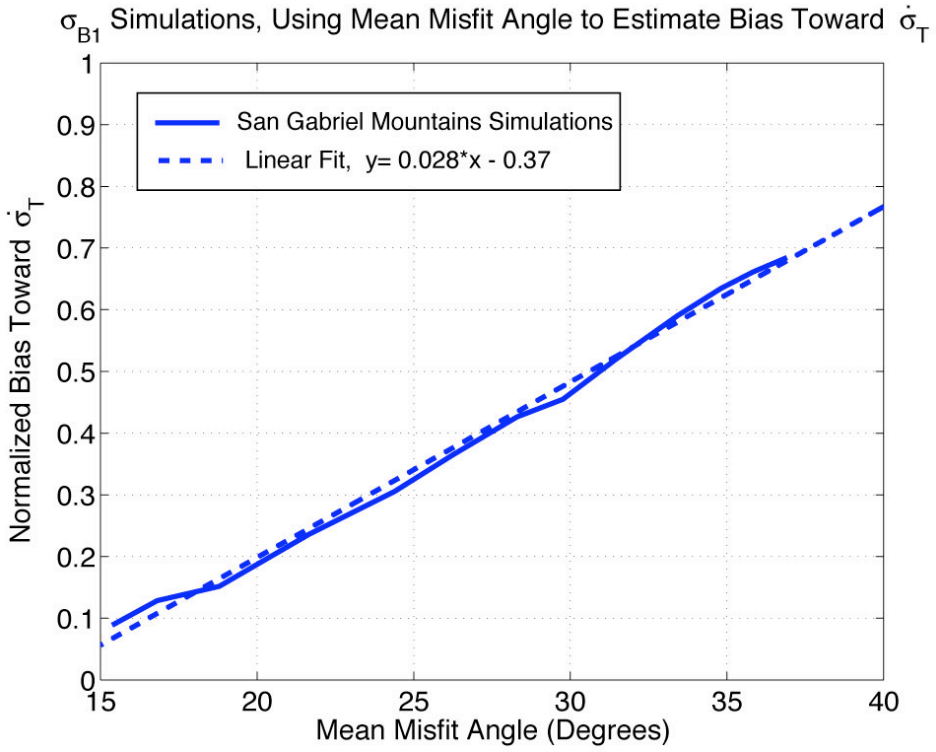

Figure 5.14 a)

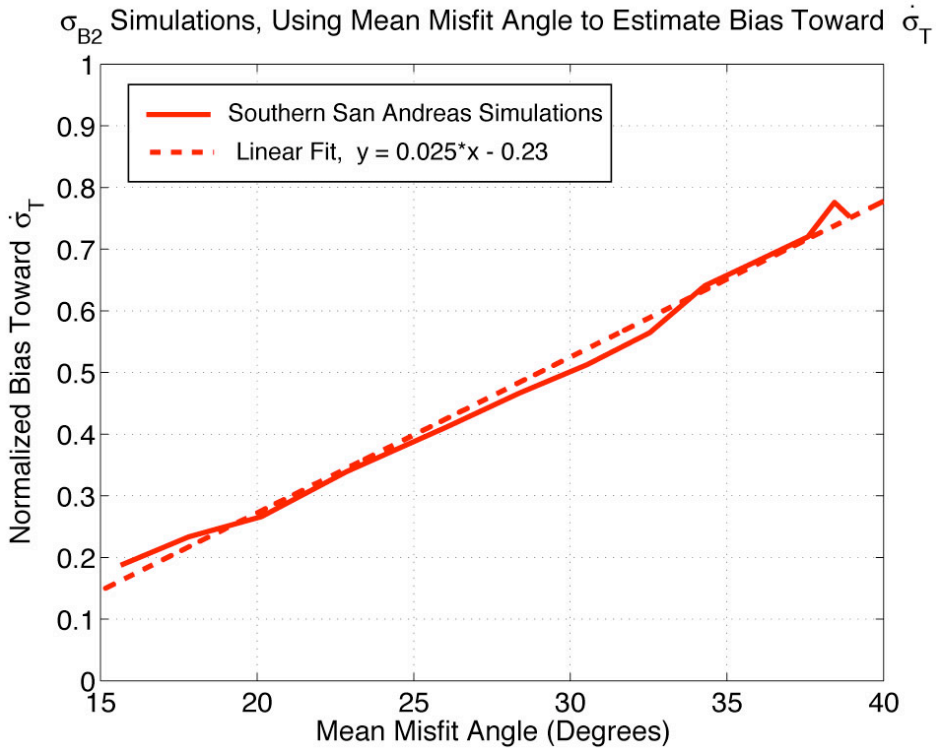

Figure 5.14 b)

Figure 5.14. *We plot paths of increasing HR in the bias toward* $\dot{\sigma}'_T$ *vs. mean misfit angle space. We use the relationship between bias and HR, and the relationship between mean misfit angle and HR to create these plots. The solid lines are our numerical simulations, synthetic focal mechanisms with* $\alpha = 1.0$*, a mean model noise deviation of 17°, averaged over 50 sets of noise. The dashed lines are the best fit linear relationships. In* ***a)*** *we plot the relationship between normalized bias and mean misfit angle for our "San Gabriel Mountains" simulations and in* ***b)*** *we plot the same relationship for our "Southern San Andreas Fault" simulations (See Chapter 4). Both sets of simulations produce a fairly linear relationship between normalized bias and mean misfit angle for a mean misfit angle range of ≈ 15–37°. The slopes and intercepts and the two lines are slightly different, but they lead to similar estimates of bias. We apply these curves to our seven regions of real focal mechanism data to estimate percent bias toward* $\dot{\sigma}'_T$ *and show the results in Table 5.4.*

Hypothetically, using this type of plot, one can subtract out the bias toward the stress rate tensor, $\dot{\boldsymbol{\sigma}}'_T$, to give the actual orientation of the background stress, $\boldsymbol{\sigma}'_B$. The procedure may be as follows:

- Select a region to study.
- Remove the aftershocks, if any, and invert the focal mechanisms within the region.
- From the mean misfit angle, estimate the heterogeneity ratio, HR, in the region and the percent bias toward the stress-rate tensor, $\dot{\boldsymbol{\sigma}}'_T$.
- Compare the orientation of the best-fit stress tensor from the focal mechanism inversion to the predicted stress-rate tensor from GPS data/modeling. Models like those of Becker et al. [2005] , which combine fault block modeling with GPS data as constraints, can provide the stress-rate tensors.
- If the focal mechanism inversion tensor and the stress-rate tensors are nearly identical, and $HR < 5.0$ (maximum bias of 70%), then one can estimate that the stress rate tensor, $\dot{\boldsymbol{\sigma}}'_T$, and the background stress, $\boldsymbol{\sigma}'_B$, are approximately aligned with one another.
- If there is a significant difference between the focal mechanism inversion tensor and the stress-rate tensor, and $HR > 0.5$ (minimum bias of 10%), then there is an even greater difference between the $\boldsymbol{\sigma}'_B$ and $\dot{\boldsymbol{\sigma}}'_T$. Use the estimate of the percent bias toward $\dot{\boldsymbol{\sigma}}'_T$, combined with the values of the inverted tensor, $\boldsymbol{\sigma}'_{Inverted}$, and $\dot{\boldsymbol{\sigma}}'_T$, to estimate $\boldsymbol{\sigma}'_B$.

In summary, this new methodology may enable seismologists to still use standard focal mechanism inversions to estimate $\boldsymbol{\sigma}'_B$, with the caveat that the interpretation is now

more complicated because any bias toward $\dot{\boldsymbol{\sigma}}'_T$ due to spatial stress heterogeneity needs to be removed. At the same time, this new methodology allows the estimation of a new parameter, HR, the ratio of the magnitudes of the spatially heterogeneous stress and the spatial mean stress, for the region. Then, using plots like Figure 5.8 to determine the spatial smoothness of the heterogeneity, α, setting the maximum sustainable stress ≈ 200 MPa, at distance of 10 cm (what one would expect for dislocations), one may be able to estimate the size of $\boldsymbol{\sigma}'_B$ for the study region, the effective strength of the crust for the study region size [*Heaton*, 2006, in preparation].

Returning to our seven regions of real focal mechanism data, we use Figures 5.13 and 5.14 to estimate HR and the percent bias toward $\dot{\boldsymbol{\sigma}}'_T$. Table 5.4 lists our estimates based on these curves. We obtain HR estimates ranging from 0.62–0.70 for the LA Basin, the least heterogeneous of our seven regions, to an HR = 1.21–1.44 for Region 5. We also obtain bias estimates anywhere from 14–42% bias toward the stress rate tensor, $\dot{\boldsymbol{\sigma}}'_T$; this indicates that the heterogeneity in Southern California is sufficient to significantly bias the focal mechanism inversions toward $\dot{\boldsymbol{\sigma}}'_T$, but not completely. Hypothetically, it should be possible to remove this bias due to spatially heterogeneous stress and extract the actual $\boldsymbol{\sigma}'_B$.

Interestingly, it appears that the seven regions we chose in Southern California are more compatible with an $HR = 1.25$ than the $HR = 1.75$ that we had calculated from Figure 5.8. As mentioned previously, the average focal mechanism difference as a function of distance for Southern California (Figure 5.8) includes both background seismicity and aftershocks, and we hypothesize that the inclusion of aftershocks raises the HR estimate and lowers the α estimate. Indeed, the curve for Southern California

begins to flatten out at the same level as East Bay San Francisco, $HR = 1.25$, then begins to rise again and finally levels out at a $HR = 1.75$. Combining this information with the HR estimates from comparing mean misfit angle information between our simulations and real data leads us to an estimate of $HR \approx 1.25$ and $\alpha \approx 0.8$ for regions with background seismicity (no aftershocks) in Southern California and East Bay, San Francisco.

Figure 5.15 shows P-T plots of simulation focal mechanisms using our best guess parameters and our model noise with mean deviation = 17°. We show one plot from our "San Gabriel Mountains" simulations with σ_{B_1} and one plot from our "Southern San Andreas Fault" simulations with σ_{B_2}. The plot from our "Southern San Andreas Fault" simulations looks similar to some of the P-T plots of real data in Figure 5.9.

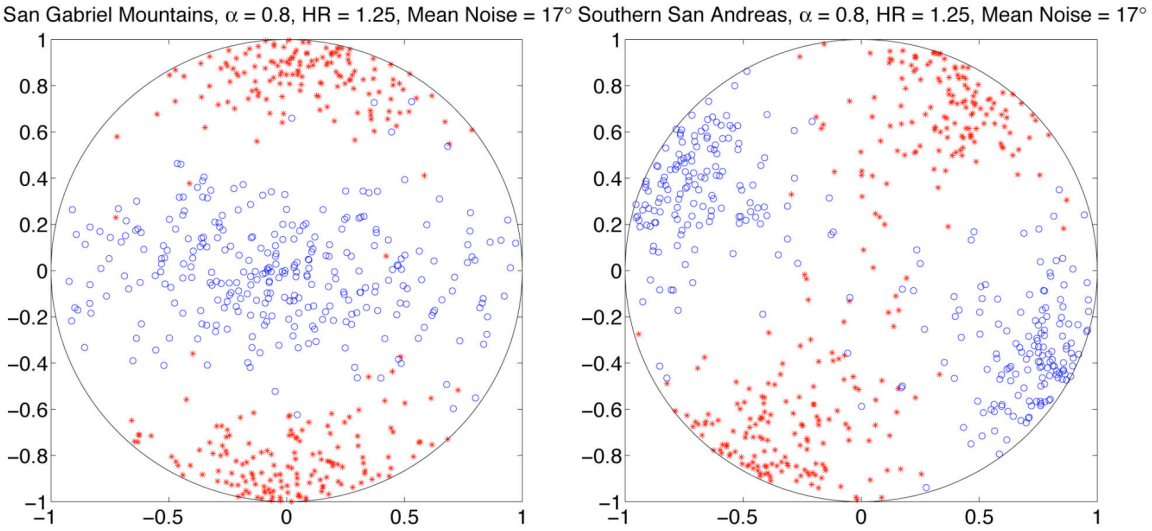

Figure 5.15. *P and T axes plotted for 300 synthetic focal mechanisms each, using our best guess stress heterogeneity parameters. We use an* $\alpha = 0.8$, $HR = 1.25$, *and a model noise with mean deviation = 17°. The strike-slip example on the right looks similar to some of the P-T plots of real focal mechanisms in Figure 5.9.*

In Figure 5.16 we plot what the spatial variation might look for a 1D cross section for 1 component of the deviatoric stress tensor, using our best guess parameters. We create 1D heterogeneous stress with 100,001 points and an $\alpha = 0.8$; we then add the following background stress tensor,

$$\boldsymbol{\sigma}'_B = \begin{pmatrix} 0 & 1 & 0 \\ 1 & 0 & 0 \\ 0 & 0 & 0 \end{pmatrix},$$

normalizing this background stress and our heterogeneity so that we have an $HR = 1.25$. We equate 1 grid spacing to 10 cm; therefore, our entire spatial bandwidth is approximately 10 km, or 5 orders of magnitude. We set the maximum stress at 200 MPa, which is what one may expect for granitic rock [*Scholz*, 1990], focus on a stress asperity, and calculate what the mean stress may be on a variety of length scales. This is motivated by a hypothesis from Heaton that strength in the Earth is length scale dependent [*Heaton*, 2006, in preparation]; if so, averagering stress over different length scales produces different estimates of strength. Interestingly, if we average over different length scales around the asperity, we calculate for one of the components of the deviatoric stress tensor, σ_{12}:

- ≈ 54 MPa if we average over 10 km
- ≈ 72 MPa if we average over 1 km, centered on the asperity
- ≈ 111 MPa if we average over 100 m, centered on the asperity
- ≈ 150 MPa if we average over 10 m, centered on the asperity

The increase of mean stress as we narrow our focus on the stress asperity, i.e., reduce the window over which we average, supports Heaton's hypothesis that strength in the crust depends on the length scale of the measurement.

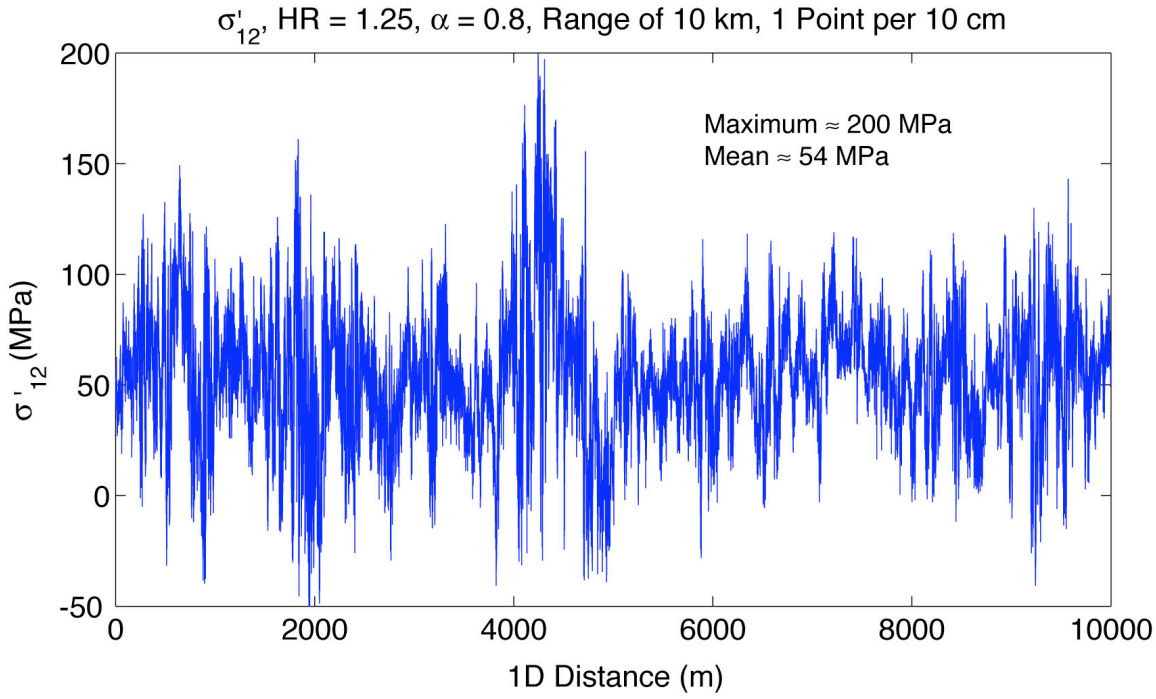

Figure 5.16 a)

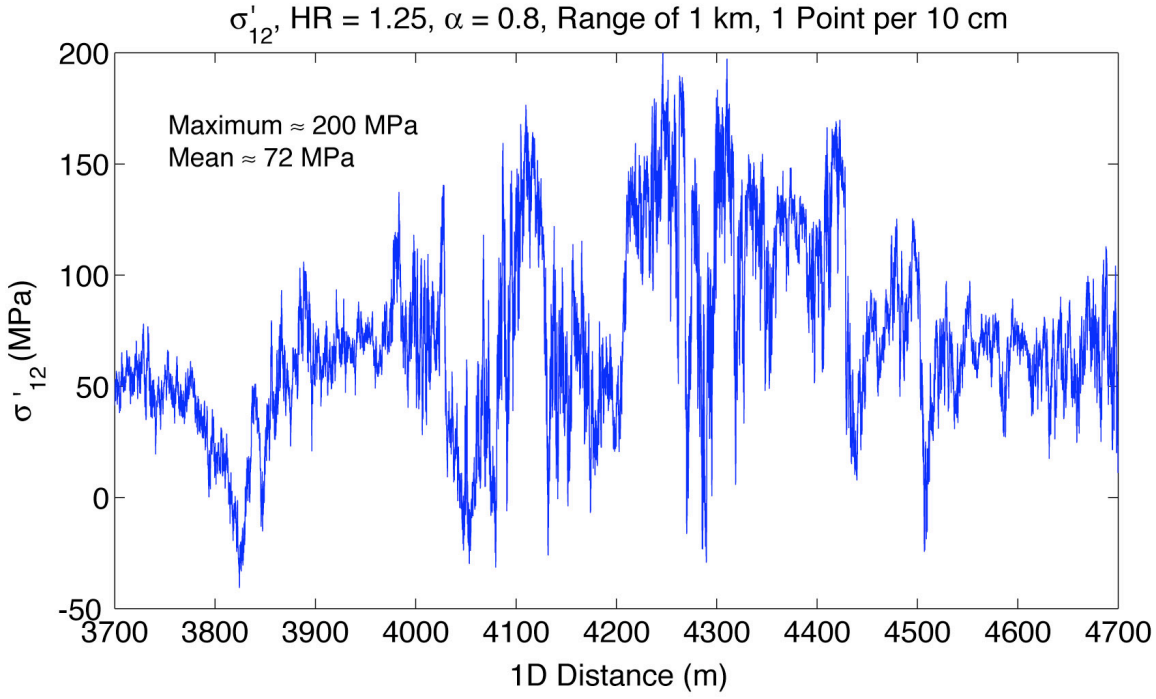

Figure 5.16 b)

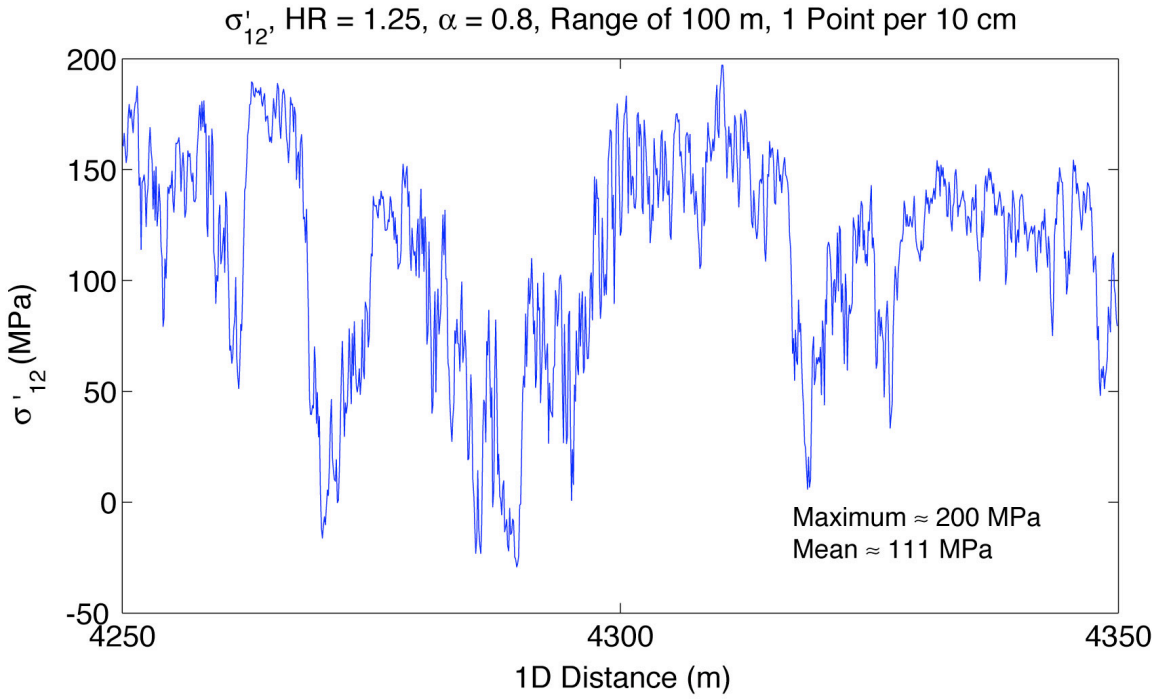

Figure 5.16 c)

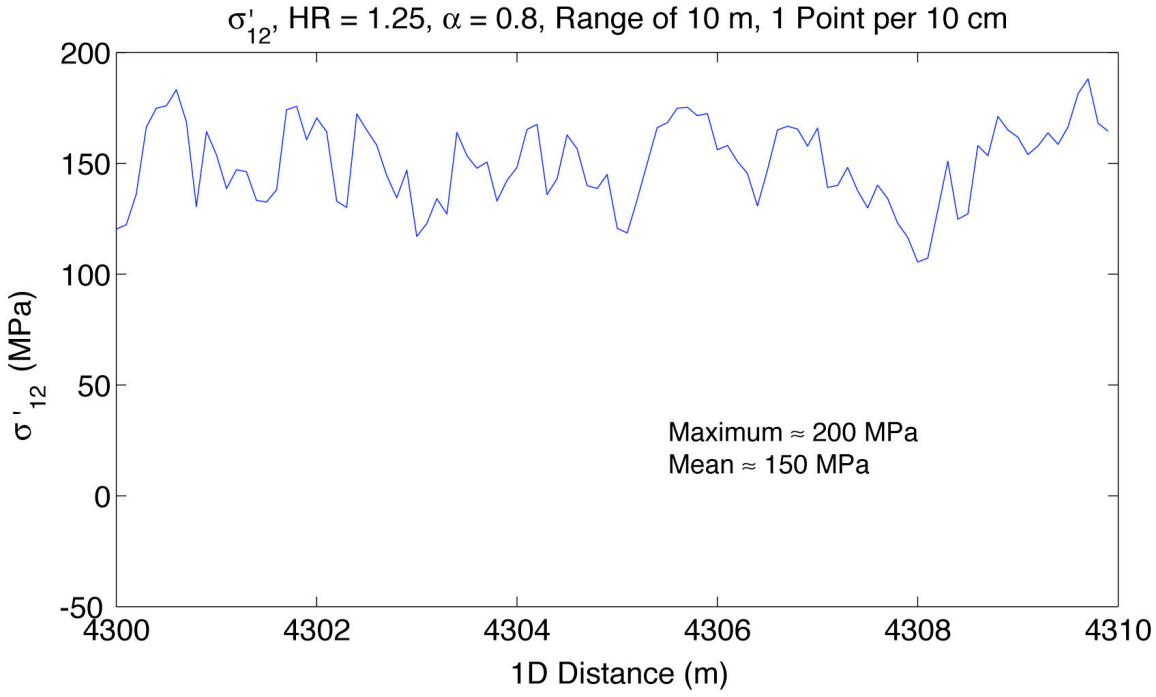

Figure 5.16 d)

Figure 5.16. *We create spatially smoothed heterogeneous stress in 1D with* $\alpha = 0.8$ *and add a spatially uniform background stress with an* $HR = 1.25$. *Therefore, it has the parameters we hypothesize for heterogeneous stress in East Bay, San Francisco and for Southern California if one were to subtract out aftershocks. We plot 100,001 points of one component of the stress tensor,* σ'_{12} *in* ***a)***. *If we let the grid spacing equal 10 cm, then the entire range of our stress 1D cross section is approximately 10 km. In* ***a)*** *we plot the entire width, a 10 km length. In* ***b)***, ***c)***, *and* ***d)*** *we successively narrow our plotting window by an order of magnitude each time, to focus in on a stress asperity. If we set our maximum stress to be 200 MPa, what one might expect for a 10 cm dislocation, then we can estimate mean stresses at different length scales for the asperity. The mean stress tends to increase as the window narrows over which we average the stress, supporting Heaton's hypothesis [2006, in preparation] that the strength of the crust is length scale dependent.*

Table 5.4. Estimates of the Heterogeneity Ratio, HR, and the Percent Bias Toward the Stress Rate Tensor for Our Seven Regions of Real Focal Mechanism Data

	Mean Misfit Angle	Estimate of Heterogeneity Ratio, *HR*	Estimate of Tensor Dot Tensor Dot Product Bias Toward $\dot{\boldsymbol{\sigma}}_T$
Test Region 1 LA Basin	18.0641	0.62–0.70	14–28%
Test Region 2 San Gabriel Mountains	24.7288	1.14–1.31	32–39%
Test Region 3	24.2155	1.09–1.24	31–38%
Test Region 4	23.6730	1.06–1.18	29–36%
Test Region 5	25.9741	1.21–1.44	36–42%
Test Region 6	22.3788	0.95–1.04	26–33%
Test Region 7	21.1410	0.82–0.95	22–30%

The estimates come from applying Figures 5.13 and 5.14 to their misfit angles. Our seven interseismic regions yield HR estimates more compatible with 1.25 than 1.75. It is possible that the Southern California parameterization of HR in Figure 5.8 is elevated to 1.75 by the inclusion of aftershock data. Indeed, the curve for Southern California (Figure 5.8) begins to maximize at an angle that is compatible with $HR = 1.25$, then increases again to an angle compatible with $HR = 1.75$. Our guess is the initial flattening is background seismicity, and the final maximum is due to aftershock data. It would be interesting to have the average focal mechanism difference as a function of distance recalculated for them separately.

References

Becker, T. W., et al. (2005), Constraints on fault slip rates of the southern Califronia plate boundary from GPS velocity and stress inversions, *Geophysical Journal International*, *160*, 634–650.

Ben-Zion, Y., et al. (2003), Large earthquake cycles and intermittent criticality on heterogeneous faults due to evolving stress and seismicity, *Journal of Geophysical Research*, *108*, ESE 1–21.

Hardebeck, J. L. (in review, 2006), Homogeneity of small-scale earthquake faulting, stress and fault strength, *Bulletin of the Seismological Society of America*.

Hardebeck, J. L., and P. M. Shearer (2003), Using S/P amplitude ratios to constrain the focal mechanisms of small earthquakes, *Bulletin of the Seismological Society of America*, *93*, 2434–2444.

Heaton, T. H. (2006, in preparation), Scale dependence of the strength of the Earth's crust.

Michael, A. J. (1984), Determination of stress from slip data: Faults and folds, *Journal of Geophysical Research-Solid Earth*, *89*, 11517–11526.

Michael, A. J. (1987), Use of focal mechanisms to determine stress: A control study, *Journal of Geophysical Research-Solid Earth*, *92*, 357–368.

Scholz, C. H. (1990), *The Mechanics of Earthquakes and Faulting*, Cambridge University Press, Cambridge.

Chapter 6. Conclusion

We created simple stochastic models of spatially heterogeneous stress in three dimensions. By breaking up the stress tensor into three invariant quantities (principal stresses) and three orientation angles (a rotation amplitude, ω, about a rotation axis $[\theta,\phi]$), we were able to produce filtered heterogeneous 3D matrices of the full stress tensor with properties that are approximately unchanged upon rotation of coordinate system. We generated random principal stresses $(\sigma_1,\sigma_2,\sigma_3)$ using Gaussian white noise and random orientations $(\omega,[\theta,\phi])$ using random unit quaternions, then filtered each quantity in three dimensions. The spatial smoothing parameter we used in the filtering is α, which is the spectral falloff of any 1D cross section through our 3D grids. We find that the larger the value of α, the greater the spatial smoothing. For our 201x201x201 grids and spatial smoothing $\alpha \le 1.0$, any orientation bias due to filtering is small and can be eliminated by stacking grids with a different random rotation applied to the stress tensors within each stacked grid. Subtracting out the pressure, we then added our filtered heterogeneous deviatoric stress in 3D, $\boldsymbol{\sigma}'_H(\mathbf{x})$, to a spatially uniform background stress, $\boldsymbol{\sigma}'_B$. This introduces our second stress heterogeneity parameter, HR, which uses a ratio of I'_2s (second invariants of deviatoric stress tensors), which are functions of the deviatoric principal stresses (σ'_1, σ'_2, and σ'_3), as a measure of the relative amplitude of the spatially heterogeneous stress, $\boldsymbol{\sigma}'_H(\mathbf{x})$, to the amplitude of the spatial mean, $\boldsymbol{\sigma}'_B$. Last, we add a stress-rate $\dot{\boldsymbol{\sigma}}'_T$, due to far-field plate loading, to bring points to failure via our Hencky-Mises plastic yield criterion.

We showed analytically that, in the presence of extremely heterogeneous stress and our plastic yield criterion, we would expect bias to which points fail as earthquakes for $HR >> 1$, a bias towards $\dot{\boldsymbol{\sigma}}'_T$. Assuming that only a small percentage of the possible failure points in the Earth actually fail, we found that if the spatial stress heterogeneity is large in comparison to the spatial mean, the most likely points to fail will have an average stress rotated toward $\dot{\boldsymbol{\sigma}}'_T$. Numerically testing this with our 3D filtered heterogeneous stress, we computed $\bar{\boldsymbol{\sigma}}'_{Failure}\left(\mathbf{x}_{i_{Failure}}\right)$ from the first 2,000 failures for a variety of simulations and show that $\bar{\boldsymbol{\sigma}}'_{Failure}\left(\mathbf{x}_{i_{Failure}}\right) \approx \boldsymbol{\sigma}'_B$ for $HR << 1$, $\bar{\boldsymbol{\sigma}}'_{Failure}\left(\mathbf{x}_{i_{Failure}}\right) \approx \dot{\boldsymbol{\sigma}}'_T$ for $HR >> 1$, and $\bar{\boldsymbol{\sigma}}'_{Failure}\left(\mathbf{x}_{i_{Failure}}\right)$ is rotated approximately halfway between $\boldsymbol{\sigma}'_B$ and $\dot{\boldsymbol{\sigma}}'_T$ for $HR \approx 2.0$.

Current stress studies using focal mechanism inversions [*Angelier*, 1975; 1984; *Carey and Brunier*, 1974; *Etchecopar, et al.*, 1981; *Gephart*, 1990; *Gephart and Forsyth*, 1984; *Mercier and Carey-Gailhardis*, 1989; *Michael*, 1984; 1987] assume that there is no bias toward $\dot{\boldsymbol{\sigma}}'_T$ in their measured focal mechanism orientations. It is assumed that the set of earthquakes used in the inversions are a good random sampler of the mean stress state in the real Earth; therefore, the tensor obtained from these inversions is equated with the spatial mean, $\boldsymbol{\sigma}'_B$. However, according to our studies, if there is significant heterogeneity, the interpretation of focal mechanism inversions is not that simple; one must take into account the bias toward $\dot{\boldsymbol{\sigma}}'_T$.

To determine whether or not this bias toward $\dot{\boldsymbol{\sigma}}'_T$ is important in the real Earth, we compared our synthetic focal mechanisms produced from spatially heterogeneous stress to real focal mechanism data and estimated our heterogeneous ratio, HR. The

parameter α has little to no effect on the percent bias toward $\dot{\boldsymbol{\sigma}}'_T$ for $\alpha \leq 1.0$. Based on our numerical simulations, if $HR \geq 1.0$, there will be a minimum 25–35% bias toward $\dot{\boldsymbol{\sigma}}'_T$ in the stress inversions. Our first step was to estimate the model noise that must be added to our synthetic focal mechanisms, i.e., how much noise there is in real focal mechanism calculations due to errors in determining the mechanisms. Our next step was to calculate the average focal mechanism difference (an average angular difference) as a function of distance for simulations with varying amounts of stress heterogeneity, HR, and compare our results to a figure from Hardebeck's recently submitted paper [in review, 2006]. Hardebeck determined these quantities for three regions, Southern California; East Bay, San Francisco; and the Loma Prieta region. We attempted to model the Southern California and East Bay, San Francisco. We also compared focal mechanisms from Hardebeck's focal mechanism catalogue [*Hardebeck and Shearer*, 2003] for Southern California to our synthetic simulations. Applying Michael's inversion program, "slick" [1984; 1987], to focal mechanisms within seven non-aftershock regions using A and B quality data and then to our synthetic focal mechanisms with model noise added, we compare misfit angle statistics. Using these two methods, our best estimate is $HR = 1.25$ for Southern California and East Bay, San Francisco in aftershock free areas. According to our simulations, this would generate an ≈ 40% bias toward the stress rate, $\dot{\boldsymbol{\sigma}}'_T$. This is a non-trivial bias; hence, we conclude that stress studies that use focal mechanism data sets and standard stress inversion tools [*Angelier*, 1975; 1984; *Carey and Brunier*, 1974; *Etchecopar, et al.*, 1981; *Gephart*, 1990; *Gephart and Forsyth*, 1984; *Mercier and Carey-Gailhardis*, 1989; *Michael*, 1984; 1987] to determine the stress state in the crust need to be reinterpreted. We illustrate how one might subtract out this bias

toward $\dot{\boldsymbol{\sigma}}'_T$ in our new heterogeneous stress paradigm to produce a more accurate estimate of $\boldsymbol{\sigma}'_B$. This new method of interpreting stress studies is significantly more complicated than current methods, but also generates a new parameter, the heterogeneity ratio, HR.

We also attempted to parameterize the spatial smoothing, α, by comparing our numerical simulations to Hardebeck's [2006] plot of average focal mechanism difference as a function of distance. We estimated an $\alpha \approx 0.8$ for non-aftershock regions. This parameter is more difficult to constrain than HR; clearly, more work can be done to refine this estimate. The exact value of α does not affect the main conclusion of this thesis, that stress heterogeneity biases stress inversion results toward $\dot{\boldsymbol{\sigma}}'_T$, but α is very important for determining the strength of the crust as a function of lengthscale.

Caveats and Future Work

As mentioned in Chapter 1, the Introduction, in our attempt to create a simple, statistical model of spatial stress heterogeneity in the Earth's crust, assumptions have been made that could have affected our results. For example, we do not update the stress field after each event; therefore, our results are best compared to stress inversions of background seismicity in between large earthquakes. If a large earthquake occurs and we wish to model its effect on the surrounding crust, namely how it produces aftershocks, we would have to modify our initial equation in Chapter 1, to take into account any 3D stress pertubations. The term we would add is:

$\boldsymbol{\sigma}_E(\mathbf{x})H(t-T_E)$ is the stress perturbation from major events that occur at time T_E (e.g., Landers earthquake). While we assume that these large events make extremely complex variations in stress in the immediate vicinity of the rupture, the stress variations can be approximately modeled with simple source models at larger distances from the rupture.

This produces our new stress equation:

$$\boldsymbol{\sigma}'(\mathbf{x},t) = \boldsymbol{\sigma}'_B + \dot{\boldsymbol{\sigma}}'_T t + \boldsymbol{\sigma}'_H(\mathbf{x}) + \boldsymbol{\sigma}_E(\mathbf{x})H(t-T_E). \qquad (0.1)$$

A future direction of research would be to use equation (0.1) to study aftershocks from a moderate to large earthquake and simulate the apparent stress rotations. The first step would be to model the pre-event $\boldsymbol{\sigma}'_B$ and $\dot{\boldsymbol{\sigma}}'_T t$ along with a spatially heterogeneous stress, $\boldsymbol{\sigma}'_H(\mathbf{x})$, with appropriate spectral properties, to produce the synthetic pre-event background seismicity. The next step would be to add a source model of Landers, Northridge, Loma Prieta, or another earthquake, calculate the static stress change within the surround medium, $\boldsymbol{\sigma}_E(\mathbf{x})H(t-T_E)$, ask which points exceed the failure threshold as a result of $\boldsymbol{\sigma}_E(\mathbf{x})H(t-T_E)$, and count these points as aftershocks. The last step would be to reapply the stress rate, $\dot{\boldsymbol{\sigma}}'_T t$, on this updated system to produce synthetic focal mechanisms that would represent the seismicity after the aftershock sequence has died off.

The point of this modeling would be to see if the pre-event seismicity, aftershock sequence, and post-aftershock seismicity have similar or different stress inversion orientations. We predict that the 3D static stress perturbation, $\boldsymbol{\sigma}_E(\mathbf{x})H(t-T_E)$, will cause a rotation of the average failure mechanism, directly after the mainshock; therefore,

stress inversions of aftershock sequences will produce a tensor rotated relative to any inversions of premainshock seismicity. Indeed, such rotations have been seen for Landers [*Hardebeck and Hauksson*, 2001], Northridge [*Zhao, et al.*, 1997], and other earthquakes. We also predict that after the aftershock sequence has died off, if the orientation of $\dot{\boldsymbol{\sigma}}'_T t$ due to plate tectonics has remained constant, then the average focal mechanism orientation and stress inversion results will rotate back to the premainshock orientation. Our predictions are based on what we learned from Chapter 4, that whatever is perturbing the system in time, be it the stress buildup due to far-field plate loading, $\dot{\boldsymbol{\sigma}}'_T t$, or the transient processes initiated by the mainshock, $\boldsymbol{\sigma}_E(\mathbf{x}) H(t - T_E)$, that affect the aftershock sequence, are what primarily determine the orientations of earthquake failures if stress is spatially heterogeneous in the crust. Therefore, in our paradigm, prior to the mainshock, $\dot{\boldsymbol{\sigma}}'_T t$, is the most important perturbation to the system, during the aftershock sequence processes related to $\boldsymbol{\sigma}_E(\mathbf{x}) H(t - T_E)$, is the most important perturbation to the system (why the average failure orientation would rotate), and after the aftershock sequence has ceased, $\dot{\boldsymbol{\sigma}}'_T t$, is the most important perturbation to the system (why the average failure orientation would rotate back to the premainshock orientation).

This is a significantly different interpretation of "apparent" stress rotations. Currently, if there is a significant rotation of stress inversion results after a mainshock, it is assumed that the mainshock produced a nearly complete stress drop and that the magnitude of the background stress, $\boldsymbol{\sigma}'_B$, is approximately equal zero. In our interpretation, $\boldsymbol{\sigma}'_B$, no longer has to approximately equal zero, it can have a significant, non-zero magnitude. Instead, it is the interaction between the spatially heterogeneous stress and the perturbations to the system that "appears" to rotate the stress tensor, when

in fact it is just changing the bias as a function of time; i.e., which spatially heterogeneous stress tensors have preference for failure changes depending upon the current perturbation to the system.

So far, we have tested this hypothesis with initial work on the reported stress rotation after the Northridge earthquake [*Zhao, et al.*, 1997] with our heterogeneous stress models. Immediately after the Northridge earthquake, Zhao and Kanamori reported an approximately 17° rotation of the P axis and found that within the months following the earthquake, it rotated back to the pre-Northridge orientation (Figure 6.1). Our initial models appear to replicate this reported rotation in average focal mechanism orientations. In our heterogeneous stress models, the average focal mechanism orientations are biased toward whatever is perturbing the system in time; therefore, any rotations in our system for large HR are a function of the perturbation, not the background stress + perturbation. We confirmed that our numerical models with heterogeneous stress are capable of generating significant rotations in average focal mechanism orientations even with non-zero background stress, $\boldsymbol{\sigma}'_B$. They also appear capable of generating the rotation back to the premainshock orientation. In essence, our heterogeneous stress models produce focal mechanism orientations biased from any aftershock time-dependent processes immediately after the mainshock. Then as aftershock processes die off and the stress rate from long-term tectonic processes become more important, the average focal mechanism orientations are predicted to rotate back. The time scale of this process is predicted to depend on the amount of slip in the mainshock compared to the long-term strain rate.

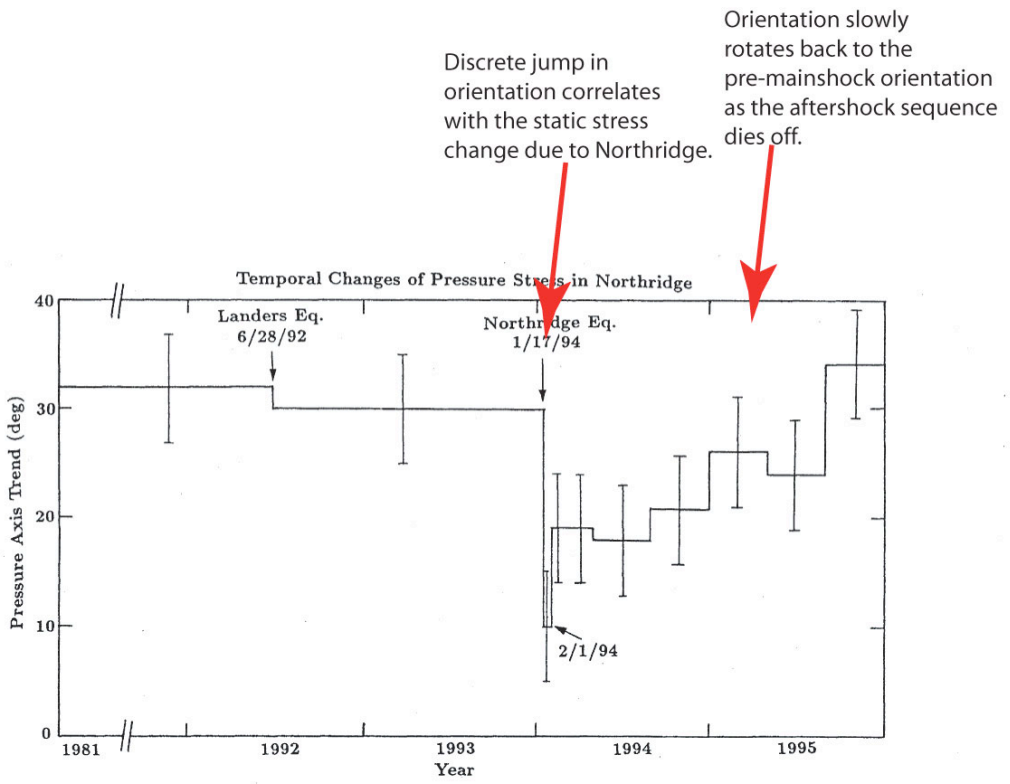

Figure 3. Azimuth of the principal pressure axis versus time in the Northridge area. The vertical bars denote the uncertainty of the azimuth estimates.

Figure 6.1. *Figure modified from Zhao et al. [1997] shows the rotation of the pressure axis as a function of time. There is a discrete jump in orientation of about 17° at the time of the Northridge earthquake then a slow rotation back over the course of two years.*

An additional route for new research would be to combine our spatially heterogeneous stress aftershock model with rate and state friction to study aftershock patterns and decays. In essence, instead of letting all the points that exceed the failure threshold after mainshock fail simultaneously, we would apply the rate and state friction law. Those heterogeneous points that exceed the failure threshold the most would fail first, and those that exceed it by a small amount would fail last. It would be a natural,

physical way to produce the time delay for some points and explain why some fail quickly while others take much longer. We would compare our statistics to those of real aftershock sequences. In turn, this comparison with real data could provide additional constraints for our two statistical parameters, HR and α.

Another comparison/test of our spatially heterogeneous stress aftershock model would be to see if we can reproduce spatial/depth variations in the aftershock orientations. Kerkela and Stock [1996; personal communication, 2006] in their borehole breakout studies of the San Fernando Valley found variability in the orientation of maximum compressive stress as a function of depth that may be compatible with our aftershock models; however, it is yet to be tested.

One other limitation of our method that could lead into future research and refinements is that we do not allow failure on non-optimal slip planes. We do not allow spatial variability in the static or dynamic coefficient of frictions, μ. It is possible that some of the heterogeneity seen in the data is due to non-optimally orientated fault planes and variable strength faults, which would lower our estimate of stress heterogeneity. Given the borehole breakout data presented in Chapter 1 that strongly indicate heterogeneity of stress orientations, we are fairly sure there is some short wavelength spatially heterogeneous stress in tectonically active regions, but of course the question is how much. A future area for research would be to try to simply model this without using dynamic simulations. To derive statistics of fault orientations, sizes, sources on the faults (i.e., heterogeneous slip) and evolve it through time, allowing for fresh fractures as well as failure on pre-existing planes. It would involve many more assumptions that could complicate the problem and possibly add in hidden biases due to the statistics of

fault/source generation, but if it could be done, it would provide a good comparison to our current method. The truest way to model the pre-existing failure and generate the heterogeneous stress field would be to employ dynamics fault failures for all faults throughout all time, but this is far beyond our current numerical capacity.

There are many other possible directions for future work, such as developing new ways of generating our 3D spatially heterogeneous stress field, using Weibull statistics or other distributions; adding in finite fault ruptures; or updating the stress field after each event. This thesis is meant to open the door for studying the effect of 3D stress heterogeneity on focal mechanisms and seismicity patterns in the real Earth and show that heterogeneity must be taken into account when interpreting stress inversions for the crust.

References

Angelier, J. (1975), Sur l'analyse de mesures recueilles dans des sites faillés: l'utilité d'une confrontation entre les méthodes dynamiques et cinématiques, *C.R. Acadamy of Science, Paris, D*, *283*, 466.

Angelier, J. (1984), Tectonic analysis of fault slip data sets, *Journal of Geophysical Research*, *89*, 5835–5848.

Carey, E., and B. Brunier (1974), Analyse théorique et numérique d'un modèle méchanique élémentaire appliqué à l'étude d'une population de failles, *C.R. Acadamy of Science, Paris, D*, *279*, 891–894.

Etchecopar, A., et al. (1981), An inverse problem in microtectonics for the determination of stress tensors from fault striation analysis, *Journal of Structrual Geology*, *3*, 51–65.

Gephart, J. W. (1990), FMSI: A Fortran program for inverting fault/slickenside and earthquake focal mechanism data to obtain the regional stress tensor, *Computers and Geosciences*, *16*, 953–989.

Gephart, J. W., and D. W. Forsyth (1984), An improved method for deteremining the regional stress tensor using earthquake focal mechanism data: Application to the San Fernando earthquake sequence, *Journal of Geophysical Research*, *89*, 9305–9320.

Hardebeck, J. L. (in review, 2006), Homogeneity of small-scale earthquake faulting, stress and fault strength, *Bulletin of the Seismological Society of America*.

Hardebeck, J. L., and E. Hauksson (2001), Crustal stress field in southern California and its implications for fault mechanics, *Journal of Geophysical Research-Solid Earth*, *106*, 21859–21882.

Hardebeck, J. L., and P. M. Shearer (2003), Using S/P Amplitude Ratios to Constrain the Focal Mechanisms of Small Earthquakes, *Bulletin of the Seismological Society of America*, *93*, 2434–2444.

Kerkela, S., and J. M. Stock (1996), Compression directions north of the San Fernando Valley determined from borehole breakouts, *Geophysical Research Letters*, *23*, 3365–3368.

Mercier, J.-L., and S. Carey-Gailhardis (1989), Regional state of stress and characteristic fault kinematics instabilities shown by aftershock sequence: the aftershock sequence of the 1978 Thessaloniki (Greece) and 1980 Campania-Lucania (Italy) earthquakes as examples, *Earth and Planetary Science Letters*, *92*, 247–264.

Michael, A. J. (1984), Determination of stress from slip data: Faults and folds, *Journal of Geophysical Research-Solid Earth*, *89*, 11517–11526.

Michael, A. J. (1987), Use of focal mechanisms to determine stress: A control study, *Journal of Geophysical Research-Solid Earth*, *92*, 357–368.

Zhao, D. P., et al. (1997), State of stress before and after the 1994 Northridge earthquake, *Geophysical Research Letters*, *24*, 519–522.

Appendix A. Equations for Translating Between Stress Matrices, Fault Parameters, and P-T Axes

Coordinate Systems and Rotations

We use the same right-handed coordinate system as Andy Michael's program, *slick [Michael, 1984; 1987]*, which is East, North, and Up.

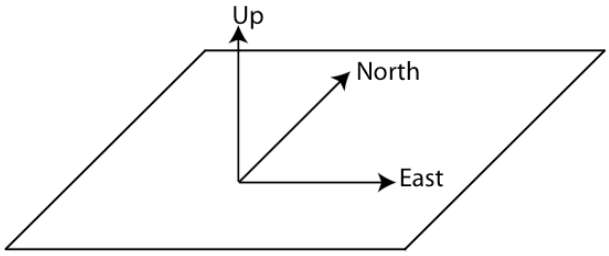

Figure A.1. *Right-handed coordinate system used in generating code that is compatible with Andy Michael's stress inversion programs. All vectors generated will have a format* $\mathbf{v} = [\hat{E}, \hat{N}, \hat{Up}]$.

Therefore, our stress matrices will have the following Cauchy stress tensor format:

$$\sigma_{ij} = \begin{matrix} \sigma_{EE} & \sigma_{EN} & \sigma_{EU} \\ \sigma_{NE} & \sigma_{NN} & \sigma_{NU} \\ \sigma_{UE} & \sigma_{UN} & \sigma_{UU} \end{matrix} . \qquad \text{(A.1)}$$

For any component of σ_{ij}, j indicates the direction of the force applied, and i describes the normal of the plane on which the force is acting. Following physics sign convention for σ_{ij}, where tension is positive and pressure is negative, if the force vector is acting in the positive direction and the normal is also in the positive direction, then the component $\sigma_{ij} > 0$. Conversely, if the force vector is acting in the negative direction and the normal

is in the positive direction, $\sigma_{ij} < 0$. For example, $\sigma_{EN} > 0$ describes one of two scenarios: 1) A force acting in the $\hat{N}$ direction on a plane with a normal in the $\hat{E}$ direction. 2) A force acting in the $-\hat{N}$ direction on a plane with a normal in the $-\hat{E}$ direction. The diagonal components of σ_{ij} describe the normal tractions (forces normal to the plane on which they are acting), and the off-diagonal components describe the shear tractions (forces tangent to the plane on which they are acting). Figure A.2 graphically shows all the components of the stress tensor. Figures A.3 and A.4 show 2D examples in more detail.

As noted in Figure A.2, our Cauchy stress matrix must be symmetric resulting in:

$$\sigma_{ij} = \begin{matrix} \sigma_{EE} & \sigma_{EN} & \sigma_{EU} \\ \sigma_{EN} & \sigma_{NN} & \sigma_{NU} \\ \sigma_{EU} & \sigma_{NU} & \sigma_{UU} \end{matrix} . \tag{A.2}$$

Figure A.3 shows in detail our convention for normal stresses and Figure A.4 shows in detail our convention for shear stresses.

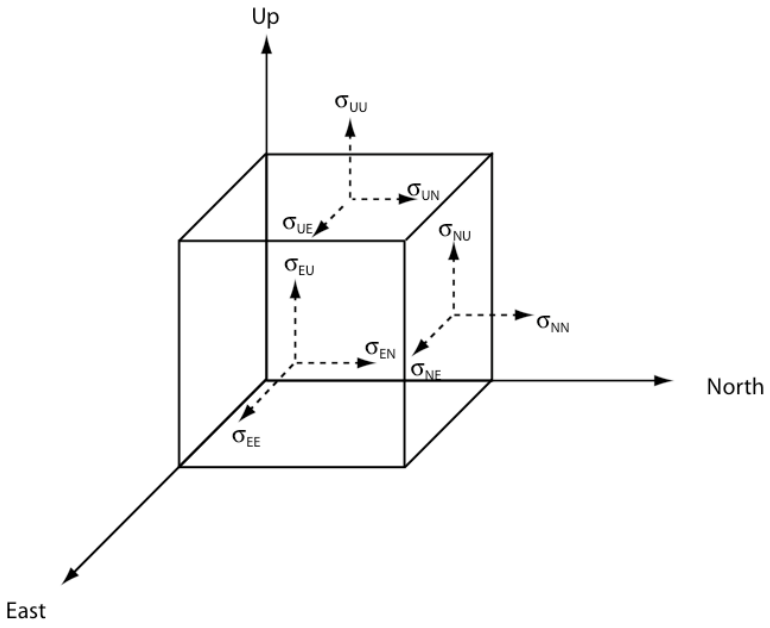

Figure A.2. *The stress vectors are shown for three of the six exterior faces on a box. Note that in our convention, the diagonal elements of our stress tensor (σ_{EE}, σ_{NN}, and σ_{UU}) for tension are >0 and for compression are <0. In this figure all the elements of σ_{ij} are positive. For example, σ_{EE}, σ_{NN}, σ_{UU} are all pointing in the same direction as their respective normal vectors, resulting in tension. The off-diagonal elements, σ_{EN}, σ_{NU}, σ_{UE}, have either a traction in the positive direction and a positive normal or have a traction in the negative direction and a negative normal for the given coordinate system. Since we are interested in systems where there is no net rotation, the matrix must be symmetric, i.e., $\sigma_{NE} = \sigma_{EN}$, $\sigma_{UE} = \sigma_{EU}$, and $\sigma_{UN} = \sigma_{NU}$ [illustration adapted from Housner and Vreeland, 1965].*

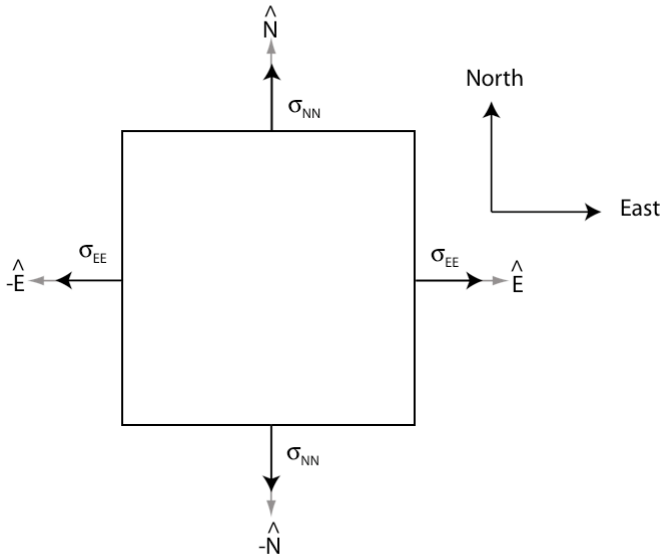

Figure A.3. *In this 2D example,* σ_{EE} *and* σ_{NN} *are both positive, i.e., the traction vectors are always pointing in the same direction as the normal vectors, resulting in* $E-W$ *tension and* $N-S$ *tension.*

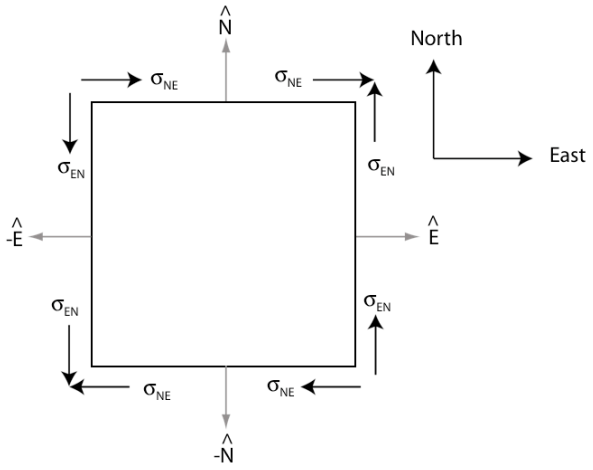

Figure A.4. *Again,* σ_{EN} *and* σ_{NE} *are positive using our convention that a traction aligned in a positive direction on a plane with a positive normal, or a traction aligned in a negative direction on a plane with a negative normal, produce a positive component in our stress tensor. Note, due to rotational symmetry,* $\sigma_{EN} = \sigma_{NE}$.

In Figure A.4, if σ_{EN} is the only stress being applied, then we could write our Cauchy stress tensor as follows,

$$\sigma_{ij}^{(a)} = A \begin{pmatrix} 0 & 1 & 0 \\ 1 & 0 & 0 \\ 0 & 0 & 0 \end{pmatrix} \tag{A.3}$$

where A is the scalar amplitude of σ_{EN}.

If we wish to rotate the stress tensor, $\sigma_{ij}^{(a)}$, then we can apply any combination of the following rotation matrices,

$$\mathbf{R}(\psi) = \begin{pmatrix} 1 & 0 & 0 \\ 0 & \cos\psi & -\sin\psi \\ 0 & \sin\psi & \cos\psi \end{pmatrix} \quad \text{for a counter-clockwise rotation } \psi \text{ of the stress tensor about the } \hat{E} \text{ axis} \tag{A.4}$$

$$\mathbf{R}(\delta) = \begin{pmatrix} \cos\delta & 0 & \sin\delta \\ 0 & 1 & 0 \\ -\sin\delta & 0 & \cos\delta \end{pmatrix} \quad \text{for a counter-clockwise rotation } \delta \text{ of the stress tensor about the } \hat{N} \text{ axis} \tag{A.5}$$

$$\mathbf{R}(\theta) = \begin{pmatrix} \cos\theta & -\sin\theta & 0 \\ \sin\theta & \cos\theta & 0 \\ 0 & 0 & 1 \end{pmatrix} \quad \text{for a counter-clockwise rotation } \theta \text{ of the stress tensor about the } \hat{Up} \text{ axis.} \tag{A.6}$$

In Figure A.5, we apply the third rotation matrix, $\mathbf{R}(\theta)$, to rotate $\sigma_{ij}^{(a)}$ about the positive $\hat{\text{U}}\text{p}$ axis by $\theta = 45°$ to produce a new Cauchy stress tensor, $\sigma_{kl}^{(b)}$. We can write out the rotation as the following set of steps:

$$
\begin{aligned}
\sigma_{kl}^{(\mathbf{b})} &= R_{ki}\sigma_{ij}^{(\mathbf{a})}R_{lj} = \mathbf{R}(\theta)\boldsymbol{\sigma}^{(\mathbf{a})}\left(\mathbf{R}(\theta)\right)^{T} \\
&= A\begin{pmatrix}\cos\theta & -\sin\theta & 0\\ \sin\theta & \cos\theta & 0\\ 0 & 0 & 1\end{pmatrix}\begin{pmatrix}0 & 1 & 0\\ 1 & 0 & 0\\ 0 & 0 & 0\end{pmatrix}\begin{pmatrix}\cos\theta & \sin\theta & 0\\ -\sin\theta & \cos\theta & 0\\ 0 & 0 & 1\end{pmatrix} \\
&= A\begin{pmatrix}\cos\theta & -\sin\theta & 0\\ \sin\theta & \cos\theta & 0\\ 0 & 0 & 1\end{pmatrix}\begin{pmatrix}-\sin\theta & \cos\theta & 0\\ \cos\theta & \sin\theta & 0\\ 0 & 0 & 0\end{pmatrix} \\
&= A\begin{pmatrix}-\cos\theta\sin\theta-\sin\theta\cos\theta & \cos\theta\cos\theta-\sin\theta\sin\theta & 0\\ -\sin\theta\sin\theta+\cos\theta\cos\theta & \sin\theta\cos\theta+\cos\theta\sin\theta & 0\\ 0 & 0 & 0\end{pmatrix} \\
&= A\begin{pmatrix}-\sin 2\theta & \cos 2\theta & 0\\ \cos 2\theta & \sin 2\theta & 0\\ 0 & 0 & 0\end{pmatrix},
\end{aligned}
\tag{A.7}
$$

and for $\theta = 45°$, we find that our rotated stress is simply

$$
\sigma_{kl}^{(\mathbf{b})} = A\begin{pmatrix}-1 & 0 & 0\\ 0 & 1 & 0\\ 0 & 0 & 0\end{pmatrix}. \tag{A.8}
$$

If we rotate the coordinate systems instead of the stress tensors themselves, the rotation matrices are the transpose of those used for rotating the stress tensors.

$$
\mathbf{R}^{T}(\psi) = \begin{pmatrix}1 & 0 & 0\\ 0 & \cos\psi & \sin\psi\\ 0 & -\sin\psi & \cos\psi\end{pmatrix} \qquad \begin{array}{l}\text{for a counter-clockwise rotation } \psi\\ \text{of the coordinates about the } \hat{E} \text{ axis}\end{array} \tag{A.9}
$$

$$
\mathbf{R}^{T}(\delta) = \begin{pmatrix}\cos\delta & 0 & -\sin\delta\\ 0 & 1 & 0\\ \sin\delta & 0 & \cos\delta\end{pmatrix} \qquad \begin{array}{l}\text{for a counter-clockwise rotation } \delta\\ \text{of the coordinates about the } \hat{N} \text{ axis}\end{array} \tag{A.10}
$$

$$
\mathbf{R}^{T}(\theta) = \begin{pmatrix}\cos\theta & \sin\theta & 0\\ -\sin\theta & \cos\theta & 0\\ 0 & 0 & 1\end{pmatrix} \qquad \begin{array}{l}\text{for a counter-clockwise rotation } \theta\\ \text{of the coordinates about the } \hat{U}p \text{ axis.}\end{array} \tag{A.11}
$$

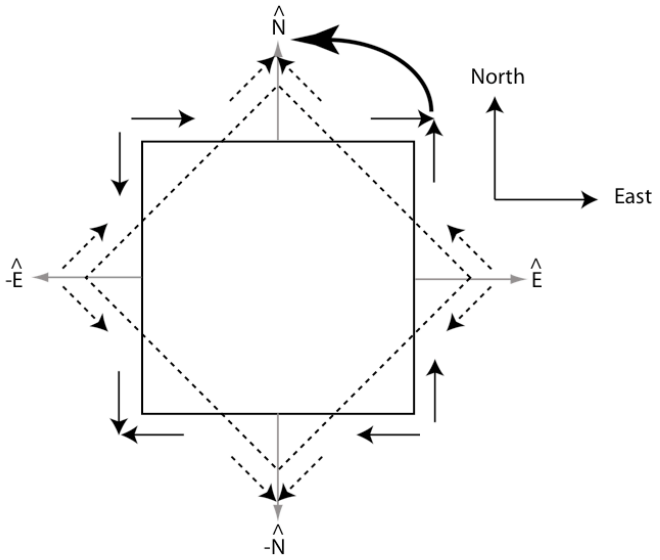

Figure A.5. *The dotted lines indicate the unrotated stress tensor and the solid lines are for the rotated stress tensor. Rotation of the stress field counter-clockwise by 45°. Note that it results in* $E-W$ *compression and* $N-S$ *tension. This agrees with our tensor,* $\sigma_{kl}^{(\mathbf{b})}$*, where* $\sigma_{EE}^{(\mathbf{b})}<0$*, i.e., compression in the* $E-W$ *direction, and* $\sigma_{NN}^{(\mathbf{b})}>0$*, i.e., tension in the* $N-S$ *direction.*

Therefore, if we start with

$$\sigma_{ij}^{(\mathbf{a})} = A \begin{pmatrix} 0 & 1 & 0 \\ 1 & 0 & 0 \\ 0 & 0 & 0 \end{pmatrix} \tag{A.12}$$

and rotate the coordinate system by 45° about the $\hat{U}p$ axis, our stress tensor in the new coordinate system is:

$$\begin{aligned}
\sigma_{kl}^{(\mathbf{c})} &= R_{ik}\sigma_{ij}^{(\mathbf{a})}R_{jl} = \left(\mathbf{R}(\theta)\right)^T \boldsymbol{\sigma}^{(\mathbf{a})}\mathbf{R}(\theta) \\
&= A\begin{pmatrix} \cos\theta & \sin\theta & 0 \\ -\sin\theta & \cos\theta & 0 \\ 0 & 0 & 1 \end{pmatrix}\begin{pmatrix} 0 & 1 & 0 \\ 1 & 0 & 0 \\ 0 & 0 & 0 \end{pmatrix}\begin{pmatrix} \cos\theta & -\sin\theta & 0 \\ \sin\theta & \cos\theta & 0 \\ 0 & 0 & 1 \end{pmatrix} \\
&= A\begin{pmatrix} \cos\theta & \sin\theta & 0 \\ -\sin\theta & \cos\theta & 0 \\ 0 & 0 & 1 \end{pmatrix}\begin{pmatrix} \sin\theta & \cos\theta & 0 \\ \cos\theta & -\sin\theta & 0 \\ 0 & 0 & 0 \end{pmatrix} \\
&= A\begin{pmatrix} \cos\theta\sin\theta + \sin\theta\cos\theta & \cos\theta\cos\theta - \sin\theta\sin\theta & 0 \\ -\sin\theta\sin\theta + \cos\theta\cos\theta & -\sin\theta\cos\theta - \cos\theta\sin\theta & 0 \\ 0 & 0 & 0 \end{pmatrix} \\
&= A\begin{pmatrix} \sin 2\theta & \cos 2\theta & 0 \\ \cos 2\theta & -\sin 2\theta & 0 \\ 0 & 0 & 0 \end{pmatrix},
\end{aligned} \tag{A.13}$$

and for $\theta = 45°$, we find that our stress tensor in the rotated coordinate system is

$$\sigma_{kl}^{(\mathbf{c})} = A\begin{pmatrix} 1 & 0 & 0 \\ 0 & -1 & 0 \\ 0 & 0 & 0 \end{pmatrix}. \tag{A.14}$$

Figure A.6 graphically shows this rotation of the coordinate system.

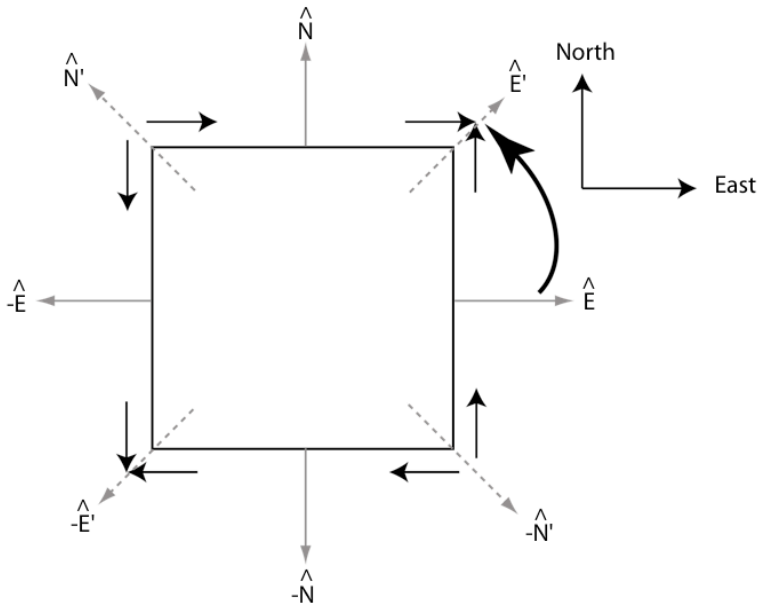

Figure A.6. *Rotation of the coordinate system counter-clockwise by 45°. The solid normal vectors represent the unrotated coordinates and the dashed normal vectors represent the rotated coordinates. Note that the rotation results in compression in the primed, or new $N-S$ direction, and tension in the new $E-W$ direction.*

Any symmetric stress matrix, $\boldsymbol{\sigma}$, can be represented in terms of a diagonal matrix $\boldsymbol{\sigma}'$, which contains the eigenvalues of $\boldsymbol{\sigma}$, and a rotation matrix $\mathbf{V}$, which contains eigenvectors of $\boldsymbol{\sigma}$, where $\boldsymbol{\sigma} = \mathbf{V}\boldsymbol{\sigma}'\mathbf{V}^T$. Once we know $\mathbf{V}$, which rotates our coordinate system to the primed coordinate system, we can rotate our stress tensor $\boldsymbol{\sigma}$ or anything else into this coordinate system. For example, $\boldsymbol{\sigma}' = \mathbf{V}^T\boldsymbol{\sigma}\mathbf{V}$. This is called the principal coordinate system, and the diagonal values of $\boldsymbol{\sigma}'$ are the principal stresses, where

$$\boldsymbol{\sigma}' = \begin{pmatrix} \sigma_1 & 0 & 0 \\ 0 & \sigma_2 & 0 \\ 0 & 0 & \sigma_3 \end{pmatrix}$$

and the principal stresses, σ_1, σ_2, and σ_3 are ordered from most to least compressive, i.e., from smallest (most negative) to largest (most positive) given that in our convention compression yields negative values and tension yields positive values. $\mathbf{V} = V_{ij}$ is the eigenvector matrix associated with the eigenvalues where V_{i1} is the eigenvector for σ_1, V_{i2} is the eigenvector for σ_2, and V_{i3} is the eigenvector for σ_3. σ_1 is the maximum compressive stress, σ_3 is the minimum compressive stress, and σ_2 is the intermediate compressive stress. Therefore, for a deviatoric matrix where the trace has been subtracted, one finds that $\sigma_1 < 0$ (compression), $\sigma_3 > 0$ (tension), and $\sigma_2 = -(\sigma_1 + \sigma_3)$. σ_1, σ_2, and σ_3, are the eigenvalues of $\boldsymbol{\sigma}$, and $\vec{x}_1 = \mathbf{V}\hat{E} = V_{i1}$, $\vec{x}_2 = \mathbf{V}\hat{N} = V_{i2}$, and $\vec{x}_3 = \mathbf{V}\hat{U}p = V_{i3}$ are the eigenvectors in the new principal coordinate system.

Translating a Stress Matrix into Strike, Dip, and Rake Earthquake Fault Parameters

Ultimately, we wish to ask, given a particular stress state described by our stress tensors, what is the failure orientation? What synthetic fault parameters (strike, dip, and rake) are produced when the material fails? These questions can only be answered once a fracture criterion, that determines the timing, locations, and possibly the orientations of the failures, has been chosen. The two fracture criteria we applied in this project were the Hencky-Mises plastic yield condition [*Housner and Vreeland*, 1965] and the Coulomb-Mohr criterion. Appendix B compares these two fracture criteria in detail; however, for

this section we need only compare how they affect the orientation of failure relative to the principal eigenvectors of the stress tensor.

In the Hencky-Mises plastic yield condition, failure always occurs on a plane at $45°$ between the σ_1 and σ_3 axes. There are two possible failure planes, and they are perpendicular to one another. In this particular case, the two possible failure planes match the two possible planes on a focal sphere. The optimally oriented planes of our plastic yield criterion are also equivalent to the failure planes in the Coulomb-Mohr criterion with coefficient of friction $\mu = 0$. If the Coulomb-Mohr failure criterion is used instead, then the failure planes will occur at $\pm\theta$ relative to the σ_1 axis, where $\theta \leq 45°$. The formula for determining θ depends on the coefficient of friction, μ, where, $\theta = \frac{\pi}{4} - \frac{\tan^{-1}(\mu)}{2}$. If $\mu > 0$, then $\theta < 45°$ and the two failure planes are no longer perpendicular to one another; thus the two possible failure planes will be associated with different focal mechanisms. Therefore, the focal mechanism will depend on which failure plane one chooses.

Once one knows θ relative to the σ_1 axis based on the fracture criterion, then it is fairly simple to calculate all four possible slip and normal vectors by rotating the σ_1 and σ_3 axes (Figures A.7 and A.8). The slip and normal vectors can then be converted to strikes, dips, and rakes. Two possible triplets of strikes, dips, and rakes are associated with each failure plane depending on which side of the failure plane one considers fixed. Typically, we choose the strike, dip, and rake with dip ≤ 90. This results in one triplet of strike, dip, and rake for each failure plane; given that we have two failure planes, we now have two triplets of strike, dip, and rake to randomly choose between when we create our

synthetic focal mechanism catalog. However, we find that it is helpful to have all four sets of slip and normal vectors when attempting to determine the minimum angle between two different focal mechanisms. It might be possible to reduce the problem to one set of slip and normal vectors per failure plane if we specify that the slip and normal vectors bound a compressional quadrant. However, for the numerical calculations in this thesis, we use all four possible sets of slip and normal vectors per failure plane when calculating the minimum angular difference between pairs of focal mechanisms.

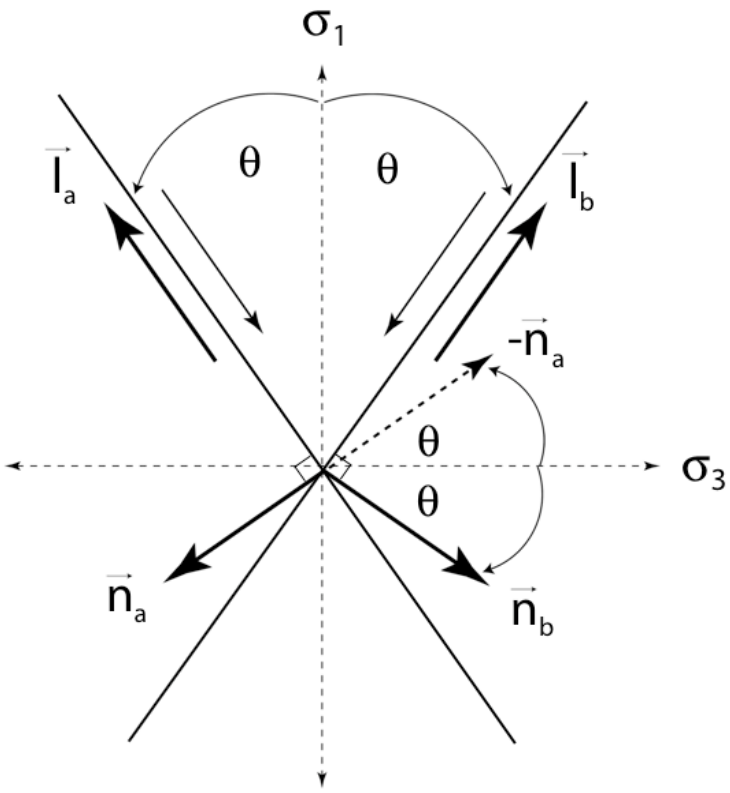

Figure A.7. *Slip and normal vectors for the two possible failure planes can be generated by rotating the* σ_1 *and* σ_3 *eigenvectors about the* σ_2 *axis. For example, our first slip vector,* $\vec{l}_a$*, is the* σ_1 *eigenvector rotated counter-clockwise through an angle* θ*.* $\vec{l}_b$*, the slip vector for the alternate failure plane, is the* σ_1 *eigenvector rotated clockwise through an angle* θ*.* $-\vec{n}_a$*, the negative of the normal vector associated with* $\vec{l}_a$*, is the* σ_3 *eigenvector rotated counter-clockwise through an angle* θ*. Last,* $\vec{n}_b$*, the normal associated with the slip vector* $\vec{l}_b$*, is the* σ_3 *eigenvector rotated clockwise through an angle* θ*.*

Figures A.7 and A.8 graphically show the rotation of eigenvectors in the principal coordinate system to produce our slip and normal vectors that will be converted into strikes, dips, and rakes. The procedure to determine the four possible slip and normal vectors from an arbitrary symmetric stress tensor, $\boldsymbol{\sigma}$, is as follows:

1) Calculate the eigenvalues and eigenvectors of $\boldsymbol{\sigma}$, where $\boldsymbol{\sigma} = \mathbf{V}\boldsymbol{\sigma}'\mathbf{V}^T$ and $\mathbf{V}$ is the eigenvector matrix.
2) Rotate the coordinate system of the σ_1 and σ_3 eigenvectors into the principal coordinate system, using the transpose of the eigenvector matrix, $\mathbf{V}^T$.
3) In the principal coordinate system, rotate the σ_1 and σ_3 eigenvectors about the σ_2 axis as shown in Figures A.7 and A.8 to produce the slip and normal vectors for the failure planes.
4) Rotate the coordinate system of the slip and normal vectors back into the unprimed E, W, and Up coordinate system using the eigenvector matrix, $\mathbf{V}$.

So the equations might look like $\vec{l}_a = \mathbf{V}\mathbf{R}(\theta)\mathbf{V}^T\vec{x}_1$, $\vec{l}_b = \mathbf{V}\mathbf{R}^T(\theta)\mathbf{V}^T\vec{x}_1$,

$\vec{n}_a = -\mathbf{V}\mathbf{R}(\theta)\mathbf{V}^T\vec{x}_3$, $\vec{n}_b = \mathbf{V}\mathbf{R}^T(\theta)\mathbf{V}^T\vec{x}_3$, and $\vec{l}_c = -\vec{l}_a$, $\vec{l}_d = -\vec{l}_b$, $\vec{n}_c = -\vec{n}_a$, $\vec{n}_d = -\vec{n}_b$,

where

$$\mathbf{R}(\theta) = \begin{pmatrix} \cos\theta & 0 & \sin\theta \\ 0 & 1 & 0 \\ -\sin\theta & 0 & \cos\theta \end{pmatrix} \tag{A.15}$$

and $\vec{x}_1$, $\vec{x}_2$, $\vec{x}_3$ are the eigenvectors for the σ_1, σ_2, and σ_3 axes.

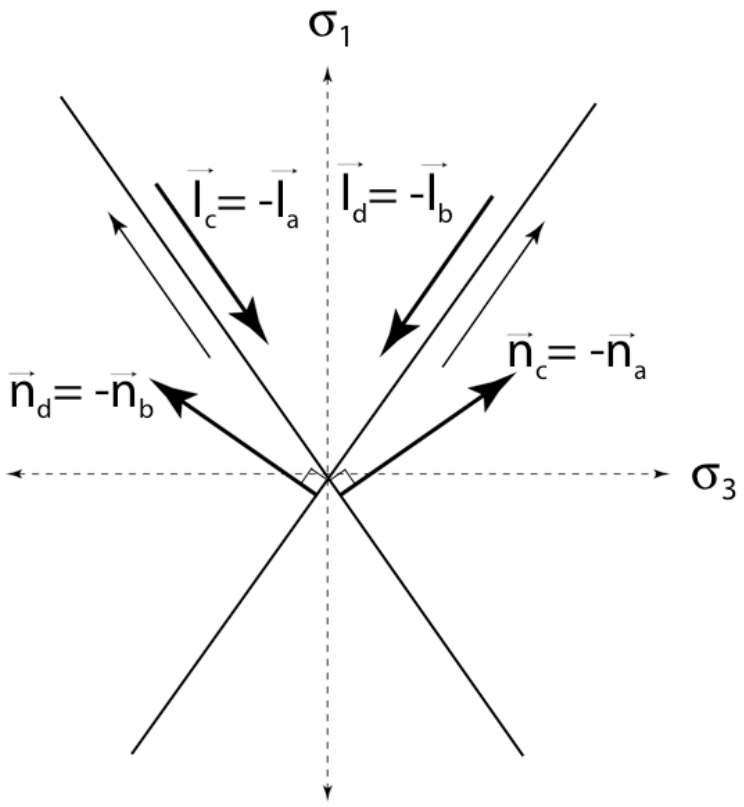

Figure A.8. *The last two sets of slip and normal vectors are simply the slip and normal vectors on the other side of the fault planes. In general, the slip vector on side two equals the negative of the slip vector on side one. The normal vector on side two equals the negative of the normal vector on side one. In a sense, these are the alternate slip and normal vectors for the two possible failure planes.*

Once we have a slip vector, normal vector pair, we can begin determining the strike, dip, and rake. Figures A.9 and A.10 illustrate how the strike and dip of a plane can be calculated from a given normal vector. The equation for the strike of the plane is

$$\theta = \tan^{-1}\left(\frac{\sin\theta}{\cos\theta}\right) = -\tan^{-1}\left(\frac{n_N}{n_E}\right), \tag{A.16}$$

and the equation for the dip of the plane is,

$$\delta = \tan^{-1}\left(\frac{\sin\delta}{\cos\delta}\right) = \tan^{-1}\left(\frac{\sqrt{n_E^2 + n_N^2}}{n_U}\right). \tag{A.17}$$

Note that if the normal vector points down, one must first switch the sign of the normal and slick vectors, $\vec{n} = -\vec{n}$ and $\vec{l} = -\vec{l}$, if $n_U < 0$ before calculating the strike and the dip of the plane.

Last, Figure A.11 graphically shows how one calculates the rake of the rupture given the strike angle and slip vector. We calculate what is the strike vector, $\vec{h}$, then find the angle between $\vec{h}$ and $\vec{l}$, which is rake, λ.

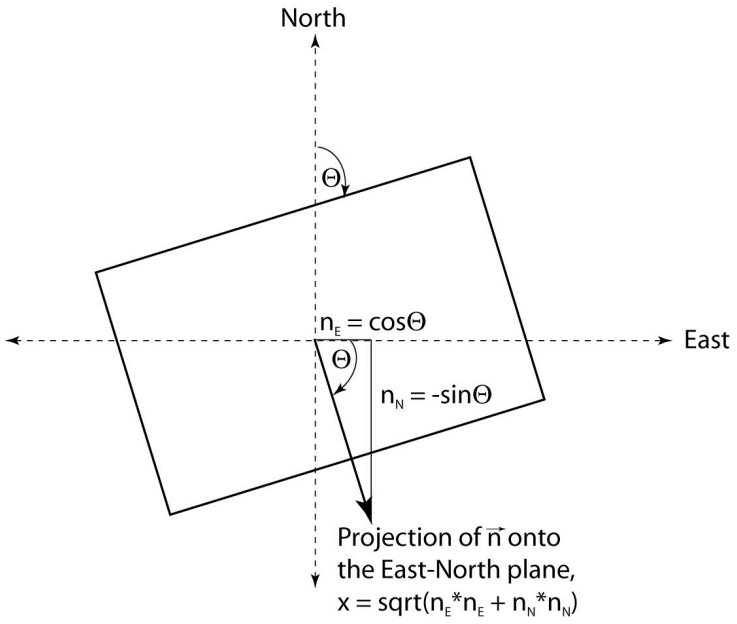

Figure A.9. *How to calculate the strike of a plane given the normal vector.*

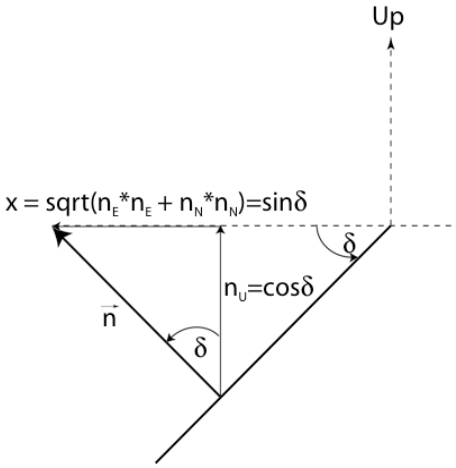

Figure A.10. *How to calculate the dip of a plane given the normal vector.*

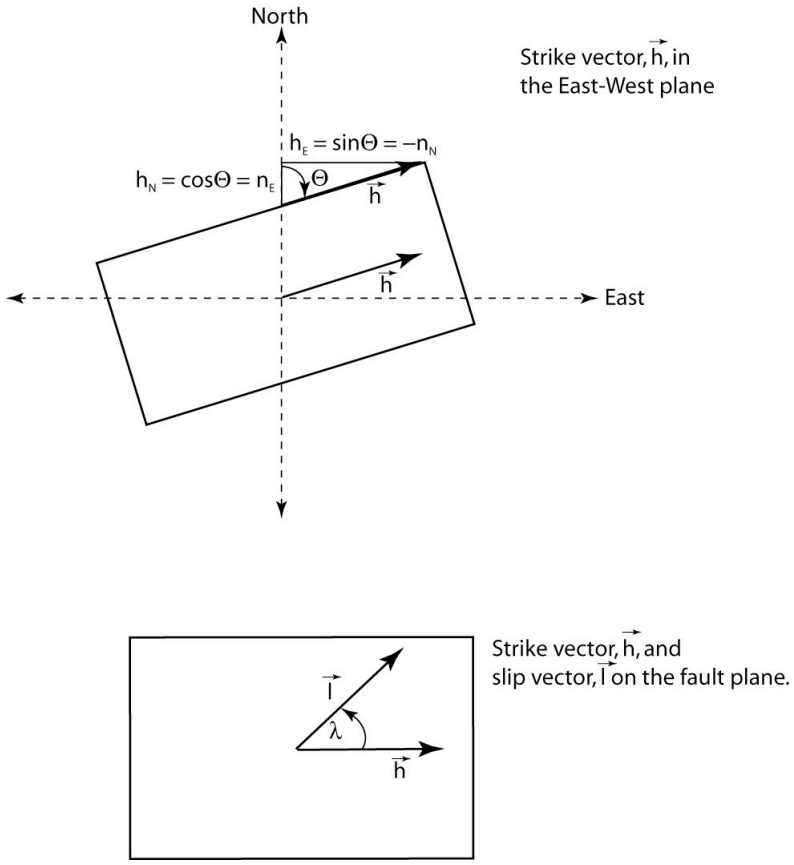

Figure A.11. *How to calculate the rake of a rupture. First, determine the strike vector,* $\vec{h}$ *, which by definition always has zero for the* $\hat{U}p$ *component. Then use the definition of a dot product of two vectors to derive the rake angle,* λ *.*

The formula for the strike vector will be

$$\vec{h} = \begin{pmatrix} \sin\Theta \\ \cos\Theta \\ 0 \end{pmatrix} = \begin{pmatrix} -n_N \\ n_E \\ 0 \end{pmatrix}. \tag{A.18}$$

Using the definition of the dot product, we can then determine the angle λ ,

$$\vec{h} \cdot \vec{l} = \| \vec{h} \| \ \| \vec{l} \| \cos\lambda$$
$$\lambda = \cos^{-1}\left(\frac{\vec{h} \cdot \vec{l}}{\| \vec{h} \| \ \| \vec{l} \|} \right). \tag{A.19}$$

These formulas work for either set of conjugate planes.

Now if one starts with the strike, dip, and rake of a failure, one knows the coefficient of friction, and one wishes to determine the stress tensor, the procedure is the inverse of what has just been done. One calculates the slip and normal vectors of the plane, then rotates these by $\pm\theta$ in the principal coordinate frame to produce the eigenvectors. We will not go through the derivation, but one can look to Jarosch and Aboodi [1970] for how to calculate the slip and normal vectors from strike, dip, and rake. For our particular coordinate system, the equations are,

$$\vec{l} = \begin{pmatrix} l_E \\ l_N \\ l_U \end{pmatrix} = \begin{pmatrix} \sin(\Theta)\cos(\lambda) - \cos(\Theta)\cos(\delta)\sin(\lambda) \\ \cos(\Theta)\cos(\lambda) + \sin(\Theta)\cos(\delta)\sin(\lambda) \\ \sin(\delta)\sin(\lambda) \end{pmatrix}$$
$$\vec{n} = \begin{pmatrix} n_E \\ n_N \\ n_U \end{pmatrix} = \begin{pmatrix} \cos(\Theta)\sin(\delta) \\ -\sin(\Theta)\sin(\delta) \\ \cos(\delta) \end{pmatrix}. \tag{A.20}$$

After we have rotated, $\vec{l}$ and $\vec{n}$ into our eigenvectors, $\hat{x}_1$ and $\hat{x}_3$, we can reconstruct the stress tensor exactly if we also know the eigenvalues. If not, then there is an ambiguity as to the magnitude the stress tensor. For example, if we have the stress tensor $\boldsymbol{\sigma}$ with its associated eigenvector matrix $\mathbf{V}$ and eigenvalue matrix $\boldsymbol{\sigma}'$, we can reconstruct $\boldsymbol{\sigma}$ exactly.

$$\boldsymbol{\sigma} = \mathbf{V}\boldsymbol{\sigma}'\mathbf{V}^T \tag{A.21}$$

See the following example.

$$\boldsymbol{\sigma} = 0.618\begin{pmatrix} 1 & 1 & 0 \\ 1 & 0 & 0 \\ 0 & 0 & -1 \end{pmatrix}$$

$$\mathbf{V} = \begin{pmatrix} 0 & 0.5257 & -0.8507 \\ 0 & -0.8507 & -0.5257 \\ 1.000 & 0 & 0 \end{pmatrix} \qquad \text{(A.22)}$$

$$\boldsymbol{\sigma}' = \begin{pmatrix} -0.618 & 0 & 0 \\ 0 & -0.382 & 0 \\ 0 & 0 & 1.000 \end{pmatrix}$$

In this case, indeed, $\boldsymbol{\sigma} = \mathbf{V}\boldsymbol{\sigma}'\mathbf{V}^T$. However, what if one does not know the eigenvalues (principal stresses) and one has to guess their values? For example, assume one might choose $\boldsymbol{\sigma}'_{Guess}$ to be

$$\boldsymbol{\sigma}'_{Guess} = \begin{pmatrix} -1.0000 & 0 & 0 \\ 0 & 0 & 0 \\ 0 & 0 & 1.0000 \end{pmatrix}. \qquad \text{(A.23)}$$

In this case our best guess for the stress matrix is, $\boldsymbol{\sigma}_{Guess} = \mathbf{V}\boldsymbol{\sigma}'_{Guess}\mathbf{V}^T$, where

$$\boldsymbol{\sigma}_{Guess} = 0.618\begin{pmatrix} 1.1708 & 0.7236 & 0 \\ 0.7236 & 0.4472 & 0 \\ 0 & 0 & -1.6180 \end{pmatrix}. \qquad \text{(A.24)}$$

One can see that $\boldsymbol{\sigma} \neq \boldsymbol{\sigma}_{Guess}$. They may be close but not quite equal to one another. They do, however, produce the same strike, dip, and rake since the same eigenvector matrix, $\mathbf{V}$, is used for both $\boldsymbol{\sigma}$ and $\boldsymbol{\sigma}_{Guess}$.

Translating a Stress Matrix into P and T axes

Viewing $\vec{P}$ (Pressure) and $\vec{T}$ (Tension) axes on an equal area plot is an excellent way to visualize earthquake focal mechanism orientations for a large number of earthquakes. The definition of the $\vec{P}$ and $\vec{T}$ vectors is

$$\begin{aligned} \vec{P} &= \frac{1}{\sqrt{2}}\left(\vec{n} - \vec{l}\right) \\ \vec{T} &= \frac{1}{\sqrt{2}}\left(\vec{n} + \vec{l}\right) \\ \vec{B} &= \vec{n} \times \vec{l} \end{aligned} \tag{A.25}$$

where $\vec{n}$ is the normal vector to a shear dislocation plane, $\vec{l}$ is the slip vector, and $\vec{B}$ is the vector normal to $\vec{n}$ and $\vec{l}$. $\vec{P}$ and $\vec{T}$ vectors are rotated ±45° relative to $\vec{n}$ and $\vec{l}$. In the case of optimally oriented planes, i.e., $\mu = 0$, $\vec{P}$ corresponds to the σ_1 (most compressive) eigenvector of the stress matrix, $\vec{T}$ corresponds to the σ_3 (least compressive) eigenvector of the stress matrix, and $\vec{B}$ corresponds to the intermediate, σ_2 eigenvector of the stress matrix. Except for Appendix C, which explicitly discusses the Coulomb failure criterion, all our results assume optimally oriented planes with the plastic yield criterion; hence, this correspondence between the $\vec{P}$ and $\vec{T}$ vectors and our stress matrix eigenvectors for optimally oriented planes is especially useful.

For example, in Figure A.12 we have the following stress matrix being represented,

$$\sigma_{ij} = A\begin{pmatrix} 1 & 0 & 0 \\ 0 & -1 & 0 \\ 0 & 0 & 0 \end{pmatrix} \tag{A.26}$$

where there is tension (blue) in the $E-W$ direction and compression (red) in the $N-S$ direction. Since $\mu = 0$, the two possible failure planes are at $\theta = \pm 45°$ from the σ_1 axes. We could take any one of the possible four sets of normal vectors and slip vectors to reproduce the same $\vec{P}$ and $\vec{T}$ axes.

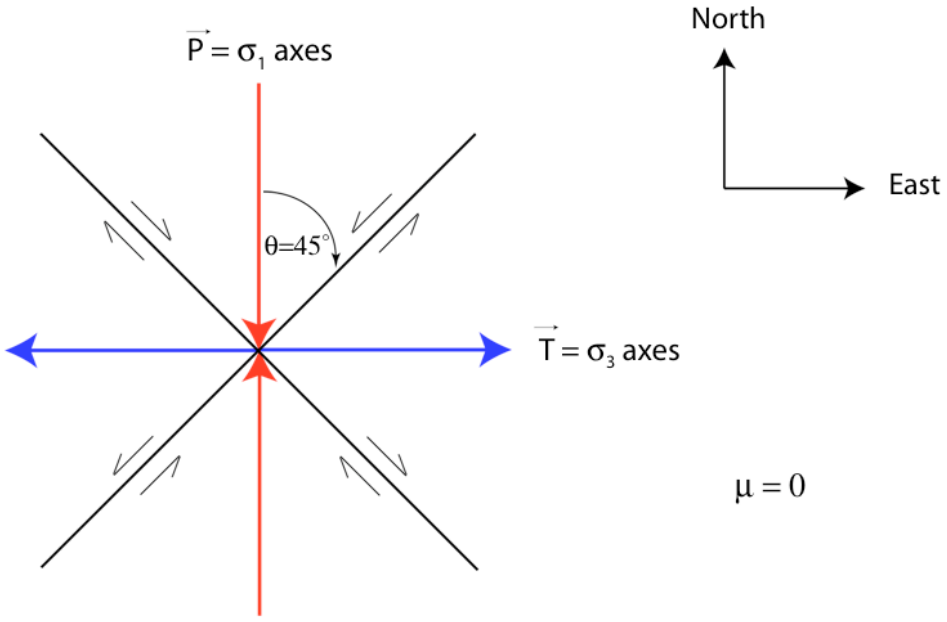

Figure A.12. *$N-S$ compression (red) and $E-W$ tension (blue). In this case of optimally oriented planes, $\mu = 0$, the stress matrix eigenvectors align with the $\vec{P}$ and $\vec{T}$ axes. The two possible failure planes are 45° from the $\vec{P}$ and $\vec{T}$ axes.*

Figure A.14 is an equal area plot of $\vec{P}$ and $\vec{T}$ axes for 1,000 synthetic earthquakes where each red asterisk represents a $\vec{P}$ axes for a single event and each blue circle represents a $\vec{T}$ axes for a single event. The average $\vec{P}$ and $\vec{T}$ orientation is approximately the same as Figure A.12. The distance from center represents the dip or plunge, δ, of the $\vec{P}$ or $\vec{T}$ vectors, where a plunge of 90° corresponds to the center and a plunge of 0° would plot

at the circumference of the circle. The azimuth, or angular distance from the top of the circle, represents the azimuth from N, θ, for the $\vec{P}$ or $\vec{T}$ vectors. Figure A.13, a cartoon of an equal area plot, visually shows these relations.

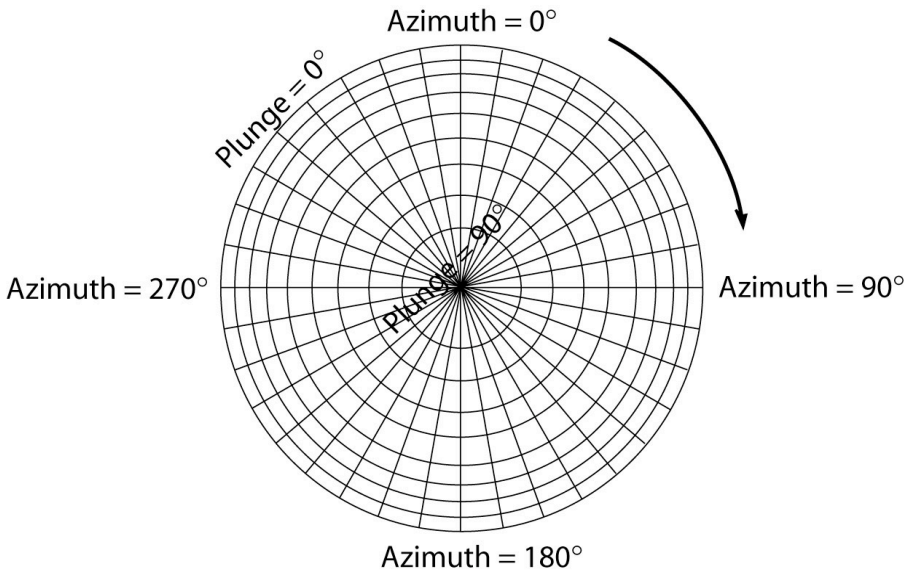

Figure A.13. *A cartoon of a typical equal area plot for P-T azimuths and plunges. The longitude, θ, is the azimuth of the circle, and plunge, δ, is plotted as a function of radial distance where, $\delta = 90°$ at the center and $\delta = 0°$, at the circumference. Note the radial lines are not necessarily to scale.*

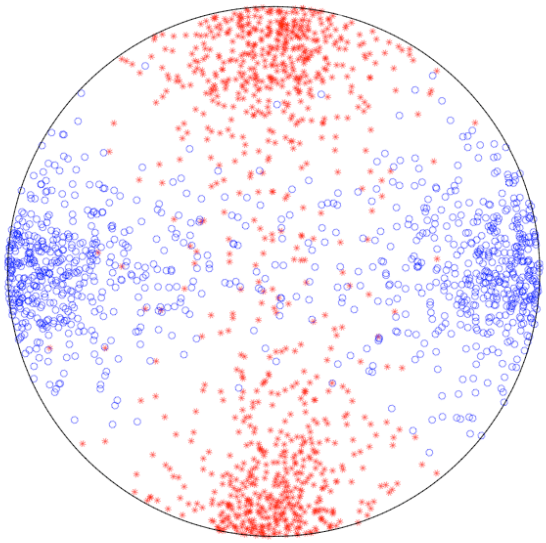

Figure A.14. *Equal area plot of* $\vec{P}$ *and* $\vec{T}$ *vectors for 1,000 synthetic earthquakes with an average compression axis in the* $N-S$ *direction and an average tension axis in the* $E-W$ *direction. The red asterisks are the* $\vec{P}$ *vectors and the blue circles are the* $\vec{T}$ *vectors. The azimuth,* θ*, of the vectors is represented by the angular distance from the top of the circle in the clockwise direction. The dip or plunge of the vectors,* δ*, is represented by the radial distance where the center of the circle is a* $\delta = 90°$*, and the circumference is a* $\delta = 0°$*.*

References

Housner, G. W., and T. J. Vreeland (1965), *The Analysis of Stress and Deformation*, 440 pp., Division of Engineering and Applied Science, California Institute of Technology.

Jarosch, H., and E. Aboodi (1970), Towards a unified notation of source parameters, *Geophysical Journal of the Royal Astronomical Society*, *21*, 513–&.

Michael, A. J. (1984), Determination of stress from slip data: Faults and folds, *Journal of Geophysical Research-Solid Earth*, *89*, 11517–11526.

Michael, A. J. (1987), Use of focal mechanisms to determine stress: A control study, *Journal of Geophysical Research-Solid Earth*, *92*, 357–368.